Yb:YAG Laser Crystals with Controlled Doping Distribution

Mikayel Arzakantsyan

ÉCOLE POLYTECHNIQUE
ParisTech

THÈSE

pour obtenir le grade de
DOCTEUR de l'ECOLE POLYTECHNIQUE
Spécialité : Physique

présentée par
Mikayel ARZAKANTSYAN

Titre de la thèse :

Yb:YAG Laser Crystals with Controlled Doping Distribution

soutenue le 21 Mars 2013 devant le jury composé de :

MM.	B. VIANA	Président du jury
	A. BRENIER	Rapporteur
	R. MONCORGÉ	Rapporteur
	J.-C. CHANTELOUP	
	V. CHANI	
	G. GALLOT	
	P. GEORGES	
	V. GEVORGYAN	

Acknowledgements

The success of a research project like this is never a work of a single person. Many individuals contributed in different ways to the preparation and completion of this work and I would like to extend my appreciation to all of them.

First and foremost, my utmost gratitude goes to head of Lucia project and my direct supervisor, Dr. Jean-Christophe CHANTELOUP. His guidance, advice, enthusiasm and encouragement provided me necessary support throughout these years to proceed and to complete my dissertation. He will always be the role model of academia researcher for me. I deeply appreciate all his efforts to help me to adapt to the life in France in the beginning of my thesis. Also, I would like to mention his extraordinary sense of humor, which I will never forget.

The work described in this manuscript was a result of fruitful and continuative collaboration between laboratory LULI, Ecole Polytechnique and "Laserayin Tekhnika" CSC.

I wish to express my feeling of a gratitude to the director of LULI Francois AMIRANOFF, who participated in the creation of this thesis visiting Armenia with Jean-Christophe CHANTELOUP and provided necessary support throughout all these years.

My profound gratitude goes also to Vahan VARDANYAN, general director of "Laserayin Tekhnika", who created all necessary conditions for the success of our numerous experiments and contributed greatly to this work. His continuous support to scientific projects in general is highly appreciated by many researchers.

I am indebted to all current and former members of Lucia team in particular: Thierry Novo, Daniel ALBACH, Sofiane BAHBAH, Antonio LUCIANETTI, Gilbert BOURDET, Philippe HOLLANDER, Vincent BERNARD and Samuel MARRAZZO. These people extended their valuable assistance by fruitful discussions, nightlong experiments and also many personal occasions.

My special esteem goes to Patrick GEORGES who accepted to be the supervisor of this work and was always ready to discuss and help with very precious advice.

It is my great pleasure to thank Bruno VIANA as the president of my PhD thesis defense jury, Alain BRENIER and Richard MOCNORGÉ, who reviewed my thesis manuscript, and also to the other jury members Vladimir GEVORGYAN, Guilhem GALLOT, Valery CHANI.

I express my kind gratitude to the staff of laboratory LULI and LASERAYIN TEKHNIKA for continuative support provided with the highest competency, as well as for excellent working conditions and personal relations.

My friends from laboratory LULI created extraordinary ambiance and many occasions from sport events to parties and by this gifted me lot of emotions and life-long souvenirs and for this I am very grateful to them. In particular I would like to thank Guillaume GARZINO who introduced me to the world of extreme sports and also supported me a lot during my stay in France to discover all aspects of this magnificent country.

I am very grateful to LUYS foundation (executive director: Jacqueline Karaaslanian) for financial and moral support throughout my thesis project, as well as in general for their contribution to educational system.

Last but not least, my special thanks to my family. Without their support none of any steps of my studies would be realized.

Here I only mentioned several names, whose contribution was obvious and crucial during these wonderful 4 years. Indeed the list is very long and my sincere feeling of gratitude goes to everyone whom it may concern.

Introduction

A revolutionary invention of the last century, the light source known by the acronym "LASER (Light Amplification by Stimulated Emission of Radiation)", is one of the most used devices as of today. In our society, most of people are in direct or indirect contact with devices using lasers several times a week. Coherent light emitted by lasers has indeed applications from daily life, medicine and urban needs to highly advanced scientific problems exploring the frontiers of knowledge of fundamental physics from nucleus scale up to universe. Depending on the purposes, lasers cover a wide range of configurations, output energies, emission wavelength, operation modes (continuous-wave or pulse), repetition rates, pulse durations and etc... In industry, lasers are used for micro- and macro-scale cutting, welding, graving, ablation, lithography. In urban needs the devices based on lasers are used to measure distances, velocities, temperature and etc. Lasers became essential tools for medical applications such as eye surgery, micro-surgeries, dental therapy, tattoo removal, imaging, and etc…

Lasers are nowadays used in almost all scientific fields: archeology, biology, chemistry,... and physics of course where one of its dedicated fields is laser-matter interaction physics. In particular laser-plasma interaction is among the hottest topics and foreseen achievements in this domain may ultimately lead to man produced stellar energy at power plant scale. This can be done by the generation of energy through thermo-nuclear fusion relying for instance on laser fusion.

Increased technological requirements on laser systems require continuous improvements at all stages of a laser chain: light generation, transport, beam-shaping amplification, temporal shaping, frequency conversion… Special attention is dedicated to the gain media stimulating the improvement of manufacturing techniques. In the quest for optimum crystals, numerous growth methods and equipment have been developed. Rather new are the laser ceramics which manufacturing recently became reliable and affordable, making this form of solid state gain media a solution of choice when the processing of crystals is technically not possible (due to the size/composition limitations imposed by crystal manufacturing techniques).

The *Laboratoire pour l'Utilisation des Lasers Intenses* (LULI) is a leading laboratory in warm and dense plasma physics research. It is a joint research unit between Ecole Polytechnique, CNRS (*Centre National de Recherche Scientifique*), CEA (*Commissariat d'Energie Atomique*) and University Paris VI. In the very early 2000 years, LULI initiated the Lucia laser project, a test-bed dedicated to study laser physics bottlenecks and challenges faced by laser chains foreseen for laser fusion applications. The aim of Lucia is to deliver 100 joules in the 1 μm wavelength region at 10 Hz repetition rate for 10 ns duration pulses. This is possible to achieve only with new technological solutions. Lucia is a Diode Pumped Solid state Laser (DPSSL) chain relying on trivalent ytterbium doped yttrium aluminum garnet (Yb:YAG) crystals/ceramics. Although its current performances (14 J/2 Hz) are likely to be improved by a factor 2 in both repetition rate and energy, limitations are foreseen due to gain medium thermal stresses and Amplified Spontaneous Emission. In the second part of this century first decade, it became obvious that a need for advanced new gain medium was

required; not only in the framework of Lucia but more generally for high average power DPSSL laser systems. The Lucia team then engaged itself, in collaboration with the Armenian company *Laserayin Tekhnika CSC*, in a new research field dedicated to laser gain medium engineering. Starting from 2006, a dedicated growth campaign aimed to improving the characteristics of existing Yb:YAG crystals was launched at *Laserayin Tekhnika CSC* premises. Two rather ambitious goals were set: -1- growing large aperture (> 50 mm) laser grade stress-free crystals and, -2- exploring the feasibility to process crystals with variable spatial distribution of activator (Yb^{3+} in this case) within the host media (YAG in this case). The importance of the first goal was justified due to the lack of large sized high quality crystals in the market and the high relevance for Lucia ASE management needs. The second goal started with an exploratory approach motivated by the very peculiar arrangement offered by the Bagdasarov furnaces of *Laserayin Tekhnika CSC*. The current work is dedicated to these two research axis.

Laserayin Tekhnika CSC is a company manufacturing laser crystals, optical elements and laser devices since 1972. Its YAG crystals with different dopants are widely used in many scientific laboratories and laser manufacturing companies throughout the world. In order to obtain high quality laser crystals, *Laserayin Tekhnika CSC* indeed uses the so-called Bagdasarov method. When proposed (1972), it proved to be a revolutionary advancement in crystal growth techniques, offering important improvements, allowing achieving very impressive results especially for YAG and corundum single crystal growth and greatly contributing to the success of this work.

The current work is divided into 6 chapters:

1st chapter gives an historical perspective indicates the criteria and justification for laser material choice. Then Lucia laser chain is also presented.

2nd chapter justifies the role of variable doping in laser crystals through a test case study. The impact on thermal management is discussed for Lucia amplifier and pre-amplifier.

3rd chapter gives an overview of crystal growth existing techniques with a focus on growth from melt, exploring the main processes which have to be taken into account for growth-from-melt methods. Then description of the Bagdasarov method with its required equipment is given with experimental data opening perspectives in method characterization and proposed further improvement.

4th chapter is summarizing the results on doping distribution for all growth sequences performed in the frame of this work. Description and cross evaluation of different measuring techniques are provided. Using the gathered experimental data, a mathematical model is derived to predict the final doping distribution from starting and growth conditions.

5th chapter describes gain distributions, temperature distributions and laser generation experiments performed with variably doped crystals. Also, a detailed study for Lucia gain medium improvement with dopant variation is given with the help of a mathematical model.

Finally, the 6th chapter gives the results on the large crystal growth campaign and describes the technological changes required for this purpose. Structural and optical characterizations of the large and variably doped crystals are presented as well as in this chapter.

1. High average power Lasers: Motivations and challenges. The Lucia Laser system

1.1. Introduction

1.1.1. Brief historical overview

Revolutionary postulate of A. Einstein in 1917 about "reverse process to absorption" gave birth to optical generators further named LASERs. Only many years ago, the practical idea to use this process in order to amplify electromagnetic radiation was proposed. June 18th, 1951 author's certificate for Soviet patent N 123209 was given to Fabrikant and the work was titled "A method for electromagnetic radiation (ultraviolet, visible, infrared and radio) amplification, characterized with the process, that radiation to be amplified passes through a medium where, with the help of auxiliary radiation or other method, the excess concentration with respect to the equilibrium of atoms, other particles or systems on upper energy levels (excited states) is created" [1.1]. This title basically includes everything, which can be called quantum amplification. The first molecular generators named MASER were demonstrated in 1954 simultaneously by two different groups: N.G. Basov and A.M. Prokhorov in Physical Institute named after P.N. Lebedev, Moscow, USSR and C.H. Townes, J.P. Gordon and H.J. Zeiger in Columbia University, New York, USA. The creation of MASER established quantum electronics as a science, as mentioned A.M. Prokhorov during his speech for his Nobel Prize award in 1964 in Stockholm. The acronym LASER was first time used by G. Gould in 1959 during the conference on optical pumping [1.2]. It was noted also that acronym LOSER (Oscillation instead of Amplification) would be more correct [1.3]. Also it is in common to use the verb "to lase" in order to indicate laser operation.

The first optical maser – a ruby laser – was constructed by T.H. Maiman and demonstrated on May 16th, 1960 [1.4]; he patented this innovation on June 13th, 1961. This was a flashlamp-pumped solid state three-level laser producing light at 694 nm and performing pulsed operation. Not long ago after Maiman, December 12th, 1960 A. Javan tested first gas laser based on He-Ne. The infrared radiation was emitted by Neon atoms. First molecular laser was built by R. Patel in 1964. This laser had an efficiency of about 10% and produced a significant power of about 10W. The theoretical investigations in the area of semi-conductor single crystals, performed by N.G. Basov and his colleagues were followed by the creation of the first semi-conductor GaAs based laser invented by B. Hall in 1962.

1.1.2. Classification

Since the creation of the first lasers, laser engineering developed very fast and, up to the present time, it is one of the most various, dynamic and challenging fields of modern science. A large variety of lasers covers all the possible areas of applications: from daily life to unique experiments. Lasers can be classified according various criteria: energy level system, operation mode, gain medium type, etc…

1.1.2.1. *Atomic structure*

To make amplification possible, a population inversion has to be achieved, which means upper energy levels (excited state) have to be populated more than lower energy levels (equilibrium state). Also some investigations on lasers without inversion are reported in [1.5, 1.6, 1.7, and 1.8].

Energy level systems lasers can be classified as four-level, three level and quasi-three levels systems. Two-level system laser cannot exist due to the fact that, in such system, the inversion of population cannot simply be achieved. Principe of energy levels for four and three levels systems is given on Fig.1.1.

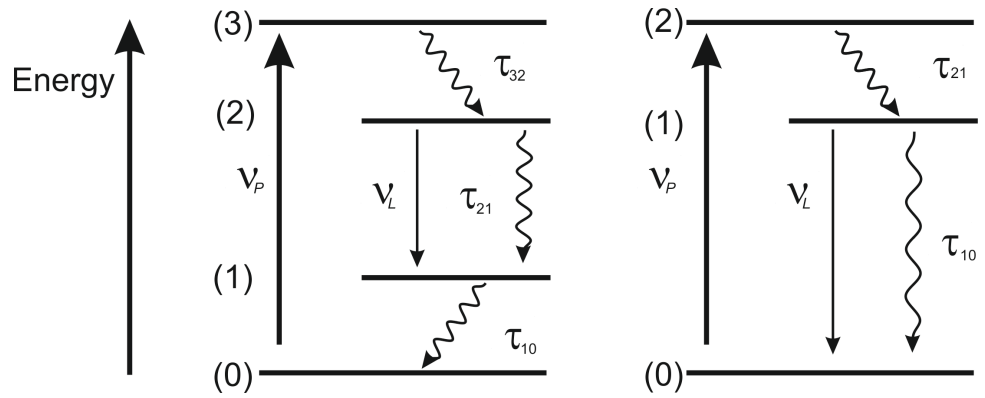

Fig. 1.1. Schematic representation of four-level (left) and three-level (right) systems

A quasi-3-level system is a particular case of a 4-level system, where energy split between upper and/or lower levels has the same order as kT, with k the Boltzmann constant. In 4-level system, ions are being excited from ground level (0) to upper level (3). Then, by radiative or non-radiative processes, they emit energy and reach the upper laser level (2). These transfers determine population of upper laser level therefore insuring the requested inversion population. Lasing occurs through the (2)-(1) transition. Afterwards ion returns to ground state and by this closes the cycle. τ_{32}, τ_{21}, and τ_{10} are the radiative lifetimes of 3rd, 2nd and 1st levels respectively. In the case of three-level system, upper pump and upper laser levels or lower pump and lower laser levels are fused together. Fig.1.1 displays the case when lower laser and pump levels are fused. In this case, the material has to be pumped really hard in order to obtain population inversion. An intermediate case also exists, when upper or lower levels are neither fused (like in three-level system) and nor strictly separated (like in four-level system), but their difference is in the order of kT, which means both levels are strongly influenced by Boltzmann distribution. This is the case of quasi-three-level system which is schematically very similar to four-level system.

1.1.2.2. *Operation mode*

Lasers can operate in continuous wave mode or pulsed mode. Continuous wave lasers are important for the applications where beam output power should stay constant over time. Only a few types of lasers cannot operate in this mode. For this operation continuous pump source is required to insure replenishment of population inversion. Pulsed operation means that the optical output has a form of pulses with a certain duration and repetition rate. This mode is required when high peak power of the pulse or large energy per pulse is needed. Pulse duration and repetition rate can vary over large ranges. As an example of pulsed laser application, one can mention laser ablation as well as laser driven inertial fusion. The peak power is very important in order to observe nonlinear effects. Very high peak powers lasers require energetic pulses of short duration.

1.1.2.3. *Gain medium nature*

With respect to the physical nature of its gain medium (also called active medium), lasers are classified as plasma laser, gas lasers, dye lasers, solid-state lasers and semiconductor lasers. As was already mentioned, the first gas laser (and the second laser in history) was built by the Iranian born American scientist A. Javan who was using He-Ne as a gain medium. Gas lasers can be based on mixture of several elements as well as made of a single-component. In general good output beam quality, near to diffraction limit, is characteristic to gas lasers, which is due to the fact, that gas medium has no significant optical distortions despite the significant temperature gradients. Some high power gas lasers rely on specific systems with forced convection and gas exchange. CO_2 lasers cover a broad application range due to the possibility to achieve high powers. These lasers operate with a mixture of CO_2, He and N_2, in some cases also H_2, H_2O vapor and Xe. The amplification occurs on CO_2 molecules and light is generated at a wavelength of 10.6 μm (the other emission lines are situated in the 9-11 μm region). The excitation of the molecules is performed through AC or DC controlled gas discharges. Nitrogen molecules, extracted by discharge, transfer the energy to CO_2 molecules by collisions. Helium is required for lower level relaxation and other gases are in use to accelerate the oxidation of generated Carbon Monoxide (CO).

The active medium of dye lasers consists of a solvent and organic dye. Traditionally, the solvent used is in a liquid phase, but currently, solid-state-like and gas dyes are used as well. This type of lasers was the first to operate in the broad range of wavelengths from UV to IR and therefore able to generate very short pulses (sub ps regime). Dye lasers were independently discovered by P. Sorokin and F. P. Schäfer (and colleagues) in 1966.

In Semiconductor lasers (also called Laser diodes), the light generation takes place due to the stimulated transitions between conduction and valence bands. These lasers are pumped electrically. The most used materials to construct semiconductor laser are GaAs , AlGaAs, GaP , InGaP , GaN, InGaAs, GaInNAs, InP, GaInP.

One of the main applications of laser diodes is to be used as a pump source for Solid State Lasers. Solid State Lasers pumped by laser diodes are usually called with the acronym DPSSL. The solid state gain media are activated by impurities (doping ions) serving as population inversion centers. Solid state lasers can operate in both CW and pulsed modes. The

host material defines optical, mechanical and thermal characteristics of a gain medium, and activator ions energy level defines spectral properties of lasing. Host material can be glass, single crystal or ceramics. Each of these three families carries advantages and disadvantages. Glasses are easy to process in large sizes and to be doped with a wide range of activators. On the other hand, the heat conductivity is very low which leads to poor thermal properties. This limits glass host material to low average power (very low repetition rate) operations. Glasses are for instance used in large scale laser systems producing only several shots per day (LULI2000 at LULI laboratory, Ecole Polytechnique [1.9], Laser Mega Joule (LMJ) [1.10] as examples of French facilities). If energetic multiple shots per second are required, then glasses should be ruled out. Single crystals are excellent host materials due to their thermal and optical characteristics, but, despite a large variety of existing fabrication methods, strong limitations occur. The largest laser quality crystals barely exceed 10 cm. Another disadvantage of single crystals is the complexity of doping management during growth process. The most promising and already widely used material is laser ceramics, which are small crystals co-sintered together. One can therefore says that ceramics are polycrystalline materials. Ceramics have better resistance to thermal shock than glasses or crystals and it is possible to produce them in large sizes. Also it is possible to obtain different doping ions concentrations within the gain medium with any request. Recent intensive development in the area of ceramics processing allowed improving its thermal and optical characteristics to match the ones for crystals in some particular cases. But still it is not easy to produce ceramics in large sizes with good optical quality. Not all the systems can be grown as ceramics: only cubic systems at the moment are reliably obtained by ceramic sintering techniques.

1.1.3. Motivation

High energy and low repetition rate laser systems deliver pulses for fundamental science studies, among them laser fusion physics. But a more applied sciences field, like laser driven Inertial Fusion Energy (IFE) power plant, higher repetition rates are required. In IFE, the goal is to ignite deuterium-tritium fuel pellets with intense enough bursts of particles (ions, photons,…) interacting at a relatively high repetition rate. The High Power laser Energy Research (HiPER) facility is dedicated to demonstrate the feasibility of laser driven IFE as an energy source of the future [1.11, 1.12]. It will face challenges not previously addressed by other multiple 100kJ-class laser systems like the National Ignition Facility (NIF) [1.13] or LMJ. HiPER project and other main large scale laser facilities in Europe are shown in Fig.1.2. We can see that, in order to demonstrate IFE economic viability, a 10 Hz repetition rate is required. Reaching this goal seems now reasonable within a few decades considering recent important scientific and technological evolutions in several key fields of laser physics (pump source, gain medium…). Considering cost of electricity (coe) [1.14] analysis and the maturity of the available technology, it is very likely that such multiple ~10 kJ/~10 kW beam lines facility will rely on diode pumped lasers instead of flash lamp technology. Taking into account thermal issues, which appear to be very critical with increasing repetition rates, glass (used up to now as a gain medium) has to be replaced by materials with better thermal conductivity: single crystals or ceramics.

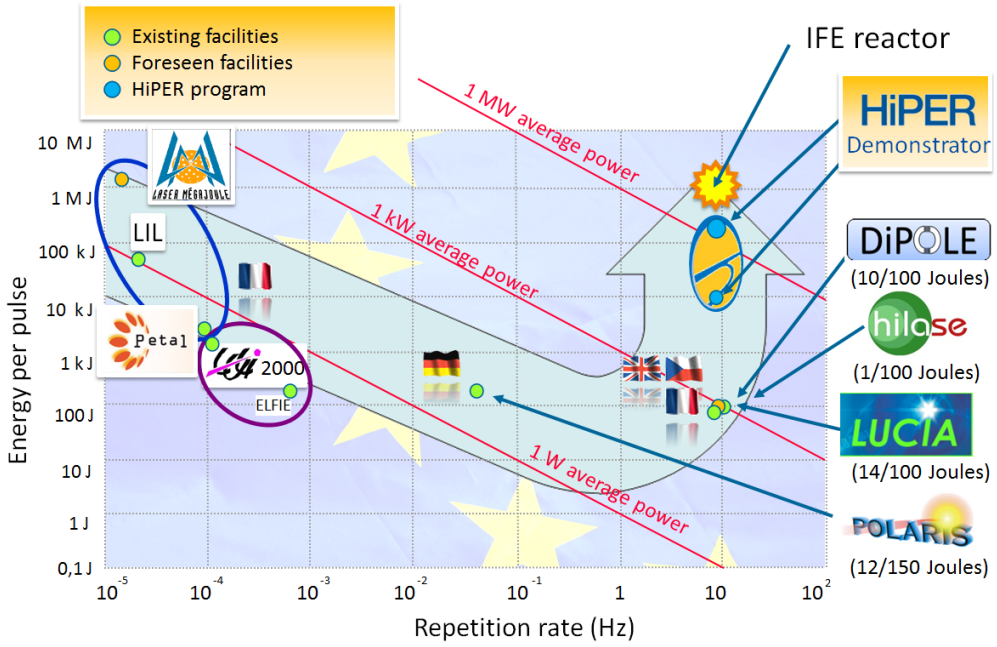

Fig. 1.2. Existing and near future large scale laser facilities towards HiPER facility and Inertial Fusion Energy power plant in Energy-per-pulse versus Repetition-rate in logarithmic scales

LULI's Lucia program takes place within this quest of a suitable driver for Laser driven IFE production. With its 100 J energetic goal, it might appear as a tiny brick for a hundred's of kJ-class facility like HiPER, but such laboratory scale laser chain allows nevertheless a rather accurate study and in depth understanding of the laser physics issues involved in such driver technology. The idea is to rely on parameters like the fluence (J/cm²), the [gain].[length] product,…taken similar to those envisioned for HiPER. The key issues expected to be faced by a laser driver for IFE and under study through the LUCIA program are:

- Laser damage threshold of the optical elements
- Thermal management
- ASE management
- Large size optics availability
- Overall system efficiency
- Pump light efficient transport and homogeneous distribution

Other issues like proton flux induced lifetime reduction of optical elements could of course not be addressed within the context of the Lucia program. This specific and crucial issue will partially be addressed through the ITER program [1.15 and 1.16] dedicated to Magnetic Fusion Energy (MFE) production but will ultimately have to be explored within the HiPER program by itself.

1.2. High Average Power Lasers

Efficiency (§1.2.1) of large laser systems operating at low (<1 shot per hour) repetition rate typically varies in the range of 0.1-1% [1.17]. Using diodes for pumping is one of the favored solutions to increase the efficiency at a competitive (in terms of coe) value of 10 to 20 %.

For high average power laser systems operating with several shots per second, the injected power is in the order of MW with most of it to be transformed into heat requiring tremendous effort to evacuate quickly enough. Otherwise, resulting heat loads in gain medium would quickly affect the beam propagation, the laser efficiency and could lead to fatal damages. The glass gain medium can therefore not be taken into consideration anymore due to its very low value of thermal conductivity; the only candidates remain the crystals and ceramics. Each of them has particular advantages and disadvantages from fabrication process to physical properties and they are essentially characterized by activator (§1.2.2) ions and host medium (§1.2.3).

As justified in this section, the selected material under study on the Lucia laser chain is an Yttrium Aluminum Garnet (YAG) doped with Ytterbium. Thermal considerations impose to shape it as a disk of similar ratio to the one expected for HiPER, i.e. a diameter about 10 times wider than the disk thickness. Amplified Spontaneous Emission (ASE) is therefore a key issue needing a specific figure of merit parameter to be introduced in §1.2.4.

1.2.1. Efficiency

One of the key parameters of a laser is its efficiency. One can talk about electro-optical efficiency (η_{eo}), or optical-optical efficiency (η_{oo}) which quantifies the ratio at which the transformation of the pump energy to lasing energy takes place [1.17]:

$$\eta_{eo} = \eta_{PS}\eta_T\eta_S\eta_A\eta_Q\eta_L(1-\pi_{ASE})\eta_{BO}\eta_E \qquad (1.1)..$$

where:

η_{PS} is the electrical to optical pump source efficiency;

η_T is the pump light transport efficiency;

η_S is the Stokes parameter, i.e. the energy ratio for pump & laser photons ($\eta_S=\lambda_P/\lambda_L$);

η_A is the absorbed fraction of the pump light;

η_Q is the quantum efficiency;

η_L is the storage efficiency due to fluorescence lifetime of upper state (τ_f);

π_{ASE} are the losses due to Amplification of Spontaneous Emission (ASE);

η_{BO} is the pump and extraction beam overlap;

η_E is the extraction efficiency.

In the right side of equation (1.1), the last seven terms can be combined as the optical to optical efficiency η_{oo} of the system and by this the equation can be rewritten:

$$\eta_{eo} = \eta_{PS}\eta_T\eta_{oo} \tag{1.2}$$

Typically, for flash lamp systems, efficiencies are in the order of few percents mainly due to the fact that only a small fraction of the emitted light is used. This can be significantly improved by using pump diodes which have emission lines well matched to absorption bands of gain medium.

1.2.2. Activator selection

The most commonly used elements as activators are transition metals and rare earths. Transition metals are very sensitive to host medium because of the absence of a shield for valence electrons [1.18]. Instead rare-earths do have the shield and the spectral characteristics are not strongly dependent from host materials. Most used transition metal doping ions are divalent, trivalent and tetravalent chromium (Cr^{2+}, Cr^{3+} and Cr^{4+}) and trivalent titanium (Ti^{3+}). Rare-earths or lanthanides are chemical elements located between atomic numbers Z = 58 and 72 in the periodic table of Mendeleev. They have very sharp spectral lines in infrared and near-infrared regions, which make it excellent candidates for solid state lasers. Neodymium doped glass has already shown its importance in numerous applications for high power laser systems. Holmium and Erbium are used if eye-safe operation is needed.

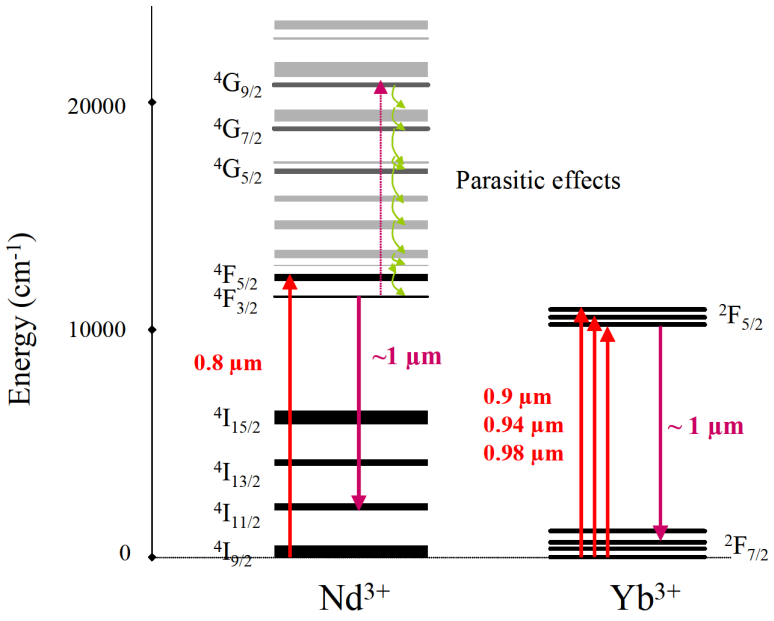

Fig. 1.3. Nd^{3+} and Yb^{3+} typical transition lines for absorption and emission: green arrows show non-radiative nature of the transitions [1.19]

With rapidly developing pump diode technology Yb^{3+} activator ions doped laser materials became excellent candidates for high energy diode pump laser systems. This dopant has a very simple energy levels system and only few pump junctions are available. Due to this fact, it was not preferred to be used with flash lamp pumping systems. Using diode pumping compared to flash lamp technology led to significant gain in efficiency. Yb-doped materials are free of parasitic effects such as upconversion, excited state absorption and crossed

relaxation due the simple energy structure of Yb^{3+} ions, which consists only of two manifolds. All these negative effects are present in Neodymium-doped materials and they lead to the significant increase of thermal load and strong depopulation of upper laser level. Comparison between energy levels of Yb^{3+} and Nd^{3+} ions is shown on Fig. 1.3. The relaxation processes from upper energy levels in case of Neodymium are non-radiative, which means they contribute to thermal load. Also Stokes parameter of Ytterbium is much higher than for Neodymium (91% against 76%). Trivalent ytterbium ions show relatively longer lifetime of upper laser state (~1ms for Yb^{3+} and ~250 μs for Nd^{3+}).

Table 1.1 allows going further in comparing Nd^{3+} and Yb^{3+} doped YAG based systems in terms of performance efficiency. Usable emission is the pump spectrum fraction spectrally overlapping with activator ions absorption spectrum. Yb^{3+} ions absorption and emission take place between $^2F_{5/2}$ and $^2F_{7/2}$ energy levels. Pumping can take place at 980 nm, 940 nm and 900 nm while emission is centered at 1030 nm.

Table 1.1: Comparison between flash lamp pumped Nd^{3+}:YAG and diode–pumped Yb^{3+}:YAG

Gain medium		**Nd^{3+} :YAG**	**Yb^{3+}:YAG**
pump source		flash-lamp	diodes
η_{PS}	Driver efficiency	0.7	0.7
	Conversion efficiency	0.5	0.6
	Usable emission	0.2	1
η_S		0.76	0.91
η_Q [1.20]		0.7	0.932

Ytterbium, as all the other lanthanides, exhibits complete 5s, 5p and 6s levels while 4f is not fully populated. Element number of ytterbium is Z=70. It forms trivalent ytterbium by losing two electrons in 6s and one in 4f. The configuration of trivalent ytterbium is then:

$$1s^2\ 2s^2\ 2p^6\ 3s^2\ 3p^6\ 4s^2\ 3d^{10}\ 4p^6\ 4d^{10}\ 5s^2\ 5p^6\ 4f^{13} = [Xe]\ 4f^{13}$$

The 4f level is missing one electron. From the electronic configuration of trivalent ytterbium, one can determine energetic levels. 4f is represented by seven quantum states, and each of them can accept two opposite values of spin s while values of orbital quantum number l belongs to the interval [–3;3]. We then obtain the following total quantum numbers:

$$S = 1/2$$
$$L = 3$$
$$|L - S| \le J \le |L + S|$$

leading to $5/2 \le J \le 7/2$. The transition between two energetic levels is possible only if $\Delta J = \pm 1,0$, meaning that only two energetic levels are possible: fundamental level $^2F_{7/2}$ and

excited level $^2F_{5/2}$, as we can see it from schematic representation of trivalent ytterbium energetic levels (Fig. 1.3).

1.2.3. Host material

Host material selection is also very critical because it defines thermal, mechanical and optical properties of gain medium. Moreover, it has to possess lattice sites that can accept dopant ions. Trivalent Ytterbium can be inserted into a large variety of matrixes. A comparison of different possible host materials is given in this section.

1.2.3.1. *Thermal management*

One of the limitations is the fact that thermal issues are quite difficult to be managed in large scale systems with high repetition rates. Even if we increase the pump efficiency up to 70% by using diode stacks for pumping, a large amount of energy will still be converted to heat. Therefore the important parameter to consider is the shock resistance parameter RT which defines the ability of the gain material to sustain induced internal stress due to the generated thermal gradients within the material. Under the influence of a temperature change ΔT, the gain medium will be subject to expansion:

$$\varepsilon = \alpha \Delta T \tag{1.3}$$

where α is the coefficient of thermal expansion expressed in K^{-1}.This deformation will induce stresses in the material in addition to residual stresses linked to growth process. Induced stress [Pa] is expressed as follows (generalized Hook's law):

$$\sigma_{\Delta T} = \frac{E\varepsilon}{1-\nu_p} \tag{1.4}$$

where E and ν_P are Young's modulus [Pa] and Poisson coefficient of the material. Combining expressions (1.3) and (1.4), we get, for induced internal stress:

$$\sigma_{\Delta T} = \frac{E\alpha}{1-\nu_p}\Delta T \tag{1.5}$$

Material robustness to sustain temperature gradient induced stress is described by thermal shock parameter [1.18].

$$R_T = \frac{\sigma_f (1-\nu_p) k}{E\alpha} \tag{1.6}$$

where σ_f is a maximum surface stress [1.18] at which fracture occurs (at the temperature ΔT_{Max}) and k is the thermal conductivity [$W.m^{-1}.K^{-1}$] This is a quite useful parameter to thermo-mechanically compare different materials: the largest it is, the higher the material ability to resist to internal thermal gradient. According to Griffith theory, the maximal stress σ_f depends on the surface quality, especially to the depth of the fractures [1.21]:

$$\sigma_f = \frac{YK_c}{\sqrt{a}} \tag{1.7}$$

where Y is a near-to-unity factor related to the geometry, K_c [Pa.m$^{-1/2}$] is the fracture toughness and a [m] is the depth of the largest flaw. This means that crystals surface quality is of a high importance. Improved polishing techniques can greatly increase the maximum stress a crystal can resist to. In order to describe the thermo-mechanic properties, which depends only of material characteristics, instead of thermal shock parameter we should consider thermal resistance parameter:

$$R_T' = R_T\sqrt{a} = \frac{K_c k(1-\nu_P)}{E\alpha} \tag{1.8}$$

The dependence of K_c from Young's modulus is given in [1.22]. The comparison of main host materials for thermal shock resistance and also some other important parameter values is given in Annex B of [1.17].

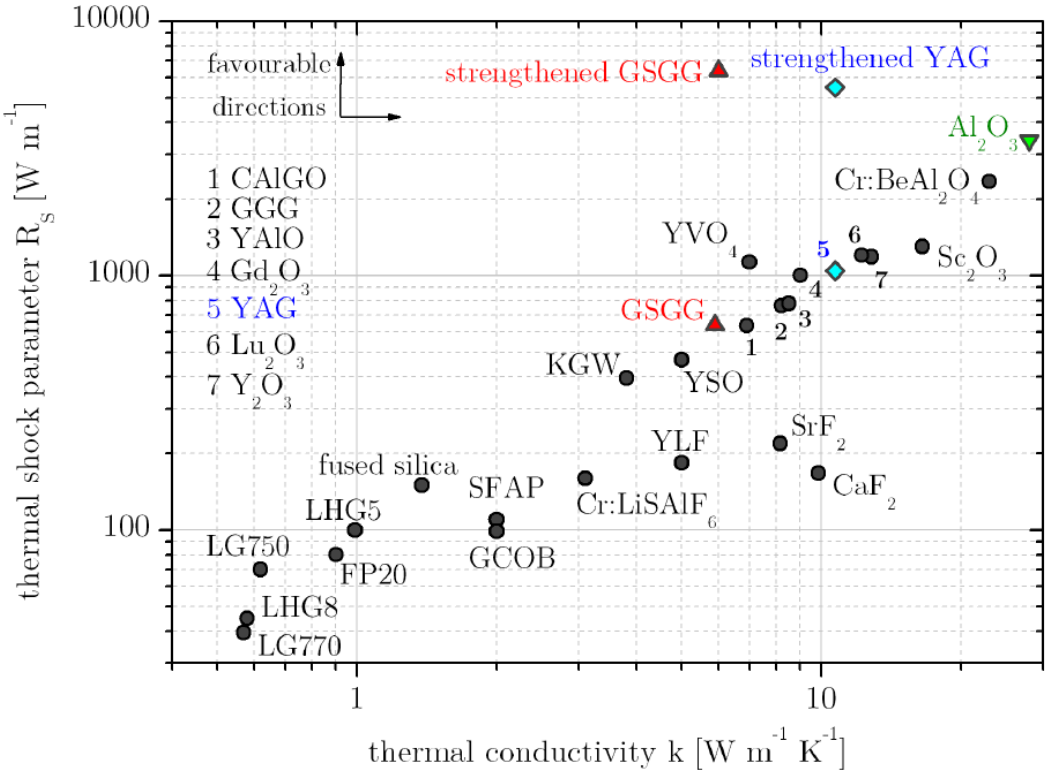

Fig. 1.4. Thermal shock parameter as a function of thermal conductivity for various host materials at room temperature

D. Albach proposed to represent thermal shock parameter as a function of thermal conductivity [1.17] (Fig.1.4). One can notice that the dependence is rather linear. In order to increase thermal shock parameter, some strengthening techniques may be applied for GSGG and YAG crystals. These techniques aim at removing damaged layer from the surface of the crystals, in order to reduce the flaws. To obtain strengthened YAG for example, some special polishing techniques should be applied on the surface in order to achieve very low values for roughness.

In [1.23], the author introduces R_f and R_t, two figures of merit to classify gain media with respect to their individual thermal characteristics. Figure 1.5 gives laser materials distribution in (R_f, R_t) space. R_f is related to the thermal focal length whereas R_t is a thermal shock parameter associated with the maximum admissible pump power. This graph reveals that sesquioxides appear to be the best host material for high average power applications.

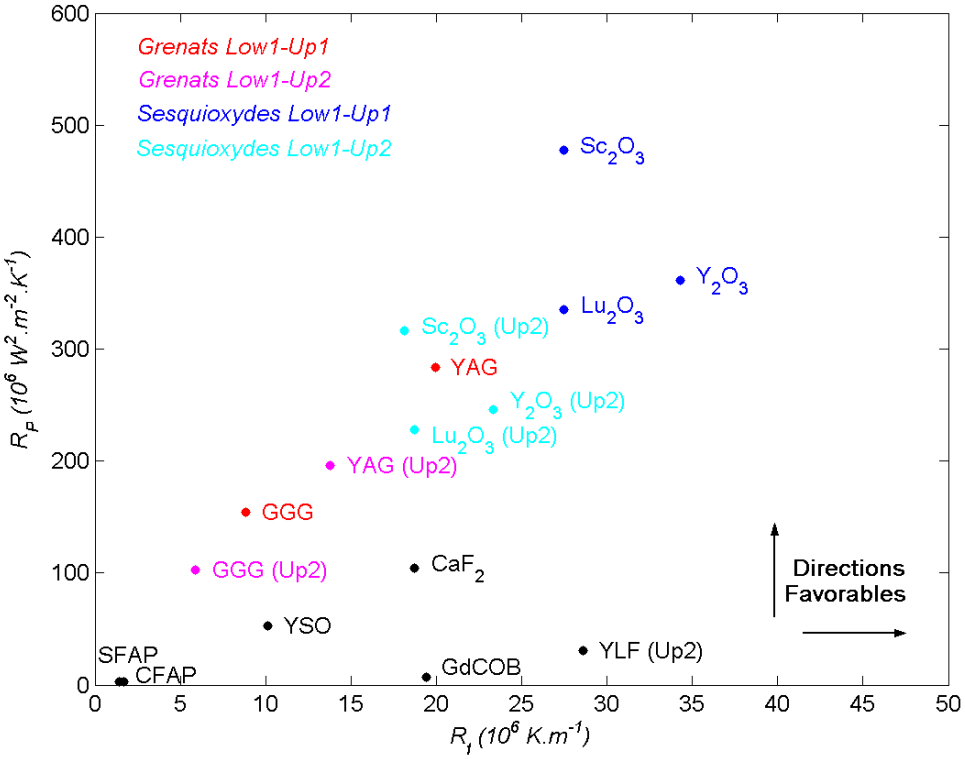

Fig. 1.5. R_f and R_p parameters for commonly used host materials [1.23]

1.2.3.2. *Availability*

Another key point to consider when selecting a host material is its availability. The extremely high level melting point temperature (~2400 °C) of rare-earth oxides makes them extremely difficult to grow with traditional bulk growth-from-melt. They are mainly obtained by crucible free methods (like Verneuil) [1.24]. Several samples have been obtained by Czochralski and Bridgman techniques without exceeding the dimensions of a few millimeters [1.24, 1.25, and 1.26]. Rare-earth oxides were grown also by micro-pulling down technique with dimensions up to Ø5x30 mm in Tohoku University. Another possibility is to grow it with the help of flux-growth technique [1.27]. Ceramic production of large sesquioxides cannot be considered at the moment since sufficient transparency cannot be achieved yet. Consequently, Yttrium-Aluminum-Garnet remains the most favorable candidate as trivalent ytterbium host material for high average power diode pumped solid state laser systems. YAG is relatively easy to grow with all tradition growth-from-melt techniques and in a wide range of Yb^{3+} ions concentrations. Yb^{3+} replaces yttrium ions without problem and full replacement (100 at % of ytterbium concentration, YbAG) can even be achieved. Besides single crystals, YAG ceramic fabrication is a mature technology and such polycrystalline material has characteristics very close to single crystal. Also, YAG ceramics can be processed over a relatively wide range of

shape and dimensions, while the maximum size for the single crystals is still strongly limited to several centimeters. However the 100 cm long sample but with diameter only 1 mm was obtained in 1999 by the crystal growth groups in Tohoku and Lyon-1 Universities. The largest crystal of Yb doped YAG with laser quality was obtained during this thesis via Bagdasarov growth technique and reported in Chapter 6.

1.3. Yttrium-Aluminum-Garnet (YAG)

YAG is currently the most commonly used solid host material for high average power lasers thanks to its low thermal expansion, high optical transparency, low acoustic losses, and rather high threshold for optical damage, hardness and stability to chemical and mechanical changes.

YAG has a cubic unit cell. Garnets have a formula $C_3A_2D_3O_{12}$ where ions *C* are located at dodecahedral sites (24(c) in Wyckoff notation), *A* ions at octahedral sites (16(a)) and *D* ions are located at tetrahedral sites (24(d)). Oxygen atoms (in red) are located in general positions (96(h)) (Fig.1.6).

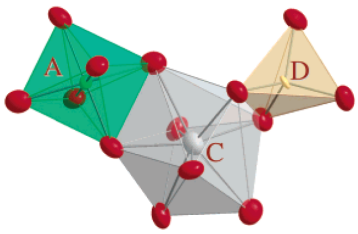

Fig. 1.6. *A*, *D* and *C* polyhedrals in the garnet structure [1.28]

Garnets crystallize in space group Ia3d which is one of the most symmetric space groups of the cubic systems. In case of YAG, the chemical formula is $Y_3Al^{VI}{}_2Al^{IV}{}_3O_{12}$. The studies on electronic structure of garnets are presented in two outstanding reports [1.28] and [1.29]. In practice, there are four important interatomic distances for YAG (Fig. 1.7): the shorter and longer cation-oxygen ion distances of the dodecahedral site (d80 and d8 respectively) and the cation-oxygen ion distances of the octahedral and tetrahedral sites (d6 and d4 respectively). The numerical values are given in [1.28].

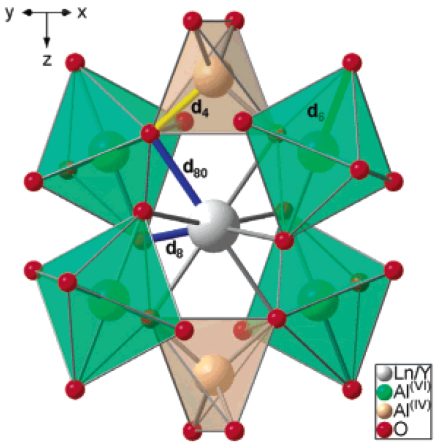

Fig. 1.7. Visualization of the key interatomic distances [1.28]

Dopant ions introduce distortions into the crystal structure of YAG due to the different radii of dopant and host ions. In our case, Yb ion radius is smaller than Y ion radius (86.8 pm vs. 90 pm) and with increasing doping, the averaged Unit Cell Parameter (UCP) changes relatively linearly as illustrated on Fig.1.8.

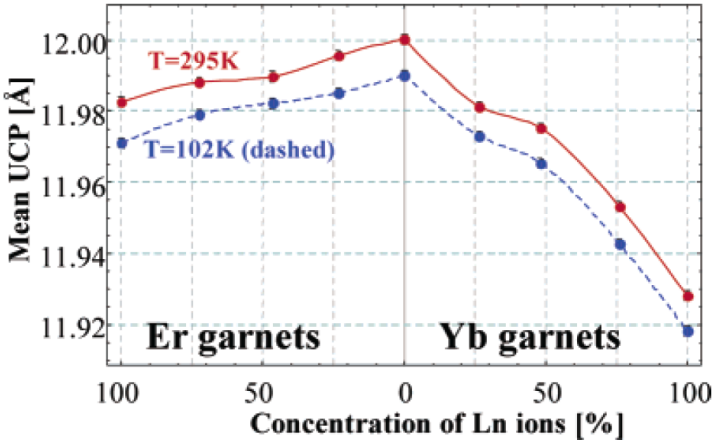

Fig. 1.8. Averaged lattice constant for YAG doped by Yb and Er for two different temperatures [1.28]

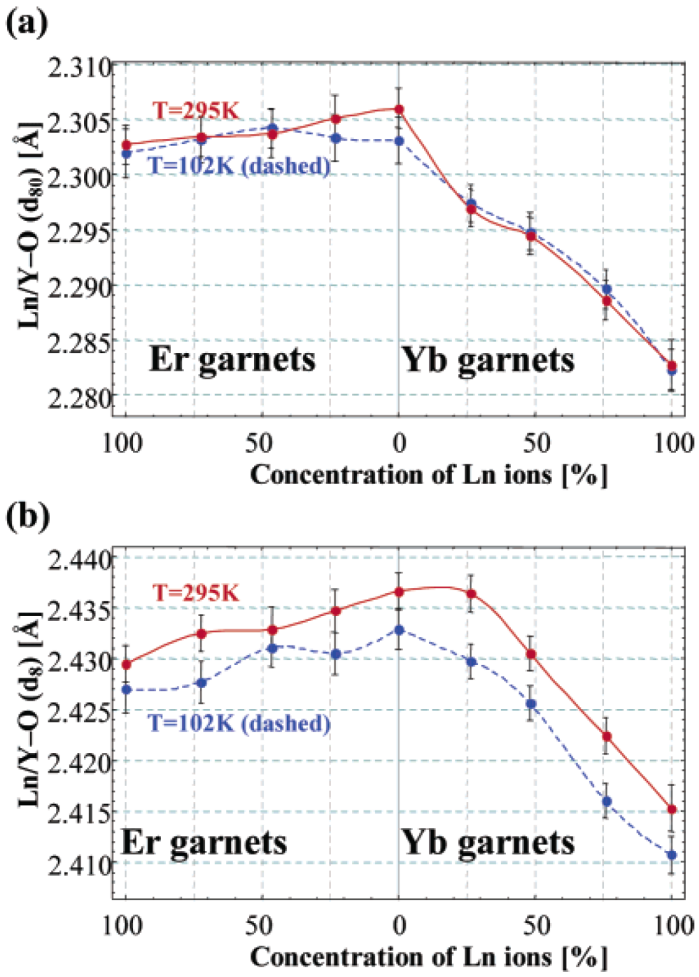

Fig. 1.9. d80 (a) and d8 (b) dependence with lanthanide concentration for Er and Yb ions at two different temperatures (102, 295 K) of [1.28]

Variation of unit cell size with temperature has been measured to a very low value of ~ 0.0001 Å/°C). In the case of Yb:YAG, it is very rare that high doping levels are used in laser configurations. Especially for large laser systems, the activator ions concentration (atomic percentage of trivalent ytterbium) should not exceed a few percents; it can even be set at sub-percent level in order to avoid significant ASE issues.

Not all interatomic distances vary the same way. With the increase of rare earth dopant concentration, both d_8 and d_{80} are decreasing. Temperature impacts only the longer (and then weaker) d_8 (Fig.1.9). The distance d_6 changes only when octahedral and/or tetrahedral sites are doped (in case of doping with Chromium for example). The interatomic distance d_4 changes with doping concentration of Y in dodecahedral site as well as with the temperature.

In order to illustrate host matrix orientation the unit cubic cell is displayed alongside different axes on Fig. 1.10.

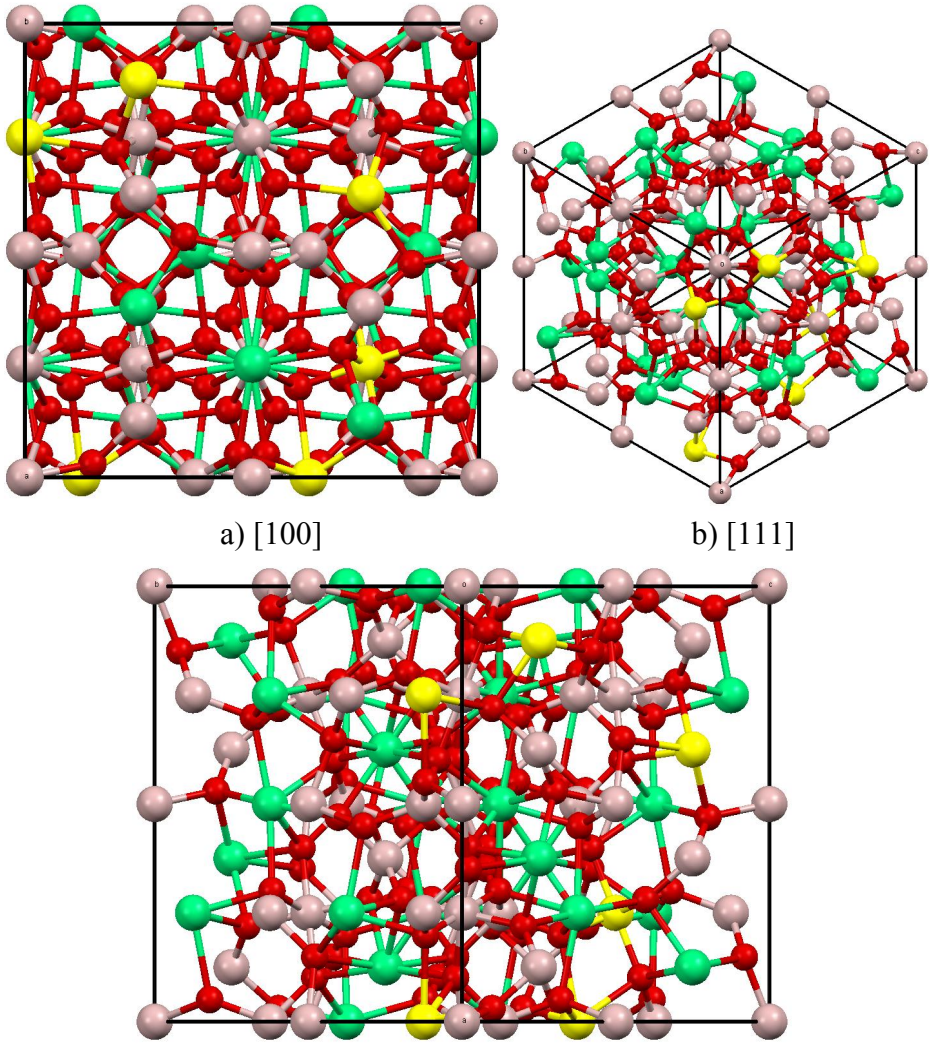

a) [100] b) [111]

c) [110]

Fig. 1.10. Yb:YAG crystal unit cubic cell alongside three principal crystallographic directions a) [100], b) [111] and c) [110]. Gray color represents Al atoms, red Oxygen and green is standing for Yttrium. Yellows are Yb ions which replaced Yttrium ions (dodecahedral sites)

Orientation directions presented in Fig.1.10 are the most commonly used in trivalent Yb doped YAG laser systems. In depth knowledge of crystalline properties helps predicting depolarization behavior of YAG crystals during laser operation. Fig. 1.11 illustrates depolarization losses of a Lucia-type disk crystal for the 3 principal crystal orientation depicted in Fig. 1.10 [1.30]. The active mirror architecture (fig. 1.13) of Lucia amplifiers imposes 13° off-axis extraction internal angle inside the YAG. Fig. 1.11 map is then calculated for such an angle of incidence. It displays single pass losses (over a 22 mm diameter pupil) with 40 W/cm² heat load. The 0 to 360° angular axis refers to the extraction beam linear polarization orientation. When crystal is oriented along [110], it suffers from the highest depolarization losses. In contrary for [001], the losses can be reduced to a minimum by rotating the crystal to an optimum position. For YAG ceramics the rotation will have no influence on the amount of losses due to its inherent polycrystalline nature.

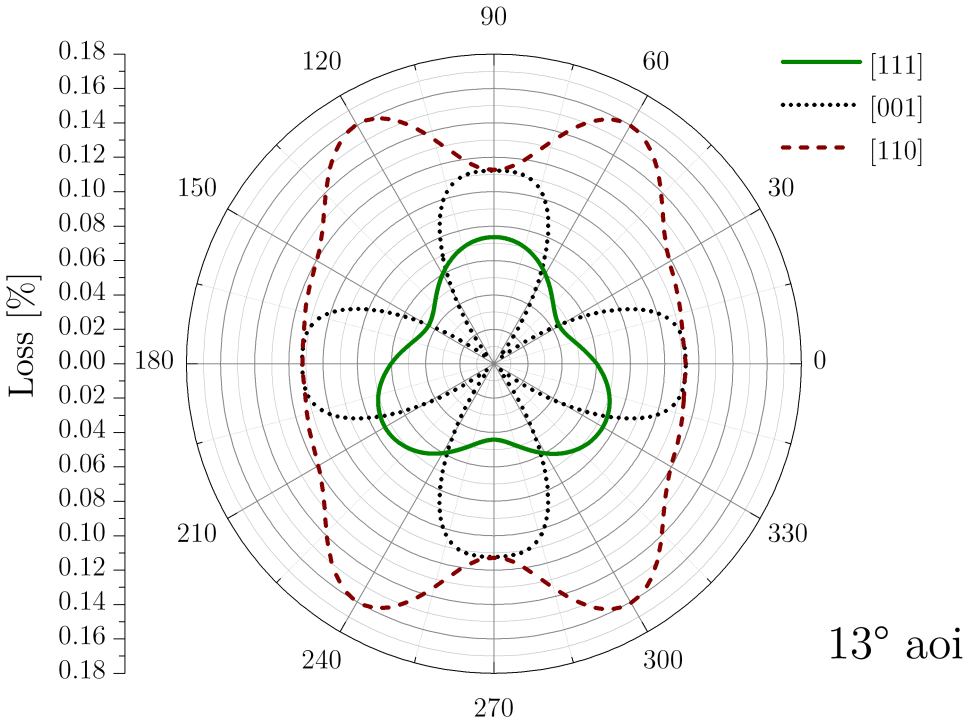

Fig. 1.11. Depolarization losses in Yb^{3+}:YAG crystal versus crystal rotation for a 13° internal propagation angle

The information provided above allow us to conclude that trivalent Yb doped YAG is the most favorable candidate for high average power laser systems. Most of currently being built laser systems rely on Yb^{3+}:YAG and efforts should be done in order to expand the availability of this material as well as to improve its key characteristics.

1.4. Amplified Spontaneous Emission

Amplified Spontaneous Emission (ASE) is one of the deleterious parasitic effects taking place in large size amplifiers. Spontaneously emitted photon gets amplified while travelling through the gain medium, leading to potentially significant depopulation of upper laser level. This phenomenon can never be eliminated but its negative impacts on laser performance may be

reduced through careful geometrical, doping and pump considerations. When this amplification becomes too important, ASE can lead to parasitic lasing between the outer boundaries of gain medium. Let us introduce simple considerations about ASE and a useful figure of merit.

The population inversion in laser gain medium can be influenced by three major physical processes. During pumping the pump light gets absorbed while propagating through gain medium and upper laser level gets populated. Simultaneously, due to the finite radiative lifetime of upper laser state, spontaneous emission takes place, depopulating upper laser state. Then spontaneously emitted photons give a birth to third process – ASE. This can be expressed mathematically:

$$\frac{d\beta}{dt} = \left(\frac{d\beta}{dt}\right)_{Pump} - \left(\frac{d\beta}{dt}\right)_{SE} - \left(\frac{d\beta}{dt}\right)_{ASE}, \text{ with } \beta = \frac{N_{Up}}{N_{Tot}} \tag{1.13}$$

where N_{Up} and N_{Tot} are upper state and total populations. Population inversion for the first term can be written as:

$$\left(\frac{d\beta}{dt}\right)_{Pump} = \int_{\lambda} g_0 \frac{I_P}{N_{tot} h\nu_P} d\lambda \tag{1.14}$$

where I_p is a spectral pump intensity [W/m^2/nm], v_p is the central pump frequency and

$$g_0 = -[\sigma_a \cdot N_{Tot} - N_{Up}(\sigma_a + \sigma_e)] \tag{1.15}$$

is the small signal gain, h being the Planck constant. σ_a and σ_e are the absorption and emission cross sections. In the second term of (1.13) we have:

$$\left(\frac{d\beta}{dt}\right)_{SE} = \frac{N_{Up}}{\tau_f} \tag{1.16}$$

where τ_f is the fluorescence lifetime of upper laser state. The origin of ASE is a photon flux Φ_{ASE} [cm^{-2}.nm^{-1}.s^{-1}] travelling throughout the crystal, so it can be written [1.17] as:

$$\left(\frac{d\beta}{dt}\right)_{ASE} = \int_{\lambda} \frac{g_0 \Phi_{ASE}}{N_{tot}} d\lambda \tag{1.17}$$

ASE reduces upper laser state and can be regarded as a local reevaluation of fluorescence lifetime. In order to quantify ASE, the so-called lifetime modifier parameter M_{ASE} is introduced:

$$\frac{d\beta}{dt} = \left(\frac{d\beta}{dt}\right)_{Pump} - \left(\frac{d\beta}{dt}\right)_{SE} \cdot M_{ASE} \tag{1.18}$$

Using the upper equations, we obtain for M_{ASE}:

$$M_{ASE} = 1 + \tau_f \int_{\lambda} \left[\sigma_a \left(1 - \frac{N_{Tot}}{N_{Up}} \right) + \sigma_e \right] \Phi_{ASE} d\lambda \tag{1.19}$$

The lifetime modifier will be used in the section 2.3 to help describe the impact of variable doping on ASE management. A relationship between the maximum achievable inversion density and M_{ASE} can be derived. It corresponds to a limiting value for the energy storage when depopulation due to ASE gets strong enough to neutralize the pump action (both hands of (1.18) will become zero):

$$\left(\frac{d\beta}{dt} \right)_{Pump} = \left(\frac{d\beta}{dt} \right)_{SE} \cdot M_{ASE} \tag{1.20}$$

Considering the monochromatic case for equation (1.14), its right hand transforms into $g_0 I_P / h\nu_P$. Emission cross-section for pump light being much smaller than absorption cross-section, we can write (1.15) as $g_0 = -\sigma_a N_{Tot} + \sigma_a N_{Up}$. Taking into account the definition $I_{sat,p} = h\nu_p / (\sigma_a \tau_f)$ of the saturation pump intensity, we obtain:

$$\beta_{\max} = \frac{I_P}{I_{sat,p} M_{ASE} + I_P} \tag{1.21}$$

This expression allows estimating the maximum possible excitation by knowing the fluorescence lifetime modifier. Also it is easy to see that, if pump intensity $I_p = I_{sat,p}$, then $\beta_{\max}$ is limited to 0.5 when ASE plays no role ($M_{ASE} = 1$).

ASE really becomes an issue when entering into a regime where parasitic oscillations take place within the gain medium. This occurs when the gain medium surfaces reflect sufficiently SE photons which are then allowed to travel a longer path within the gain medium due to internal reflections. On the LUCIA laser system several methods were put in place in order to mitigate the occurrence of parasitic oscillations and by this partially eliminate ASE induced population inversion depletion; these are described briefly in the section 1.5.3.

1.5. The Lucia Laser System

1.5.1. Overview

The LUCIA program started at LULI in 2002. A recent update of its performances is given in [1.31] together with a detailed presentation of its successive stages. In the coming three sections, the Lucia specifications the most relevant for this work are described. Lucia laser is a DPSSL system aiming at producing 100 J pulses at 10Hz repetition rate (kW average power). Desirable pulse duration is around 10 ns. The Lucia system is a test bed devoted to the exploration of key challenges faced by high average power laser systems. This includes ASE mitigation techniques, thermal management, and specifically engineered gain medium. This program includes also wave front management and cryogenic amplification studies.

Lucia is a Yb^{3+}:YAG based Master-Oscillator Power-Amplifier (MOPA) DPSSL which flow chart is illustrated in Fig. 1.12 : A cavity dumped oscillator generates a 8 ns/0.5 mJ/1030 nm pulse train to be successively amplified in 3 multiple-pass fully image-relayed stages.

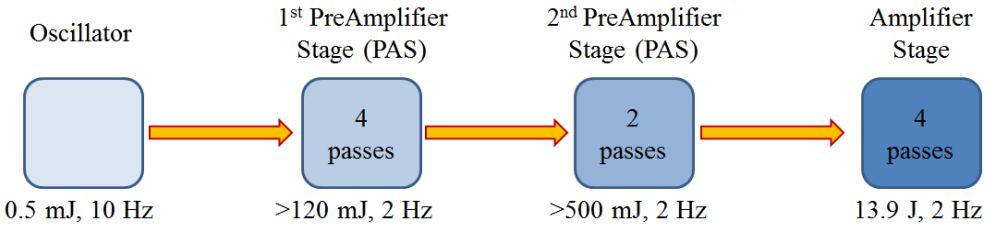

Fig. 1.12: Lucia DPSSL laser chain flow chart detailing the 4 steps amplification process to ramp up the energy from the mJ level up to 14 J.

A specific feature of Lucia is the fact that all amplification stages rely on so-called active mirror concept for pumping and extraction concept (Fig.1.13).

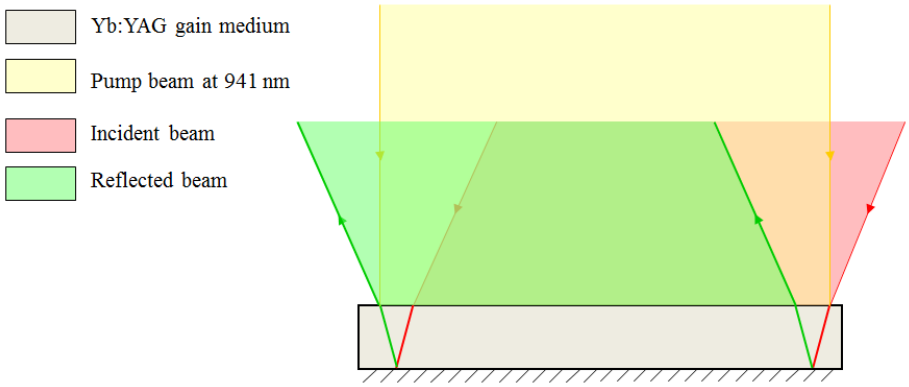

Fig. 1.13. Active mirror principle: Both pump and extraction lights are being couple inside the gain medium through refraction at the AR coated top surface. Whereas almost all pump light is absorbed after reflection at the bottom HR coated surface, the incident (red) extraction beam is amplified and coupled out through a second refraction at the top surface. Such scheme is named "active mirror" to illustrate the amplification property of such mirror.

Pulses generated by oscillator get magnified and amplified in two pre-amplifiers still staying in sub-J level. Afterwards beam gets shaped and magnified. The main amplifier provides amplification of the beam up to 14 J. Cryogenic amplifier is expected to be functional in the end of 2013 and is predicted to provide beam amplification up to 30 J by 2015.

1.5.2. Lucia Front-end

1.5.2.1. *Oscillator*

Fig.1.14 illustrates the setup of LUCIA oscillator [9]. The difference of this setup from typical cavity-damping systems is the fact that it is not driven with high-repetition rate. The repetition rate indeed can be set from single shot to 10 Hz. Pulse creation is performed through several steps: pumping the gain medium which is hosted in a lossy cavity, establishing low loss cavity

in order to store the energy inside the cavity and coupling out the pulse at a speed related to the cavity length and the switching rate.

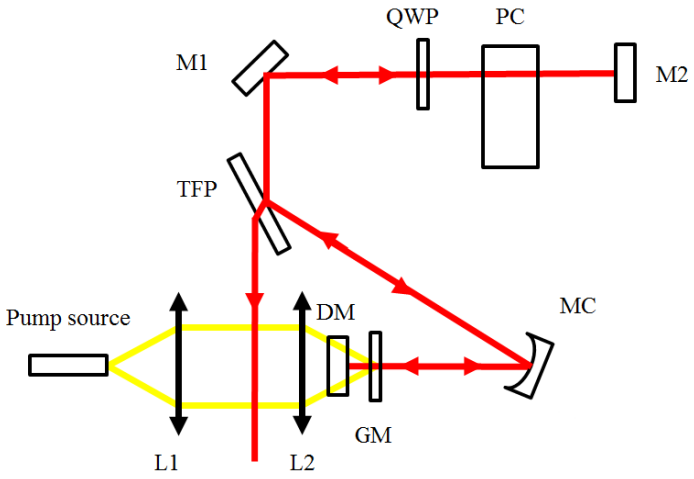

Fig. 1.14. Oscillator setup, M1 45° mirror, M2 0° mirror, λ/4 wave plate, PC Pockels cell, TFP thin film polarizer, SM spherical mirror, GM Yb^{3+}:YAG crystal, DM dichroic mirror, 4F 4-f imaging system of the pump, FCL fiber-coupled laser diode, MC curved mirror

Pumping takes place at 970 nm (zero line) with a fiber-coupled laser diode (LUMICS GmbH) which can deliver CW power up to 10W at 12 A. The crystal used is 3 mm thick and doped at 10 at% grown by Bagdasarov method at "Laseayin Tekhnika". Both sides are anti-reflectively (AR) coated for pump and emission wavelengths. The oscillator emission spectrum in cavity-dumped operation regime and the pulse energy as a function of pump source current are illustrated on Fig.1.15. The 8 ns outgoing pulse train exhibits a near TEM00 beam shape (Fig.1.16).

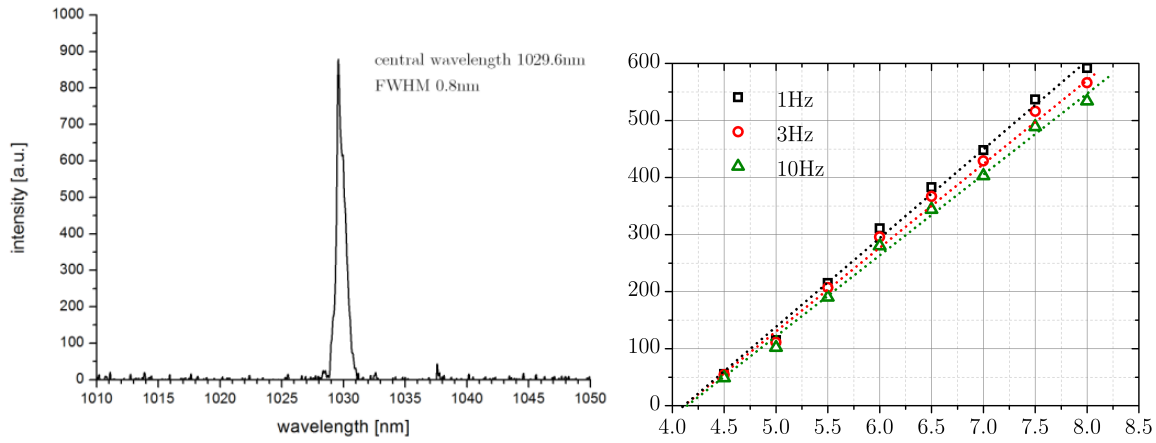

Fig. 1.15. Oscillator 1029.6 nm centered, 0.8 nm bandwidth spectrum (left) and output pulse energy [μJ] versus the pumping diode driving intensity [A] (right) for three different repetition rates

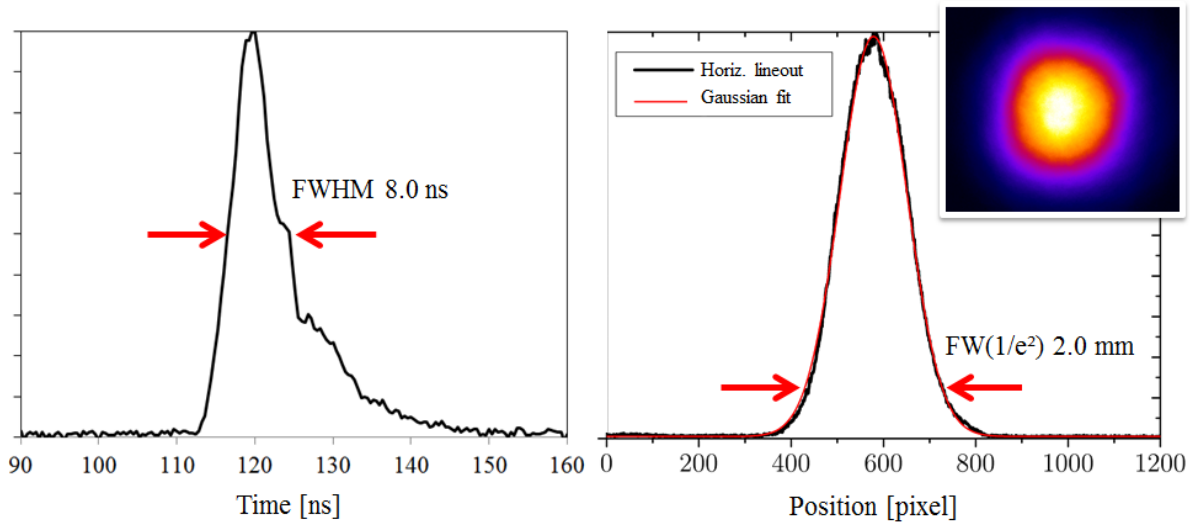

Fig. 1.16. Oscillator 8 ns temporal profile (left) and near field profile (right), recorded for an 8 A pump intensity at 10 Hz

1.5.2.2. *Pre-amplification Stage*

The pulse generated by the oscillator travels through a Faraday isolator and is amplified by two pre-amplifiers (PAS1 and PAS2) as sketch on fig. 1.17. 15 to 20°C water cooled preamplifiers rely on 3mm thick 30mm diameter 2at% doped Yb:YAG disks also grown by Bagdasarov method.

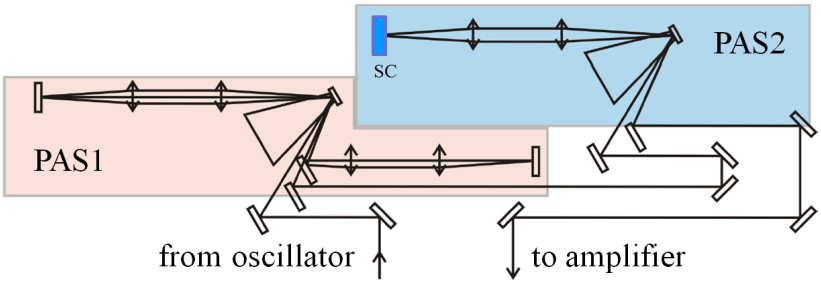

Fig. 1.17. Schematic overview of Lucia pre-amplifying stage: Double arrows symbolize the six 500 mm focal length telescope lenses. The thirteen large rectangles are mirrors whereas the two small ones are the 30 mm gain media in front of which large isosceles triangles (representing the pumping heads) are pointing. SC stands for the Static Corrector compensating accumulated astigmatism [1.31]. The 2x magnification image relay telescope between both stages is not represented.

PAS1 pump source is a micro-lensed 25 bars laser diode stack delivering 3 Joules in 1 ms (i.e. 3 kW peak power) when driven at 150 A. Pump light brightness is 15 kW/cm² over a ~4x3 mm² area. PAS1 output energy exceeds 120 mJ with a good beam quality as illustrated in Fig. 1.18. This energy level is achieved through 4 fully image relayed extraction passes, leading to a single pass average gain of 4.

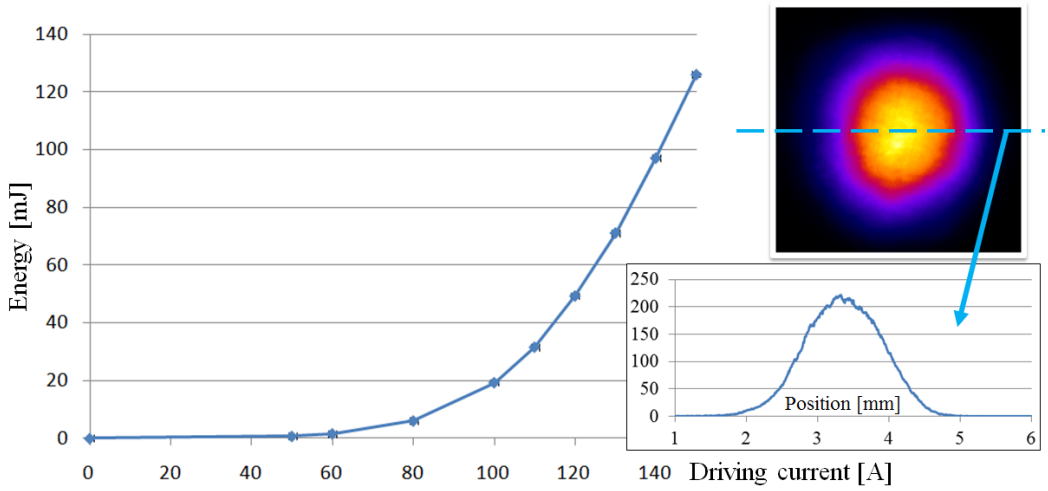

Fig. 1.18. First Pre Amplifier Stage (PAS) output energy (mJ) vs. stack driving current. The maximum 126 mJ was obtained with 2 J pump energy at the crystal level. Output beam profile at maximum energy level is displayed on right together with a horizontal lineout leading to 2.1 mm FW at 1/e² (vertical scale is related to pixel counts)

A 2x magnification telescope brings the beam size to 3 mm diameter before heading towards PAS2 after which the energy reaches approximately 590 mJ in two passes (single pass average gain of 2.4) as illustrated in Fig. 1.19. The pump source is a 2x2 array of 4 stacks similar to the one use for PAS1. The pump light is distributed over a 7.5x10.5 mm² rectangle with 90% transmission efficiency, leading to 10 to 11 Joules at 940 nm coupled in the gain medium.

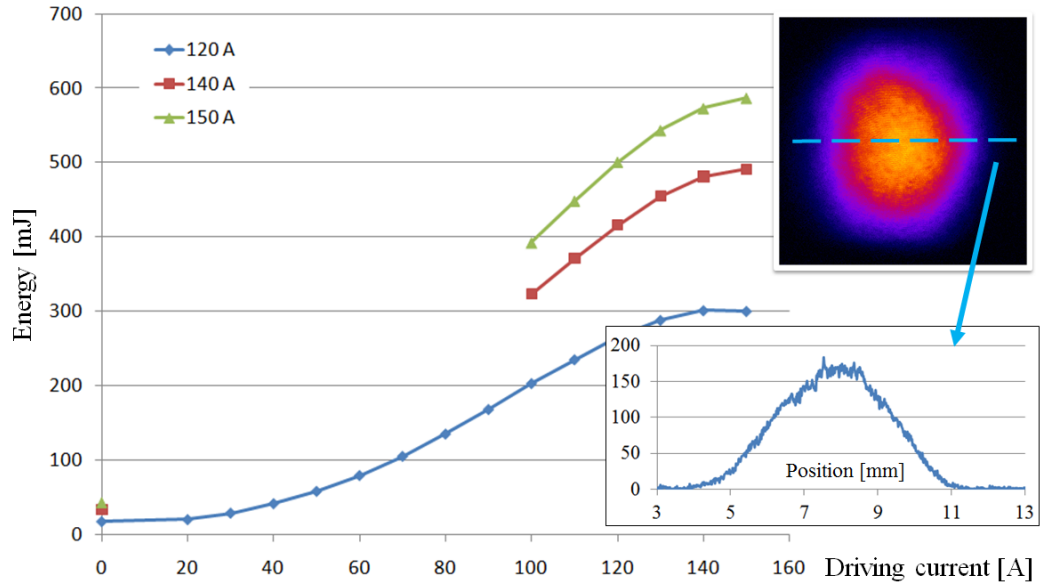

Fig. 1.19. PAS2 output energy (mJ) vs. stacks driving current for 3 different PAS1 stack driving current (120, 140 and 150 Amperes). The maximum 586 mJ were obtained with 150 A applied on all 1+4 stacks of both PAS. This corresponds to about 11 Joules of pump light. Output beam profile at maximum energy level is displayed on right together with a horizontal lineout leading to 5.5 mm FW at 1/e² (vertical scale is related to pixel counts)

As observed in Fig. 1.19, PAS2 output beam is vertically elongated (6.4 mm vs. 5.4 mm at $1/e^2$). Before entering the main amplification section of Lucia laser chain, the beam is apodized with a circular serrated aperture, spatially filtered and magnified to obtain a clean 20 mm beam.

1.5.3. Main amplifier

Lucia amplifier stage is composed of a pumping array [1.32], a Pump Light Delivery Optical System (PLDOS) and a water cooled laser head as illustrated by the pictures of Fig. 1.20. Pump light is concentrated with vertical prisms and aluminum mirrors to reach 16 kW/cm² brightness over a 30x26 mm² area when driving the stacks at full power.

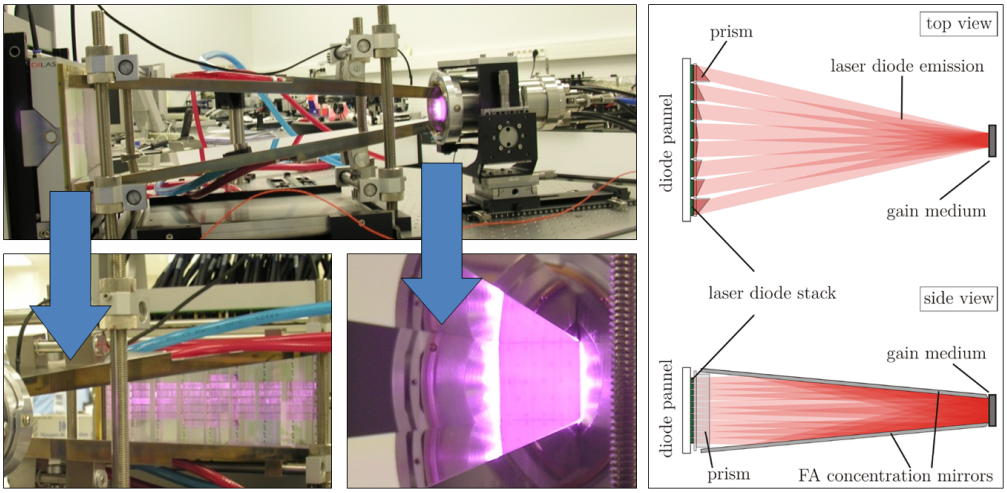

Fig. 1.20. Top picture is a side view of Lucia amplifier head with the pair of concentrating aluminum water cooled mirrors at the center. The bottom left picture shows the partially filled diode array where 41 individual stacks can be observed in pinkish color. The last picture shows gain medium fluorescence. A careful look reveals the darker tiny holes of the jet plate located behind the Yb^{3+}:YAG disk. The right sketches illustrate how the 940 nm light emitted by the individual stacks is concentrated onto the gain medium

Tremendous efforts were dedicated [1.33] to circumvent the onset of parasitic oscillations due to ASE. As illustrated by Fig. 1.21, the pump light is efficiently used over the full 1 ms pump duration since no gain saturation (parasitic oscillation signature) can be observed over this period. Careful engineering of the gain medium mount proved to be an important step towards unwanted ASE reflection mitigation but was not the only action considered. Indeed, in order to reach a small signal gain value above 4, the disk peripheral structure had to be modified so that any transverse amplified ray could be efficiently absorbed. A cladding material had therefore to be added. But, processing a composite crystalline structure was ruled out due to time, cost and technological considerations. The selected solution was to significantly increase the crystal diameter (from 45 to 60 mm). With a pump area limited to 30 mm, we take advantage of the 1030 nm absorption of Yb^{3+}:YAG. The un-pumped periphery of the disk is therefore acting as the cladding layer. Getting such large crystals (see chapter 6) with laser grade quality was made possible only through a dedicated crystal growth research program which has been running at LULI for several years in collaboration with *Laserayin Tekhnika*.

Above mentioned difficulties in processing a crystalline composite gain medium vanish when considering ceramics. Indeed processing a Cr^{4+}/Yb^{3+}:YAG cosintered ceramics was proven to be fast, economic and without any major engineering issue. Figure 1.21 gives two pictures of the crystal and ceramic YAG disks used on Lucia main amplifier.

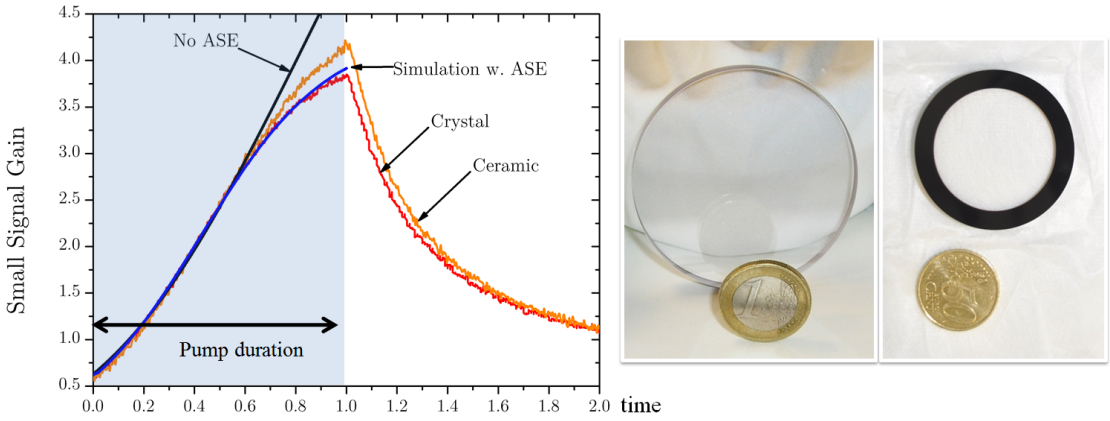

Fig. 1.21. Small signal gain recorded for a 1 ms single pump shot at 16 kW/cm² during 2 ms (left). The gain build up can be observed without any saturation until an exponential decay takes place when pumping stops. Orange curve was obtained with the cosintered ceramics (right picture) whereas the red curve results from measurements perform with the crystal (central picture). The solid curves are simulations with (blue) and without (black) ASE

Considering the foreseen development (section 4) of the Lucia program with a second amplifier head expected to operate in the range of 100 to 200 K, the choice of co-sintered ceramic appears the only relevant one due to the fact that Yb^{3+}:YAG reabsorbtion at the laser wavelength is largely reduced at lower temperature [1.34], therefore losing its self-cladding properties using an unpumped periphery.

After a 4 pass fully image-relayed path, PAS2 output pulses are amplified up to 13.7 J and 13.9 J intensity respectively with 60 mm diameter crystal and 45 mm co-sintered ceramics at 2 Hz.

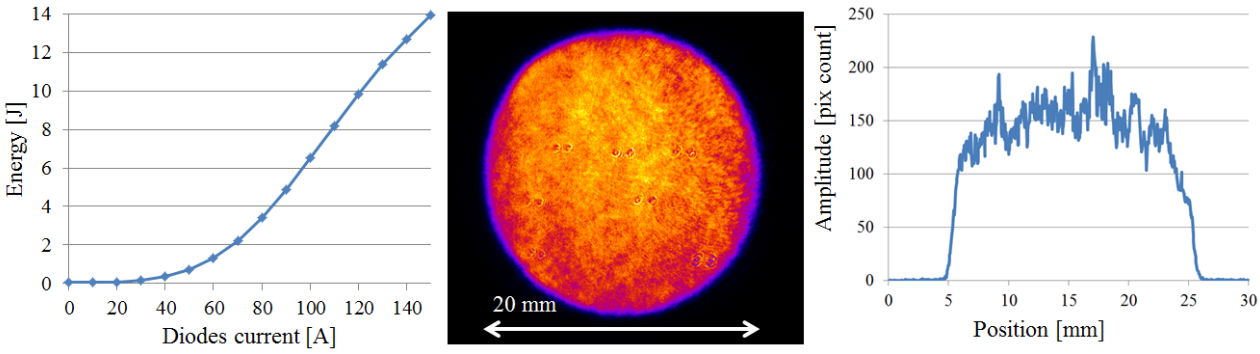

Fig. 1.22. The left graph is the energy build up when the diode array driving current is increased up to 150 Amperes. Near field profile is illustrated on the central picture from which a horizontal lineout was extracted (right, units are pixel number, and 8 bits grey level)

1.6. References

[1.1] Bayborodin Yu.V. “Fundamentals of Laser Techniques” 2nd edition, Kiev, 1988 (in Russian)

[1.2] Gould R. G. (1959) "The LASER, Light Amplification by Stimulated Emission of Radiation" In Franken, P.A. and Sands, R.H. (Eds.). The Ann Arbor Conference on Optical Pumping, the University of Michigan, 15 June through 18 June 1959. p. 128. OCLC 02460155

[1.3] Chu S., Townes C., "Arthur Schawlow" In Edward P. Lazear (ed.), Biographical Memoirs vol. 83 National Academy of Sciences p. 202, ISBN 0-309-08699-X (2003)

[1.4] Maiman T. H., "Stimulated optical radiation in ruby", Nature 187 (4736): 493–494. Bibcode 1960 Natur.187.493M

[1.5] Harris S. E. “Lasers without inversion: Interference of lifetime-broadened resonances” Phys. Rev. Lett. 62, 1033–1036 (1989)

[1.6] Scully M. O. and Zhu S.U., “Degenerate quantum-beat laser: Lasing without inversion and inversion without lasing”, Phys. Rev. Lett. 62, 2813–2816 (1989)

[1.7] Narducci L. M., Doss H. M., Ru P., Scully M. O,. Zhu S. U., Keitel C. “A simple model of a laser without inversion” Optics Communications, Volume 81, Issue 6, 15 March 1991, Pages 379–384

[1.8] Narducci L. M., Scully M. O., Keitel C. H., Zhu S. U., Doss H. M. “Physical origin of the gain in a four-level model of a Raman driven laser without inversion” Optics Communications, Volume 86, Issues 3–4, 15 November 1991, Pages 324–332

[1.9] http://www.luli.polytechnique.fr/

[1.10] http://www-lmj.cea.fr/

[1.11] www.hiper-laser.org/

[1.12] Dunne M., “A high-power laser fusion facility for Europe”, Nature physics, 2 (2006)

[1.13] http://en.wikipedia.org/wiki/National_Ignition_Facility

[1.14] Meier W. R., “Systems Modeling for a Laser-Driven IFE Power Plant using Direct Conversion”, The fifth International Conference on Inertial Fusion Sciences and Applications (IFSA2007) IOP Publishing. Journal of Physics: Conference Series 112 (2008)

[1.15] www.iter.org/fr/accueil/

[1.16] http://en.wikipedia.org/wiki/ITER

[1.17] Albach D., “Amplified spontaneous emission and thermal management on a high average-power diode-pumped solid-state laser: the LUCIA laser system”. (doctoral thesis), Ecole Polytechnique, 2010

[1.18] Koechner W. “Solid-State Laser Engineering”, Springer, 1999

[1.19] Chénais S., Druon F., Forget S., Balembois F., Georges P., “On thermal effects in solid-state lasers: The case of ytterbium-doped materials”. Progress in Quantum Electronics 30 (2006) 89-153

[1.20] Barnes N. and Walsh B. M. “Quantum efficiency measurements of Nd:YAG, Yb:YAG, and Tm:YAG”. In ‘Advanced Solid-State Lasers,’ Optical Society of America, 2002, p.TuB15

[1.21] Marion, “Fracture of Solid-state Laser Slabs” J. of App. Phys., 60(1), 1986 pp. 69–77

[1.22] Gaume R. “Relations structures - propriétésdans les lasers solides de puissance à l’ytterbium. Elaboration et caractérisation de nouveaux matériaux et de cristaux composites soudés par diffusion” (doctoral thesis), l’Universite Pierre et Marie Curie - Paris VI, 2002

[1.23] Casagrande O. “Etude théorique et expérimentale de l’architecture d’un laser à solidemonocristallin ou céramique dope ytterbium pour la génération d’impulsions de grande énergie a haute cadence” (doctoral thesis), Ecole Polytechnique 2007

[1.24] Peters V. “Growth and Spectroscopy of Ytterbium-Doped Sesquioxides”, (doctoral thesis) Hamburg, 2001

[1.25] Fornasiero L., “Nd^{3+} und Tm^{3+} dotierte Sesquioxide” (doctoral thesis) Hamburg, 1998

[1.26] Mix E., “Kristallzüchtung, Spektroskopie und Lasereigenschaften Yb-dotierter sesquioxide” (doctoral thesis) Institute of Laser-Physics, University of Hamburg, Germany (1999)

[1.27] Veber P. et al., brevet FR 09 57772 (03/11/2009), PCT Int. Appl. WO 2011055075, 2011and Philippe Veber et al., “Flux growth of Yb^{3+} -doped RE_2O_3 (RE=Y,Lu) single crystals at half their melting point temperature”, CrystEngComm, (2011)

[1.28] Dobrzycki Ł., Bulska E., Pawlak D. A., Frukacz Z., Wozniak K. “Structure of YAG Crystals Doped/Substituted with Erbium and Ytterbium” Inorg. Chem. 2004, 43, 7656-7664

[1.29] Xu Y. N., Ching W. Y., “Electronic structure of yttrium aluminum garnet Y3Al5O12” Phys. Rev. B Volume 59, N16, 1999

[1.30] to be published

[1.31] Gonçalvès-Novo T., Albach D., Vincent B., Arzakantsyan M., Chanteloup J.-C., “14 J / 2 Hz Yb^{3+}:YAG diode pumped solid state laser chain” accepted for publication in Optics Express,

[1.32] Chanteloup J.-C., Albach D., Assémat F., Bahbah S., Bourdet G., Piatti P., Pluvinage M., Vincent B., Le Touzé G., Mattern T., Biesenbach J., Müntz H., Noeske A., and Venohr R., “Wavelength tunable, 264 J laser diode array for 10 Hz/1ms Yb:YAG pumping,” J. Phys.: Conf. Ser. 112 (2008) 032056

[1.33] Albach D., Chanteloup J.-C, and le Touzé G., "Influence of ASE on the gain distribution in large size, high gain Yb3+:YAG slabs", Optics Express, Vol. 17, No. 5, pp. 3792-3801 (2009).

[1.34] Brown C. et Al., “Yb:YAG Absorption at Ambient and Cryogenic Temperatures”,IEEE J.of Sel. Top. Quant Elec, Vol.11, No.3, 2005

2. Gradient Doped Gain Medium

2.1. Introduction

As illustrated in chapter 1, Yttrium Aluminum Garnet $Y_3Al_5O_{12}$ (YAG) crystals doped with trivalent Ytterbium ions (Yb^{3+}) are materials of choice for DPSSL applications. To our knowledge, all operating laser facilities rely on crystalline or ceramic gain medium with uniform volume doping distribution: no Yb^{3+}:YAG crystal exhibiting continuously variable doping distribution has ever been used due to the lack of availability for such a gain medium. In this section we illustrate numerous advantages potentially offered by such structures (Amplified Spontaneous Emission management, thermal management, gain media volume requirement). These issues are indeed of high relevance for laser programs like the European High Power laser Energy Research facility (HiPER) dedicated to demonstrate the feasibility of laser driven fusion as a future energy source [2.1]. Section 2.2 illustrates the technological context in terms of laser system. In the section 2.3, the impact on different parameters is discussed briefly, while sections 2.4 and 2.5 will provide explanation of the mathematical model and detailed analysis of the impact of variable doped gain medium on thermal management. Finally section 2.6 will conclude and present foreseen evolutions.

2.2. Motivation

Engineering high energy / high average power laser system like the HiPER [2.1] laser program requires facing challenges not previously addressed by other multiple 100kJ-class laser systems like the National Ignition Facility (NIF) or Laser Mega Joule (LMJ). Indeed, HiPER's goal being to demonstrate Inertial Fusion Energy (IFE) production through Fast Ignition in a mode of operation similar to a reactor of a real IFE power plant. Such an operation requires a minimum repetition rate of ~10 Hz [2.2]. Considering the *cost of electricity* [2.3] analysis and maturity of the available technology, it is very likely that such multiple ~10 kJ/~10 kW beam line facility will rely on diode pumped lasers.

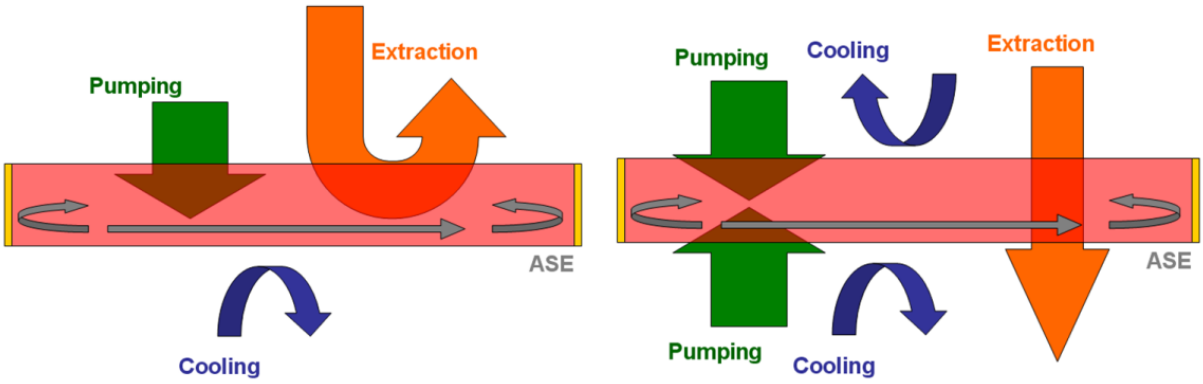

Fig.2.1. Pumping, extraction and cooling axis configurations in 2 cases for large/thin laser gain medium (pink): left, the active-mirror approach and right the slab architecture. ASE favored directions are also shown in grey arrows inside the gain media. Yellow peripheral layer is an ASE absorbing cladding material

Damage threshold limitations and cooling efficiency are among the constraints justifying a high aspect ratio for the gain medium geometry. Fig. 2.1 illustrates two different amplifier architectures currently explored [2.4]: a dual side pumped slab and single side pumped active mirror concepts.

In addition to common issues with LMJ/NIF facilities (ASE, gain medium large volume management…), a high repetition rate operation brings thermal management on the forefront of key laser issues. Current laser gain media used on such large laser facilities rely on uniformly doped solid state laser materials (glass, crystal or ceramic). We present in this section the advantages of variable doping on gain medium volume requirement, ASE and thermal management. Since this work was performed within the framework of the active mirror based Lucia DPSSL program at the LULI, the theoretical discussion takes place within this specific context. Of course the principle remains true for a dual side pumped slab.

2.3. Impact of Energy Storage distribution on ASE

Let us consider a test case illustrated by Fig. 2.2 where a 1.9 at% uniformly doped Yb^{3+}:YAG crystal is pumped from the left (green arrow) with an intensity of 14 kW/cm². The pump light is absorbed when travelling through this 0.75 cm thick gain medium, but also on its way back after being reflected on the High Reflectivity (HR) coated (right) face.

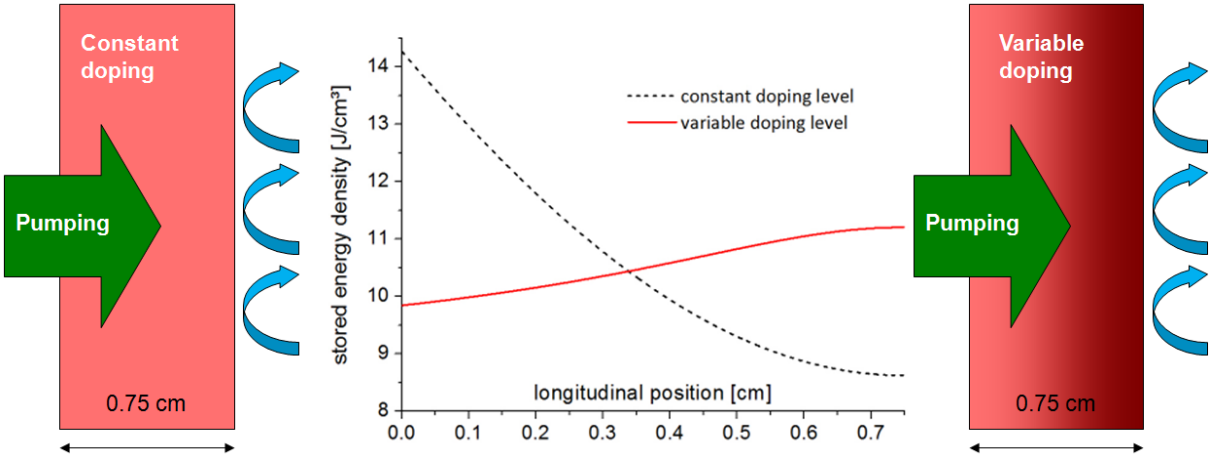

Fig.2.2. Stored energy distribution for a single side pumped active mirror with uniform doping distribution (left and dotted curve) and variable doping distribution (right and red curve). Pumping originates from the left (green arrows) whereas cooling takes place on the opposite side (blue arrows)

Only this HR face can practically be actively cooled, which is not optimum since the heat load is located in the vicinity of the pump face, as shown by the curve plotting the stored energy density along the gain medium thickness. Consequently, a noticeable temperature gradient takes place. Resulting internal stresses therefore affect both the amplified laser beam quality and the long term physical integrity of the crystal. Relying on a gradient doped crystal (1.3 at% (pumped face) to 2.3 at% (cooled face)) helps circumventing these issues as illustrated in the right sketch of Fig. 2.2. The associated stored energy density curve (red) reveals indeed a much more homogeneous heat load distribution.

Considering the square meter scale aperture typically required for kJ laser chain, the foreseen amplifiers would be subject to ASE losses and parasitic lasing if the product gain [g_0 in cm^{-1}] times width [L (dimension in transverse direction) in cm] becomes too high. A commonly used criterion setting the maximum ASE gain tolerance is $g_0.L \leq 4$: in that case, $\exp(g_0.L) = 55$ and the loss to such amplified signals must be at least 98% at the edge of the amplifier material in order to avoid any transverse oscillations. Such a loss level can be achieved by the use of i.e. liquid index matching or an absorbing cladding (as described in section 1.5.3, such absorbing cladding of Cr^{4+} is used for DPSSL Lucia main amplifier ASE management). In this particular example, the crystals are considered to be 4 cm wide (rectangular shaped crystals originally used for the Lucia first main amplifier, afterwards replaced by 60mm diameter crystals/ceramics disks); therefore such criterion is reached when $g_0 = 1$ cm^{-1}.

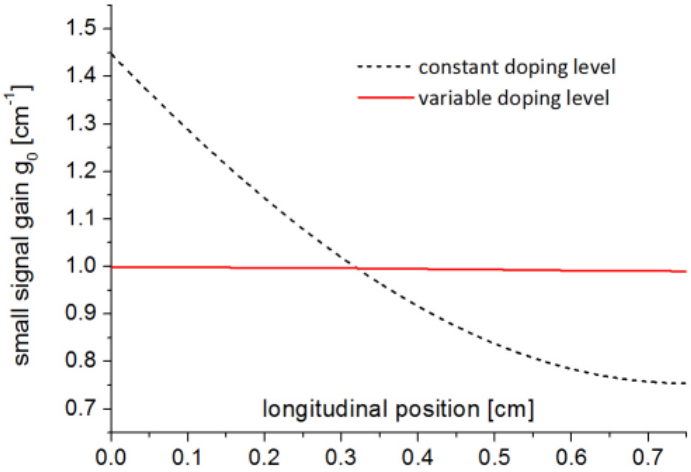

Fig.2.3. Small signal gain distribution for a single side pumped active mirror with uniform doping distribution (dotted curve) and variable doping distribution (red curve)

For the gradient doped crystal, the small signal gain is below 1 cm^{-1} everywhere, as illustrated in Fig. 2.3 (red curve) - no dramatic losses due to oscillations are expected. In the case of the uniformly doped crystal, the $g_0.L$ product will be higher in the layers located between z = 0 and approximately 0.3 cm, reaching values as high as 1.45 cm^{-1} (dotted curve) nearby the entrance pump face.

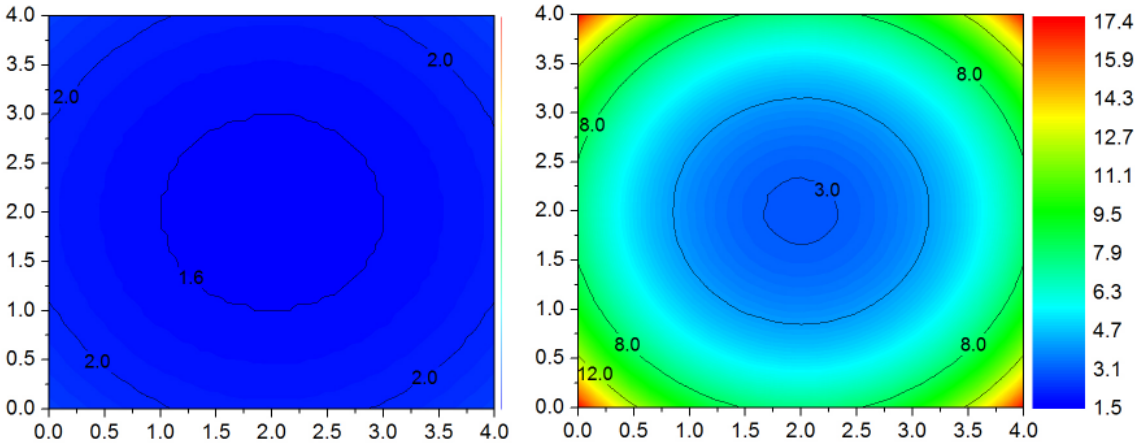

Fig.2.4. Distribution of M_{ASE} in $z = 0$ layer for variable (left) and homogeneous (right) doping distributions in 4x4 cm² crystals

This volume will therefore very likely host transverse oscillations affecting the available local gain. M_{ASE} (see section 1.4) distribution in z = 0 layer is shown on the Fig. 2.4 where a three dimensional ASE simulation clearly illustrate the strong gain depletion occurring there. A seven times higher (17.5 vs. 2.5) M_{ASE} can indeed be observed in the edges.

These ASE calculations were performed with a specific ASE model developed in the frames of Lucia program *(Albach's model)*.

2.4. Impact of Energy Storage distribution on volumic energy storage

Let us also mention a specific advantage for LMJ-like large size laser systems, where several thousands of glass slabs weighting more than 100 tons are required [2.5]. As it can be seen in Fig. 2.5, the gradient doping has a positive impact on the extractible energy density for a given gain medium volume. A 0.75 cm thick crystal (central sketch) is sufficient to reach the extraction capacity (~6 J/cm²) of a 1.15 cm thick uniformly doped crystal (left image). In both cases, doping has been adjusted in such a way that the $g_0 < 1$ cm^{-1} constraint is satisfied for any layer inside the crystal. Such a 35 % decrease on the requested volume can have a dramatic impact on HiPER or any large laser requiring high amounts of laser gain media. The same figure also shows (right sketch) the case of an equivalently thin (0.75 cm), but uniformly doped crystal from which a similar extractible energy density would be achievable, when neglecting ASE. Doping ion concentration must then be increased from 1.3 to 1.9 at%, implying a 50 % increase for the maximum gain at the entrance face (g_0=1.5 cm^{-1}). ASE losses will then become important and actually the 6 J/cm² extractible value will not be achievable.

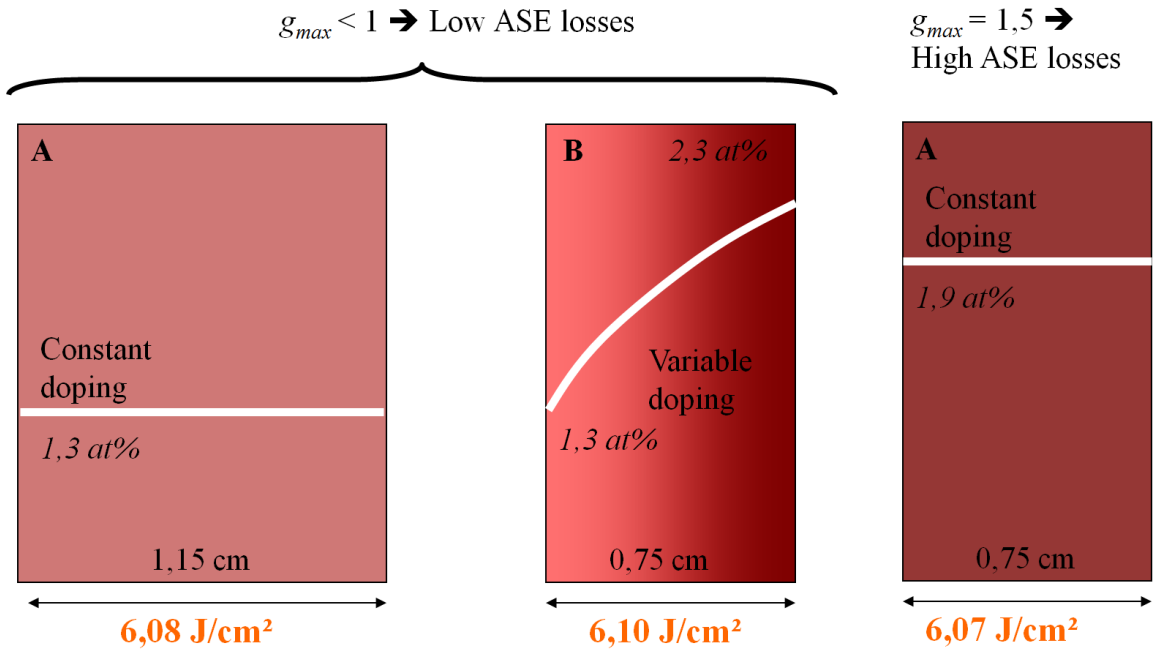

Fig.2.5. Requested volumes to reach a similar extractible energy density (~6J/cm²) in absence of ASE for three different doping distributions

The decreased size will have a crucial impact also in terms of the thermal management as it will be shown in the following section.

2.5. Impact of Energy Storage distribution on thermal management

Thermal management is of key importance on high repetition rate laser systems. Thermally induced effects can indeed strongly degrade beam quality, leading to thermal lensing or birefringence. Stresses introduced by thermal gradients among different area of the gain medium as well as thermal expansion introduced by temperature increase, can bring to the destruction of gain medium. All these limit the average output power of DPSSL systems and decrease their efficiency.

After defining the heat source term (2.5.1), we will define the thermal conductivity (2.5.2), how the heat flow propagate inside the gain medium (2.5.3) and, in (2.5.4), we will discuss obtained results and advantages of gradient doped gain medium.

2.5.1. Heat Generation

Heating of the gain medium occurs due to the non-radiative relaxation in the pumping/lasing cycle. Radiations, stimulated as well as spontaneous, reduce the inversion on the upper laser state. In [2.6], Fan measures the fractional thermal loading η_h, i.e. the ratio between the heat generated ($C_P.m.\Delta T$) and the absorbed energy ($\tau.P_{abs}$) of YAG samples. C_P is the heat capacity per unit mass of YAG, m the sample mass. ΔT the steady-state temperature elevation reached with pumping. P_{abs} is the absorbed pump power. When pumping stops, the temperature decay is recorded as a function of time and the thermal time constant τ extracted from the resulting curve. In the same letter, Fan expresses η_h as follows:

$$\eta_H = 1 - \eta_P \left[(1 - \eta_L) \eta_R (\lambda_P / \lambda_F) + \eta_L (\lambda_P / \lambda_L) \right], \qquad (2.1)$$

where η_P is the pump quantum efficiency, η_R the radiative quantum efficiency (related to quantum efficiency η_Q via $\eta_Q = \eta_R \eta_P$) for the upper metastable level, and η_L is the fraction of ions excited to this level that are extracted by stimulated emission (i.e. through a lasing process). λ_L is the stimulated emission wavelength, λ_P is the pump wavelength and λ_F is the average fluorescence wavelength. Assuming no pumping of non radiatives sites, we have $\eta_P = 1$. In the absence of concentration quenching or multiphonon non radiative decay, we have η_R=1, so in this quantum defect limited operation case, we have also $\eta_L = 1$ and (2.1) simplifies into:

$$\eta_H = \eta_{QD} = 1 - \lambda_P / \lambda_L$$

For Yb:YAG (λ_P = 940 nm, λ_L = 1030 nm), we obtain a quantum defect limited efficiency of 8.7%. Fan's experimental result leads to a maximum value of 11%.

No lasing case (η_L=*0*) leads the value of η_H around 15.1% for Yb:YAG which twice more that in quantum defect limited case.

Let us finally introduce the volumetric heat production Q which will act as the heat source term in our model (see §2.5.3). It is defined as the ratio between the fraction of absorbed pump power converted into heat $P_{abs}.\eta_H$ and the gain medium volume V:

$$Q = \frac{P_{abs} \cdot \eta_H}{V}.$$

2.5.2. Thermal Conductivity

In the crystalline materials under consideration here, heat transport is performed via phonons and thermal conductivity in perfect crystals is limited only by phonon-phonon interactions. Real crystalline structures are not free of crystalline structure defects such as dislocations, irregularities, impurities such as metallic or other inclusions, bubbles (depending on growth process), doping introduced structure distortion, etc... All these determine critically electrical and mechanical properties of real materials. Debye derived the expression of thermal conductivity [$W/(m \cdot K)$] as follows:

$$k = \frac{1}{3} C_P v \lambda$$

where C_P is the heat capacity at constant pressure, v the velocity of phonons and λ the mean free path. At low temperatures T, phonon-phonon interaction being omitted, thermal conductivity will increase with a T^3 law. Debye temperature for Yb:YAG is between 505K and 750K [2.7]. The temperature increase brings up Umklapp processes [2.8], causing thermal conductivity decrease. For higher temperatures, Gaume derived a qualitative model [2.9], taking into account chemical and structural properties of the crystals where the thermal conductivity is defined as:

$$k = \frac{1}{T} \cdot \frac{A}{\gamma^2 \varepsilon^3} \cdot T_{mp}^{3/2} \cdot \rho^{2/3} \cdot M^{1/3} \cdot n^{-1/3} \cdot \mu^{-3/2},$$

where A is a numerical constant independent of the material properties and can be an adjustable parameter determined experimentally, γ is a parameter measuring the deviation to a pure harmonic behavior of chemical bonds, ε is an interatomic distance increase factor, T_{mp} is the melting temperature, ρ is the material density, M is the molar mass, n is the number of atoms per formula unit and μ is the reduced mass (harmonic average of all ion masses per formula unit).

Dopant ions differ in diameter and mass from substituted atoms. It therefore induces distortions of the crystal lattice. The doping concentration is then impacting the thermal conductivity. Yb^{3+} dopant ion has an 86.8 pm ionic radius and a 173 $g.mol^{-1}$ molar mass to be compared with the substituted Y^{3+} ion where the respective values are 90.8 pm and 88.9 $g.mol^{-1}$.

Fig. 2.7 and 2.8 illustrate the thermal conductivity of Yb^{3+}:YAG single crystal as a function of temperature for different doping concentrations and thermal conductivity curves as a function of Yb^{3+} concentration in YAG host matrix for several temperatures.

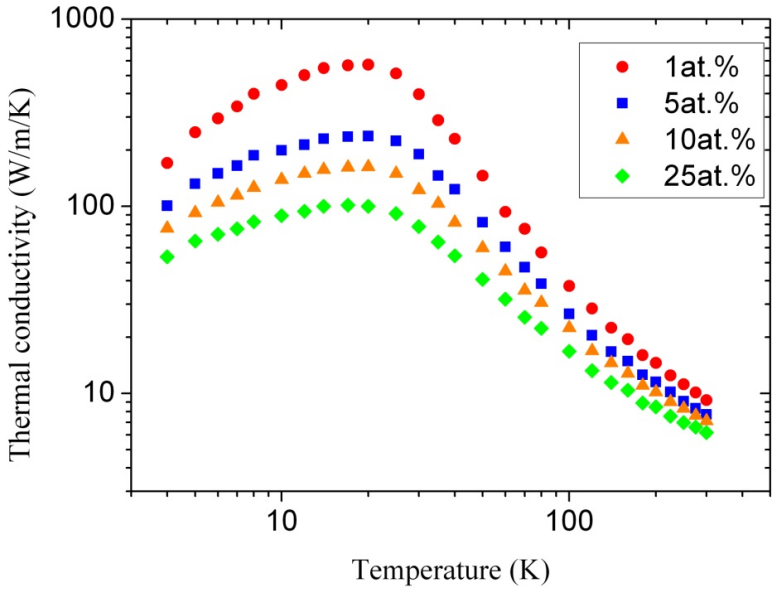

Fig.2.7. Thermal conductivity of Yb^{3+}:YAG as a function of temperature for different doping concentrations [2.10]

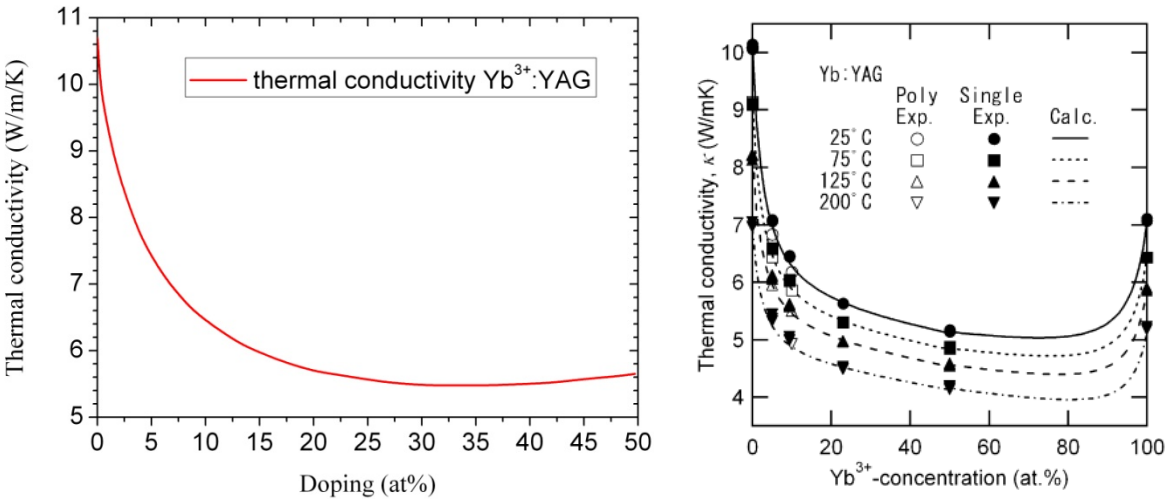

Fig.2.8. Variation of the thermal conductivity of Yb^{3+}:YAG as a function of dopant ion concentration. The theoretical curve (on the left) [2.9] and experimental data (on the right) [2.7] are presented

2.5.3. Heat Transport

The heat transport is described by the following partial differential equation:

$$\rho C_P \frac{\partial T}{\partial t} = \nabla(k \cdot \nabla T) + Q\,, \tag{2.2}$$

where Q is the heat source introduced in section 2.5.1 and k the heat conductivity. In general for YAG crystals, thermal conductivity can be taken as isotropic but, in our case, the doping is not homogeneous and, as shown in the previous section, the thermal conductivity is a function of doping concentration, and consequently it will change along the axis of doping variation. Also ρ, C_P and k are functions of temperature. The solution of this partial differential equation is determined by gain medium and cooling system design.

Fig. 2.9 represents four cooling design simplified schemes. In rod and sandwich design cases, heat evacuation direction (blue arrows) is perpendicular to pump direction (red arrow) while for thin disk and slab cases pump and heat axis coincide. Lucia system is based on active mirror concept illustrated by the thin disc scheme (Fig. 2.9: top right). The main disadvantage of this cooling design is the fact that coolant is in contact only with the "cold" surface of the disc (surface opposite to pumped one). The description of the mathematical model used for solving the equation (2.2) is presented in annex B.

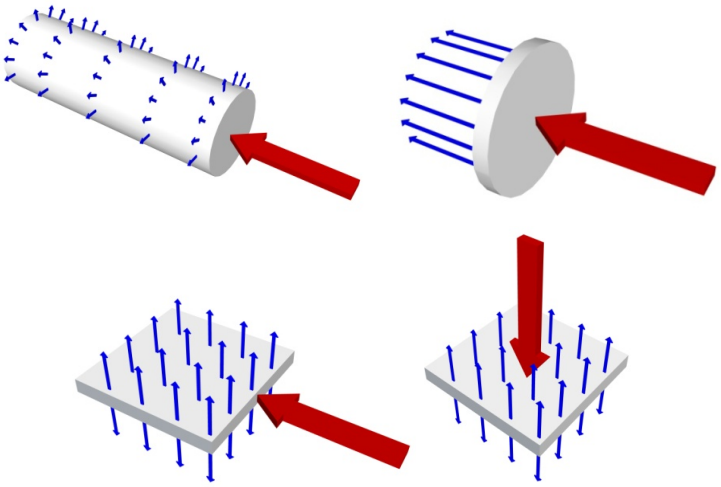

Fig.2.9. Left to Right, top to bottom: Rod, Thin Disk, Sandwich and slab cooling/pumping architectures. Red arrows indicate the pump direction while blue ones show heat evacuation directions

2.5.4. Results

The constants used in the calculations are set considering Lucia laser system. The surface of the gain medium is pumped at approximately 16.5 kW/cm^2 for 1 ms. It is currently operating at 2 Hz but the ultimately planned operation is aiming at 10 Hz. Both repetition rates are taken into consideration. Heat exchange coefficient with water is h_{water} ≈15000 W/m^2 K. The water or other coolant temperature is considered as being equal to 286.15 K. From the pump geometry, it is clear that, thinner the gain medium, more efficiently will be the cooling and less temperature gradient will be obtained between pumped and cooled faces. Decrease in gain medium thickness leads to its doping concentration increase to keep the amplification level maintained, which will stimulate parasitic oscillations and reduce thermal conductivity. Therefore, a compromise should be found. The gradient doping is a perfect solution to reach such optimum. The limitation for amplified spontaneous emission $g_0^{\max} \cdot L < 4$ constraint is taken, where L is the maximum transverse length along which parasitic oscillations can develop. In the case of our cylindrical amplifier, it is equal to its 60 mm diameter. For pre-amplifiers, this value is much less (the crystals used there have a diameter of 12 mm).

First, let us estimate the temperature distribution for the three cases of Fig.2.5 for 10 Hz operation rate and after stabilization is achieved. As it can be seen from Fig. 2.10 for gradient doped and highly doped 7.5 mm crystals, thermal stabilization is achieved after approximately 600 pulses, while for the low doped thicker crystal, even after 1200 pulses, full stabilization is

not achieved yet and maximum temperature is significantly higher. This illustrates the great dependence of temperature distribution with crystal thickness.

Comparing the temperature distribution for gradient doped and uniformly doped cases with the same crystal thickness (Fig. 2.11), we observe that a difference, although not very significant, can still be observed. But, as already mentioned, in the case of the 1.9 at% doped crystal, ASE losses will be very important and the energy storage will never be maintained.

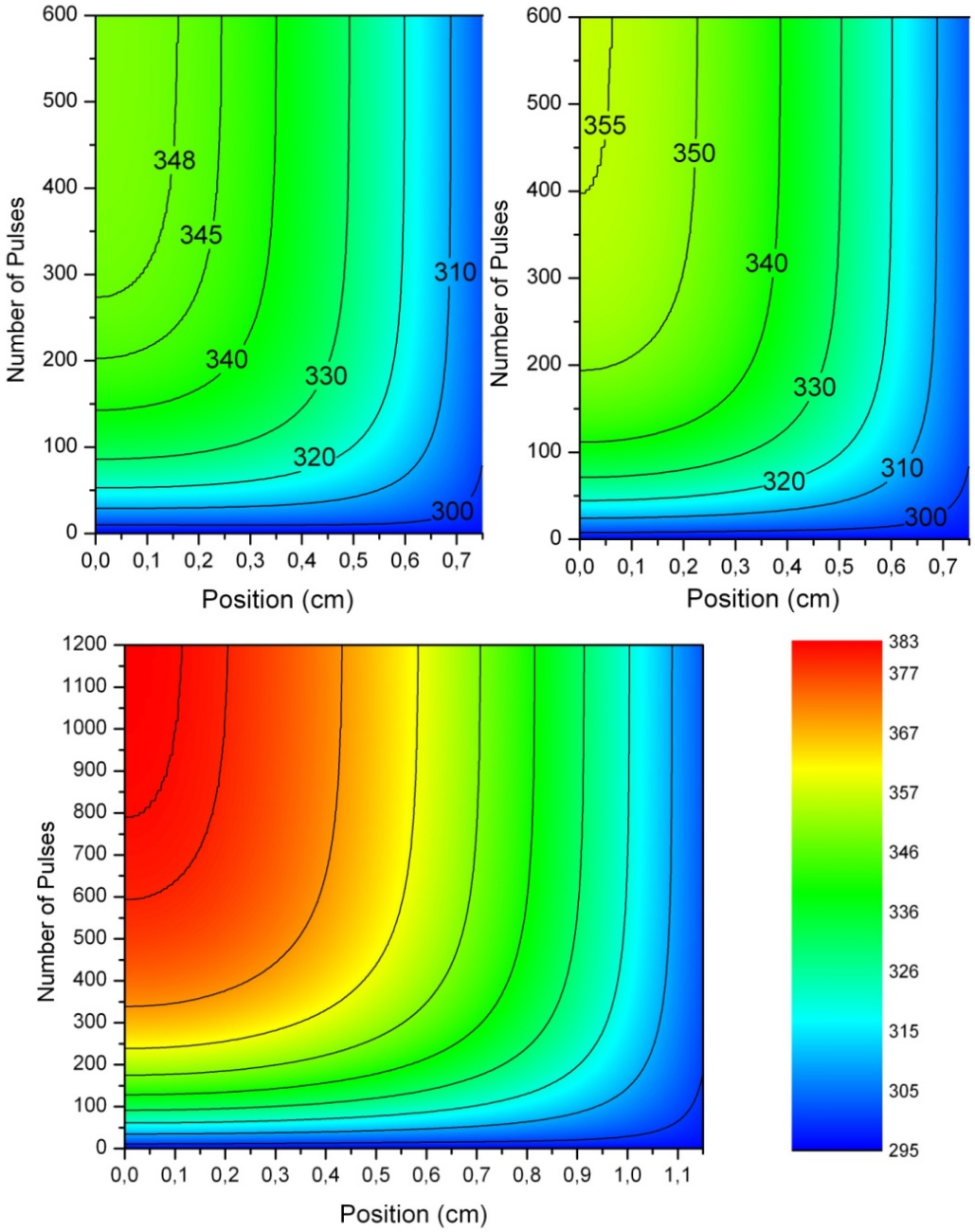

Fig.2.10. Maps giving the thermal longitudinal distribution evolution with the number of pump pulses at 10 Hz for three crystals: 7.5 mm thick gradient doped crystal (top left) with 1.2 to 2.3 at% Yb^{3+} concentration variation. 7.5 mm thick 1.9 at% uniformly doped crystal (top right. 11.5 mm thick, and 1.3 at% uniformly doped crystal (bottom)

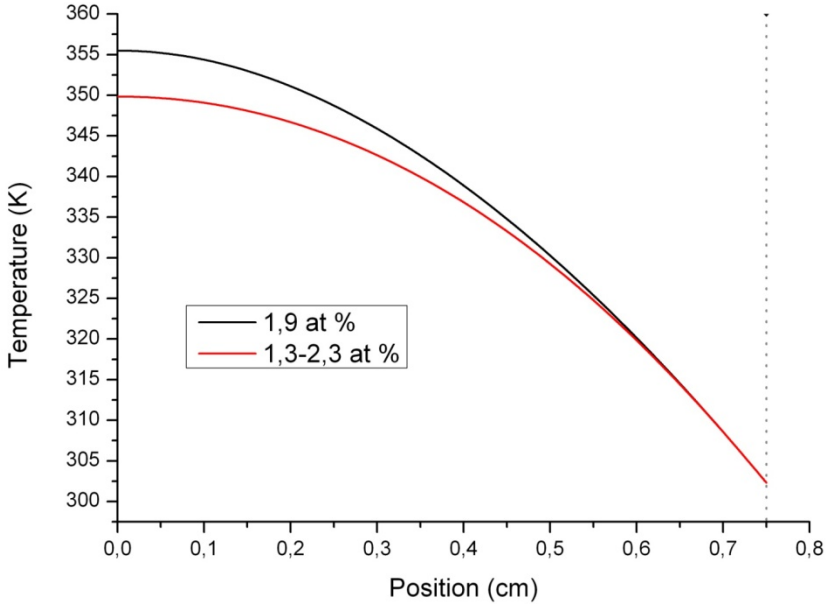

Fig.2.11. Temperature distribution after stabilization for 1.9 at% and 1.3-2.3 at% doped crystals of 0.75 cm thickness at 10 Hz repetition rate

Several attempts have been performed to obtain gradient doped crystals through successive crystallogenesis campaigns. The growth processes and resulting crystals characteristics will be reported in detail in the next chapters. The maximum gradient obtained reaches a value of 2 at% per cm. It seems quite feasible to increase it up to 3 at%.cm^{-1} without major changes in the current growth modus operandi.

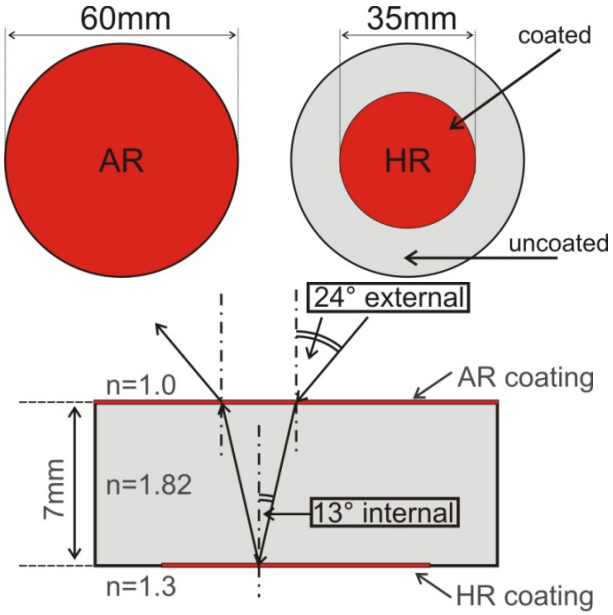

Fig.2.12. 60 mm crystal used for Lucia main amplifier. The pump zone has only 35 mm diameter. The un-pumped outer part of the crystal is used to absorb ASE. Laser beam incident angle is 24°

Let us try to estimate what would be the contribution of such doping gradients application to Lucia laser current configuration where 60 mm diameter, 2 at% homogenously doped crystals are used (Fig. 2.12). The central 30 mm diameter area is pumped with 40 DILAS diode stacks emitting at 940 nm.

After pump light concentration, 14 kW/cm^2 intensity is reached. Table 2.1 compares temperature and ASE for amplifier configuration. The homogeneously doped 2 at% crystal (currently used in Lucia amplifier) is compared with a linear gradient doped crystal of identical thickness and a linear gradient doped crystal with a 0.6 cm optimized thickness. All three cases have approximately the same energy storage capacity. Temperature difference between crystal faces (ΔT) and maximum temperature T_{max} are compared after a 1000 pulses sequence, where steady state is already established.

Table 2.1: Thermal characteristic for Lucia amplifier

Doping level	2 at%		1-3 at%		1.4-3.4 at%	
Thickness	0.7 cm		0.7 cm		0.6 cm	
Pump Intensity	14 kW/cm^2		14 kW/cm^2		14 kW/cm^2	
Repetition Rate	2 Hz	10 Hz	2 Hz	10 Hz	2 Hz	10 Hz
$g_0^{max}.L$	4.6		3.7		3.99	
ΔT	9.88 K	49.59 K	8.37 K	42.77 K	7.59 K	38.90 K
T_{max}	297.63 K	343.04 K	296.22 K	336.31 K	295.46 K	332.51 K

Fig. 2.13 shows temperature distribution in the crystal at steady state for the 4 first cases of Table 2.1. By changing doping from 2 at% to 1-3 at%, ASE management is greatly improved. For 10 Hz operation there is also a small improvement in terms of temperature distribution (Fig. 2.13) while it is negligible for 2 Hz operation. Further improvement can be achieved by increasing doping concentration extremes up to 1.4 and 3.4 at% and reducing crystal thickness by 0.1 mm. This will lead to maximum temperature decrease up to 11 K.

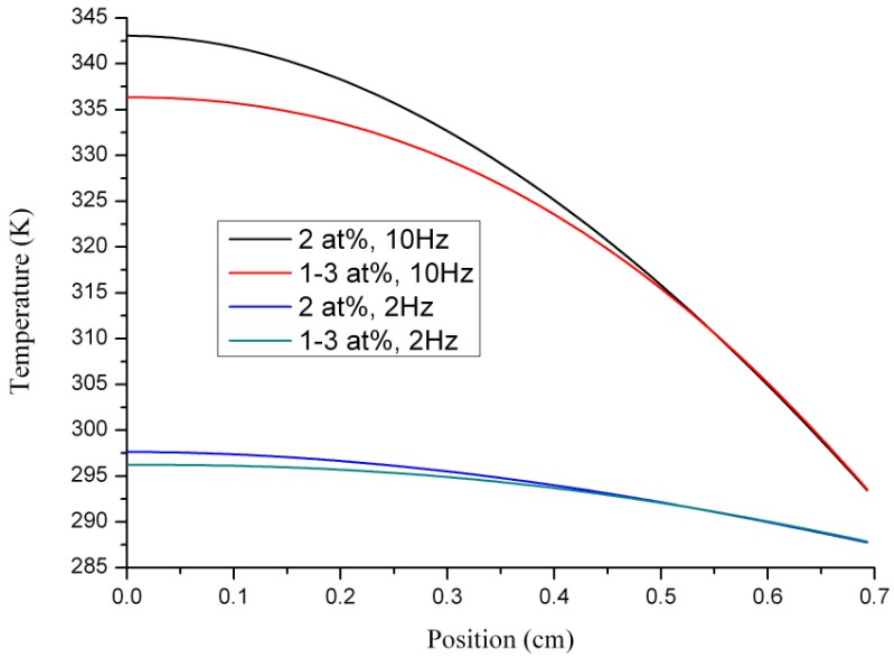

Fig.2.13. Temperature distribution in the crystal at steady state for the four first cases of Table 2.1

Keeping the same limitations due to ASE, let us now build the comparison table for Lucia pre-amplifier. In this case an area of 3.3 mm x 3.8 mm is pumped at 20 kW/cm^2, although the operational pump intensity is closer to 15 kW/cm².

Table 2.2: Thermal characteristic for Lucia Pre-amplifier

Doping level	8 at%		7.5-8.5 at%	
Thickness	0.5 cm		0.5 cm	
Pump Intensity	20 kW/cm^2		20 kW/cm^2	
Repetition Rate	2 Hz	10 Hz	2 Hz	10 Hz
$g_0^{\max}.L$	3.86		3.62	
ΔT	18.70 K	90.16 K	18.45 K	89.15 K
$T_{\max}$	307.16 K	387.56 K	306.91K	386.55 K

Doping concentration gradient with technically available values does not introduce significant changes in temperature distribution for the pre-amplifier configuration and g_0L does not really evolve.

Existing gradients are not strong enough to introduce major changes, but they still can help reducing ASE and thermal effects. Another major impact is the lower gain medium volume requirement taking place while replacing homogenous doped crystals by gradient doped crystals with the same lasing characteristics. Improvements offered by gradient crystals are also discussed in Chapter 5.

2.6. References

[2.1] www.hiper-laser.org.

[2.2] Dunne M., "A high-power laser fusion facility for Europe", Nature physics, 2 (January 2006).

[2.3] Meier W. R., "Systems Modeling for a Laser-Driven IFE Power Plant using Direct Conversion", The fifth International Conference on Inertial Fusion Sciences and Applications (IFSA2007) IOP Publishing. Journal of Physics: Conference Series 112 (2008).

[2.4] Chanteloup J.-C., Ertel K., Hein J. et Le Garrec B. J., "Multi kJ Level Laser Concepts for HiPER facility", Sixth International Conference on Inertial Fusion Sciences and Applications (IFSA 2009), 6-11 september 2009, San Francisco, USA.

[2.5] http://www-lmj.cea.fr/

[2.6] Fan T.Y. 'Heat-Generation In Nd-Yag And Yb-Yag.' Ieee Journal Of Quantum Electronics, 29(6):(1993) pp. 1457–1459.

[2.7] Sato Y., Akiyama J., and Taira T. "Effects of rare-earth doping on thermal conductivity in Y3Al5O12 crystals" Optical Materials, 31(5):(2009) pp. 720–724.

[2.8] Ashcroft N.W., Mermin N.D. "Festkörperphysik" Oldenbourg, 2001.

[2.9] Gaume R., Viana B., Vivien D., Roger J.P., and Fournier D. "A simple model for the prediction of thermal conductivity in pure and doped insulating crystals" Applied Physics Letters, 83(7):(2003) pp. 1355–1357.

[2.10] Albach D., "Amplified spontaneous emission and thermal management on a high average-power diode-pumped solid-state laser: the LUCIA laser system". (Doctoral thesis), Ecole Polytechnique, 2010.

3. YAG growth from melt: Bagdassarov Method

3.1. Motivation

This chapter is dedicated to crystal growth techniques. While section 3.2 gives a brief historical overview, section 3.3 introduces currently operated crystal growth techniques. Then, in section 3.4, emphasis is given on growth from melt techniques and its limitations for YAG growth, especially for gradient doped crystals. Finally section 3.5 provides detailed description and characterization of Bagdasarov growth technique experimental results gathered in the frame of this work. Growth process details as well as physical properties of the crystals on their own will be described in the next chapters.

3.2. History and overview of crystal growth

Crystals are as ancient as the world. Mankind interacted with crystals in the forms of snowflakes, or minerals. Salt and sugar crystallization techniques were used in the ancient Chinese and Indian civilizations [3.1]. Crystals are solid materials of regular atomic structures leading to periodicity and anisotropy for most of their physical properties. Crystals exhibit a various and wide range of external shapes, and the same species may present different crystal forms. Such diversity is among the reasons which stimulated scientific interest for this type of materials. The subject of crystal growth includes all areas of crystal formation: from natural processes to preparation of crystals in laboratories and factories. First scientific approach to crystal growth was given by Kepler who, in 1611, correlated crystal morphology and structure, followed by Steno, Descartes etc… At the beginning of the 20^{th} century, Crystal Growth was recognized as a separate scientific branch and gradually became one of the basic disciplines of material science. Kossel, Donnay-Harker, Volmer and Burton, Cabrera and Frank proposed several theories. Without the complicity of growth techniques and instrumentations and with poorly controlled growth parameters, only small and fine crystals were grown up to World War II. Technological progresses gave access to relatively large bulk crystal growth processes and techniques during that war. Over the last six decades, crystals became key materials for many fields of technological applications, like electronics, optoelectronics … and by this crystal growth became a strategic technology. Today applications of artificially grown crystals cover all spheres of human society. Crystals in nature are generally polycrystalline. The aim of crystal grower is generally to obtain perfect single crystals with desired shapes by "arranging" particles (atoms, ions, molecules) in periodic three-dimensional arrays. Real crystals are never free of defects such as dislocations, impurities and etc… This leads to continuous development and improvement of growth and characterization techniques. Currently grown single crystals cover the size range from bulk (~100 cm) to nanoscale.

Crystal formation always represents a phase transition: solid – solid, liquid – solid or vapor – solid. Solid – solid transition is rarely used and there is usually always an intermediate liquid phase. Liquid/vapor to solid transition is of major importance for crystal growth various processes. Growth process does not take place when the crystal phase is in dynamic

equilibrium with the disordered phase (the number of particles exchanged between both phases is equal). For the growth process to take place, this equilibrium has to somehow be perturbed by changing chemical potential, pressure, temperature or other parameters, which will stimulate nucleation (a process which is part of crystallization). Growth process can be described as the succession of three steps:

- supercooling or supersaturation,
- nucleation center formation,
- formation of single crystal from nuclei

Growth components supersaturation or supercooling conditions must be satisfied in order for the crystallization to take place. Indeed nucleation centers will then form spontaneously but this process can also be induced artificially by physically introducing nucleation centers (seed). Center formation inside a melt takes place when the following condition is satisfied:

$$\Delta H_L \left(\frac{T_L - T_R}{T_L} \right) = \frac{2\sigma V}{R}, \qquad (3.1)$$

where T_L and T_R are respectively the melting temperatures of a large crystal and a crystal with radius R, H_L is the fusion latent heat per molecule.

Main crystal growth theories are surface energy theory, diffusion theory, adsorption layer theory and screw dislocation theory. Being out of scope of this thesis, the details of these theories are not provided here but are well described in [3.2, 3.3].

3.3. Classification of crystal growth techniques

Crystal growth is a physico-chemical process resulting in the production of solid materials with a three dimensional periodic arranged structure. This process may or may not include different phases simultaneously, but the final product is always solid. Crystal growth processes can be classified accordingly to Table 3.1 (from [3.2] with some modifications).

Solution growth approach relies on materials decomposed in a liquid solvent. This is the oldest technique, used not only for crystals for advanced technologies, but also to produce daily use goods as in food industry for instance. In solution growth techniques, it is very important to know the behavior of solvent with pressure, temperature, growth required component(s) concentration(s) etc… Solution growth technique offers the possibility to grow crystals from materials which decompose below melting point with full control of solution temperature, viscosity parameters and equipment simplicity. With the help of these techniques, crystals of strategic importance such as GaAs, InP, GaP, etc… are being grown. Several methods for solution growth exist which will not be covered here.

Table 3.1: Example of crystal growth techniques classification. Column 1 gives the processes generic names. Column 2 gives the source materials. Column 3 indicates the key parameter (Pressure or Temperature) and column 4 lists the different solidification techniques.

Solid – Solid	Solid	T →	Solid Devitrification Strain annealing Polymorphic phase change Precipitation from solid solution
Liquid – Solid			
Melt growth	Molten material	Dec. T →	Crystal Verneuil Czochralski Kyropoulus Bridgman Bridgman-Stockbarger Temperature-Gradient-Technique Zoning Bagdasarov
Flux growth	Solid(s)+flux agents	Dec. T →	Crystal(s)
Solution growth	Solid(s)+solvent	Low T →	Crystal(s) Evaporation Slow cooling Boiling solutions
Hydrothermal	Solid(s)+solvent	High T →	Crystal(s) Hydrothermal sintering
		High P	Hydrothermal reactions Normal temperature gradient Reversed temperature gradient
Gel growth	Solution+gel	Low T →	Crystal Reaction Complex decomplex Chemical reduction Solubility reduction Counter-flow diffusion
	Solution	→	Crystal(s)+products
Gas – Solid	Vapor(s)	→	Solid Sublimation-Condensation Sputtering Epitaxial Ion-implementation

Solid growth is an approach based on particles diffusion, usually very slow and mostly used in metallurgical processes.

Vapor growth approach is the most efficient for epitaxial growth. These methods are widely used for low-cost fabrication of semiconductor materials. The chemical processes of gas-phase are quite complicated. Despite that fact, vapor-growth technique has a great success mainly due to the easy manipulation of low- and high-pressure vapor-phase elements [3.2]. The temperatures are quite below melting temperature, implying that produced crystals are

almost free of crystal defects such as point defects and dislocations in contrary to growth from melt technique, making therefore these methods the only choice for incongruent melting. In a congruent melting, the composition of the liquid is the same as the composition of the solid. In an incongruent melting, the substance does not melt uniformly and decomposes into another substance. During the phase-growth process, liquid or solid are heated to high temperatures to form vapor, which afterward is being transported in the vacuum by kinetic energy of evaporation or by inert gas and deposited on the growth surface by chemical reaction or condensation.

Growth from melt is the subject of the next section for the specific case of YAG.

3.4. Crystal growth from melt: Case of Yttrium Aluminum Garnet

3.4.1. Yttrium Aluminum Garnet Growth

The description of Yttrium Aluminum Garnet crystals, as well as laser characteristics of Yb doped YAG materials is given in chapters 1 and 4. Let us here concentrate on YAG growth characteristics and methods. As it has already been mentioned, one of the main advantages of YAG is the fact that it is quite easy to grow with a large variety of doping elements as well as using different growth methods. In Y_2O_3-Al_2O_3 phase diagram (Fig.3.1), three intermediate compounds $Y_3Al_5O_{12}$ (YAG), $YAlO_3$ and $Y_4Al_2O_9$ exist. The second and third compounds are called Yttrium Aluminum Perovskite (YAP) and Yttrium Aluminum Monoclinic (YAM) [3.4]. YAP can have orthorhombic [3.5] and hexagonal [3.6] crystal structures called polymorphs. YAG normally exists in cubic form, although the existence of a high-temperature tetragonal polymorph has been reported [3.7]. The decomposition of YAP and YAM components to YAG was observed at elevated temperatures, and it was then concluded that YAG was the only stable component of this system [3.8]. YAG and YAP are widely used as laser material: numerous groups report on lasers based on $YAlO_3$ matrix doped by Ho, Nd, Yb and other ions [3.9, 3.10 and 3.11]. In order to obtain a YAG phase, the mol ratio of yttrium oxide and aluminum oxide has to be 3:5.

Depending on the concentration of Y_2O_3 and Al_2O_3, other chemical compounds may form:

- Zone 1 on the phase diagram is situated above the liquidus (phase diagram boundary to solid-liquid interface), therefore corresponding to the melt,
- Zone 2: Y_2O_3+$2Y_2O_3{\cdot}Al_2O_3$
- Zone 3: $2Y_2O_3{\cdot}Al_2O_3$+$Y_3Al_5O_{12}$ (YAG)
- Zone 4: $Y_3Al_5O_{12}$ (YAG) + αAl_2O_3
- Zone 5: $2Y_2O_3{\cdot}Al_2O_3$ + $Y_3Al_5O_{12}$ (YAG)
- Zone 6: melt + $2Y_2O_3{\cdot}Al_2O_3$
- Zone 7: melt + $Y_3Al_5O_{12}$ (YAG)

The melting temperature of YAG varies among authors [3.4, 3.8, 3.13] between 1930 °C and 1975 °C. [3.12] shows that, at 1935 °C, Al_2O_3 and $YAlO_3$ phases are already present in the

YAG sample under study and that the sample fully collapses at 1955°C. On the phase diagram (Fig.3.1), a 1924 °C melting temperature is considered for YAG.

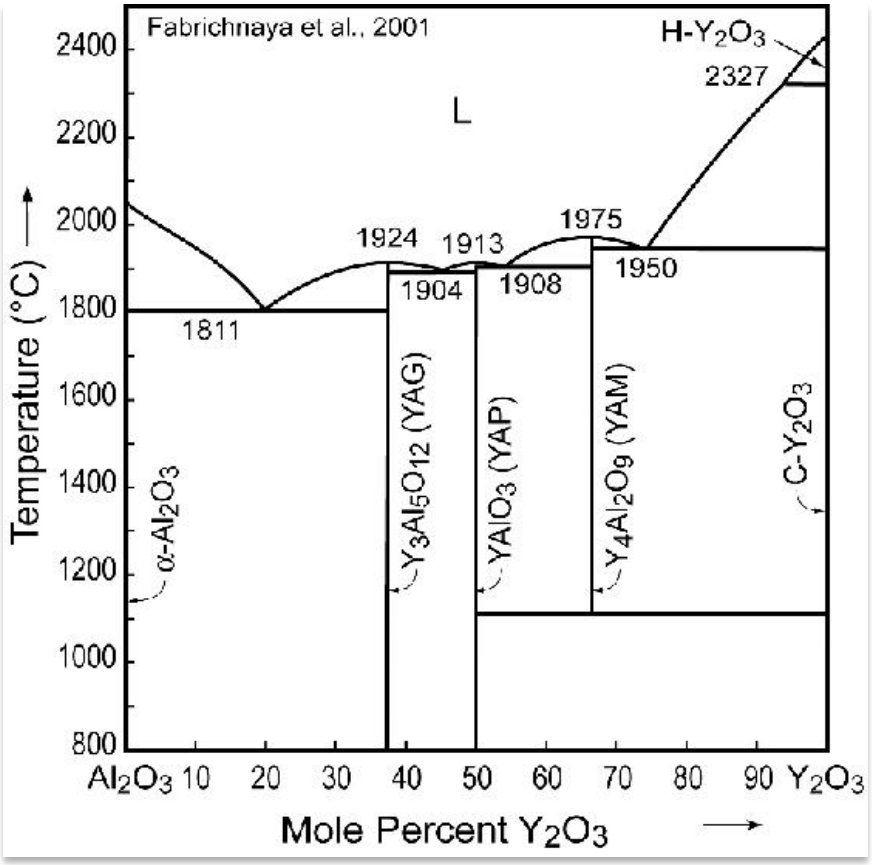

Fig.3.1. Phase diagram for Y_2O_3 - Al_2O_3 system[3.14]

3.4.2. Activators distribution within the grown material

YAG can be doped with a large spectrum of chemical elements. Activators like Ce, Nd, Er, Tu, Eu, Cr, Ho are used to produce laser or scintillator materials. In general, for melt growth techniques, depending on activator and matrix characteristics, the distribution of activator content in the host medium can be quite different. For example, Neodymium concentration in YAG crystals almost never exceeds 1 at% (in ceramics, it can achieve up to 10 at%) [3.15], while Yb doping level can reach values up to 100% (and then transforming YAG to YbAG) without any particular difficulty [3.16, 3.17]. Besides doping level, the activator can also present variations of spatial distribution within the grown-from-melt crystal. This is due to a process called segregation (the content of the dopant/impurity is different in the liquid phase and solid phase) [3.18]. The process of segregation is different for atomic-rough and facet growth (Fig. 3.2). The predominance of one of these two processes over the other is highly related to the transverse (with respect to the growth axis) temperature gradient (see fig. 3.12). The atomic-rough growth process is the most favored one. It requires a growth front as flat as possible, i.e. a minimized transverse gradient.

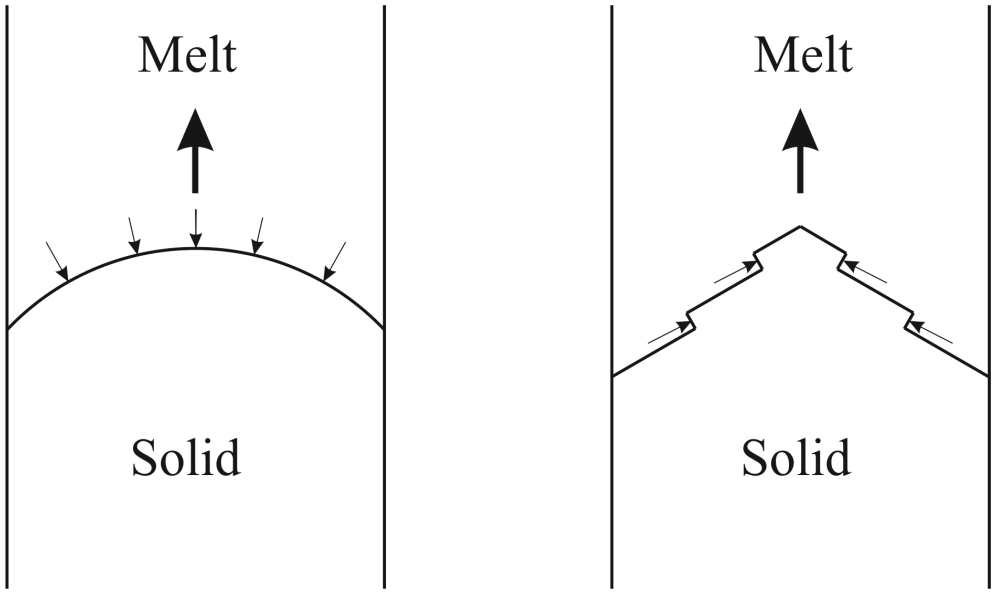

Fig.3.2. Atomic-rough (non-facet) growth (left) and facet-growth (right) principle schemes. Bold arrows show the direction of growth while small arrows indicate where new particles attach to the crystal. In case of facet-growth, the facets grow in the opposite to the direction indicated by the small arrows and the particles from the melt attach to the growth steps' edges providing so-called tangential growth. The solidification interface moves further due to one after one added layers which grow in tangential direction. Atomic rough growth is called normal growth because the new particles from the melt attach to the solid everywhere on the solidification interface.

The rate of crystallization can be expressed as $V=\chi\Delta T$ [3.29], where χ [m/s/°C] is the degree of atomic-roughness of the crystallization front (higher the value is, higher the roughness of the surface), and ΔT [°C] is the degree of supercooling of the melt near the interface. In general, both atomic-rough and facet growths occur simultaneously, but here, only the case of atomic-rough growth is discussed, because, in our experiments, this is by far the dominating type of growth. Segregation is characterized by the so-called segregation coefficient $k_s=C_S/C_L$, where C_S and C_L are the dopant concentrations in solid and liquid phases. This coefficient can be below, above or equal to unity. The dopant concentration in liquid may change during growth and this leads to a continuous variation of dopant concentration in the solid phase. When all the content of growth material is molten at the beginning of the process and the crystallization front is flat, the solidification process is called normal crystallization [3.19]. During normal crystallization, segregation processes can either be described as [3.19]:

-1- diffusion of dopant takes place in solid and liquid,
-2- no diffusion in solid and immediate diffusion in liquid,
-3- no diffusion in solid and limited diffusion in liquid without convectional mixing,
-4- limited diffusion and moderate convectional mixing.

The first case does not present any significant interest since it leads to homogeneous distribution of the dopant in the solid because of the diffusion present in this phase, making the introduction of a segregation coefficient unnecessary ($k_s = 1$). But usually, diffusion is

quite weak and is present only at high temperatures (in annealing processes for instance), especially in crystals.

The other three cases offer more practical interest when at least convectional mixing or diffusion are present in the liquid. Let us consider the process when the crucible is filled with a melt and being frozen from one end (Fig 3.3). The concentration of dopant in the melt is C_0 and immediate diffusion/mixing of the liquid is considered. The equations and figures used from now on to describe the segregation process are related to $k_S < 1$ but the logic remains the same for the opposite case. Due to the freezing, the solid phase appears with a dopant concentration $k_S C_0$ less than the concentration C_0 in the melt. The exceeding dopants stay in the melt and, through instantaneous diffusion, consequently increase the concentration in the melt. Therefore, the concentration in upcoming solid layers increases. Mathematically, this can be expressed taking into account that the quantity of dopant enriching the melt has to be equal to the part refused by the solidification process:

$$(C_L - C_S)df_S = (1 - f_S)dC_L \tag{3.2}$$

where f_S is the mass fraction of solid part ($f_S = m_S/(m_S+m_L)$) and df_S indicates the differential variation of f_S. Taking into account that, at the beginning of the process, we have $C_S(0) = k_S C_0$, and integrating, we obtain:

$$C_S = k_s C_0 (1 - f_S)^{k_S - 1} \tag{3.3}$$

Or, for liquid phase:

$$C_L = C_0 f_L^{k_S - 1} \tag{3.4}$$

where $f_L = m_L/(m_S+m_L)$:

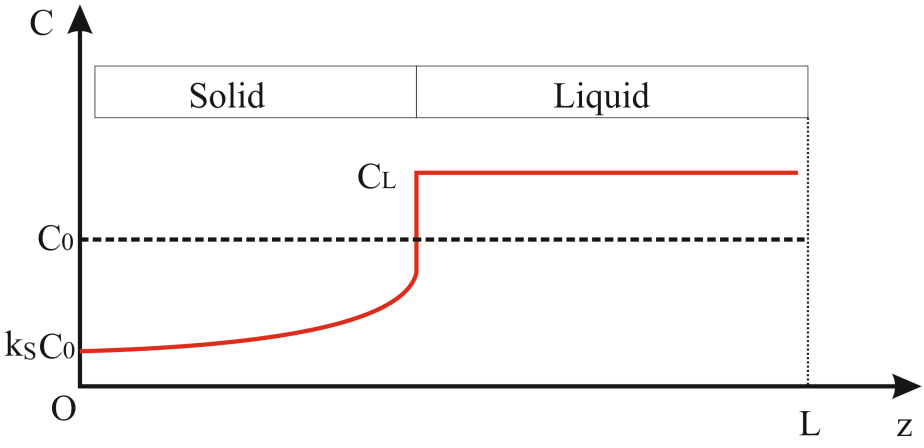

Fig.3.3. Dopant concentration distribution during the process with a complete mixing (by immediate diffusion or convection) in liquid phase versus L the distance of growth interface from the seed (the starting position of crystallization interface)

The above discussed process is valid at a very slow speed where this approximation gives indeed very good results.

Another interesting case (-3-) is the limited diffusion in the melt without convectional mixing. In this case as well, the solidification process will enrich the melt with rejected dopants. But it is qualified as "limited diffusion" because the dopant ions rejected from solidification interface will mainly enrich the liquid phase located in the immediate vicinity of growth front. If the crucible is long enough, the concentration of these near-interface liquid layers will reach a stable value (C_0/k_S).

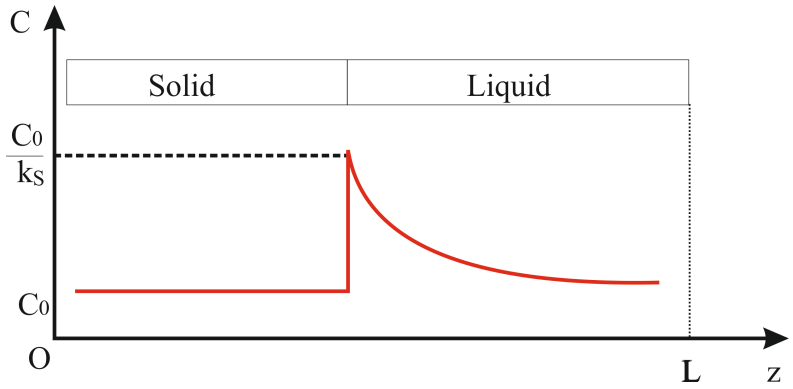

Fig.3.4. Dopant concentration distribution during the process with diffusion present in liquid phase without convection mixing, case 3. L shows the distance of growth interface from the seed (the starting position of crystallization interface).

This will happen because the amount of ions rejected from the solidification interface is equal to the amount of ions diffusing from the near-interface layer towards the other extremity of the crucible. Considering long enough crucibles implies that such migration will not change considerably the concentration of the whole melt. This process is shown schematically on Fig. 3.4.The crystal formed after this equilibrium has a concentration equal to C_0. This means that the concentration in the melt at the solidification interface is C_0/k_S. The distribution of the dopant in the near-interface melt can be found solving the following differential equation:

$$D_L \frac{d^2 C_L}{dz'^2} + V_{\text{int}} \frac{dC_L}{dz'} = 0 \qquad (3.5)$$

where z' is the distance from the growth interface, D_L [m^2/s] is a coefficient of diffusion of the dopant in liquid phase and V_{int} [m/s] is the growth speed. As boundary conditions, we have $C_L(z'=0) = C_0/k_S$ and $C_L = C_0$ at $z' = \infty$. And also, since the dopant global quantity must be conserved, the concentration gradient in the liquid at the interface ($z' = 0$) can be expressed:

$$\left(\frac{dC_L}{dz'}\right)_{z'=0} = -\frac{V_{\text{int}}}{D_L} C_L (1 - k_S) \qquad (3.6)$$

The solution of (3.5) is found by authors of [3.20]:

$$C_L = C_0 \left(1 + \frac{1 - k_S}{k_S} \exp(-z' V_{\text{int}} / D_L)\right) \qquad (3.7)$$

D_L/V_{int} is the distance above which the difference C_L-C_0 becomes smaller than e times its C_0/k_S-C_0 initial value.

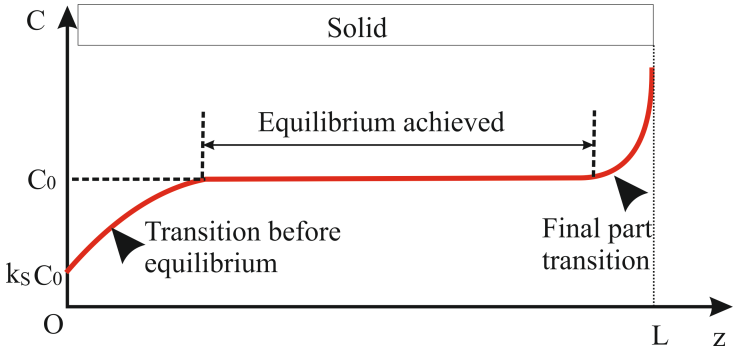

Fig.3.5. Resulting dopant concentration distribution in the final crystal obtained with the growth process with diffusion present in liquid phase without convection mixing, case 3. L shows the distance of growth interface from the seed (the starting position of crystallization interface).

During this type of process, the formed crystals have nearly homogeneous dopant distribution. The exceptions are the solid part formed at the beginning of the process (when the equilibrium is not achieved yet) and the end of the process where the last part of the liquid with high concentration of the dopant crystallizes. The dopant concentration distribution for this phase is given in Fig. 3.5 from [3.21].

The final practical case (-4-) considers limited diffusion with moderate convectional mixing [3.22]. This case is illustrated in Fig.3.6 where we observe a layer of length δ where only diffusion takes place while, in the other part of the liquid, the mixing is performed via convection.

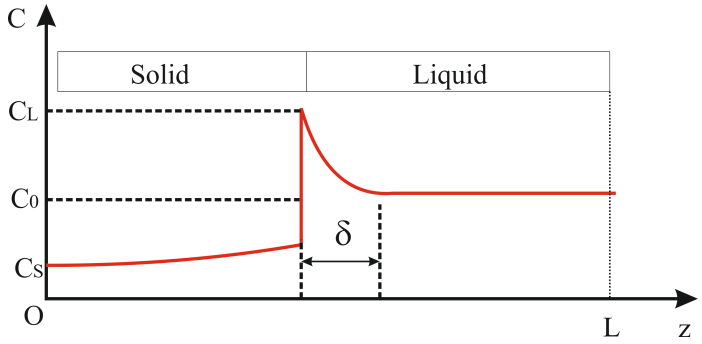

Fig.3.6. Dopant concentration distribution during the fourth process scheme where diffusion takes place in the layers within δ from the interface while convection mixing is present in further away layers: L shows the distance of growth interface from the seed (the starting position of crystallization interface). Notice that the resulting shape is intermediate between figures 3.3 and 3.4.

The solution can be found from the differential equation (3.5) taking into account that dopant concentration in the liquid equals C_L at the interface and C_0 at $z' = \delta$:

$$\frac{C_L - C_S}{C_0 - C_S} = \exp(V_{\text{int}}\delta / D_L), \qquad (3.8)$$

An effective segregation coefficient $k=C_S/C_0$ can be introduced in (3.7), giving:

$$k' = \frac{k_S}{k_S + (1-k_S)\exp(-V_{\text{int}}\delta / D_L)} \tag{3.9}$$

k' can replace k_S in (3.3) and (3.4) to describe this case of limited convectional mixing with diffusion in near-interface layers.

Experimentally, segregation coefficient can be determined by measuring the concentration in different parts of the grown crystal. If the concentration at the top of the crystal (in case of TGT, see § 3.4.9.) or near the seed of the boule (Bagdasarov, see § 3.5) is equal to C_T, then the segregation coefficient will be:

$$k' = \frac{C_T}{C_{SM}} \tag{3.10}$$

where C_{SM} is the concentration of the dopant in starting material. Although in our discussion we always considered a segregation coefficient below 1, leading to an increase of dopant quantity in the melt, cases where $k_S > 1$ are also possible leading to a deficit of the dopant in the melt. This does not change the main logic of the discussion. The dopants which have segregation coefficient greater than 1 are called solid-favoring while in the opposite case (segregation coefficient < 1), the expression "liquid-favoring" is used [3.23]. The radius of Nd ion (1.12 Å) is considerably greater than for Y ion (1.01 Å) and as a result, the segregation coefficient is lower than 1 for Nd in YAG matrix. In [3.24], the segregation coefficient for Cz grown Nd:YAG is around 0.15-0.20 with a growth rate varying between 1 and 3 mm/h. In the same paper, a segregation coefficient of 0.8 is even achieved with a micro-pulling-down technique relying on a very high growth rates (5 mm/min), a value clearly different from the 0.1 obtained for the same technique reported in [3.23]. Similar values of segregation coefficients are found for TGT method [3.25] where authors report 0.18-0.20 for TGT and Cz techniques. At "Laserayin", Nd:YAG crystals grown with Bagdasarov method (3 mm/h) give a segregation coefficient of ~0.23 which is higher comparing with Cz and TGT techniques. This result is in very good accordance with the 0.234 value found for Nd:YAG crystals grown with the same technique in Harbin institute of technology, China [3.26]. This explains the difficulty to grow homogeneously doped Nd:YAG crystals. These results illustrate also the difficulty to grow highly doped homogeneous Nd:YAG crystals.

The situation is quite different with Yb. Most of the values reported for Yb segregation in YAG are close to unity [3.15, 3.23, 3.27 and 3.28]. This fact greatly facilitates the growth of homogeneous Yb:YAG crystals. In case of the Yb:YAG crystals grown by Bagdasarov method, no significant difference is found between different parts of the crystal (chapter 6) of Yb:YAG and segregation coefficient is considered to be ≈1 for all calculation of chapter 4.

The segregation coefficient in ceramics is discussed in details in [3.15].

3.4.3. Melt growth techniques: Overview

High quality YAG materials are mainly grown by melt growth techniques. These techniques are the most used methods today and the major part of technologically important oxides, halides, semiconductors and metals production is grown this way. The most important condition is the absence chemical activity. High chemical activity can disturb the crystallization front as well as interact with crucible material, promoting the formation of physical and chemical defects. In most of the cases, materials used in melt growth techniques have simple chemical structures. One of the main advantages of this method comparing to solution and vapor-phase growth processes is its higher growth rate. Also, it is been empirically demonstrated that the more complex are the materials crystallized, the lower is the growth rate. Melt growth techniques can be divided into two main groups [3.29]:

- *Crucible-free methods* with strictly limited molten zone,
- *Crucible methods* where the molten zone is defined by the physical aperture of the crucible.

The size of the molten zone is very important for heat and mass transport processes and physico-chemical processes of high temperature crystallization. The crystallization atmosphere can be vacuum, recovering or neutral. In large melt volumes, convective flows propagate freely, while in small volumes of the melt, mass and heat transport is mainly due to self-diffusion.

Crystallization from melt generally consists in several physico-chemical processes which can be classified as follows [3.30]:

a. Processes defining the content of the melt: thermal dissociation of mother (also called starting or source) material, chemical interaction of the melt with crucible and atmosphere, evaporation of growth components and impurities,
b. Kinetic processes at the front of crystallization,
c. Heat transport processes defining temperature,
d. Mass and specific impurity (doping) transport processes due to the convection flows and diffusion defining the final crystal composition.

3.4.4. Crystallization atmosphere and evaporation

The nature of the crystallization atmosphere has a great impact on the intensity of crystallization material evaporation. This impact is due to the physico-chemical interactions of atmosphere and melt. The atmosphere can be recovering, neutral or vacuum. The recovering atmosphere contains the components easily evaporating from the melt: which means that, for oxides, oxidizing atmospheres are favorable, for nitrides, nitrogen containing is preferred, and so on. Neutral atmospheres (helium, argon) minimize evaporation losses and are used mostly in the cases where it is strictly required to keep the stoichiometry of growing materials. But this also means that the evaporation of impurities will be also significantly

reduced and therefore makes impossible the use of such atmospheres if during-process purification of the growth material is required. Another challenge is to highly purify the atmosphere on its own from oxygen and humidity before utilization. That is why vacuum is largely used. It provides very effective purification of the material from solved gases, easy flying impurities and products of thermal dissociation. For high temperature (>1800 °C) crystallization processes, the residual vacuum pressure must be below 3-4x10^{-5} Torr otherwise the oxidation of the heating elements and their further destruction will occur. The characterization of evaporation during growth process varies with growth techniques. Indeed, for some techniques, the surface (through which evaporation takes place) of the melt stays constant (Bridgman-Stockbarger, Czochralksi,…) while it evolves during the growth process for others (Bagdasarov, Kyropoulos,…).

Selective evaporation of one of the components will break the stoichiometry leading to crystallization of undesired phases. In order to obtain a crystal with the desired final phase from a system of two components M_1 and M_2, the following stoichiometric ratio at the beginning of the process has to be considered:

$$\frac{M_1}{M_2} = \frac{\alpha}{1-\alpha} \tag{3.11}$$

where α is M_1 component mass fraction. At some point, the amount of each component will be diminished by $\gamma_1 St$ and $\gamma_2 St$ where γ_1 and γ_2 are surface evaporation rates [kg/(m^2·sec)] of the components, S is the area of the melt surface (which in general can vary in time) and t is time. The stoichiometry will not be broken if the evaporation is completely absent or if the evaporated parts have the same ratio as starting amounts:

$$\frac{\gamma_1}{\gamma_2} = \frac{\alpha}{1-\alpha} \tag{3.12}$$

If (3.12) is not satisfied, at one moment, the relation between component amounts will reach a critical value W, when further crystallization of desired phase becomes impossible while other phases appear in the final crystal. Moving from a time system towards a spatial coordinate system can be performed considering the relation $z = t \cdot V_{int}$, where V_{int} is the crystallization speed. Therefore the moment when W occurs corresponds to a specific distance $z = Z$ where:

$$\frac{M_1(Z)}{M_2(Z)} = W \tag{3.13}$$

In [3.31], Z is obtained considering equal densities (ρ) for melt and crystal. Also, the evaporated amount of the components are assumed to be very small: $\gamma_1 tS << M_1(t)$ and $\gamma_2 tS << M_2(t)$. The solution for Bridgman-Stockbarger (see section 3.4.9) is:

$$Z = \frac{L_0}{1 + (\gamma_1 - W\gamma_2)/\xi\rho V_{\text{int}}} \tag{3.14}$$

where L_0 is a starting length of the melt and $\zeta = \alpha - W(1- \alpha)$ is a constant. This shows the length of the crystal with desired phase.

The solution for Bagdasarov method is:

$$Z = L_0 + \frac{\zeta \rho h V_{\text{int}}}{\gamma_1 - W\gamma_2} + \sqrt{L_0^2 + \left(\frac{\zeta \rho h V_{\text{int}}}{\gamma_1 - W\gamma_2}\right)^2} \qquad (3.15)$$

For both cases, if condition (3.12) is fulfilled, $Z = L_0$, which means that the melt fully crystallizes and only the desired phase appears in final crystal.

YAG can be grown in neutral, oxygen containing atmospheres or in vacuum. The non-desired phase which can appear in the final product is YAP. As we already know, an Y_2O_3 and Al_2O_3 system of has to be considered (Fig. 3.1). In order to obtain YAG, these two components should be weighed so that $\alpha = 0.429$ (Fig.3.1) for exact stoichiometry. During YAG vacuum growth, the stoichiometry of the content is ultimately broken due to selective evaporation of aluminum and oxygen atoms (the evaporation coefficients γ_1 and γ_2 for Y_2O_3 and Al_2O_3 are indeed significantly different [3.32]). This leads to excess of yttrium oxide component and by this stimulates the co-crystallization of YAP and YAG phases.

For methods where all the content of the crucible is crystallized (Bagdasarov, Bridgman, TGT etc…) the last crystallized layers of melt do not contain only YAG phase. This explains the presence of so-called "tails" at Bagdasarov (or similar method) grown boules extremity.

[3.31] mentions a ~2 cm tail length for an initial melt length of 15 cm. This value is obtained for experimentally measured $W = 0.587$ and V_{int}=8 mm/h while the values for evaporation rates were taken from [3.32]. In our experiments, we get higher values for the tails: 1 to 3 cm. This is due to the fact that we use much lower velocities for the growth process (1-3.5 mm/h) which allows more time for evaporation.

In order to reduce as much as possible the length of the tail, Al_2O_3 additive (about 1 to 2 mass %) are placed at the end of the crucible (for Bagdasarov method). It is nevertheless almost impossible to exactly predict the amount of the required quantity and then completely eliminate the formation of the "tail".

The impurities/dopants present in the melt are also subject to evaporation. In general this should also be taken into account when calculating the final concentration distribution C_s of the dopants/impurities in the solid. It can be expressed while considering the following approximations:

- the segregation coefficient varies linearly with the concentration of impurities/dopants,
- the segregation coefficient does not depend on growth rate,
- the impurities/dopants are distributed homogeneously in the melt.

Then for Bridgman-Stockbarger method one obtains [3.33]:

$$C_s = k'C_0(1-z)\left(\frac{k' + \frac{\gamma_{dop}}{C_0 \rho V_{\text{int}}}}{1 + \frac{\gamma_{host}}{\rho V_{\text{int}}}}\right) - 1 \qquad (3.16)$$

where γ_{dop} and γ_{host} are the evaporation rates for dopant/impurities and host material and z is the current coordinate of solidification interface. With the same considerations for Bagdasarov method, the final concentration distribution is:

$$C_s = k'C_0(1-z)^{k'-1}\left(1 - \frac{\gamma_{host}}{\rho V} \cdot \frac{L_0}{h_0} z\right)^{\frac{\gamma_{dop}}{\gamma_{host}}-1} \qquad (3.17)$$

We found no significant differences for evaporation of different rare-earth oxides either in the literature or in our experiments. Therefore, the evaporation rates for rare-earth oxides are assumed to be same ($\gamma_{dop} = \gamma_{host}$).

3.4.5. Crucible material

Several key factors should be kept in mind while choosing a crucible for melt growth techniques. The first is that chemical interactions and mutual solubility of crucible material and the melt have to be excluded. As a general rule, one can mention that the chemical binding forces of the crucible material have to have a completely different nature comparing to the ones for crystallizing material. That is why dielectric crystals are being grown mainly in metallic crucibles. The second rule is the capability of the container to sustain the melting temperature of the grown material without significant destruction. The similarity between thermal dilatation behavior of crucible and growing material will help to avoid stress formation in cooling phase. The possibility of mechanical manipulation and pre-growth chemical cleaning is also an important factor to be considered for the container material. In case of High Frequency (HF) heating, the electrical conductivity of the crucible has to be considered as well. For YAG, mainly iridium, molybdenum and tungsten containers are used.

3.4.6. Growth parameters choice and processes at crystallization front

In order to obtain high quality crystals with very small densities of defects like dislocations, stresses or inclusions, growing parameters (growth speed, temperature gradient, atmosphere content and pressure) have to be chosen very carefully. Thermal dissociation of components, interaction with atmosphere and container as well as evaporation of components has significant impact on the structure of the resulting crystals and the intensity of these processes depends on temperature-time parameters. These parameters can only be estimated and have to be empirically adjusted for each furnace and type of host material and dopant. The more components are involved in growth process, the more complicated is the parameters choice because, besides physical phase changes, also chemical phase transitions have to be taken into account. This all makes crystal growth often being presented as half science, half art. The important place taken by the growth station designer and operators' know-how is probably a

reason why crystal growth is very often depicted as a craft technique relying on very specific human skills and talents not always obvious to be analyzed with scientific criteria.

The chemical dissociation, container-material chemical interactions and components evaporation processes are all imposing limits on the speed of the growth and make unfavorable very low speeds. In general, it is preferred to avoid leaving the material in molten phase for a long time. On the other hand, too high speeds lead to non-complete diffusion of the melt, which, in case of a segregation coefficient less than 1 can lead to crystallization of impurity/dopant directly in the vicinity of the growth front: the inclusions are less effectively rejected from the solidification interface and more often freeze in the crystal creating local defects. Also the growth from dissociated melts (Y_2O_3, Al_2O_3, AlO, AlO_2, O for YAG melt as an example) is usually slower than growth from associated melts (single component melt as an example) in order to avoid non-stoichiometry at crystallization front due to the difference in diffusion for the different components. If the growth speed is higher than the diffusion speed, the accumulation of excessive components will occur at the crystallization front, leading to non-stoichiometry of the melt in near-solidification layers. This process is called concentrational supercooling [3.33] limiting the stability of the growth interface and perturbing the morphology of the crystal. For Al_2O_3, if the critical speed of crystallization is exceeded, the formation of inclusions resulting only from the material on its own (dissociated components) cannot be avoided. Moreover, with the growth speed increase, the value of residual stresses increases and can generate fractures within the crystal.

Another important parameter is the temperature distribution. Ideally, a three-dimensional description would be required but, in many practical cases, it can be simplified into two- or even one-dimensional cases. The temperature gradient along the growth axis is of key importance. High temperature gradients across the crystallization front lead to smaller facets formation on it, keeping stable the normal growth process. Spatially and morphologically stable crystallization front is necessary to obtain high quality melt-grown crystals. Heat exchange during growth takes place by three well known mechanisms: conduction, convection and radiation. For different materials, the growth processes can be divided into three cases: $\sigma_{abs}d >> 1$, $\sigma_{abs}d \sim 1$ and $\sigma_{abs}d << 1$, where σ_{abs} is the absorption coefficient and d the characteristic absorption length inside the material along the heat radiation direction. The first case corresponds to optically non-transparent materials (like growth of semiconductors) and Fourier's law can be considered:

$$Q = -\lambda_{ph}\nabla T \tag{3.18}$$

where Q [J] is the transferred conductive heat, λ_{ph} [J/°C/m] is the thermal conductivity characterized by phonon-translation and the derivation takes place along the axis along which this heat transfer occurs.

$\sigma_{abs}d << 1$corresponds to systems optically transparent at the wavelength corresponding to the maximum of Planck function (black body emission distribution) of the heat source (for instance, tungsten spires) and λ_{ph} has to be replaced by λ_{rad}, the radiative heat conductivity:

$$Q = -\lambda_{rad} \nabla T \tag{3.19}$$

When we have $\sigma_{abs} d \sim 1$, then the system is considered as semi-transparent and both mechanisms (conduction and radiation) of heat exchange take place simultaneously:

$$\lambda_{eff} = \lambda_{ph} + \lambda_{rad} \tag{3.20}$$

For the second and third cases, heat exchange through radiation is very significant and must absolutely be taken into account. The optical characteristics of the crystal and the melt are very different and therefore leads to discontinuities at the growth interface for the radiative term ($\lambda_{rad\_melt} \neq \lambda_{rad\_crystal}$).

The temperature gradients in directions other than growth axis are also very important. If the gradient is absent for other two directions, we have a flat solidification interface perpendicular to the growth direction. A uniform gradient (linear temperature variation with space) for these axes leads to tilt of the front while a non-uniform gradient (for instance a transverse parabolic profile) leads to curvature of the front.

In an ideal case, the temperature gradient along the growth axis should be relatively high from crystallization front to the melt (right part of the curve of figure 3.7) and low on the other side of the front towards the crystal [3.33].

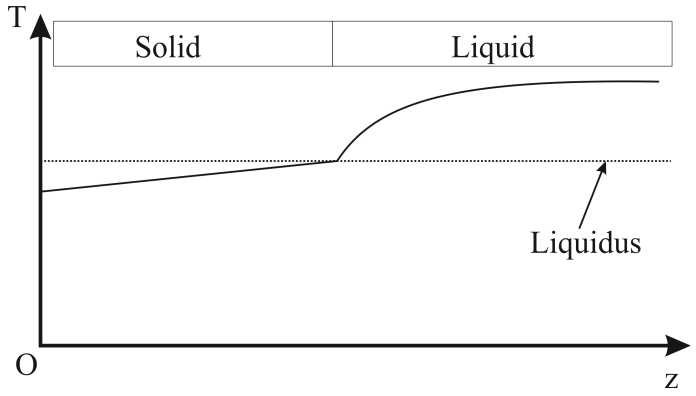

Fig.3.7. Ideal temperature distribution within the crucible along the growth axis Oz. The temperature gradient should be minimized in the solid section to minimize stresses potentially leading to cracks whereas it should be above a minimum value in the liquid part in order to ensure growth front stability.

As it has been already mentioned above, for yttrium oxide and aluminum oxide systems, three phases are possible and the crystallization of the YAG phase is closely related to the crystallization of the $YAlO_3$ (YAP) phase. At melting temperature, dissociates are already formed in the melt:

$$Y_3Al_5O_{12} \rightarrow Y_2O_3, Al_2O_3, AlO, AlO_2, O$$

The melt starts to lose aluminum and oxygen ions leading to formation of unwanted YAP. This means that, for YAG crystallization, extreme overheating (melt temperature difference above fusion temperature) is not allowed and the materials should not stay in melt phase for a too long period. On the other hand, with too low overheating temperatures, the diffusion is

less active which is a negative fact in terms of melt homogenization. Therefore, an intermediate temperature has to be chosen carefully. It has been shown experimentally [3.33] that higher is the crystallization speed, higher is the amount of YAP in the final crystal.

The modeling of growth processes, especially for semi-transparent systems, is quite complicated since simultaneous considerations of mass and heat transport processes have to be taken into account in space and time dimensions. It can be solved only in particular cases with rather strong approximations. It is out of the scope of the current work to derive a mathematical modeling of the growth processes. But some experimental characterizations for YAG growth with Bagdasarov method are presented in section 3.5.

3.4.7. Technical evolution of growth methods

One of the first methods for crystal growth from melt was proposed by Verneuil [3.29]. He was the first to establish method for 6g Rubin single crystals serial production in 1897. *Verneuil method*, even more than 100 years after its proposal, is still used almost without any evolutions despite many attempts to modify it. *Verneuil method* was the ancestor for all other methods and therefore labeled as -1- (left) in Fig. 3.8. In 1917, Czochralski proposed to pull out the crystals from the melt hold in the crucible. This method allowed growing the crystals with strictly controlled temperature fields and vacuum atmosphere was firstly used. Several modifications of *Czochralski* technique were proposed by Kyropoulos (-2-), Musatov (-3-) and Stepanov (-4-). For *Kyropolous method*, the crystal is not being pulled out but instead the melt is cooled and by this is crystallizing in the crucible. This method is used for large size industrial sapphire growth. Shmid and Viechnicki (-6-) proposed, instead of using seeds, to use spontaneously formed seed by locally cooling the melt before starting the gradient cooling and crystallization of the whole content of the crucible. Meantime with Czochralski, Bridgman proposed another method where the single crystal is being grown inside a vertically placed cylindrical crucible with conic bottom by placing the crucible vertically in the hot zone. Stockbarger proposed modification of *Bridgman method* (-5-) where the temperature gradient is applied at the crystallization front with the help of thermal diaphragm. The relative translation of the temperature zone results in full crystallization of the content. This modification of *Bridgman method* is called also *Temperature Gradient Technique (TGT)*. In 1964, a new approach was established. Academician of USSR National Academy Kh. S. Bagdasarov proposed to use boat-type crucible with seed apartment for *Horizontally Directed Crystallization (HDC)* of single crystals (-7-). The method relies on a source material filled crucible horizontally translated in the hot zone. *Zone melting* method is characterized by vertical or horizontal relative travels of crystallization material and hot zone which leads to gradual melting and crystallization of source material in a very narrow zone. This method is widely used for purification and stoichiometry improvement.

The choice of the growth method mainly depends on the crystal to be obtained as well as of specific issues like melting temperature, crystallization atmosphere, etc... Metal single crystals with melting point <1800 ^{o}C are usually grown by *Stockbarger method*, while the ones with higher melting point by *Zone melting* method. Semiconductors are mainly grown by *Czochralski* and *Zone melting*, while for dielectrics such as laser crystals, *Czochralski*,

Stockbarger or *Verneuil* and *Bagdasarov* methods are used. Large laser crystals are grown by *TGT* and *Bagdasarov* techniques (Chapter 6).

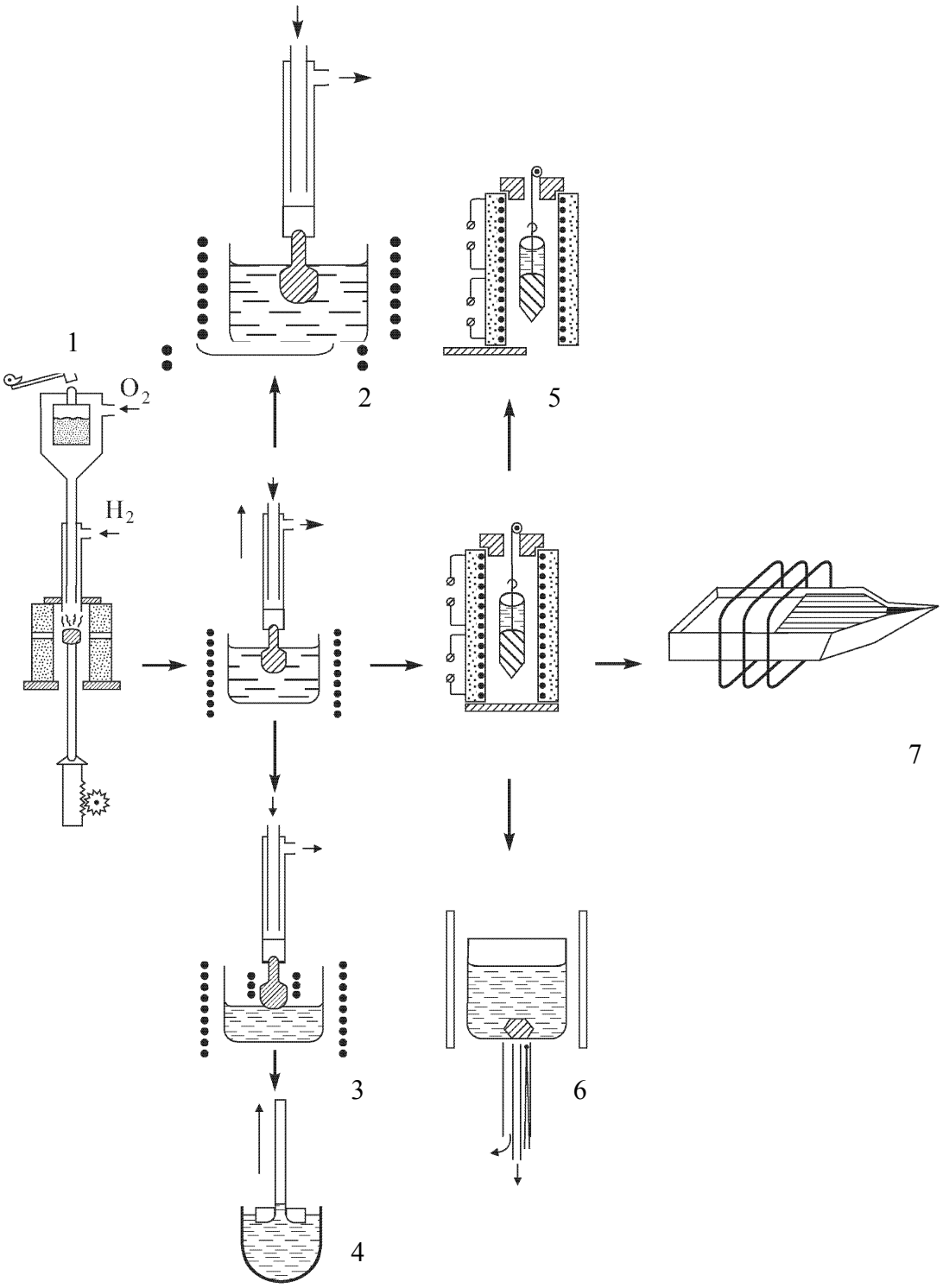

Fig. 3.8. Schematic representation of the evolution of crystal growth from melt methods [3.29]. 1 – Verneuil technique, 2 – Kyropoulos, 3 – Czochralski (Musatov modification), 4 – Stepanov, 5 – Bridgman (Stockbarger modification) , 6 – Kyropolous (Shmid and Viechnicki modification), 7 – Bagdasarov

3.4.8. Czochralski technique

Czochralski technique falls in the "crucible" method category. Before the crystallization process, the source material is completely molten in the crucible, which is hold at a constant temperature. The seed is in contact with the top of the molten phase and is slowly being pulled upwards (Fig.3.9).

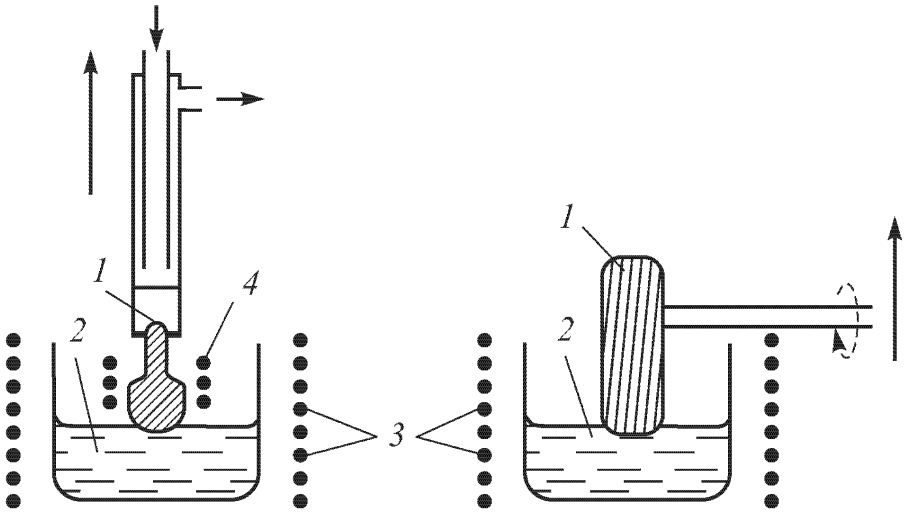

Fig.3.9. Schematic representation of Czochralski process for rod shape crystal (left) and disc shape crystal (right) 1. single crystal, 2. molten phase, 3. heater, 4. additional heater. The arrows indicate direction of single crystal travel, cooling flow and rotation [3.29]

The absence of direct contact of grown crystal with the crucible leads to reduction of intrinsic stresses. Another advantage of this technique is the possibility to detach and remove the grown crystal at any stage of growth process. The temperature of the molten phase as well as the velocity of the single crystal translation defines the geometrical shape of the crystal. Dislocations concentrate mainly at the outer surface of the crystal. Garnets are usually grown with a rate of 2 mm per hour, while for other materials growth rate can be up to 10 mm per hour. A great disadvantage of this method is related to the crucible material losses (when solid fractions of the crucible can be found in the melt), and also, very often, crucible is a source of undesirable impurities. The mathematical model for *Czochralski growth* is quite sophisticated due to the numerous factors impacting the growth kinetics such as tensions and deformations in the crystal, temperature field dynamics, hydrodynamic flows in the liquid, etc... The results of calculation with some approximations are given in [3.34]. Main disadvantage of Czochralski grown YAG crystals is cores appearing in the crystals. This limits the ability of this technique to obtain large size laser materials. The growth process is connected with large loss of costly iridium crucible therefore increasing the global manufacturing cost.

Due to the popularity of rod shape growth of Cz crystals, disk shape growth is not used very often. With some modifications we propose, this technique can provide several very important advantages. In the frames of the LUCIA program, we use the laser material Yb:YAG with cladding of Cr:YAG to absorb parasitic oscillations by this reducing ASE (Fig. 1.21). Unfortunately current available crystal growth techniques do not allow obtaining such single

crystals which imposes to use laser ceramics instead. Disk shape Cz growth can solve this issue. The high optical quality disc shape crystal (central part) can be used as a "seed". The cladding can be grown on the outer edges of the disk by rotating the periphery of this crystal in a melt of Cr:YAG and simultaneously moving it up. With increasing diameter of the crystal the translational velocity and angular speed of the rotation should be continuously reduced. The same can be used to grow crystal with radial gradient or steps of doping distribution by several steps each time changing the composition of the melt (Fig. 3.10).

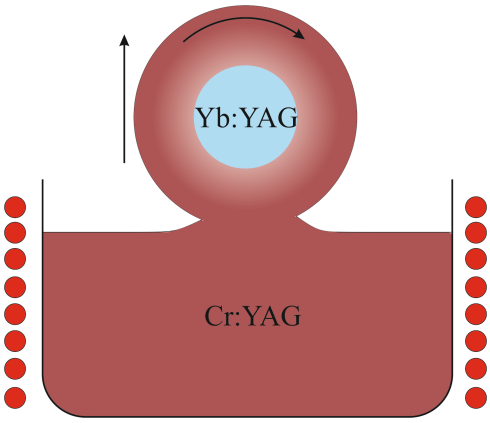

Fig.3.10. Schematic representation of Czochralski process for disk shape growth. The arrows show rotation and translation directions. The mounts are not shown on the image and heaters are symbolized by red circles. Additional heater might be necessary around the grown part in order to avoid high temperature gradients

3.4.9. Bridgman technique and TGT

Bridgman method is another "crucible" technique. The main difference with *Czochralski technique* is the fact that all content of the crucible is being crystallized at the end of the process. Conic bottom of the crucible is necessary to form seed for single crystal growth. Bridgman technique was modified my Stockbarger who introduced thermal diaphragm (thermal shield) allowing to control the temperature distribution near the crystallization front. This method is also called Temperature Gradient Technique (TGT). Schematically it is represented on Fig. 3.11 where T_0 is the temperature at the thermal diaphragm.

TGT equipment is technically very simple which makes it the most used method for growing a wide range of crystals. It is widely used for new crystal research. The main disadvantage of this method is the lack of possibility for crystallization front observation during the growth process. Another disadvantage is the interaction of the crucible with the grown crystal which may result in stresses. Also, the extraction of the single crystal from the crucible poses technical issues.

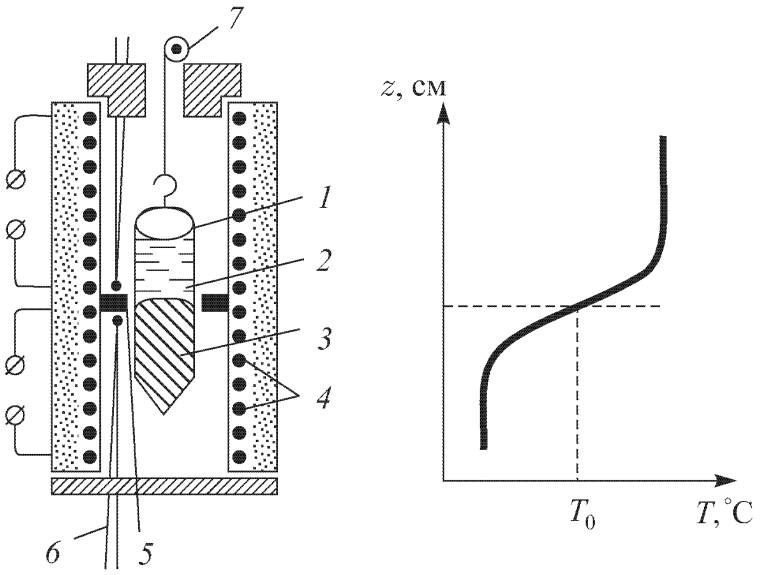

Fig.3.11. Schematic representation of TGT equipment (left) and temperature distribution near the growth front (right). 1 – crucible, 2 – molten zone, 3 – single crystal, 4 – heater, 5 – thermal diaphragm, 6 – thermocouples for measuring temperature near thermal diaphragm, 7 – mechanism for relative transition of the crystal in temperature field [3.29]

3.5. Bagdassarov method

3.5.1. Method description

The Bagdasarov technique, also called *boat technique* (referring to the boat shape of the crucible), horizontal Bridgman technique or Horizontal Direct Crystallization (or solidification) was suggested by Kh.S. Bagdasarov in 1964 in *Proceedings of the Fourth All-Union Conference on Crystal Growth, Tsakhkadzor, Armenia, 1972*. Besides exploring theoretical and experimental developments of this technique, Bagdasarov, together with his colleagues, developed series of crystallization stations for this method which are used up to the present day with only minor modifications performed to adapt it to specific needs (growth of sapphire large single crystals, of high quality laser crystals etc…). Bagdasarov technique is currently widely used all over the world and thousands of high quality sapphire and garnet crystals have been obtained with it (http://roscrystal.ru/fr/, "institute of Single Crystals", Kharkov, Ukraine, Center for Composite Materials, Harbin Institute of Technology, Harbin, People's Republic of China). Kh. Bagdasarov and his colleagues published numerous articles and book on development, characterization and improvement of the technique, but the method keeps being developed even today and several horizons are waiting to be explored.

Bagdasarov growth process relies on a horizontal container (with the form of a boat) filled with starting material, which can be pressed powder, crystalline crackle or ceramics. While travelling through a heating zone, the content of this crucible is melting and gradually crystallizing while exiting the heat zone. In order to obtain an oriented crystal, a seed is located in a special compartment located at the front-end of the crucible (Fig. 4.2, in Chapter 4).

This method offers several advantages when comparing to the other growth techniques:

- The height of the crystallizing material is much lower than the length, which creates favorable conditions for evaporation of non-desired easy-flying impurities from the melt. This is actually why this method can be used for purifying different materials via several recrystallization sequences.
- This makes requirements on the purity of the starting material components less strict than for the other melt-growth techniques.
- The open interface of the melt theoretically allows adding chemical elements at any step of the crystallization process. But, in practice the access to the melt open interface is quite complicated due to the sophisticated system of thermal shields and heating elements as well as the high temperatures in this area.
- Due to the relatively small height (a few cm), the convective motions are almost absent in the melt which increases the stability of the growth front.

These advantages can be equally regarded as disadvantages for some materials. Indeed, the large surface of melt cannot be acceptable for a series of materials with high evaporation rate. Also, the relatively limited height is restricting the production to optical elements shaped with a low third dimension. With Bagdasarov technique, all the content of the crucible is crystallized; this induces a technical inconvenience while extracting the grown boule from the crucible due to the adhesion of the material to the container walls. This also creates residual stresses near these areas.

All three temperature gradients are very important (and usually present) for Bagdasarov technique. The temperature gradient along the growth axis (*Oz*) is easy to control in order to obtain relatively stress free crystals. The temperature gradient in perpendicular to growth directions (*Ox, Oy)* can lead to the following solidification front orientations (Fig. 3.12):

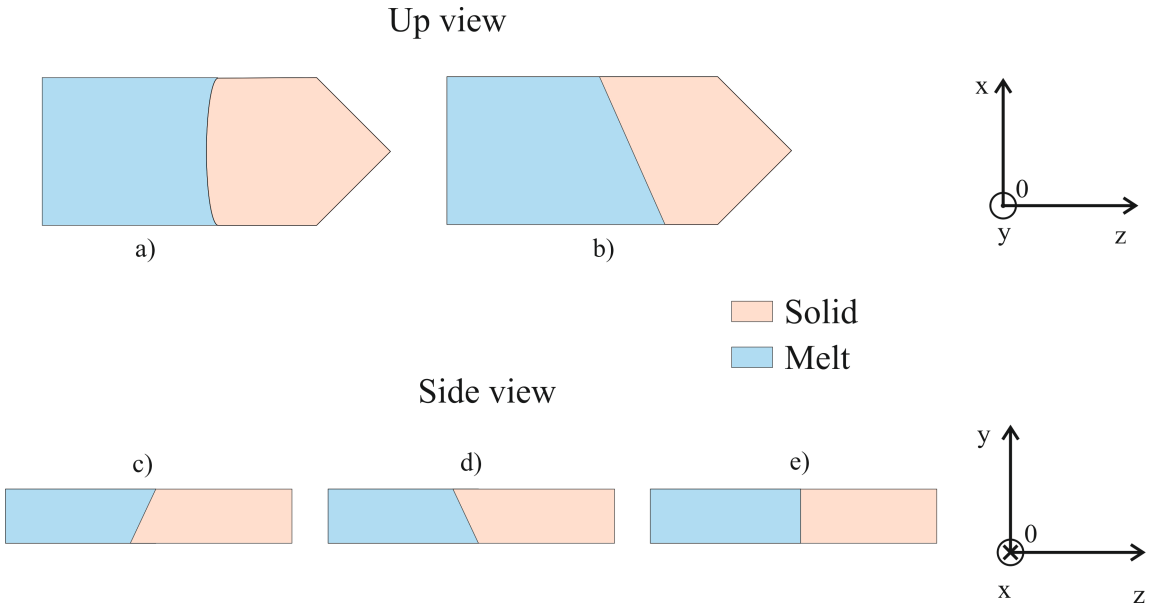

Fig.3.12. Front orientations for Badgasarov growth (explanation in the text)

Temperature gradient along the *y* direction leads to the three cases *c)*, *d)* and *e)* displayed in Fig.3.12. The case *d)* is the less favorable because, due to gravity considerations, the lower density products of dissociation accumulate at the growth front instead of being allowed a free propagation to the surface like in cases *c)* and *e)*. This gradient is responsible for convection: when it is eliminated, the convection is absent, while if convection is necessary, the gradient in this direction must be increased.

The gradients in *Ox* direction lead to curvature of the front (case *a)*). For our experimental Bagdasarov growths, we observe mostly the combination of cases *a)* and *c)*. The curvature of the front is nevertheless quite small and its shape is actually close to a plane, especially in the middle part of the boule, allowing therefore facet-free growth (Fig. 3.2). After mechanical elimination of near-crucible parts of the grown boule, it is possible to obtain defect free crystals. The Bagdasarov growth sequence for our experiments consists of the following steps:

- weighting of crystallization components in stoichiometric ratio,
- melting the mixed powders in order to obtain a solid solution,
- breaking the solid solution by thermal shock and preparing the crackle (which is the starting material),
- placing the crackle in the crucible and inserting the crucible filled with starting material into the furnace,
- melting and crystallizing the content via horizontal translation through the heating zone,
- cooling the crucible and extracting it from the furnace,
- breaking the crucible and extracting the crystal,
- eliminating the tail and near-crucible parts for the grown boule by mechanical cutting.

The resulted crystal can then undergo a quality procedure (polarimetry and microscopy) and ultimately be ready for final optical elements production.

3.5.2. Method equipment

Over the years, different growth stations for Bagdasarov growth have been built but the main architecture stays similar to original furnace Sapphire-1 designed by Kh. Bagdasarov and his colleagues. Our experiments are performed on Sapphire-2MG growth stations, some of them modified in order to obtain larger size crystals. Our growth furnace is shown on Fig. 3.13:

A sketched cut of the growth furnace is given in Fig.3.14. The observation window located at the top of the dome allows visual observation of the seeding process as well as the crystallization front during a significant period of the growth process. Another observation window is placed on the left extreme of the furnace on the so-called starting chamber (not numbered on the sketch but pictured at the top right of Fig. 3.13).

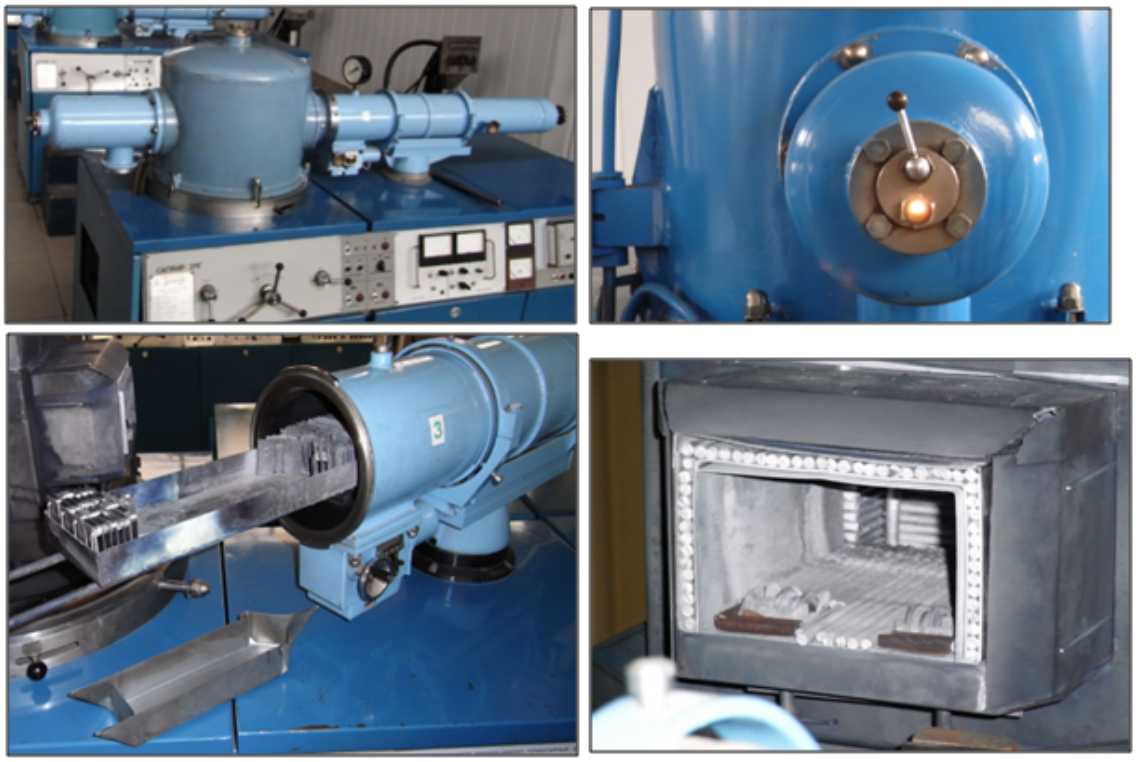

Fig.3.13. Bagdasarov growth furnace (top left), observation window (top right), crucible carrier with thermal shields (bottom left) and heating cavity (without heater) (bottom right)

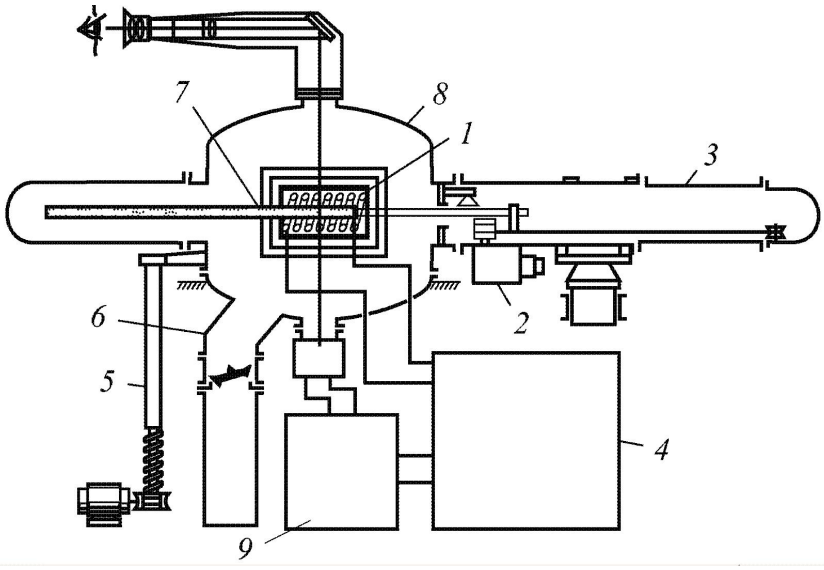

Figure 3.14: Saphir-2MG crystallization furnace detailed description: 1 - heater; 2 - reducer; 3 - inlet chamber; 4 - transformer; 5 - dome lifting mechanism; 6 - diffusion pump; 7 - container with material; 8 - vacuum dome; 9 - control unit and stabilization (from [3.29])

The heating system consists in a tungsten heater (right image of Fig. 3.15) and thermal shields (Fig. 3.15):

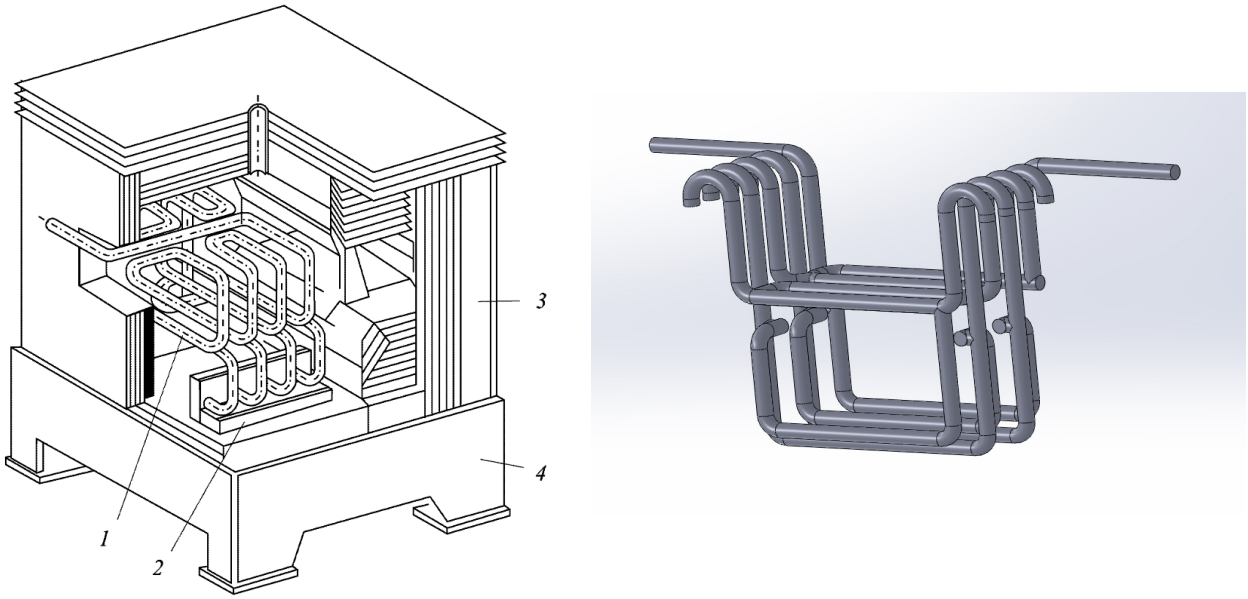

Fig.3.15. Saphir-2MG crystallization furnace heating system description (left): 1 – heater made out from tungsten (right); 2 – insulator; 3 – shields; 4 – basement [3.29]. The right CAD view depicts our heater specific shape.

The heater dimensions vary with furnaces and are adapted to the maximum size of the crystals to be grown. The used crucibles for our growth sequences are made out of molybdenum. The crucible used for crackle preparation significantly differs from the one used in the final crystal growth process (Fig. 3.16) since it indeed has a rectangular shape (no seeding is needed).

Fig.3.16. Solid solution preparation crucible made out of molybdenum: empty (top) and with solid solution (bottom)

The boat shape crucible can also differ in dimensions which are nevertheless ultimately limited by the heating system aperture. Fig. 3.17 pictures a boat shaped crucible filled with crystalline crackle as a starting material and ready for growth sequence.

Fig.3.17. Boat shape molybdenum crucible filled with starting material

Molybdenum sheets of variable thicknesses can be used for crucible preparation (0.3-0.5 mm). Thick sheets induce higher stresses in the crystal due to its reduced flexibility for extension while very thin material can lead to breakage during growth process and leakage of the melt. The crucible is inserted into the carrier (Fig. 3.18) which moves by being attached to a step machine. The translation speeds can vary over a wide range starting from 0.5 mm/hour.

Fig.3.18. Molybdenum crucible carrier with molybdenum thermal shields

The molybdenum thermal shields are located in front and at the back of the crucible. It prevents the temperature gradients within the grown crystal to be too high which would lead to cracks or highly stressed final crystal formation. One millimeter molybdenum wires are placed at the bottom of the carrier to prevent any adhesion of the crucible and the carrier.

In our experiments we used vacuum atmosphere. The growth furnaces can be operated under a vacuum down to $6.7 \cdot 10^{-3}$ Pa.

3.5.3. Characterization

The characterization of the method is very important to find the optimum set of growth parameters. Several processes occurring during growth induce consequences which can be observed by carefully examining the final crystal. For instance, the inclusions of dissociates are called growth witnesses and give valuable information about the morphology of the crystallization front. In Chapter 4, we introduce a new method for crystallization front analysis through iso-doping surfaces measurements.

As already mentioned, it is very important to have the knowledge and the full control over the temperature fields present in the furnace during the growth process. Bagdasarov and his group [3.29, 3.33, 3.35, and 3.36] performed such characterization for sapphire growth with Bagdasarov method. C type thermocouples were inserted in the starting material. These sensors were allowed to move together with the crucible during the growth process. The temperature temporal evolution at different location within the boule could then be recorded. Besides the temperature gradients along the growth axis (*Oz* axis on Fig. 3.18), temperature gradients in other directions) were also examined with the help of thermocouples placed at different heights along the *Oy* axis. These experiments are very complex and were performed on specially designed experimental furnace. Unfortunately, it is impossible to perform the same experiments on the furnaces used for our experiments due to several reasons. During growth, the crucible total translation covers 20 cm, meaning that an equivalent thermocouple wire length has to be stored inside the furnace or be fed from outside. The first is impossible due to the high fragility of the C type thermocouples. Feeding thermocouple wires inside the chamber can neither be a solution, because used vacuum feed-through systems do not allow this option. Taking into account all these factors, it was decided, as a first step, to perform much more simple experiments: measuring the temperature distribution within the boule (alongside growth axis) at different locations without translation of the crucible. The aim of these experiments were more to verify the reliability of such measurement technique and to identify the potential difficulties to address in order, in a second experimental phase, to set up experiments for a more advanced characterization of this growth method. The results of these first experiments should therefore only be considered as qualitative. Three C type thermocouples are attached to the crucible and inserted into the starting material (YAG crackle) (Fig.3.19).

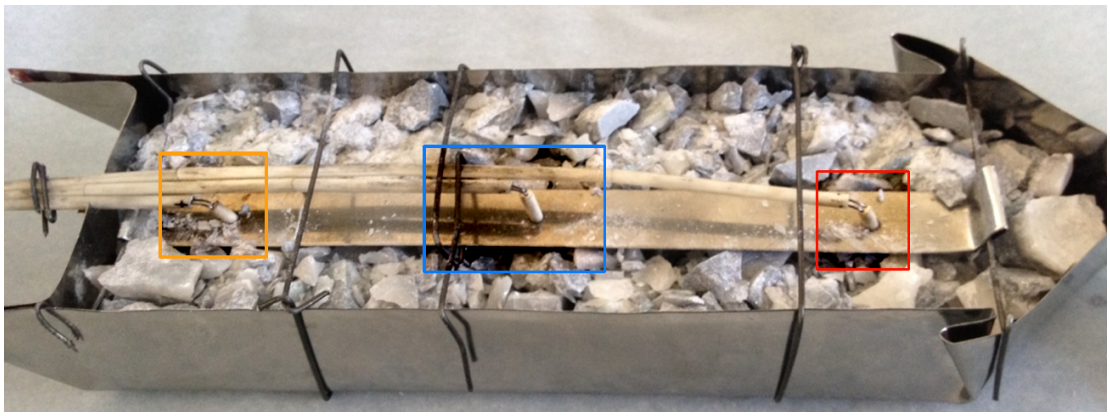

Fig.3.19. Crucible with starting material and thermocouples in colored rectangles.

The thermocouples are insulated by aluminum oxide ceramics. Then the crucible is placed into the furnace at a starting position where the seed compartment is located right in front of the last spire of the heater (Fig. 3.20). This is the first step of the experiment.

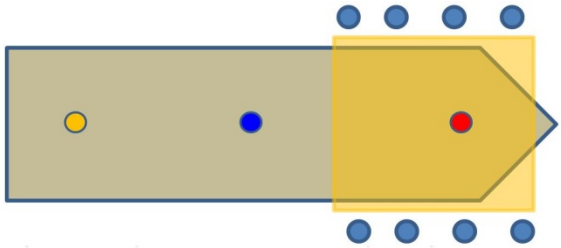

Fig.3.20. Relative position of the crucible and the heater spires (blue circles) for the 1st step. Yellow area represents the heating zone. The localizations of the three thermocouples are shown with red, beep blue and yellow circles.

The thermocouple wires are inserted through the vacuum feed-through system shown on the Fig. 3.21, which is located in place of the observation window of starting chamber (Fig 3.13, upper right). The thermocouples are finally connected to a recorder.

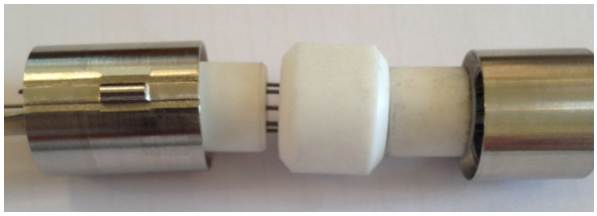

Fig.3.21. Vacuum feed-through system

After the crucible is inserted at its appropriate position and the vacuum is established, the heating sequence is applied with a maximum voltage on the heater equal to 23.2 V. The temperature recorded by the thermocouples is shown on the Fig. 3.22. The thermocouples are numbered from the nose to the end of the boule.

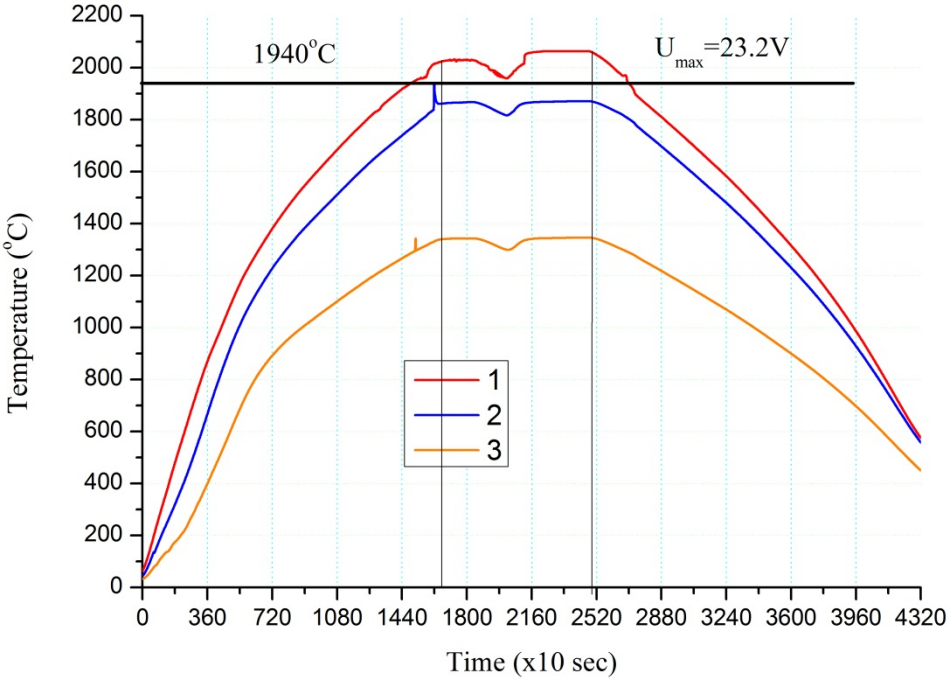

Fig.3.22. Temperature evolution over time for three different locations inside the boule for the 1st step (the black horizontal line indicates the liquidus position)

On this image, we observe a heater transient failure (small dips around 20000 seconds), a rather rare phenomenon. The important observation is that only the first thermocouple records a solid-liquid-solid phase transition. The maximum temperature obtained is 2062 °C which corresponds to almost $\Delta T = 100$ °C of overheated melt, a value in accordance with the data provided by Bagdasarov in [3.36]. The second thermocouple (blue) is located quite close to the liquid-starting material interface (Fig. 3.23). As expected, we observe a rather low difference (~190 °C) with the temperature given by the first thermocouple (red) located directly in the melt.

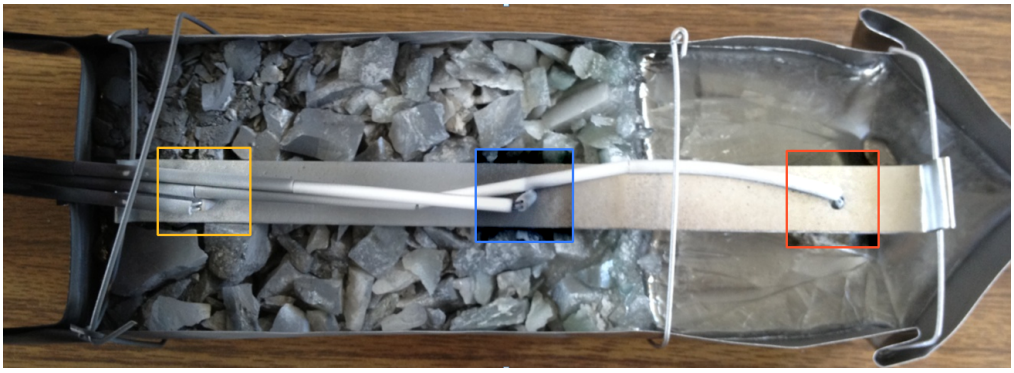

Fig.3.23. Resulting boule after the first step

After the first heat sequence is complete, the furnace is open and the crucible is translated by 9.5 cm (length of the molten-crystallized part) (Fig. 3.24) and the second heat sequence (step 2) can start.

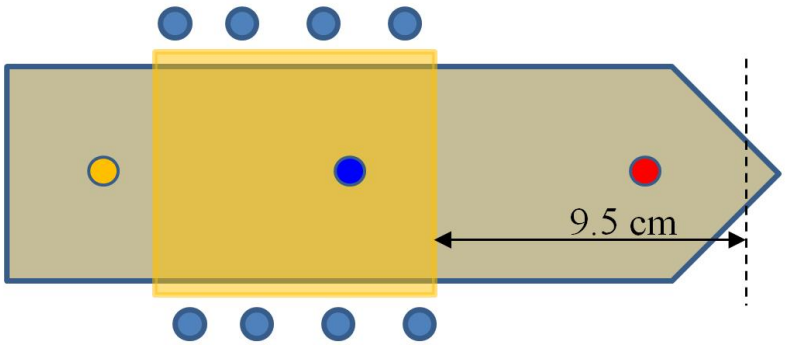

Fig.3.24. Relative positions of the crucible and the heater spires during the 2nd experimental step.

The temperature evolution recorded for a similar heating sequence is displayed on Fig. 3.25.

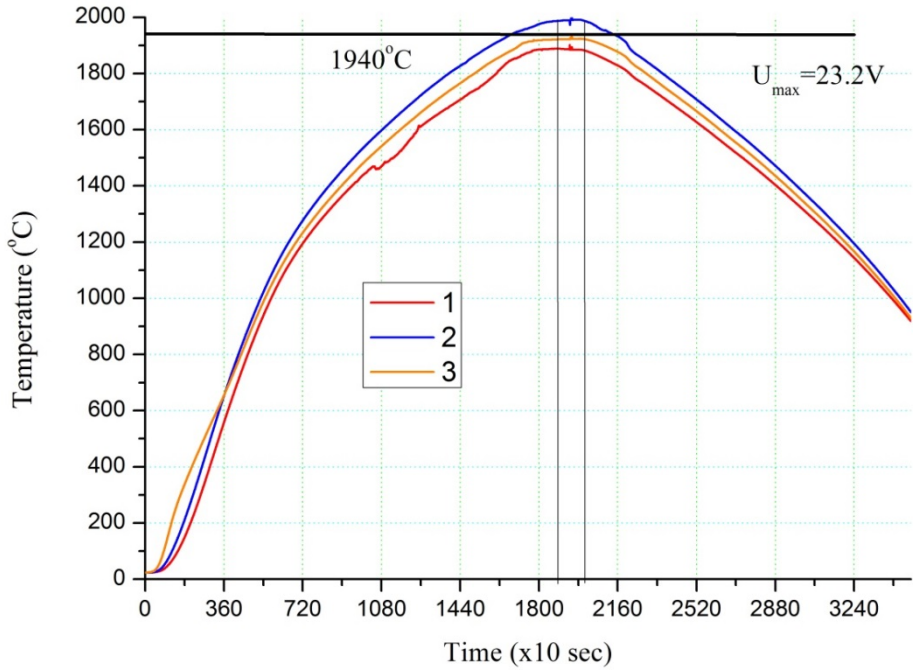

Fig.3.25. Temperature evolution over time for three different locations inside the boule for the 2nd step (the black horizontal line shows liquidus position)

In this case, only the second thermocouple reveals a phase transition, the 1st thermocouple being inserted in the crystal and the 3rd thermocouple in the crackle. The final boule is displayed on Fig. 3.26.

Fig.3.26. Resulting boule after the second step

This time, the maximum temperature of the melt is only 1989 °C which means we have no more than a few tens of degrees of overheating. This is due to the fact that the previously formed crystal (during the first step) provides very effective heat transport (the same phenomenon is causing shortening of melting zone as explained in Chapter 4). A similar conclusion can be derived from the fact that the 1st and 3rd thermocouples show quite close temperatures despite that the 3rd is much closer to the molten zone than the 1st. As it has been mentioned, these experiments were mainly performed for technique verification and as a starting point for further more detailed characterization experiments.

3.6. Outlook

Melt growth techniques are still the most reliable way to obtain high quality laser crystal. New requirements on laser systems like gradient distribution of the dopant concentration or presence of absorbing claddings are all motivating requests for crystal growth. And it brings new challenges for melt growth techniques. For instance, the cladding growth technique for Cz method briefly described in this chapter (§ 3.4.8) could be a promising solution for ASE damping laser crystals fabrication.

Detailed characterization and understanding of the physics and chemistry taking place in Bagdasarov method grown YAG crystals will undoubtedly bring another important step towards better management of growth parameters and perfection of laser crystals obtained by this method. Currently, one of the premises at "Laserayin Tekhnika" CJSC is being transformed in order to be adapted for more complex thermocouple measurements. In the new furnace, it will be possible to measure temperature distribution of not only stationary but also moving crucibles. This will provide the necessary information required to build a mathematical model (similar to one presented in [3.36]) to fully describe YAG growth by Bagdasarov technique and then explore potential new improvements.

3.7. References

[3.1] "Crystal Growth Technology" Springer, 2003

[3.2] Dhanaraj G., Byrappa K."Handbook of Crystal Growth" Springer 2010

[3.3] Hanna Vehkamäki "Classical Nucleation Theory in Multicomponent Systems" Springer 2006

[3.4] Warsaw I. and Roy R. Journal of American Ceramic Society 42 1959

[3.5] Geller S., Wood E.A., Acta Crystallography 9 (1956) 536

[3.6] Bertaut F., Mareschal C.R., Hebd. Seances Acd. Sci. 257 (1963) 867

[3.7] Keith M.L., Roy R., ibid. 39 (1954)

[3.8] Abell J.S., Harris I.R., Cockayne B., Lent B. J. Material Science 9 (1974) 527

[3.9] Yao Bao-Quan *et al*, "A Continuous-Wave Ho:$YAlO_3$ Laser with Output 8.5 W Pumped by a 1.91 μm Laser at Room Temperature" 2009 *Chinese Phys. Lett.* **26** 044203

[3.10] Yiou S., Balembois F., Georges P., and Brun A. "High-power continuous-wave diode-pumped Nd:YAlO3 laser that emits on low-gain 1378- and 1385-nm transitions" (2001) Vol. 40, No. 18, Applied optics

[3.11] Kisel VE, Kurilchik SV, Yasukevich AS, Grigoriev SV, Smirnova SA, Kuleshov NV.

"Spectroscopy and femtosecond laser performance of Yb3+:YAlO3 crystal", Opt Lett. 2008; 33(19):2194-6

[3.12] Caslavsky J.L., Viechnicki D.J. “Melting behaviour and metastability of yttrium aluminium garnet (YAG) and YAIO3 determined by optical differential thermal analysis” Journal of Materials Science 15 (1980) 1709-1718

[3.13] Toropov N.A., Bondar I.A., Galadhov F. Ya., Nikoghosyan Kh.S., Vinogradova N.V. Izvestiya Akademii Nauk SSSR, Seriya Khimia 7 (1969) 1112

[3.14] Fabrichnaya O, et al. “The assessment of thermodynamic parameters in the Al2O3-Y2O3 system and phase relations in the Y-Al-O system” Scandinavian Journal of Metallurgy 2001; **30**: 175–183

[3.15] Chani V.I., Boulon G., Zhao W., Yanagida T, Yoshikawa A., Correlation between Segregation of Rare Earth Dopants in Melt Crystal Growth and Ceramic Processing for Optical Applications” Japanese Journal of Applied Physics 49 (2010) 075601

[3.16] Xu X., Zhao Z, Xu J., Deng P. “Crystal growth and spectral properties of $Yb_3Al_5O_{12}$” Journal of Crystal Growth 257 (2003) 272–275

[3.17] Fagundes-Peters D., Martynyuk N., Luenstedt K., Peters V., Petermann K., Huber G.,

Basun S., Laguta V., Hofstaetter A. “High quantum efficiency YbAG-crystals” Journal of Luminescence 125 (2007) 238–247

[3.18] Zhang Q. L., Yin S. T., Sun D. L., Wan S.M. “Segregation during crystal growth from melt and absorption cross section determination by optical absorption method” Science in China Series G: Physics, Mechanics & Astronomy (2008)

[3.19] Flemings, “Solidification processing” (Russian translation), Mir, Moscow 1977

[3.20] Tiller W.A., Jackson K.A., Rutter J.W., Chalmers B., Acta Met., 1, 428 (1953)

[3.21] Smith V.G. et al, Can. J. Phys., 33,723 (1955)

[3.22] Burton J.A. et al, J. Chem. Phys., 21, 1987 (1953)

[3.23] Simura R., Yoshikawa A., Uda S., “The radial distribution of dopant (Cr,Nd,Yb or Ce) in yttrium aluminum garnet ($Y_3Al_5O_{12}$) single crystals grown by the micro-pulling-down method”, Journal of Crystal Growth 311 (2009) 4763–4769

[3.24] Chani V., Yoshikawa A., Kuwano Y.,Hasegawa K., Fukuda T. “Growth of $Y_3Al_5O_{12}$:Nd fiber crystals by micro-pulling-down technique” Journal of Crystal Growth 204 (1999) 155-162

[3.25] Jiang B, Xu J., Li H., Wang J. and Zhao G. “A Comparison between TGT and Cz Grown Nd:YAG” J. Mater. Sci. Technol., Vol.22 No.5, 2006

[3.26] Zhang M. et al, “Distribution of Neodymium and properties of Nd:YAG crystal by horizontal directional solidification” Journal of Crystal Growth 340 (2012) 130–134

[3.27] Xu. X., Zhao Z., Zhao G., Song P.X., Xu J., Deng P. “Comparison of Yb:YAG crystals grown by Cz and TGT method”, Journal of crystal growth 257 (2003) 297-300

[3.28] Zhao G.,Si J., Xu X., Xu J., Song H, Zhou Y., “Growth of large-sized Yb:YAG single crystals by temperature gradient technique”, Journal of Crystal Growth 252 (2003) 355–359

[3.29] Bagdasarov Kh.S., “Visokotemperaturnaya kristallizaciya iz rasplava”, 2004 ISBN 5-9221-0482-9

[3.30] Chernov et al, “Modern Crystallography”, Vol. 3, Moscow 1980

[3.31] Oganesyan L.A., Khaimov-Mal'kov V.Ya., “Yttrium aluminum garnet crystal growth in vacuum with account for melt evaporation” Journal of Crystal Growth, 52, Part 2, 1981, 530–533

[3.32] Oganesyan L.A., Khaimov-Mal'kov V.Ya., Kristallografiya 25 (1980) 886

[3.33] Bagdasarov Kh.S. “Fiziko-ximicheskie osnovi visokotemperaturnoy kristallizacii i metodi virashivaniya monokstallov” Moscow

[3.34] Nunes E.M. et al, “A volume radiation heat transfer model for Czochralski crystal

growth processes”, Journal of Crystal Growth 236 (2002) 596–608

[3.35] Bagdasarov Kh.S., “Virashivanie dielektricheskikh lazernykh kristallov”, Moscow 1981

[3.36] Bagdasarov Kh. S., Goryainov L.A., Teplo- i massoperenos pri virashivanii monokristallov napravlennoy kristallizaciey” Moscow, 2007

4. Gradient Crystals: Growth and Characterization

4.1. Motivation

This chapter is dedicated to the growth and characterization of variably doped crystal obtained during this thesis. After presenting the state of art in variably doped YAG crystals (section 4.2), I will briefly introduce the growth method used to obtain variably doped crystals and describe a simple model for predicting final doping distributions resulting from several growth sequences (section 4.3). In order to select the most suitable and accurate process to measure doping distribution in final crystals, a comparison of several techniques is given in section 4.4. Presentation and discussion of results on doping distribution achievements is the subject of section 4.5 and a more advanced model predicting more accurately the distribution of trivalent Yb ions doping level is derived in section 4.6. Finally this chapter is ending by presenting and discussing doping variations along non-desired directions (section 4.7).

4.2. State of Art

Numerous advantages offered by controlled variably doped crystals have been exposed in chapter 2 in terms of thermal, ASE and volume management. Manufacturing of such crystals is nevertheless still in its early development stage and, as of today, almost all experimental realizations are dedicated to doped/undoped composite garnet structures. In our laser applications, where only a fraction of pump energy is converted to laser radiation, the remaining energy causes inhomogeneous heating and deformations of the gain media.

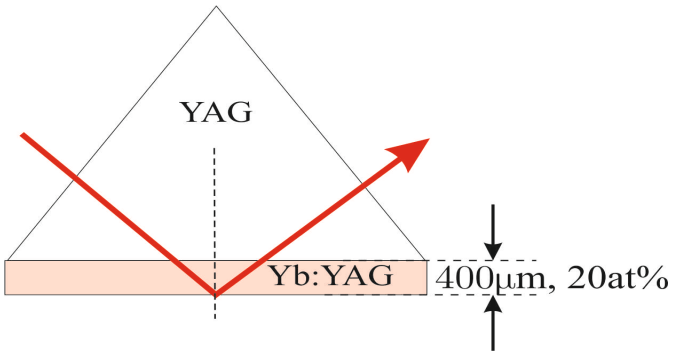

Fig.4.1. Composite YAG/Yb:YAG gain media geometry for TRAM laser. The amplified laser ray is shown in red, an optical path along which the beam does not experience Fresnel losses (AR coating; total internal reflection in the Yb doped part). ASE originating in the Yb:YAG is coupled out efficiently towards the white (undoped) YAG.

Using YAG/Yb:YAG composite crystals helps to avoid this issue since the undoped part acts as a heat sink. Also the great advantage of using such composite YAG structure is illustrated in terms of ASE management on the TRAM [4.1] architecture. The adjunction of a large undoped YAG section above the thin Yb doped YAG layer minimizes ASE effective

amplification length. Due to perfect index matching at the junction of this composite structure (Fig. 4.1), the ASE parasitic rays do not stay trapped into the highly amplifying layer anymore.

4.2.1. Cosintered ceramics

Let us first mention transparent polycrystalline garnet materials made of randomly oriented single crystal grains, called laser ceramics. Currently, laser quality ceramics have a noticeable impact on solid-state laser research and appear to be a very serious alternative to melt-grown crystals. Among its numerous advantages, one can cite the high purity of the resulting gain medium and the ability to grow large size elements. Ceramics offer a qualitative lead when special arrangements are needed that cannot be obtained with current crystal growth techniques. As an example, in Chapter 1 we described the laser ceramics for LUCIA amplifier which possesses specifically designed cladding surrounding the gain media in order to absorb ASE and by this to mitigate parasitic oscillations: Cr^{4+} doped YAG ceramics are co-sintered around Yb:YAG ceramics. One can imagine that ceramics layers with different dopant concentrations could be co-sintered together and, by this, a gain media with almost any controlled doping distribution profile could be obtained. Despite the maturity of ceramics manufacturing process, it would still remain a quite expensive solution. Many research groups currently study laser ceramics sintering processes throughout the world but the most prominent successes have so far been achieved mainly by Japanese researchers [4.2, 4.3, 4.4 and 4.5].

4.2.2. Composite crystals

Another way to obtain variable doped gain media is to produce so-called composite crystals. The first composite laser rod for diode-pumped application was obtained through diffusion bonding by the Onyx Optics company in 1991 [4.6]. Also some studies were performed in Japan [4.7]. In [4.8] the authors report 1060 W cw operation laser based on Yb:YAG/YAG composite. Influence of different technological parameters on thermal bonding [4.9] processed Yb:YAG/YAG composites is studied in details in [4.10]. The authors used Cz grown crystals with a 10x14 mm bonding area. Quality parameter for both surfaces to be bonded was 10/5 smooth finish, flatness $< \lambda/10$ and parallelism < 10'' after final polishing. Afterwards chemical polishing and ultrasonic cleaning of the samples was required. The main steps of composite preparation were the following: the polished surfaces were put in contact to establish an optical contact (Van der Waals attraction), and then the composite was sintered for some time under specific pressure and temperature, and, finally, slowly cooled. The effect of several factors such as chemical polishing presence/absence, different temperature and pressure was observed. A composite crystal without any transition line was obtained with chemical polishing, a 113 kPa pressure at 1550 °C. Authors did not observe any light scattering on the transition surface of the composite sample. These results illustrate the high efficiency of this method for producing composite YAG crystals.

Alternative methods rely on non-diffusion bonding. This is for instance the case of a synthesis method developed by two Russian research groups in Nizhny Novgorod (Institute of chemistry of High purity substances and Institute of Applied Physics). In Self propagating

High temperature Synthesis (SHS), orthophosphoric acid is applied to bonding surfaces before diffusion bonding actually takes place [4.11]. In this case, the requirements on the surface quality are less strict because the liquid phosphates allow to achieve an excellent optical contact and no pressure or high temperatures are needed. For large size composites, when the bonding of large surfaces is required, diffusion bonding methods might face some problems at the polishing level, while for SHS, authors claim to be able to bond the surfaces with any sizes of currently available crystals (<100 mm for YAG, see chapter 6 (large crystals)).

4.2.3. From composite structure to continuous doping variation

In order to be produce crystals with volumic variable distribution of dopant, several layers with different constant dopants concentration have to be bonded together. More layers have to be bonded to obtain smoother distribution of dopant ions. This consequently will bring more interfaces and will sophisticate the fabrication. Also thinner layers will be more difficult to manipulate.

Epitaxy [4.12] is also a technically feasible approach although not tailored for mm scale thickness requirements for laser applications.

Ion implantation [4.13] could also be used but here again this technique is more suitable for semiconductor device fabrication.

The third method for gradually doped crystal growth is to rely on melt growth techniques and is at the core of the work described here. These processes are highly dependent on the nature of the dopant for a specific host matrix. As it has already been mentioned, YAG can host many types of dopants. For some dopants (Yb, Er) very high doping values can be obtained, while for others, only low levels are feasible (the most well-known case being Nd). The ability of the dopant to be captured from the melt during YAG crystal is quantified by the so-called segregation coefficient (k_S) which is the ratio of the dopant concentration in the melt and in the solid phases. $k_S = 1$ means the dopant will be homogeneously distributed in the grown crystal. When the segregation coefficient is lower than one, the grown solid will only partially capture the dopant ion present in the melt. The out-thrown ions will feed the melt and lead to an increased dopant concentration in the melt. In the case of complete diffusion of dopant in the melt, each new grown layer of the crystal will exhibit a higher concentration, therefore leading to a variable distribution of the dopant in the final crystal. The most known case of this phenomenon is taking place with Nd:YAG crystals where segregation coefficient is measured to be between 0.01 and 0.8 depending on solidification rate and growth method [4.14]. This leads to hyperbolic profile of Nd ions distribution in YAG matrix for roughened growth [4.15]. Considered at first sight as a negative effect, its advantages were later taken into consideration and such crystal was used in order to provide power-scaling of end-pumped rod lasers by longitudinal concentration gradients [4.16, 4.17, and 4.18]. The rods used in these experiments exhibit hyperbolic distribution of Nd ions with a total 1.5 at% difference within 25 mm.

Also crystals with slightly varying Yb^{3+} concentration have been obtained by melt growth techniques such as Czochralski and Temperature-Gradient Technique [4.19]. A doping variation of 0.3 at%/cm was observed for TGT growth. Such behavior takes place due to the fact that segregation coefficient of trivalent Yb ions is slightly different from 1 (calculated to be 1.09 for Cz and 1.08 for TGT in [4.19]). However, in this work, this effect was regarded as a drawback not possible to control. In order to be able to grow crystals exhibiting controlled variable doping distribution, a growth method where the composition of the melt can be continuously controlled during growth process is needed. Some simple schemes for gradient doped crystal growth via Cz and TGT method is described in the previous chapter while here we concentrate on gradient doped crystals obtained by Bagdasarov method.

4.3. Growth experiments overview

For Bagdasarov technique (discussed in section 3.5), the boat-shape crucible loaded with starting material travels through a heat zone causing the melting of the crucible content located within that heat zone. The crystallization starts as soon as the content exits the heat zone. Consequently all three phases, starting material (green), melt (blue), and crystalline (pink) can simultaneously be present in the crucible as illustrated on Fig. 4.2. This is a key factor allowing us obtaining gradient doped crystals with this method, because it allows controlling the melt composition during the growth.

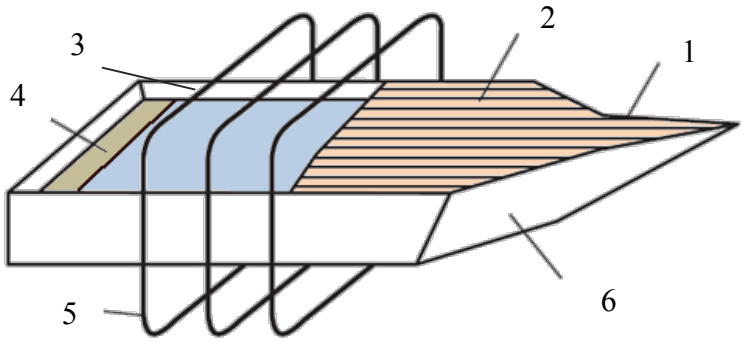

Fig. 4.2: Schematic representation of Bagdasarov method. 1-seed, 2-crystallized part, 3-melt phase, 4-starting material, 5-heater, 6-boat-chaped crucible

Homogeneously doped YAG crystals are grown in crucibles loaded with starting material with stoichiometric ratio of ytterbium oxide, alumina and yttria according to the targeted final concentration level N ($0 < N < 100\%$) of Yb. For gradient doped crystal growth, starting materials with different concentration of Yb are prepared and each of them is loaded at separate locations in the crucible (Fig. 4.3). The respective doping levels of these starting materials will define the doping distribution in resulting final crystal.

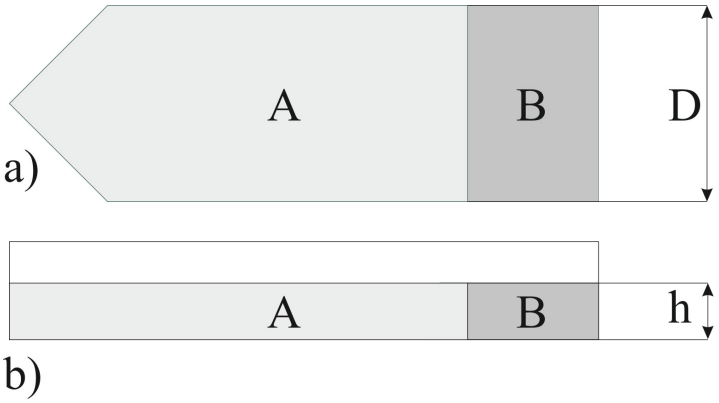

Fig.4.3. Top view (a) and side view (b) of the crucible loaded with two (A & B) different starting materials for gradient doped crystal growth. D and h are respectively the width and height of the crucible.

At the beginning of the growth process, the heat zone is located in sector A, so the melt will have the same constitution as starting material in the sector A. During the growth process, the molten zone will move due to the relative motion of crucible and heat zone and will gradually grab starting material from sector B. This will lead to change of the melt composition. On the other side of the melt zone, the crystallization takes place and each new solidified layer will have the same composition as the melt at the moment of its crystallization. By this the crystalline layers will have different composition and we will end up with variable profile of Yb concentration. We propose here to derive a very simple model to predict the final distribution of the Yb concentration, but we first have to consider several hypotheses:

We assume a segregation coefficient equal to unity for Yb . As we have already seen this is not totally true (it can actually even lead to some naturally present gradients in Cz and TGT grown YAGs). Nevertheless, Bagdasarov grown constantly doped samples exhibit rather homogeneous distribution of Yb ions (see chapter 6 where we give a typical value), which means that our assumption is justified.

Also, we shall consider instantaneous diffusion of newly grabbed Yb ions within the melt. Such approximation is actually true only for extremely low growth rates. However we cannot proceed with infinitely low growth rates, because it will cause other issues like insufficiency of Al because of selective evaporation, bubble inclusions generation, crucible induced impurities, damage of the crucible, potentially leading to melt outflow. So for the typical (1.5 to 2.5 mm/h) crucible speed, it is likely that such full diffusion hypothesis is a very idealistic approach because of the absence of active mixing (unlike Cz method) :newly grabbed starting material is not able to change significantly the concentration of the melt at the other end of the molten zone, where solidification occurs. This assumption may lead to overestimation of gradient values.

Finally, we consider that the molten zone will keep a constant parallelepipedic shape all over the growth process with length (L_m) and height (h) constant for all phases and positions, the third dimension, the width D, being obviously constrained by the crucible width (we do not take into account the triangle shape of the crucible at the seed position, because the gradient growth occurs in the rectangular part). This means that we assume the melt will keep its

constant volume during growth. Another limitation to this assumption is that melt, crystalline and starting material have a different density. Specific in-situ growth parameters changes are required in order to keep melt length constant; without such during-the-growth adjustment, shrinkage occurs along Lm. Also, the height is never constant. It can be seen from grown crystal which becomes thinner closer to the end. At the end of this section, it is shown how molten zone evolves during the growth process. Also, especially in the early stages of the growth process, crystallization interface exhibits some curvature (visual observation and [4.20]) which disappears afterwards. This is a minor effect and can be neglected.

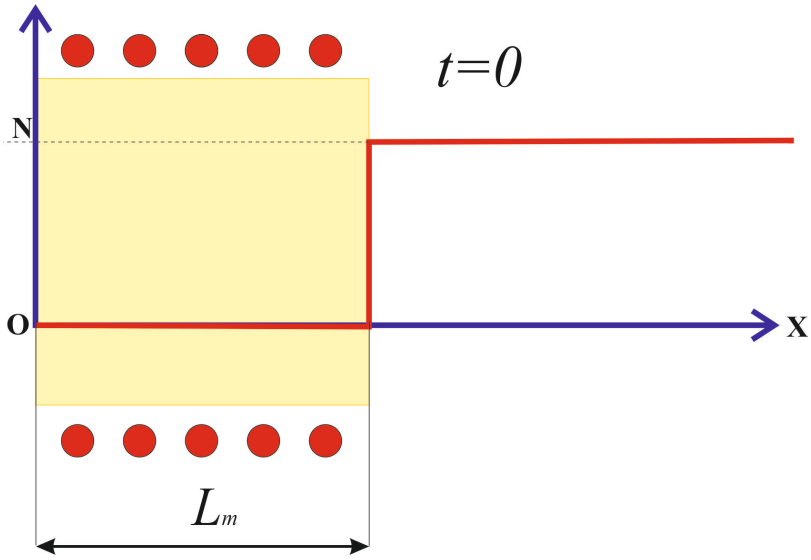

Fig.4.4. Distribution of the Yb ions within the starting material. The origin is at the end of triangular part of the boule. The molten zone and the heater spires are symbolized by yellow rectangular and red circles respectively (at t=0)

Considering this set of hypothesis, each newly grown crystalline layer will have the same composition (doping level) than the melt at that moment. To be able to predict the dopant final distribution in the crystal, the concentration of the melt at every moment i.e. at any position (crucible-heater relative translation rate is constant) must be known. Let us imagine that the concentration of Yb ions in starting material located in zone *A* is 0 at% while in zone *B*, it is *N* at% (Fig. 4.4).

During a period of time *dt*, the crucible will move by *dx* with respect to the heater. This will cause a similar motion of the molten zone (liquid phase) inside the crucible. The *dx* long layer of molten material exiting the heat zone will then crystallize. Simultaneously, a *dx* long layer of starting material will be injected into the melt therefore bringing the Yb ions concentration in the melt at a higher level (Fig. 3.5).

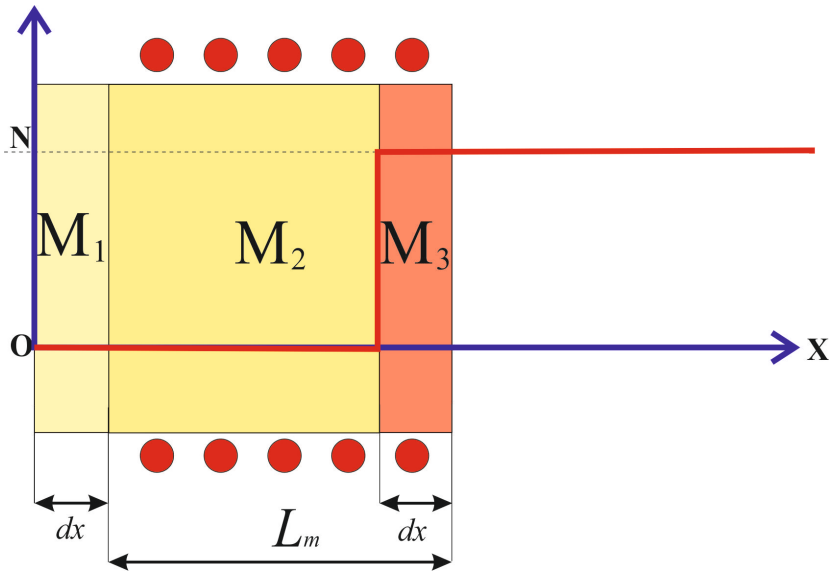

Fig.4.5. Position of the molten zone after a *dx* crucible translation. *M1* represents the total amount of Yb ions which left the molten zone because of the crystallization, *M2* the remaining ions and *M3* is the total amount of inserted ions due to the melting of starting material.

At position *x*, the total amount of Yb ions in the melt is $C(x) \cdot L_m \cdot h \cdot D = M_1 + M_2$ where $C(x)$ is the concentration of Yb ions in the melt and D is the width of the crucible. The total amount of Yb ions at the position of the melt $x + dx$ is $M_2 + M_3$. The total amount of Yb ions which left the melt due to the crystallization is $M_1 = C(x) \cdot dx \cdot h \cdot D$. The quantity of Yb ions which entered the melt due to the melting of starting material is $M_3 = N \cdot dx \cdot h \cdot D$. Here h does not represent the physical height of starting material but the equivalent height of the melt obtained from newly molten starting material (the height of starting material is higher due to the difference in the densities). Thus, for the total amount of Yb ions in the melt at the position $x + dx$, we obtain:

$$C(x+dx)\cdot L_m \cdot h\cdot D = \underbrace{C(x)\cdot L_m \cdot h\cdot D}_{1} - \overbrace{C(x)\cdot dx\cdot h\cdot D}^{2} + \underbrace{N\cdot dx\cdot h\cdot D}_{3}, \quad (4.1)$$

where term 1 corresponds to the melt composition on previous position, term 2 is the amount of Yb ions which left the melt (crystallized part) and term 3 represents the amount of newly entered ions (melt starting material).

Taking into account the initial condition $C(0) = 0$, we obtain the following solution for the above concentration distribution differential equation:

$$C(x) = N\left(1 - e^{-\frac{x}{L_m}}\right) \quad (4.2)$$

If the Yb ions concentration is not a simple step function, the differential equation (3.1) has to be solved considering $N(x)$ dependence with the position. It does not make any sense to assume something else than homogeneous distribution in the starting material for the area

$x \in (0, L_m)$ because in any case we consider it will be instantly homogenized. Predicted dopant distributions for different values of *N* are presented on Fig. 4.6.

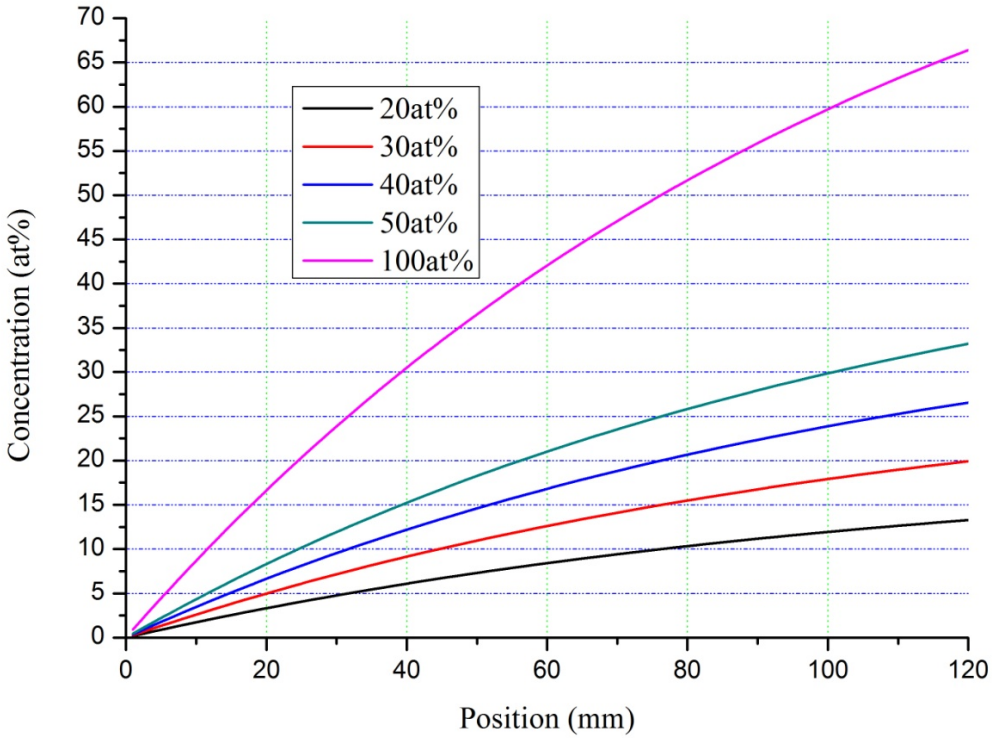

Fig.4.6. Trivalent Yb ions final distribution resulting from the simple model for different starting material doping steps

For this calculation, the considered molten zone length was L_m = 110 mm. According to this simple model, doping gradient values can be adjusted by changing zone B starting material doping level.

Several successful growth sequences were performed and Yb^{3+}:YAG crystalline boules exhibiting doping gradient distributions were obtained, demonstrating the repeatability and robustness of the technique. The results on four of gradually doped boules are presented here. The starting distribution of Yb ions for these growth processes is given in Fig. 4.7. The YAG seed placed at the crucible bow is oriented along the requested preferential crystallographic axis [111] direction perpendicular to the plane shown on the Fig. 4.7. The crucible lengths (defining the boule size) used for the three growth sequences were 220, 235 and 220 mm respectively (not considering the triangular part). Unlike for standard constant doping growth processes, here, as a starting material, we used crackle prepared from the crystals with very homogeneous doping distribution preliminary grown by Bagdasarov technique. For this crystals preparation high purity powders of Y_2O_3 (99.999%), Yb_2O_3 (99.999%) and Al_2O_3 (99.999%) were weighed out in appropriate stoichiometric mole ratios for 0, 20, 50 and 8 at% concentrations and constant doping growth processes were performed. The resulting homogeneously doped boules were turned into crackle by thermal shock and placed in the crucible forming the starting material for gradient doped crystal growth, distributed according to the profiles displayed on Fig. 4.7.

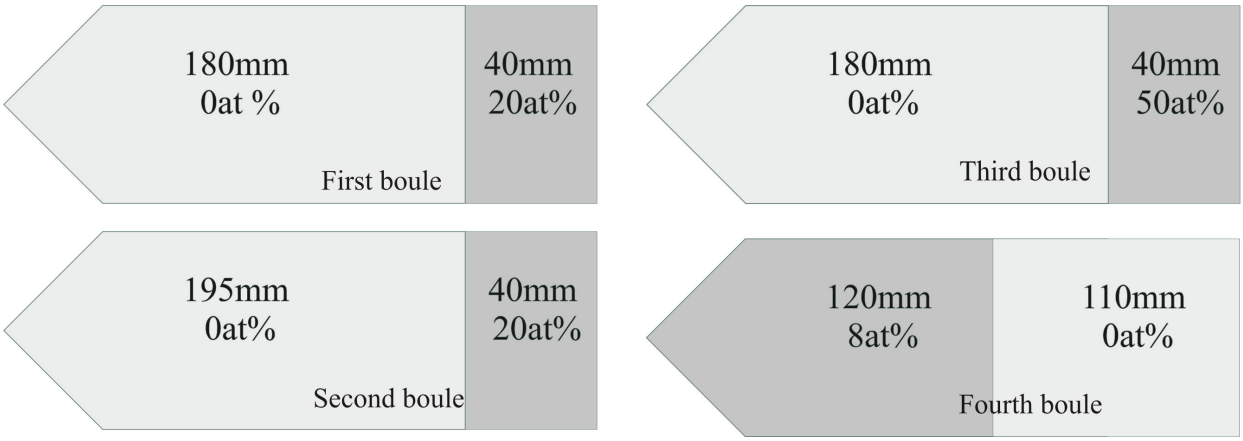

Fig.4.7. Trivalent Yb ions distribution in the starting material for four growth sequences

The growth process of the third boule differs from the others. As illustrated in Fig. 4.7, 0 and 50 at% doped starting materials were used. But the main different is that the grown boule was not extracted from the crucible after the full growth cycle ended. Due to optical inhomogeneities present in the boule (in the form of color cone and bubbles), it was put again in the furnace to undergo another cycle of growth. This surely led to a smoother spatial distribution of the dopant.

The starting material for the fourth boule was placed in reverse order when compared with the 3 previous runs: the doped part was first entering the heat zone, and then followed by the undoped part. In this case, the differential equation (4.1) has to be revised. We don't have any more the amount M3 of Yb ions which enter the melt. So (4.1) will transform into:

$$C(x+dx)\cdot L_m \cdot h\cdot D = \underbrace{C(x)\cdot L_m \cdot h\cdot D}_{1} - \overbrace{C(x)\cdot dx\cdot h\cdot D}^{2} \qquad (4.3)$$

In the right part of the differential equation (4.3) the term 1 represents the amount of the Yb ions at the previous step and term 2 shows the number of ions left from the melt due to crystallization. Solution of this equation gives the final distribution of Yb ions in the crystal:

$$C(x) = N\cdot e^{-\frac{x}{L_m}} \qquad (4.4)$$

4.4. Measuring trivalent Yb ions concentration

4.4.1. Overview

The doping ions concentration in the host matrix is a key parameter for predicting lasing characteristics and estimating thermal or ASE effects. Various research groups refer to different methods for doping concentration evaluation. In order to define the most suitable and reliable technique for our application, we performed a series of measurements with

different methods on several constantly doped samples. Among the most popular methods are Inductively-Coupled Plasma Mass/Atomic spectroscopy (ICP-MS/AES), Electron Probe Micro Analysis (EPMA,) Rutherford Back Scattering (RBS), Energy-Dispersive X-Ray Spectroscopy (EDX), Neutron Scattering and etc… These methods are widely used not only for optical materials but also for wide range of different materials in order to finely define its composition. Transmission/absorption measurements can be useful to define doping concentration but they are strongly limited to optical materials. EPMA, EDX and RBS are surface techniques while ICP-MS is a bulk technique. We did not found any literature dedicated to the comparison of the different techniques for doping measurements in YAG crystals. For gradient doped crystals, it is very important to accurately measure the distribution of the doping ions at any point of the grown boule. That is why we dedicated a significant part of our time to cross evaluate these techniques. Brief introductions to all evaluated techniques as well as results obtained on homogeneous samples are given in this section. Also the comparison of the different methods is provided.

4.4.2. Inductively Coupled Plasma-Mass Spectroscopy

ICP-MS is a bulk measurement destructive technique. The samples are dissolved into liquid solution. Inductively Coupled Plasma[1] is used as an excitation source to generate ions. These ions are introduced to the mass analyzer, separated and collected and the total ratio of elements of interest is measured.

Among several crystals, two samples with constant doping of 2 at% and 20 at% doping concentration due to the growth reference were tested. These crystals are named respectively Sample A and Sample B. The crystals were grinded to powder and a solution protocol by alkaline fusion was used to dissolve the YAG powder.

Two separate fractions for each crystal were dissolved. The similar Yb concentration found illustrates the good crystal homogeneity. The measurements gave the following results for trivalent Yb ions concentration:

	Growth reference	ICP-MS
Sample A (at%)	2	1.9 +/-0.04
Sample B (at%)	20	17.94+/-0.36

These results were obtained using Chem-Lab MISA-01 standards as a reference. The measurements were performed with Argon ICPMS Spectrometer (Fig. 4.8) at LSCE/IPSL - Laboratoire des Sciences du Climat et de l'Environnement, CEA-CNRS-UVSQ, Gif sur Yvette, France.

[1]Inductively coupled plasma (ICP) is a type of plasma source in which the energy is supplied by electric currents which are produced by electromagnetic induction, that is, by time-varying magnetic fields.

Fig.4.8. Argon ICPMS Spectrometer at Laboratoire des Sciences du Climat et de l'Environnement.

4.4.3. Electron Probe Micro Analysis

Electron Probe Micro Analysis (EPMA) provides quantitative and qualitative determination of chemical composition at the micrometer scale in solid materials without any destruction.

It is a surface technique which allows deriving dopant ions distribution maps for any crystal. The sample is bombarded with a beam (5-10 nm diameters) of low energy electrons. Emitted x-rays at characteristic wavelengths for the elements are recorded and analyzed (wavelength dispersive spectrometry-WDS). The analyzed volume at one measurement point is in a range of 0.3-3 μm^3. CAMECA SX 100 microanalyzer equipped with four WDS spectrometers (Fig.4.9) at the Laboratoire Magmas et Volcans (LMV), Clermont-Ferrand, France, was used for these measurements.

Fig. 4.9. CAMECA SX 100 micro-analyzer equipped with four WDS spectrometers at the Laboratoire Magmas et Volcans (LMV)

With the help of EPMA technique one constantly doped and several variably doped crystals were tested. For constant doped sample (2 at% growth reference) the value of 2.01 at% was obtained with an error bar of 0.2 at%. The measurements on gradient doped crystals were performed along principal axis (variable concentration of Yb ions) as well as in other directions. These results are detailed in the next sections of this chapter.

4.4.4. Energy-Dispersive X-Ray Spectroscopy

Energy-dispersive X-ray spectroscopy (EDS or EDX) is another analytical technique used for the elemental analysis or chemical characterization of a sample. It is one of the variants of X-ray fluorescence spectroscopy which relies on the investigation of a sample through interactions between electromagnetic radiation and matter, analyzing X-rays emitted by the matter in response to being hit with charged particles. Characteristic X-rays emission stimulation is somehow similar to EPMA technique. A high-energy beam (e^-, p^+, X-rays) is focused into the sample to be studied and excites characteristic radiations. The number and energy of the X-rays emitted from the specimen are analyzed by an energy-dispersive spectrometer.

EDS measurements were performed in Laboratory of High Temperature Superconductivity, Institute of Physical Research of National Academy of Sciences, Armenia. This method allows qualitative (presence of impurities within the crystals) and quantitative measurement (Yb3+ doping level) of atomic component relative concentration. Samples with constant doping distribution as well as YAG crystals exhibiting variable doping level were investigated. Before being placed in the Silicon detector (model EDS7378), the samples were coated with a Carbon conductive coating to evacuate charged particles from the surface. On Fig. 4.10, the equipment used for EDX measurement is presented and the screenshot of characteristic spectrum for Yb:YAG is shown on the Fig. 4.11. The sample compartment puts a strong limitation on the sample size to be tested. The maximum size which can fit onto the holder is 15 mm. This implies cutting long reference samples with variable doping distribution into the smaller pieces.

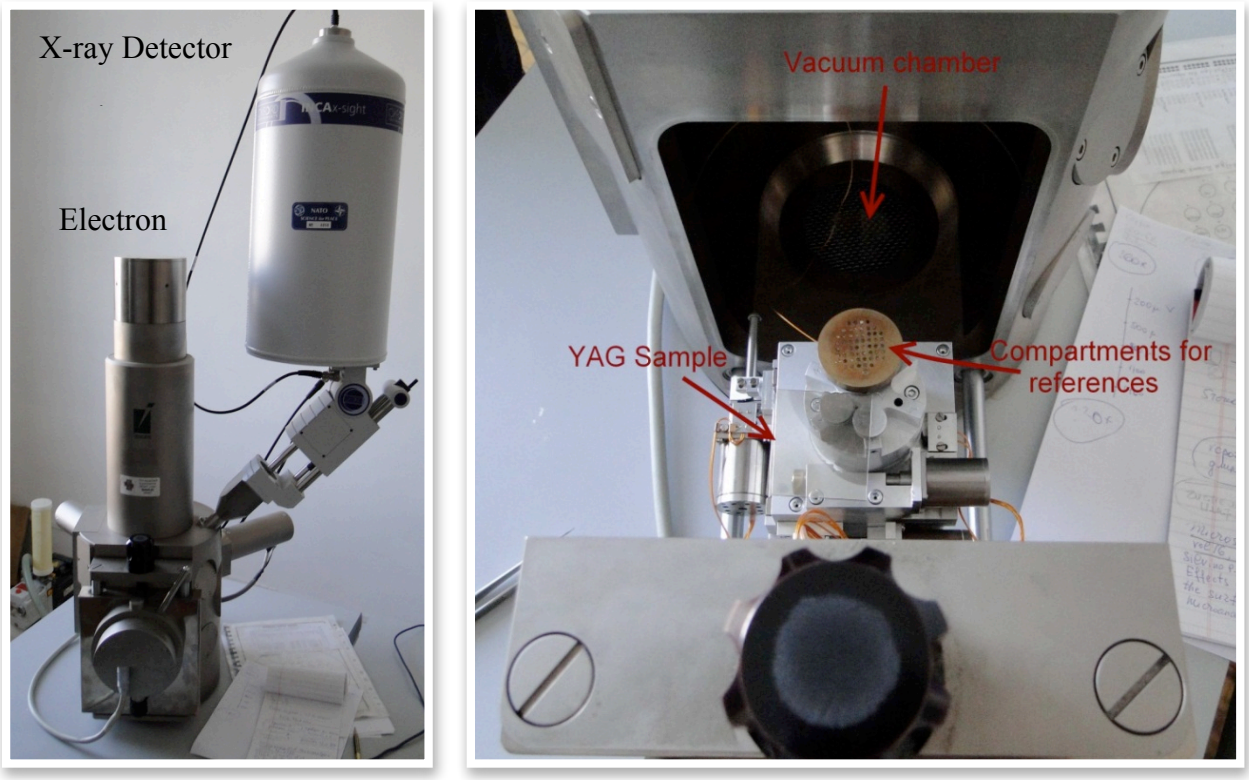

Fig.4.10. Equipment used for EDX measurements

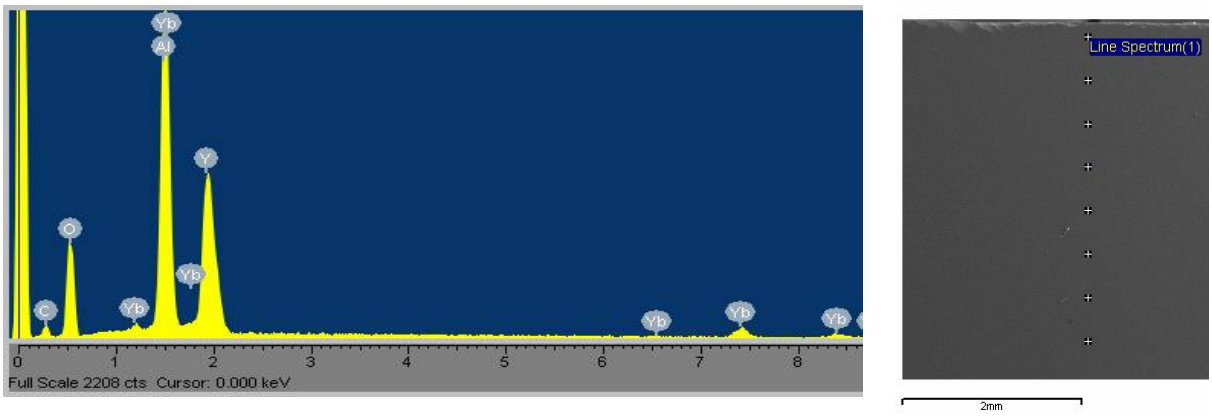

Fig.4.11. Screenshot of characteristic EDX spectrum for Yb:YAG (left) and target points on the sample (right)

The constant doped samples with growth reference of 2at% and 20at% of Yb doping level were tested in several points. The measured value confirmed expected value with some error bar of 0.6 at% and 2 at% respectively with almost the same central value for all points. The measurements performed on gradient doped crystals are discussed in next sections of this chapter.

4.4.5. Rutherford Backscattering Spectrometry

Rutherford Backscattering Spectrometry (RBS) is a nuclear method dedicated to the near surface analysis of solids [4.21], it is quantitative without the need for reference samples, non destructive and very sensible for heavy elements. Ions with energy in 0.5-4 MeV range bombard the target and the energy of backscattered particles is recorded with an energy sensitive solid state detector. The penetration depth is 2 µm for incident He-ions and 20 µm for incident protons. RBS is firstly described in [4.22] and full description of current applications for RBS method is given in [4.23] Scattering with non-Rutherford cross-sections or forward scattering is also called RBS. Using inelastic scattering and nuclear reactions is called Nuclear Reaction Analysis (NRA), while detection of recoils at forward angles is called Elastic Recoil Detection Analysis (ERD or ERDA

For our samples, RBS measurements were performed with the Van der Graaff ion accelerator (Fig. 4.12) of the Institute de Nanosciences de Paris.

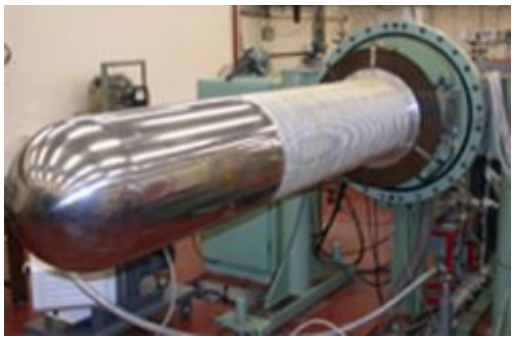

Fig.4.11. Van der Graaff ion accelerator

The atomic ratio of Yb and Y ions can be directly deduced from the recorded data. RBS spectra for two samples with 2 at% and 20 at% doping references were registered at two different points for each one (Fig. 4.12).

The sample holder is attached to a step machine allowing acquiring measurements on several points and even on several samples by one loading. The measurement in different points for each sample illustrates the good homogeneity of the doping distribution. The doping distribution can be directly derived from the spectrum by simply comparing Yb/Y steps. The most convenient way is to model the RBS spectrum with the help of SIMNRA software. We can see a very satisfying accordance of the SIMNRA simulated RBS spectrum for 2 at% Yb doped YAG crystal with experimentally measured data (Fig. 4.13).

With this technique, for both samples, we obtain 19.3 and 2 at% respectively with precisions of 0.2 and 0.1 at% respectively which is in very good accordance with other measuring techniques.

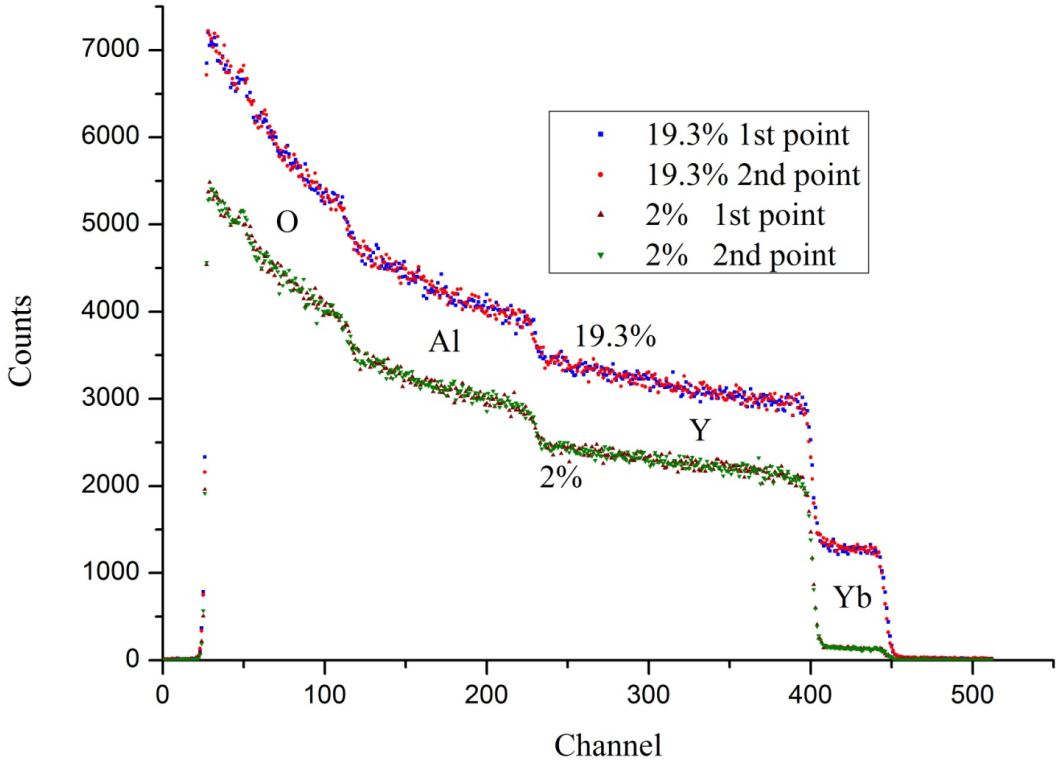

Fig.4.12. RBS spectrum for Yb:YAG samples with 2 at% and 20 at% doping levels

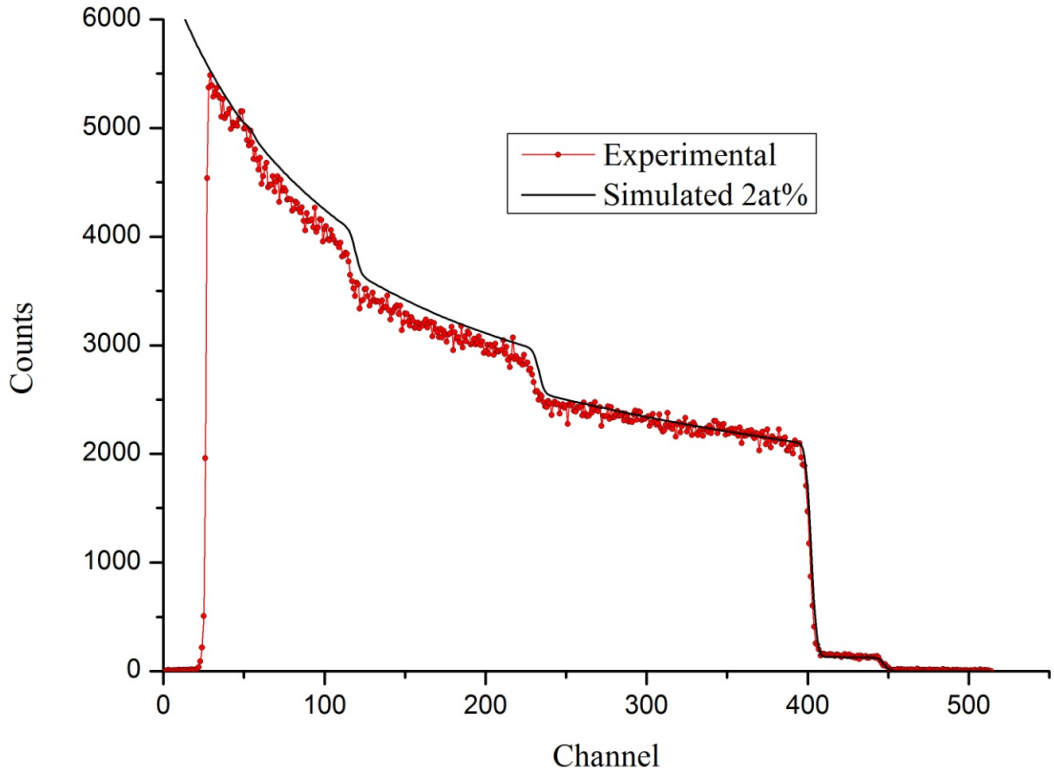

Fig.4.13. Simulated and measured RBS spectrum for 2 at% Yb doped YAG sample. Only the first two left steps (associated with Y and Yb presence) are of interest for us.

4.4.6. Absorption/transmission measurement

Another method used for our measurements was optical transmission/absorption technique. The collimated light travels through the crystal after which the transmission spectrum is recorded. Taking into account Fresnel losses and optical length, the crystal absorption can be calculated by Lambert's law leading to the doping level. Incident I_0 and transmitted I intensities are related to α, the absorption coefficient and z, the length of optical path through the following equation:

$$I = I_0 e^{-\alpha z}$$

The absorption coefficient is the product of the number of absorbing particles and the absorption cross-section, for a specific wavelength:

$$\alpha = N_0 \cdot A \cdot \sigma_{abs},$$

where N_0 is the concentration of absorbing particles (Yb) at the doping level of 1 at%, A is the doping level and σ_{abs} is the absorption cross-section.

Transmission/absorption measurements were performed at the Laboratoire LULI, on a Cary500 spectrophotometer (Fig. 4.14).

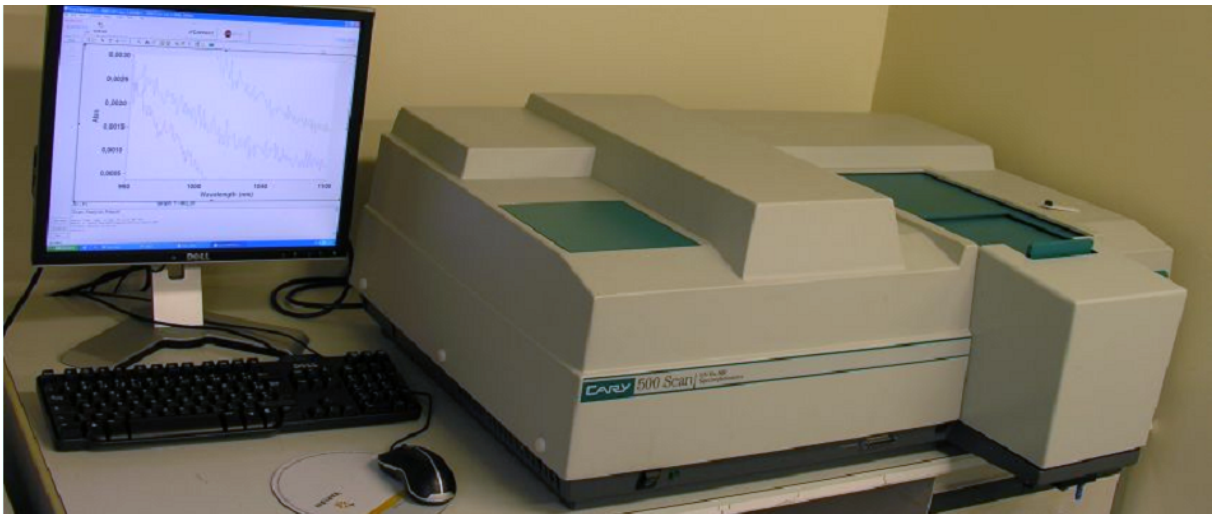

Fig.4.14. Cary 500 spectrophotometer at LULI, Ecole Polytechnique

This method is very suitable also for gradient doped crystals in order to obtain Yb ions concentration distribution. Fixing the sample to a spatially labeled platform to be inserted in the spectrophotometer allows us to measure absorption in crystal at different positions. The obtained doping value for each point represents the average value over the optical path (*z* integration) and beam surface (*x* and *y* integration). Longitudinal integration can be an issue when an unwanted/unexpected doping gradient is present along this direction (see section 4.7).

4.4.7. Cross evaluation of the different techniques

Each of these doping measurement techniques carries its advantages and disadvantages. Point-by-point spatially resolved measuring techniques are connected with somehow larger values of errors and uncertainties. On the other hand, it provides maneuverability which cannot be offered by volume measurement techniques. The performed measurements of constant samples revealed quite similar values for most of the cases. The largest divergence was observed between ICP-MS and other techniques. In Table 4.1 the different techniques doping measurement results for 2 at% and 20 at% (reference growth stoichiometry) are presented:

Table 4.1: Trivalent Yb doping level in two YAG samples measured with different techniques

Crystal	Growth reference	EPMA (at%)	ICPMS (at%)	EDS (at%)	RBS (at%)
Sample A	20	18.53+/-0.1	17.9+/-0.3	-	19.3+/-0.2
Sample B	2	2.01+/-0.1	1.9 +/-0.04	2+/-0.3	2+/-0.1

These results give, according to our best knowledge, the most complete cross evaluation of different measurements technique for trivalent Yb ion concentration in YAG matrixes.

EPMA, EDS and RBS give very close values which are also in a very good agreement with the growth reference.

ICPMS leads, for both samples, underestimated doping values. Also, it is a destructive technique and implies some technical difficulties to get YAG in soluble forms. These drawbacks make this technique the less favorable for our application.

EDS technique gives too large error bars which can be crucial for precise measurements. Moreover, the rather strong size limitation for the samples to be tested with the available EDS device let us considered this technique also as very favorable for doping gradient measurements.

RBS and EPMA seem to be the most convenient techniques. Unfortunately RBS requires running a large installation with access and time constraints. In contrary, EPMA is much simpler and faster in use technique and also not less precise. It was ultimately chosen as the most favorable technique for doping measurements together with transmission/absorption optical methods.

These results offer the possibility to estimate the absorption cross-section $\sigma_{abs}(\lambda)$ at 1030 nm. Relying on absorption data obtained from 2 at% doped sample, we obtain 9.55 10-22 cm². Different values for absorption cross-section can be found in the literature ranging from 9.5 10-22 cm² [4.24] to 1.1 10-22 cm² [4.25]. In the reference [4.24] the authors use 2 at% doped sample and for room temperature they obtain 9.5 10-22 cm² which is very close to the value obtained for our sample. From now on, in this document, 9.55 10-22 cm² will be used for the absorption cross-section at 1030 nm.

4.5. Results on doping distribution in gradient crystals

4.5.1. First grown boule

From the first grown boule, a 25x10x2.9 mm^3 the only extractable sample had to be cut at a 40° angle with the growth direction (25 mm dimension). The average doping distribution gradient in the sample is 0.45 at%/cm, and it achieves its maximum value of 0.65 at%/cm in some areas (Fig.4.15). The crucible velocity V_c was equal to 2 mm/h.

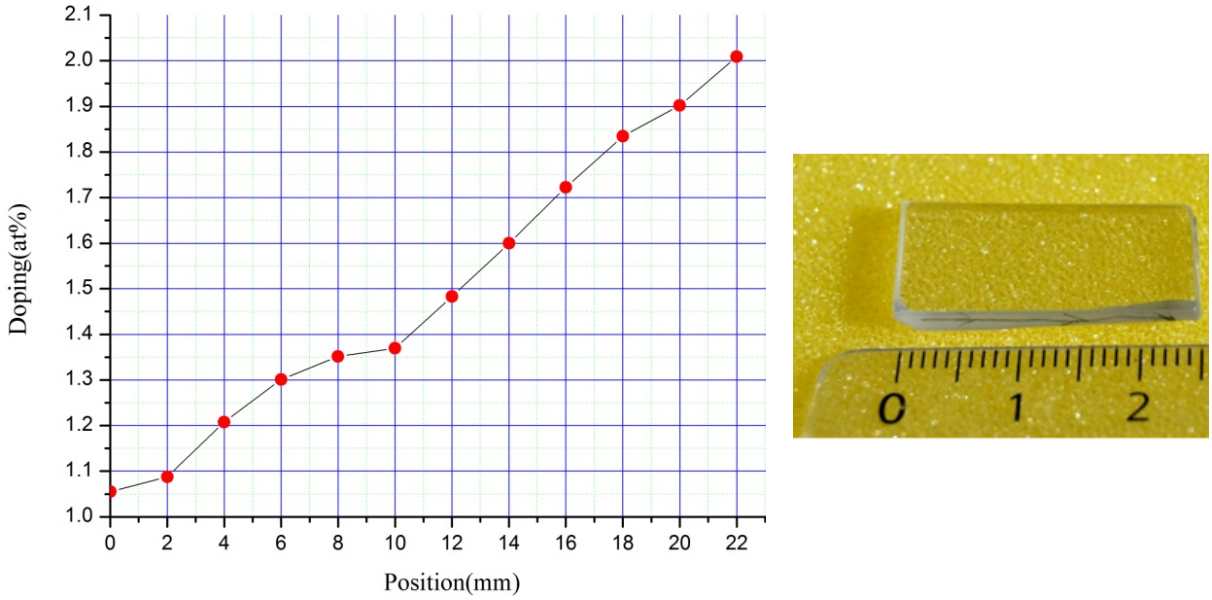

Fig.4.15. Yb ions distribution in the crystal extracted from the first boule obtained through transmission/absorption technique at 1030 nm

Despite the gradient value was quite weak for this first run, it is still clearly observable and it exhibits well defined almost linear distribution. Unfortunately there were no other samples extracted from this boule and no further experiments were performed. Nevertheless, this first run proved to be very encouraging for our approach.

4.5.2. Second grown boule

The second boule was grown in a specifically designed crucible with a much narrower and slightly longer shape. Narrow shaped crucibles are not favorable, because the part of the crystal near the interface of the crystal and crucible is usually not usable since all the stresses are concentrated mainly in these parts. But in this specific case, our purpose was to obtain the variable distribution and to demonstrate the repeatability of the process successfully achieved with the first run. A narrow boule indeed allowed us to follow this logic at a lower cost in terms of starting material. The crucible velocity V_c was set to 2.5 mm/h. Several samples from different parts of the crystal were extracted (Fig.4.16), polished and tested with different methods among the ones presented in the previous section.

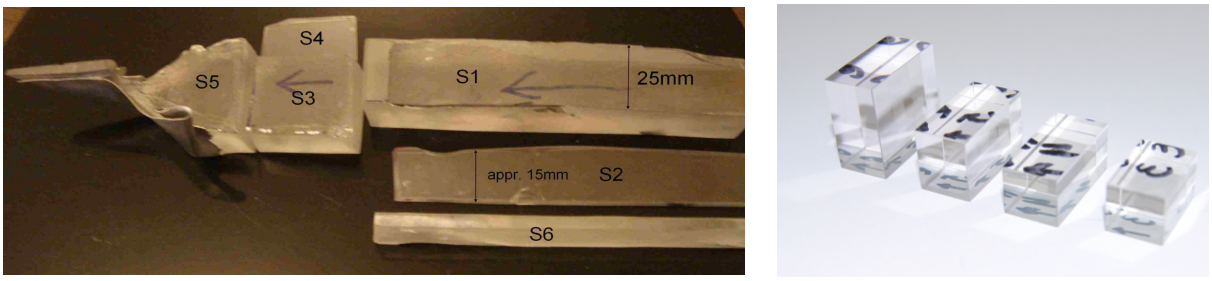

Fig.4.16. The 2nd boule after cutting (left) and extracted samples (right) from S1.

The sample named S2 (displayed on the left part of Fig. 4.16) was cut along the growth direction and was used for defining the doping distribution. It served as a reference for the rest

of the boule. After recording the Yb doping profile on S2 (Fig. 4.17), several samples were cut from S1 for further testing (Fig. 4.16, right).

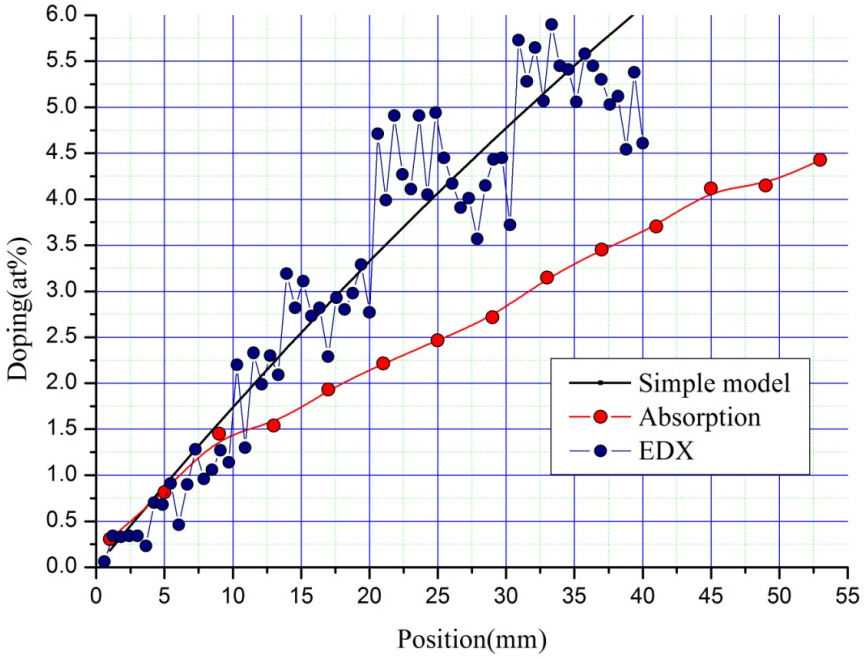

Fig.4.17. Doping distribution for second boule obtained by Transmission/absorption and EDX techniques. The measurement error is 0.3 at% for EDX measurement and 0.2 at% for absorption

The estimated gradient value locally reaches values of about 1 at%/cm. As we can see, with EDS, many fluctuations are present, which makes difficult any interpretation or accurate calculation of the gradient. We detect quite large discrepancy between absorption measurements on one side and, the model and EDS on the other side. The reason of this shift is not totally clear. In transmission/absorption measurements, unlike to other methods, we "see" only trivalent Yb^{3+} ions. The samples are not annealed, and presence of oxygen vacancies would lead to the decrease of Yb^{3+} in favor to Yb^{2+}, forming color centers. This effect could be detected on the transmission/absorption spectrum by absorption peaks at wavelength non-characteristic for trivalent Yb and can be greatly reduced by annealing (all samples used in this work are as-grown). Another possibility is the presence of doping gradients in undesired directions, which will critically impact the choice of the target measurement points along the sampling line parallel to the expected gradient direction. The model improvement and doping level variations in other directions are discussed in section 4.6 and 4.7 respectively.

Finally, let us mention that, due to the relatively high speed of the crucible translation, the instantaneous diffusion considered in the model is a bit too idealistic. The effective homogenization of the melt takes some time after the newly molten phase enters the melt. The melt closer to the crystallization front carries thus a lower concentration than the average and explaining why the obtained gradient is weaker.

4.5.3. Third grown boule

The third boule, as was mentioned before, underwent a double run sequence. After the first, a color zone and cracks were observed in the boule (Fig.4.18) and it was decided to put the crucible with the crystal back in the furnace and to proceed with another run. The crucible velocity V_c was set to 2 and 2.5 mm/h for first and second runs respectively.

Fig.4.18.Third boule after 1st run

This would of course make smoother the predicted gradient distribution. After the second run the boule was free of such defects as can be seen from Fig.4.19.

Fig.4.19.Third boule after 2nd run

As for the second boule, two reference samples with a width of 10 mm and length (growth direction, gradient direction) of 40 mm and 60 mm were extracted from the grown boule and transmission/absorption measurements were performed. Afterward the second reference sample (60 mm) was cut into smaller pieces with length of 15 mm in order to fit in EDS device. The results are shown on Fig. 4.20. The lack of data point at 40 mm is related to the cut between the two reference samples.

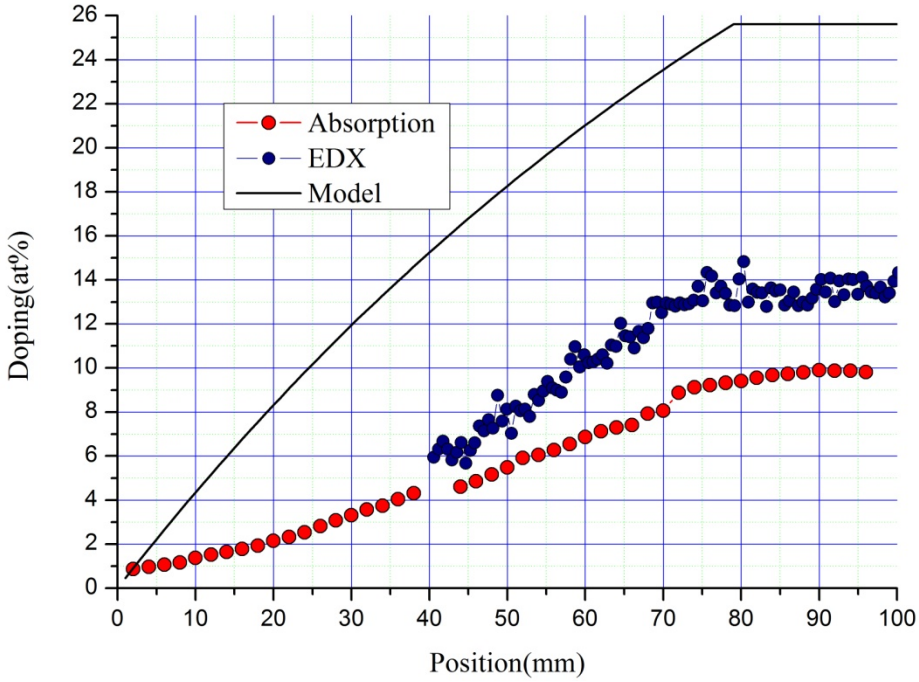

Fig.4.20.Doping distribution in the third boule obtained by transmission/absorption and EDS techniques in comparison with model prediction. The error are the same as for Fig.4.17

After 70 mm, we observe on both measurement curves that the zone with homogeneous doping commences. The average doping obtained by EDS is ~2 at%/cm while it is ~1.2 at% with the absorption technique. This is the highest value of gradient obtained up to now. The reasons of discrepancy between two techniques are the same as for the second boule.

4.5.4. Fourth grown boule

Growth process of the fourth boule was quite different from the others:

Doped and undoped locations of starting material are exchanged in the crucible as illustrated on figure 4.7. The length of the first part is 120 mm, which is longer than the molten zone length at the starting position. Therefore the first layer of crystal has to exhibit an 8 at% doping level. The crucible translation speed is reduced almost 2.5 times, which means that the diffusion in the melt has much more time to take place while the crucible is moving at V_c = 1 mm/h. The temperature of the process was higher and, most of the time, the crystallization front position was kept under the observation window.

Similarly to other boules, three reference samples were extracted (Fig. 4.21) and measured point by point via EPMA technique as well as with our spectrometer. The shortest sample (top right, 27 mm) was the one cut in the vicinity of the boule first crystallized layer.

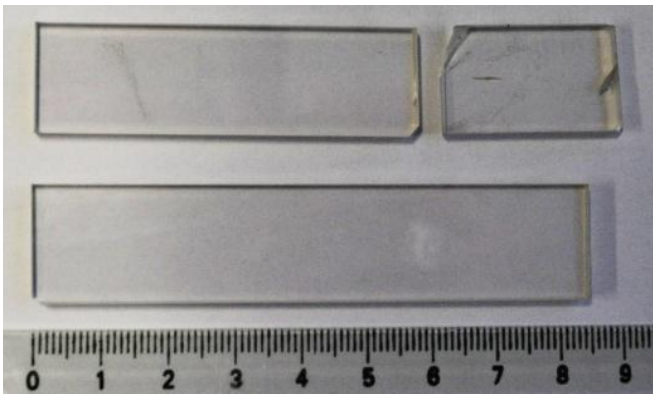

Fig.4.21. Three reference samples extracted from 4th boule: 27, 56 and 74 mm

The obtained gradient was quite weak going only up to 0.5 at%/cm but it agrees well with the calculated profile (Fig. 4.22) given by equation 4.3. An offset of 9.5 mm has to be considered to reflect the 7.3 at% highest value experimentally observed. Indeed, if the 27 mm sample would have been cut right at the beginning of the gradient doped onset, a value of 8 at% would have been observed.

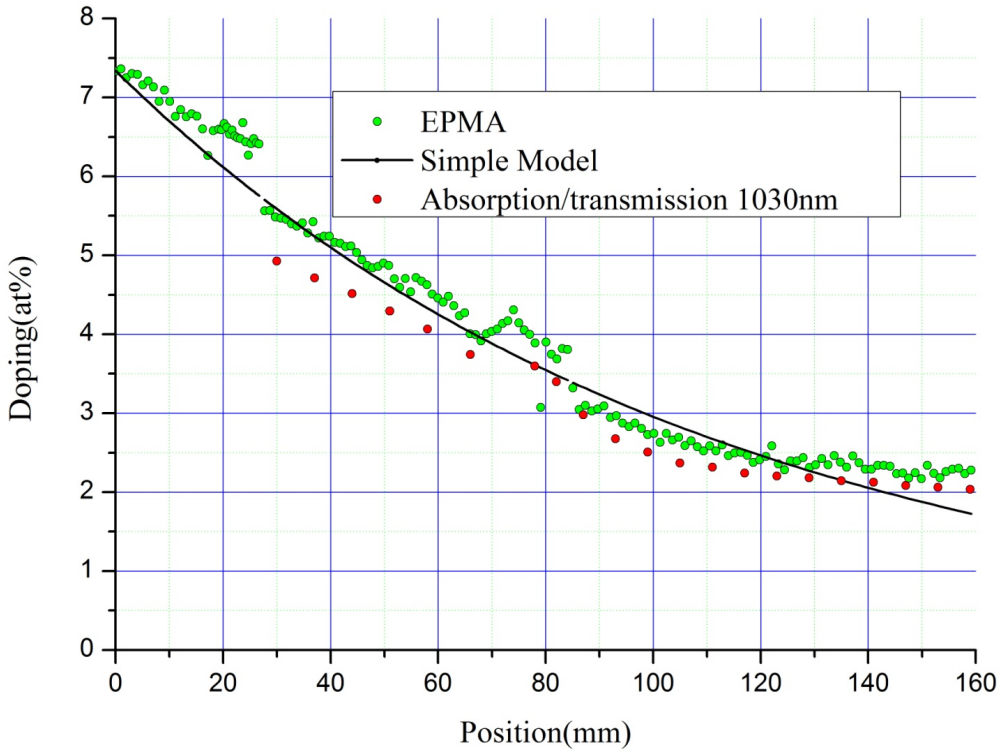

Fig.4.22. Doping distribution in the fourth boule measured by EPMA technique and predicted by simple model. The good accordance of both curves shows validity of the model in this specific experimental case where the crucible speed was very slow and temperature is higher. The error for EPMA measurement is about +/- 0.1 at%

The simulated profile results from equation (4.4). The spatial interruptions of the curves correspond to the physical cuts between samples. EPMA and absorption/transmission

measurements are in good agreement. Experimental care was considered to measure the doping by absorption alongside the same line it was measured by EPMA.

4.6. Improving the gradient doped crystal model

The simple model appears to be lacking accuracy and can be considered as sufficient only when rough estimate of the dopant distribution are requested or in cases similar to boule number 4. We indeed observe that a satisfying agreement was found only in the case of the last boule. The model indeed almost totally ignores the growth conditions. Therefore, assumed simplifications have to be revised in order to get better agreement with experiment. That is why some experiments were performed and a more advanced model was derived.

4.6.1. Molten zone evolution

In the simple model, I considered the molten zone geometry constant during the growth process. But, in practice, the molten zone length Lm (i.e. dimension along the growth direction) can be kept constant only with specific experimental efforts and conditions. This was somehow implemented for 4th boule where the temperature was kept at higher level and the position of the crystallization front was under observation through the window during the full growth process (with no significant shrinkage observed). The height h of the melt also changes due to differences between starting material, melt and crystal densities. It could be possible to maintain the height of the melt somehow constant by distributing starting material with a variable height at the beginning of the process. Finally, the crystallization front shape and inclination also changes during growth. The last two phenomena are discussed in the next section. Let us first concentrate on evaluating the molten zone length evolution during growth.

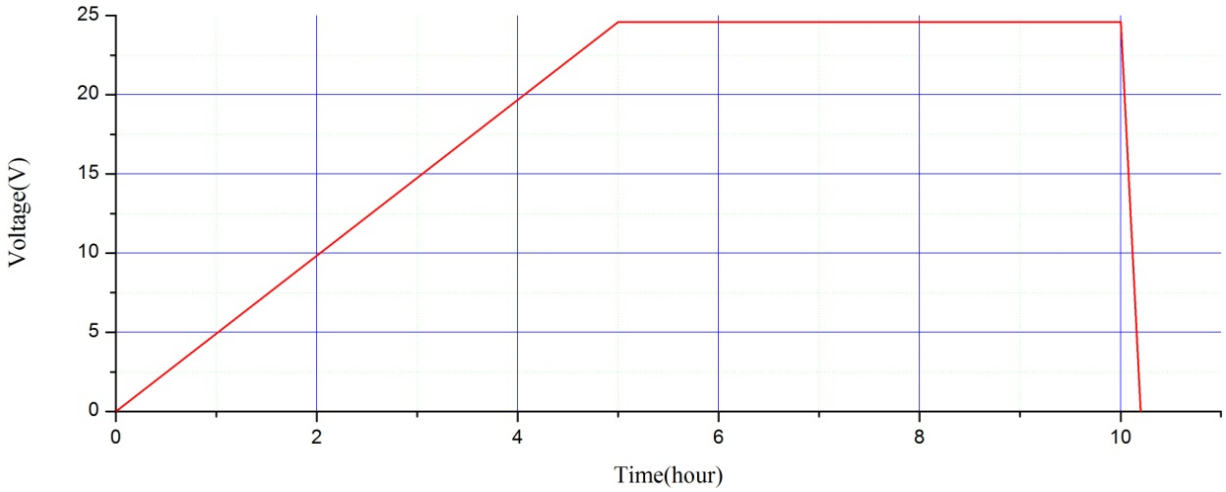

Fig. 4.23.Heat sequence applied for the first step of molten zone length measurement

Naturally, one observes that the molten zone shrinks during the growth process. This is related to the fact that the grown crystalline part carries a higher thermal conductivity therefore providing a very efficient heat evacuation channel. To evaluate this shrinkage, a simple two step experiment was performed. In the first step of the experiment, the crucible,

filled with starting material, is placed in the furnace at the starting position of the growth. Then the standard heating sequence described on fig 4.23 is applied.

For this first run, the crucible is never put in motion. The resulting boule is depicted on Fig. 4.24 where a 110 mm long crystal can be observed. This means that the molten zone length at the beginning of the growth process can be considered equal to the heat zone length, i.e. 110 mm.

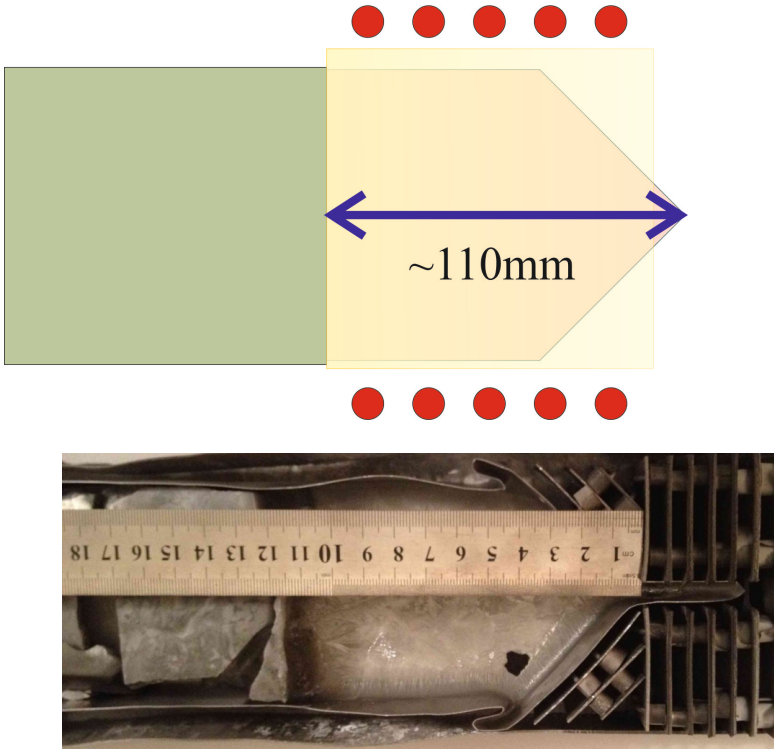

Fig.4.24. Schematic view of the crucible position relative to the heater (top) and picture of the 110 mm crystal observed in the resulting boule (bottom)

As a second step, the resulting boule from the first step is placed again at the starting position and a standard growth process is performed: after a similar 5 hours ramp up of the furnace temperature, the translation of the crucible starts at a 2 mm/hour rate. The heating sequence for this case is shown on Fig. 4.25.

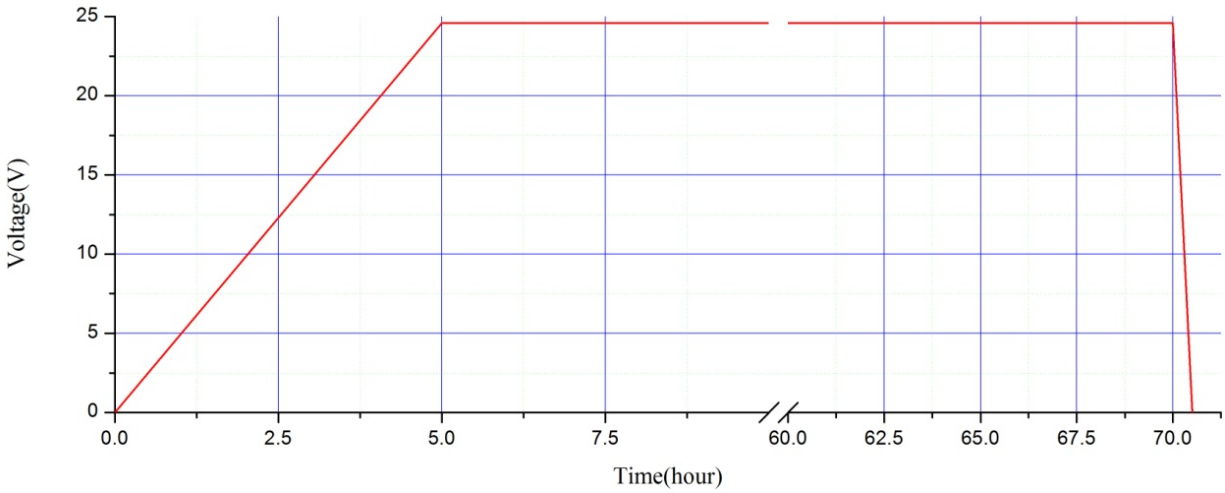

Fig. 4.25.Heat sequence applied for the second step of the molten zone length measurement experiment.

The cooling phase of the crucible starts at the end of the 130mm translation (i.e. 65 hours after the end of the initial ramp up). At that moment, the end of the crucible coincides with the position of the heater first tungsten spire.

The final cooling sequence applied to both steps of this experiment is much faster (a few minutes) than for a standard procedure. Such quick cooling was require to allow a rapid solidification of the melt so the different phases could easily be observed later on as illustrated on Fig. 4.26 where we clearly see the YAG crystalline phase after 70 mm. Between 0 and 70 mm, the "frozen" solid phase obtained is not a YAG monocrystal and varying color can also be seen.

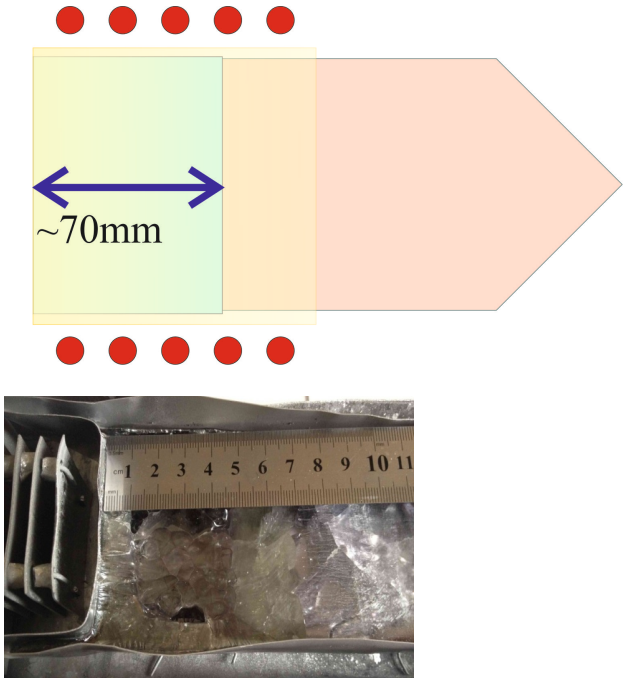

Fig. 4.26.Crucible position relative to the heater (top) and the molten zone length in resulting boule (bottom) for final position

We can deduce from this experiment that the molten length encounters a non-negligible shrinkage during the growth sequence. It indeed reduces from 110 mm down to 70 mm. It could be possible to eliminate shrinkage by continuously adjusting the heater temperature, but such temperature variation sequence was not implemented for first three boules where all the growing processes took place with natural shrinkage. Therefore, if we assume a linear shrinkage process with time, the new expression for the molten zone length Lm, turns into:

$$L_m(x) = L_m(0) + x\frac{L_m(final) - L_m(0)}{d} \quad , \qquad (4.5)$$

where d is the total translation of the crucible. The shrinkage of the molten zone means that the crystallization front (melt/crystal interface) moves faster than the crucible during the growth process.

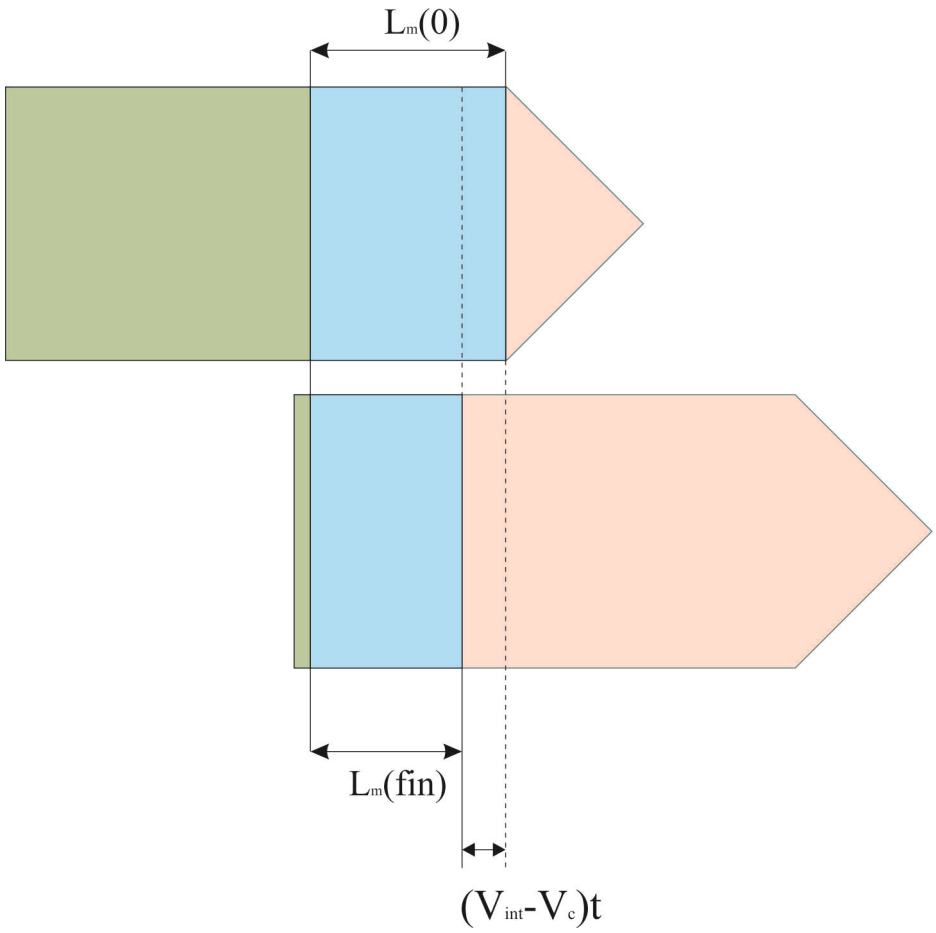

Fig.4.27. Schematic visualization of the molten zone shrinkage through the growth process

The concentration distribution differential equation can be reformulated by replacing the constant molten zone length L_m by a linear expression $L_m(x) = Kx+a$; the obtained solution is:

$$C(x) = \frac{N}{K+1}\cdot\left(1 - a^{\frac{K+1}{K}}(Kx+a)^{-\frac{K+1}{K}}\right) \qquad (4.6)$$

In the case of inversed location of doped and undoped parts (boule 4), the expression is:

$$C(x) = N \cdot a^{\frac{K+1}{K}} (Kx + a)^{-\frac{K+1}{K}} \tag{4.7}$$

Finally, using expression (4.5), the interface velocity V_{int} can be calculated as:

$$V_{\text{int}} = V_c + \frac{(L_m(0) - L_m(final))}{d / V_c}, \tag{4.8}$$

where V_c is the crucible translation speed.

4.6.2. Effective doping and homogenization rate

Another hypothesis of the simple model was to consider an instantaneous diffusion of Yb ions. Obviously this is somehow overestimated and this phenomenon takes place at a certain rate we call V_d which can be seen as a "diffusion speed" or a "homogenization rate". Even for very slow translation speeds V_c, the particles will not diffuse completely in the melt and homogeneous distribution will not be achieved easily. The component mixing quality is actually highly related to the melt internal convective process (convective cells speed, size, etc…).

In order to somehow take such phenomenon into consideration, one replace in the differential concentration distribution equation, the initial level N of the doped sector by an effective doping level N_{eff}.

In the simple model, the diffusion was considered instantaneous. The good agreement between experimental data and this model for boule 4 indicates that such hypothesis can actually be considered as true if the crucible is moving slowly enough: $\lim_{V_c \to 0} N_{eff} = N$.

A second limit condition is that when the diffusion rate is very high, we also satisfy our initial hypothesis: $\lim_{V_d \to \infty} N_{eff} = N$. We therefore propose the following expression for the effective doping level inserted in the melt after each new tiny growth translation step:

$$N_{eff} \sim N(1 - e^{-V_d / V_{\text{int}}}) \tag{4.9}$$

The height of the melt obtained from newly incorporated molten starting material is not always identical to the height h of the existing melt. This height impacts the volume, and consequently the number of ions introduced. Moreover the respective densities of solid and liquid phases differ. A volume matching coefficient ζ_{VM} can be introduced to take into consideration this effect, leading to the following expression for the effective doping:

$$N_{eff} = \zeta_{VM} N(1 - e^{-V_d / V_{\text{int}}}), \tag{4.10},$$

where ζ_{VM} is the volume matching coefficient.

A definition of the effective doping N_{eff} can therefore be as follows: it is the doping value of the doped sector in gradient crystals grown by Bagdasarov method if the diffusion in the melt is complete and instantaneous and melt and starting material have the same densities and heights. Having no easy access to the solid and liquid phases respective densities, the matching coefficient is taken equal to unity because it does not significantly change the further logic.

4.6.3. Introducing a more advanced model

The effective doping value can be obtained through experimental curves fitting, N_{eff} being the sole fitting parameter. For the 2nd boule a $N_{eff} \approx 11.5$ at% value was required in order to fit the experimental data (Fig. 4.28). Such low value of effective doping can be related to the fact that the crucible translation rate (and therefore the growth rate) was quite high for Yb:YAG crystals ($V_c = 2.5$ mm/h).

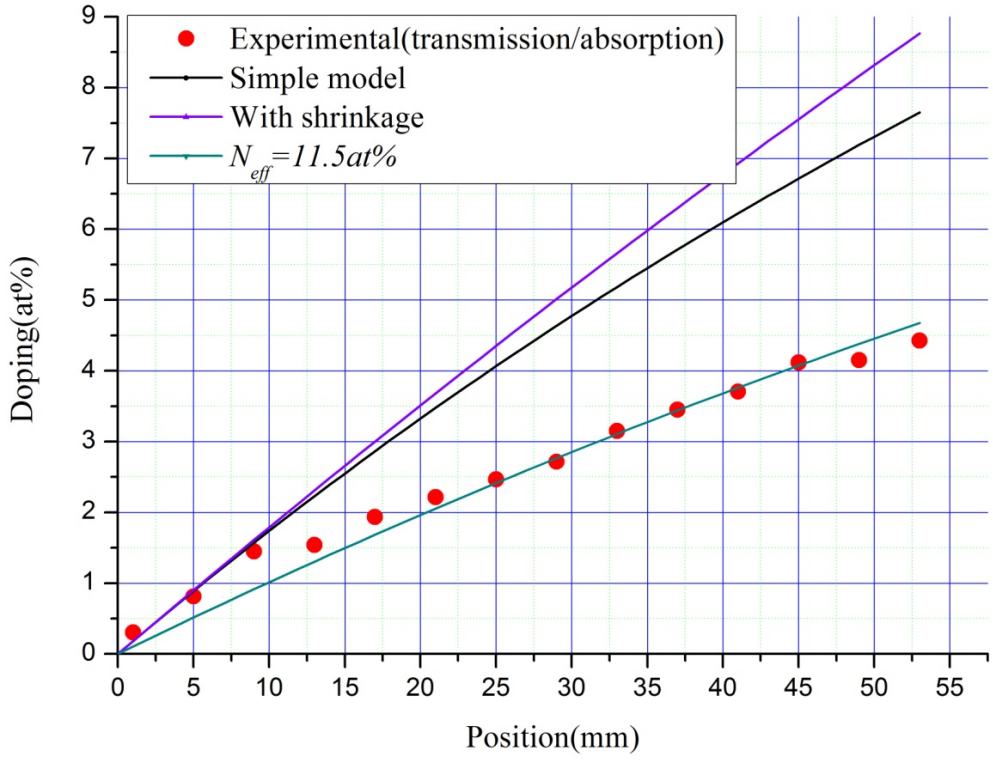

Fig.4.28. Experimentally measured (transmission/absorption method) doping distribution (red dots), versus simple model with (purple line) and without (black line) shrinkage. An 11.5 at% value of effective doping is required in order to fit the experimental data points.

On this graph we also observe that, if L_m shrinkage is taken into consideration (purple curve versus black one), an increase in the expected gradient is observed. This is logical since each new added layer of Yb doped sector will liquefy into a smaller and smaller molten zone within which the Yb ion concentration increase a bit after each step.

For the 4th boule, the relatively low growth speed allows achieving almost complete homogenization of Yb ions within the melt. For this case even shrinkage is not necessary to take into account. Indeed, during the growth process, the temperature adjustment allowed to

keep the crystallization front within the observation window which offers a field of view of about 1.5 cm. Then at worst, 1.5 cm shrinkage might have occurred.

The combined knowledge of Neff and the crucible translation speed V_c, allows us to estimate the homogenization rate for a specific (here for boule 2 with $N = 20$ at%) growth sequence (Fig. 4.29). In this case, $V_c = 2.5$ mm/h, meaning $V_{int} = 3.3$ mm/h when considering equation (4.8). The corresponding curve is therefore the green one on Fig. 4.29. Since N_{eff} has been estimated to be 11.5 at%, we can deduce a homogenization rate V_d around 2.8 mm/h.

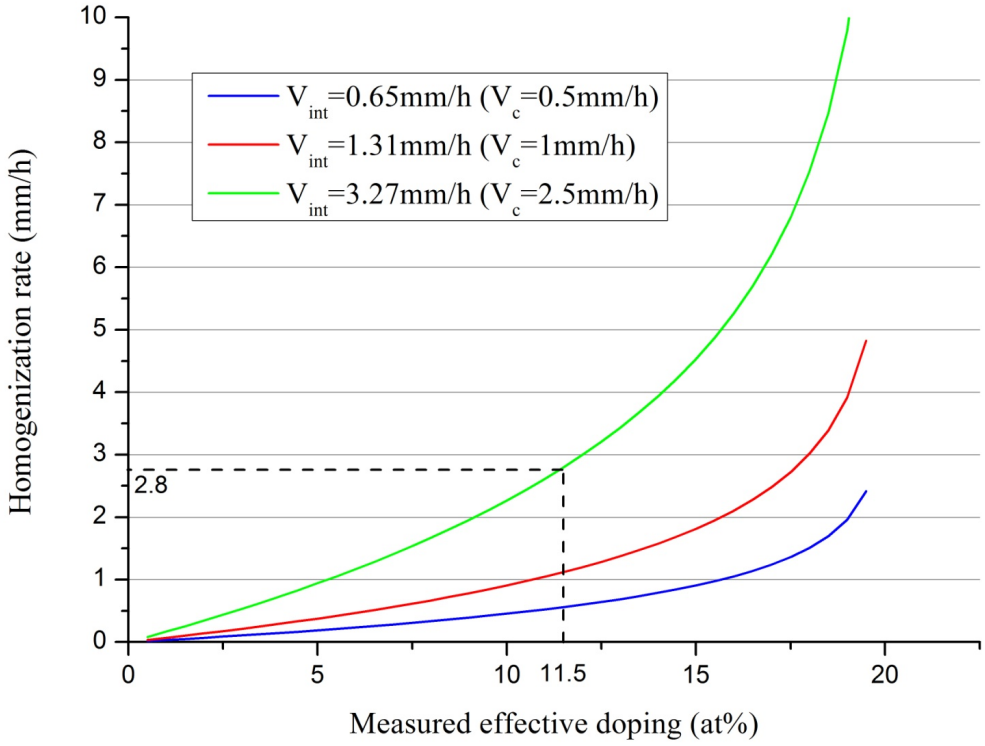

Fig.4.29. Melt doping homogenization rate can be obtained from estimated effective doping Ne and known crucible velocity V_c.

Let us know study the respective impacts of the crucible speed V_c and the homogenization rate V_d. Figure 4.30 shows that, getting closer to the maximum allowable doping level (i.e. $N = 20$ at%) at a reasonably slow diffusion speed, would request to slow down the crucible speed (jumping from the green to the blue curve).

Another way to look at this is illustrated on Fig. 4.31 where we see that increased crucible speed put further away any hope to reach a high level of doping ion in the resulting crystal.

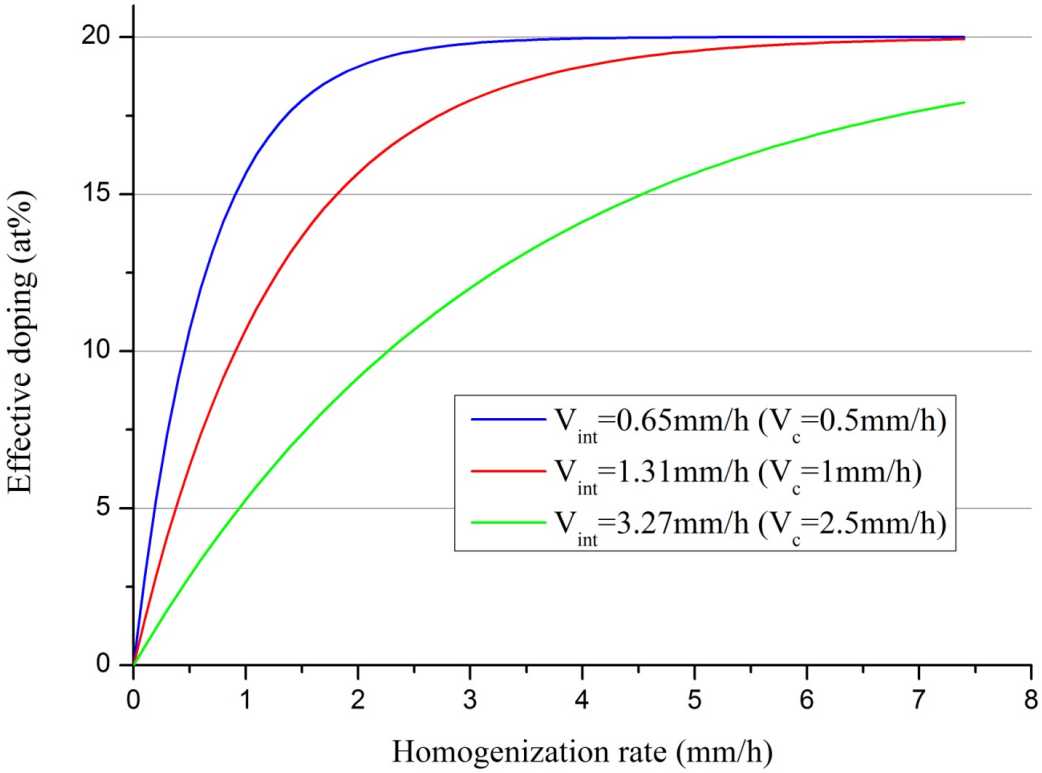

Fig.4.30. Effective doping versus Yb ion homogenization rate for three different crucible velocities (0.5, 1 and 2.5 mm/h)

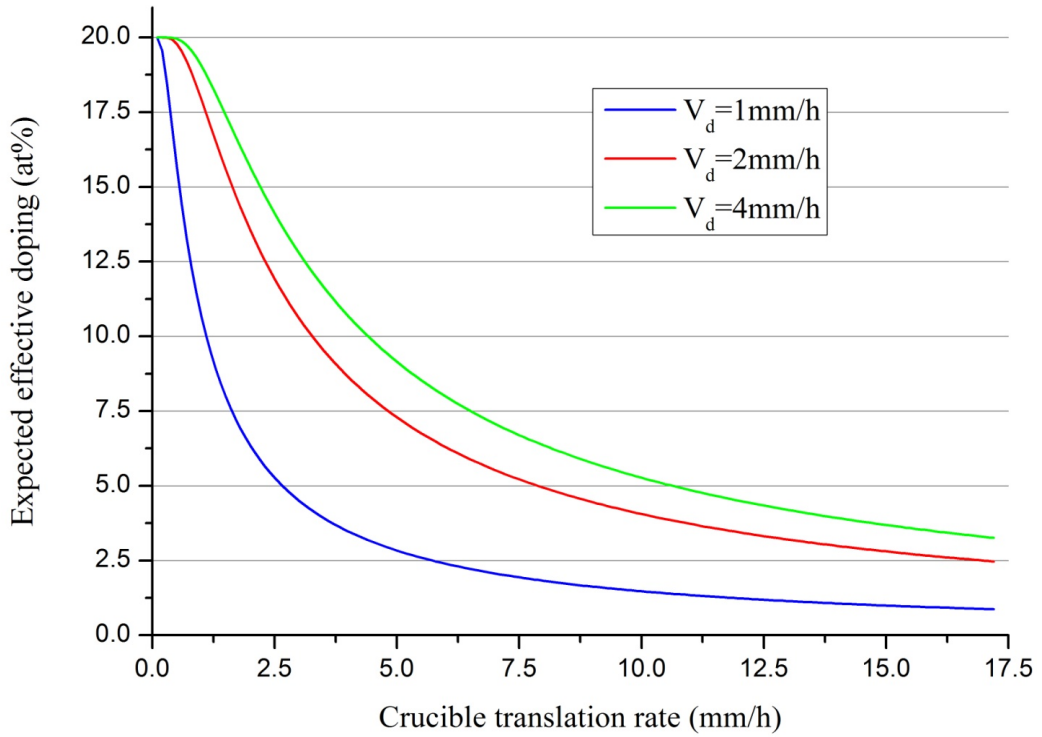

Fig.4.31. Effective doping versus crucible velocity for three different Yb ion homogenization rates (0.5, 1 and 2.5 mm/h)

4.7. Crystallization front orientation

For both the simple and the advanced models, we assumed that the crystallization front was always a plane perpendicular to growth direction. This is an idealized case. During a real growth process, the crystallization front never exhibits such orientation. The associated mechanisms and explanations are given in the previous chapter; in this section, we will concentrate more on experimental illustration of the fact that the crystallization front is actually exhibiting a shape not as simple as first considered. We indeed had access to a quite complete tridimensional doping level mapping for one of the grown crystal. It provided quite reliable information about crystallization front orientation. Fig. 4.32 illustrates most common possibilities for crystallization front orientation.

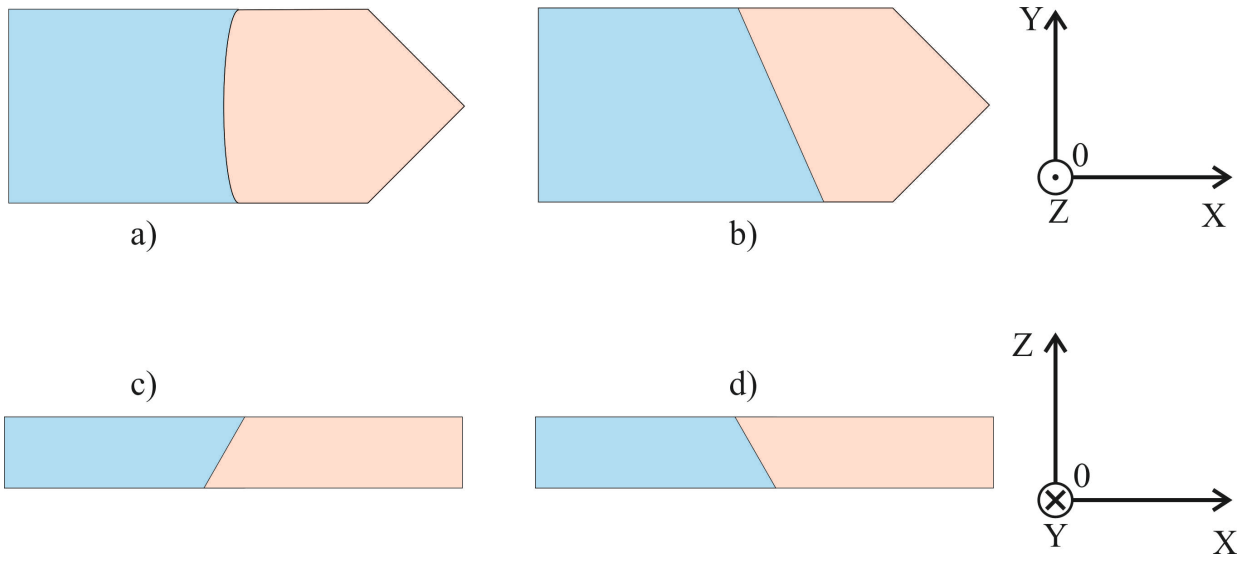

Fig.4.32. Most common orientations for crystallization front: top view (*a* and *b*), and side view (*c* and *d*).

All these cases can be observed by measuring the doping distribution in the relevant direction. The direction *X* is parallel to the growth direction, i.e. along the desired doping distribution gradient. The existence/absence of any gradient in *Y* direction is related to a front orientation like displayed on the cases *a* and *b* of Fig. 4.32. The vertical inclination of the crystallization front can be detected by observing the doping distribution along the Z direction. Several combinations of these cases are theoretically possible and only c and d cases are mutually exclusive. Tridimensional mapping of the grown boule allows reconstructing the front geometry at any position, i.e. at any moment of the growth process.

The curvature (Fig. 4.32a) of the crystallization front almost always exists with a radius of curvature evolving during the growth. It is nevertheless significant only at the beginning of the boule (triangular part), the end of the boule and more pronounced near the lateral edges (interface between the boule and crucible). The effect of this curvature does not play any major role for gradient doping crystal growth because:

- the starting material is distributed in such a way, that we do not obtain any doping variations in the triangular part,
- the crystal layers near the lateral edges and the tail are discarded.

So practically speaking, one should not observe any doping variation in Y direction in our extracted samples.

Trivalent Yb ion concentration in all three directions has been measured by the EPMA technique for a 10x10x12 mm^3 sample extracted from the 2nd boule (Fig. 4.33).

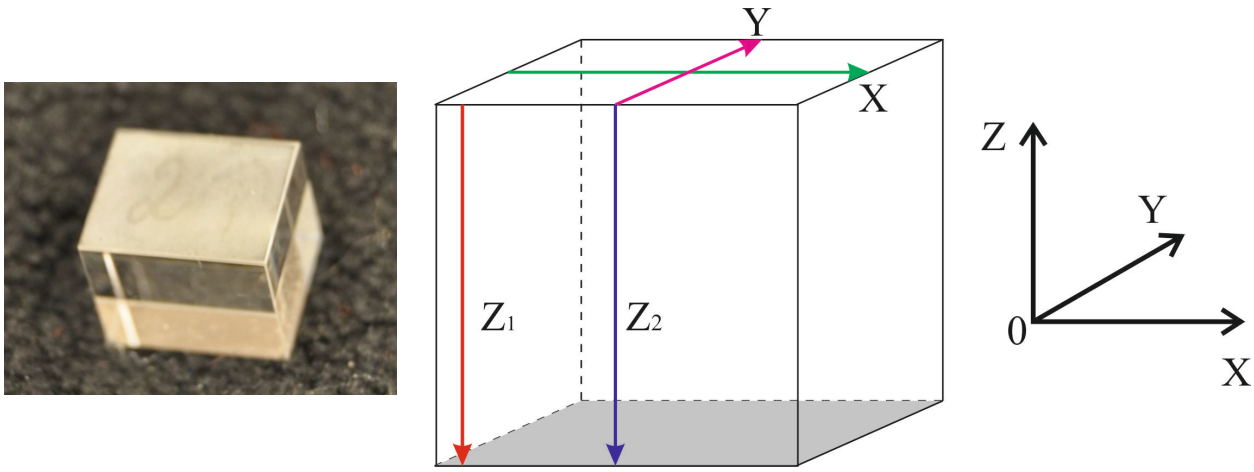

Fig.4.33. Picture (left) and schematic representation (right) of the extracted sample. Colored arrows indicate lines along which measurements were performed. The coordinate system is equivalent to the one presented on the Fig. 4.32

Fig. 4.34 gives Yb ion doping distributions along *X* and *Y* directions. The measurement along the Y direction clearly indicates that the crystallization front stays parallel to this axis. A 1 at%/cm pretty linear gradient is observed along the *X* axis. The intersection of both set of experimental points reveals that the *Y* measurements were recorded on a line at an $x = 5$ mm distance from the edge.

Fig. 4.35 illustrates the doping distribution along the *Z1* and *Z2* axes shown on Fig. 4.33. A non negligible (~0.5 at%/cm) variation is revealed which shall be related to an inclination of the crystallization front.

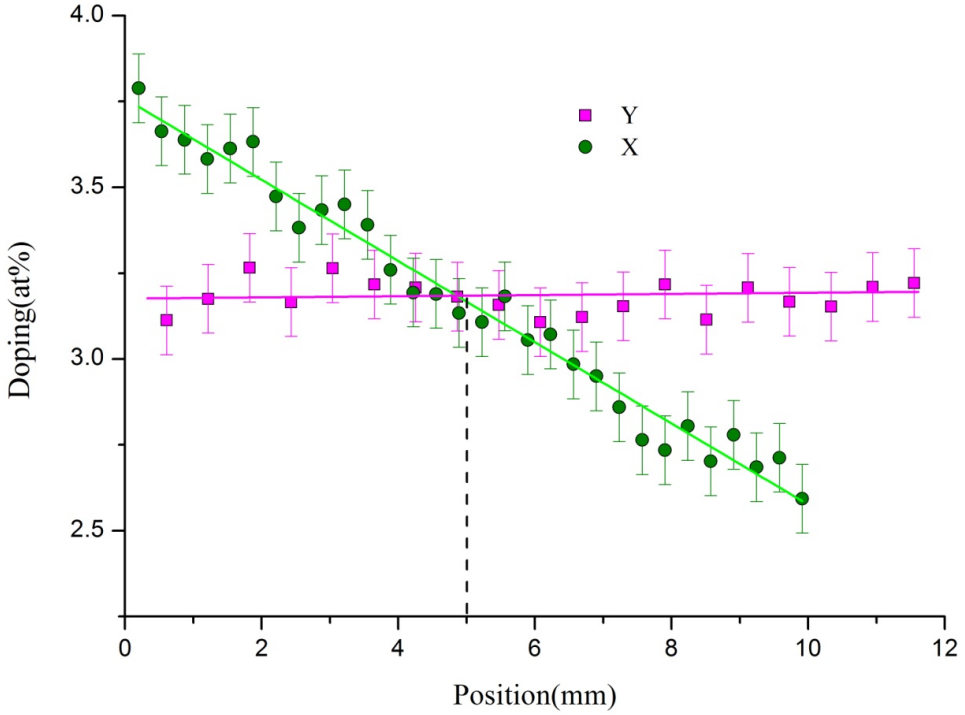

Fig.4.34. Yb doping distribution alongside *X* (green) and *Y* (magenta) axes. The doping level is quite homogeneous in Y direction and was recorded approximately at x = 5 mm, i.e. the middle of the sample.

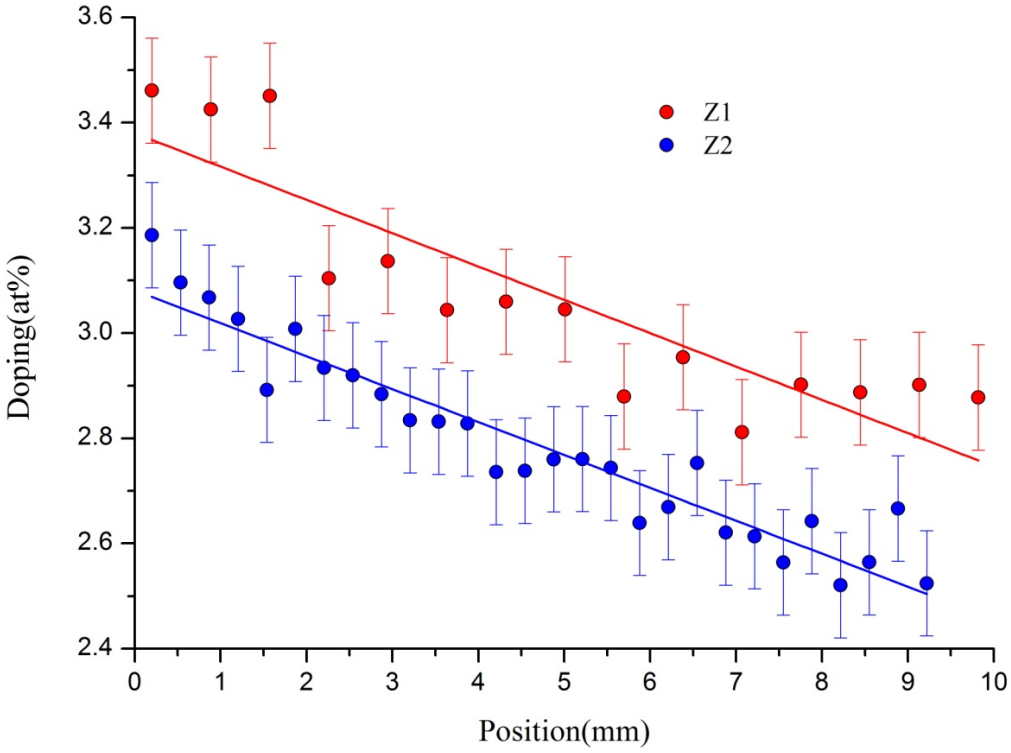

Fig.4.35. Doping distribution alongside *Z1* (red) and *Z2* (blue) axes. The variation of doping level clearly refers to the inclination of growth front. The starting values are in a good accordance with the data measured along *X* axis.

Considering linear fits, the generalized doping spatial distribution can be derived as:

$$A(x,z) = (2.88 \cdot 10^{-4} x - 6.43 \cdot 10^{-2}) z - 0.12x + 3.76 \qquad (4.11)$$

Using expression (4.11), the doping value at any point of the sample can be obtained. Figure 4.36 gives a doping distribution map in the *Oxz* plane. We observe iso-doping curves with a 35° inclination for this 1 cubic centimeter sample. These lines are footprints of the crystallization front.

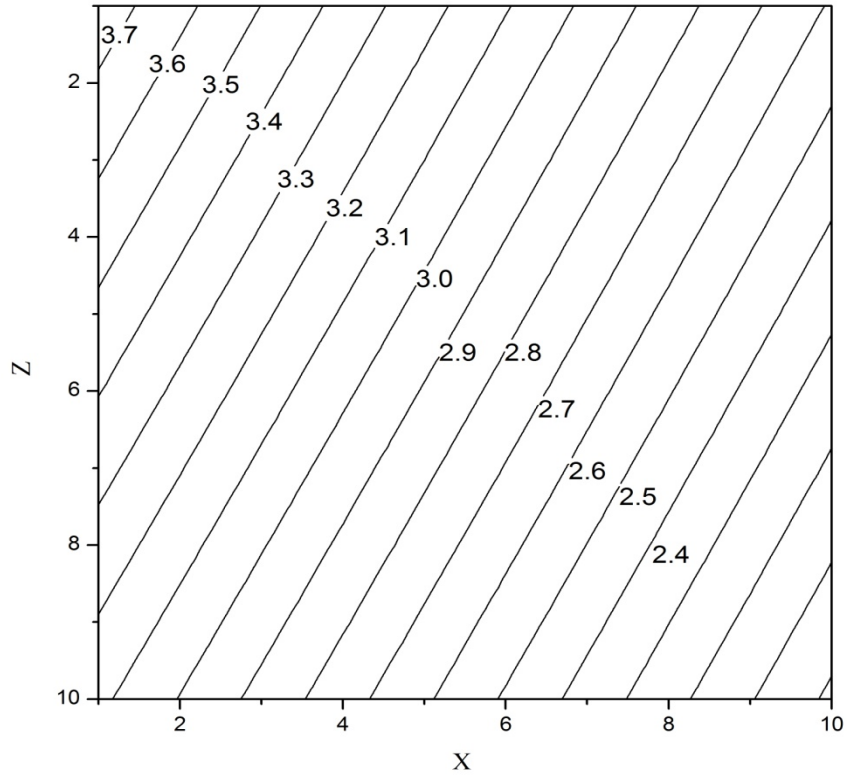

Fig.4.36. Doping distribution map in the Oxy plane the boule 2 cubic centimeter sample

4.8. References

[4.1] Furuse H., Kawanaka J., Miyanaga N., Chosrowjan H., Fujita M., Takeshita K., and Izawa Y., "Output characteristics of high power cryogenic Yb:YAG TRAM laser oscillator", Optics Express, Vol. 20, Issue 19, pp. 21739-21748 (2012)

[4.2] Taira T., "RE^{3+}-Ion-Doped YAG Ceramic Lasers", IEEE Journal of Selected Topics in Quantum Electronics, (2007)

[4.3] Dong J., Ueda K., Yagi H., Kamisnkii A., Cai Z., "Comparative study the effect of Yb concnentrations on laser characteristics of Yb:YAG ceramics and crystals" Laser Phys. Lett. 6, No. 4, 282–289 (2009)

[4.4] Taira T., "Domain-controlled laser ceramics toward Giant Micro-photonics" Optical Materials Express, Vol. 1, Issue 5, pp. 1040-1050 (2011)

[4.5] Ikesue A., Kinoshita T., Kamata K., Yoshida K., "Fabrication and Optical Properties of High-Performance Polycrystalline Nd:YAG Ceramics for Solid-State Lasers" Journal of the American Ceramic Society, Volume 78, Issue 4, pages 1033–1040, (2005)

[4.6] Lee H.C., Brownie P. Messiner E., "Diffusion bonded composites of YAG single crystals"*Proc. SPIE* 1624, Laser-Induced Damage in Optical Materials: 1991, 2 (July 29, 1992)

[4.7] Tsunekane M., Tafuchi N., Kasamatsu T., Inaba H., "Analytical and experimental studies on the characteristics of composite solid-state laser rods in diode-end-pumped geometry" IEEE Journal of Selected Topics in Quantum Electronics, (2007)

[4.8] Liu Q, "Corner-pumped Yb:YAG slab laser emitted up to 1 kW" Applied Physics Letters (2006)

[4.9] Meissner et al., "Composite solid state lasers of improved efficiency and beam quality" US patent, Patent number 5 563 899

[4.10] Wang X.D., Zhao Z.W., Xu X.D., Wang J.Y., Bourdet G., Chanteloup J.C. "Bonding quality of Yb:YAG/YAG composite crystals" Science in China Series E Technological Sciences

[4.11] Mukhin I.B., Perevezentsev E. A., Palashov O.V., "The New Technique Of Thermal Bonding For Composite Active Elements Fabrication", in Laser Optics - 2012, p. ThR1-27

[4.12] Kucera M.,Nitsch K., Nikl M., Daniš S., Hanuš M., "Growth and properties of epitaxial Ce-doped YAG and LuAG films for scintillators" (2010) *Journal of Physics.: Conference. Series.* **249** 012020

[4.13] Townsend P.D., “Optical effect of ion implantation” *Reports on Progress in Physics.* **50** 501

[4.14] Chani V.I., Boulon G., Zhao W., Yanagida T, Yoshikawa A., Correlation between Segregation of Rare Earth Dopants in Melt Crystal Growth and Ceramic Processing for Optical Applications” Japanese Journal of Applied Physics 49 (2010) 075601

[4.15] Bagdasarov Kh.S. “Fiziko-ximicheskie osnovi visokotemperaturnoy kristallizacii i metodi virashivaniya monokstallov” Moscow

[4.16] Wilhelm R., Freiburg D., Frede M., Kracht D., “End-pumped Nd:YAG laser with a longitudinal hyperbolic dopant concentration profile” Optics Express, Vol. 16, Issue 24, pp. 20106-20116 (2008)

[4.17] Wilhelm R., Frede, M., Kracht, D., “Power Scaling of End-Pumped Solid-State Rod Lasers by Longitudinal Dopant Concentration Gradients” IEEE Journal of Quantum Electronics, (2008)

[4.18] Wilhelm R., Freiburg D., Frede M., Kracht D., Fallnich C., “Power scaling of diode end-pumped Nd:YAG lasers via multi-segmented rods” In proceeding of Conference on Lasers and Electro-Optics, 2005. (CLEO), Volume: 1

[4.19] Xu X., Zhao Z., Zhao G., Song P.X., Xu J., Deng P. “Comparison of Yb:YAG crystals grown by Cz and TGT method”, Journal of crystal growth 257 (2003) 297-300

[4.20] Lukanina M.A., Hodosevitch K.V., Kalaev V.V., Semenov V.B., Sytin V.N., Raevsky V.L., “3D numerical simulation of heat transfer during horizontal direct crystallization of corundum single crystals” Journal of Crystal Growth Volume 287, Issue 2, 25 January 2006, Pages 330–334

[4.21] Mayer M., “Rutherford back scattering spectrometry” Lestures given at the Workshop on Nuclear Data for Science and Technology: Materials Analysis, Trieste, Italy, 19-30 May 2003

[4.22] Rubin S., Passell T.O. and Bailey E., Analytical Chemistry 29 (1957)736

[4.23] Tesmer J.R., Nastasi M., “Handbook of Modern Ion Beam Materials Analysis” Materials Research Society, Pittsburgh, Pennsylvania, 1995

[4.24] Boulon G., Laversenne L., Goutaudier C., Guyot Y., Cohen-Adad M.T. “Radiative and non-radiative energy transfers in Yb3+-doped sesquioxide and garnet laser crystals from a combinatorial approach based on gradient concentration fibers” Journal of Luminescence 102–103 (2003) 417–425

[4.25] Petermann K., Huber G., Fornasiero L., Kuch S.,Mix E., Peters V., Basun S.A. “Rare-earth-doped sesquioxides”, Journal of Luminescence 87-89 (2000) 973-975

5. Doping distribution impact on pumped gain medium

Measuring the Yb^{3+} spatial concentration distribution is one important step to validate the HDC technique ability to produce controlled gradient doped crystals (chapter 3). But, ultimately what really matters in terms of laser physics is the impact over the gain spatial distribution when pumping from one side along the gradient direction as illustrated on figure 2.3 of chapter 2. A dedicated experiment was set up to explore this point (section 5.1). After successfully fitting the collected experimental data, the developed model (described in annex) was use to simulate expected gain distributions if both room temperature and cryogenic Lucia amplifiers were filled with gradient doped crystals.

The heat load distribution along the gradient axis (as illustrated on figure 2.13) is the subject of Section 5.2. Finally, performances of such gain medium in a laser cavity are studied (section 5.3).

5.1. Gain distribution

5.1.1. Sample crystal analysis

Fluorescence imaging is chosen as a simple way to have access to the gain distribution. The fully characterized 10x10x12 mm^3 crystal extracted from the 2nd boule (Fig. 3.35) is used for this experiment. It is pumped at 940 nm while fluorescence is recorded in a transverse direction as depicted on the experimental setup (Fig. 5.1).

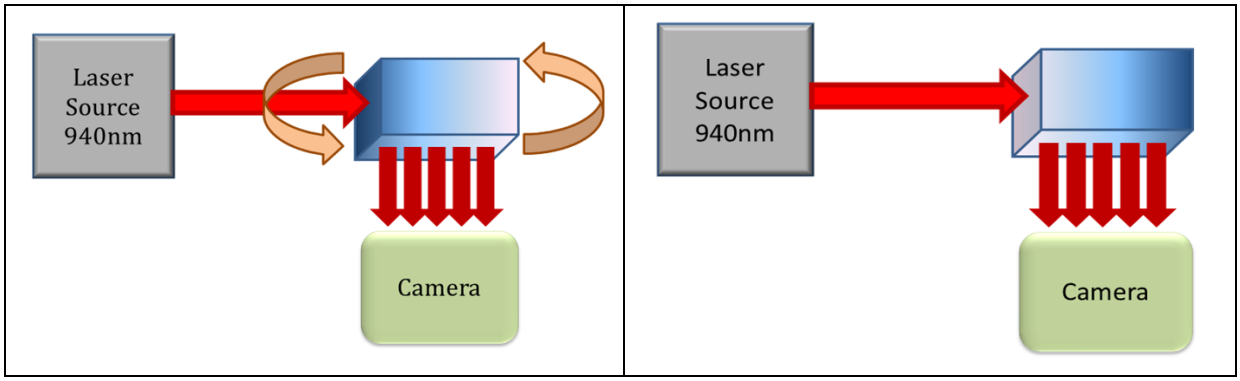

Fig.5.1. Experimental setup for fluorescence measurement. The crystal is pumped along counter-gradient direction (left), and gradient direction (right). The fluorescence is recorded through a CCD camera in the transverse direction

The 13.2 mW pumping power is delivered with a Lynx Sacher Lasertechnik, PilotPZ 500 laser. The CW laser beam diameter is around 1 mm, leading to an average intensity below 2 W/cm^2. It travels through the crystal at a depth of about 1mm below the imaged face. Fluorescence images recorded for both crystal vs. pump laser relative orientations are given in Fig. 5.2

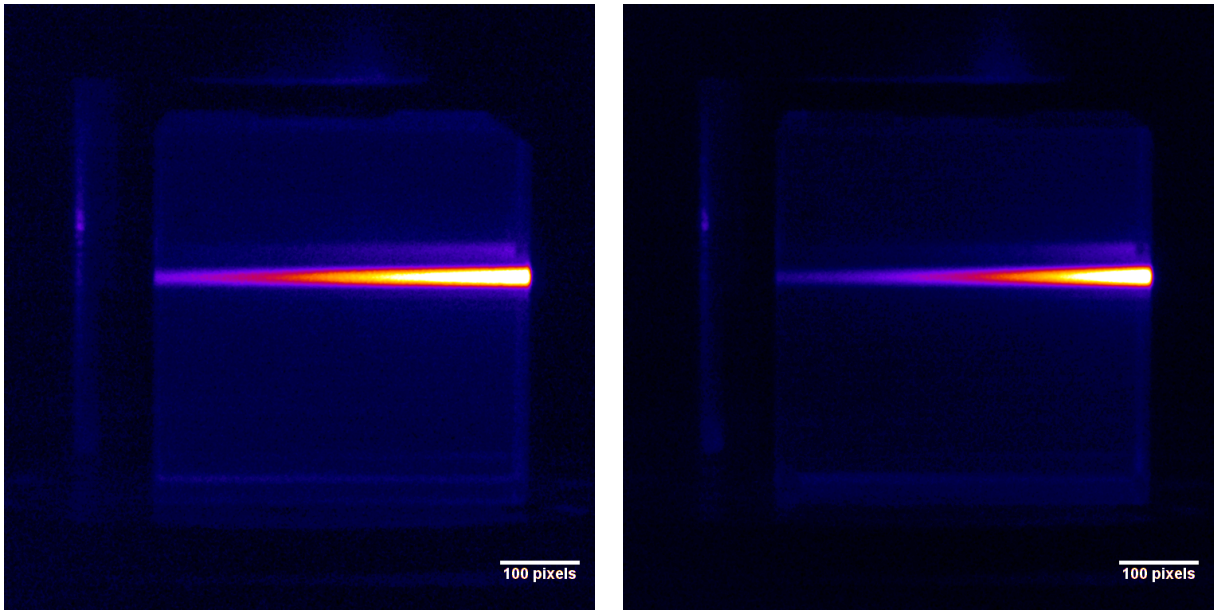

Fig.5.2. Left image illustrates the fluorescence signal recorded when the pump laser enter (right side) the crystal through its low doped face. The right image was obtained after rotating the crystal by 180° so that the laser beam hits the crystal highly doped face

The location of the laser beam within the crystal is shown on Fig.5.3. The EPMA Yb^{3+} distribution map appears in red. The pump beam enters the crystal at a location where the doping level is around 2.2 to 2.3 at% whereas it exits it where the doping reaches 3.4 to 3.5 at%.

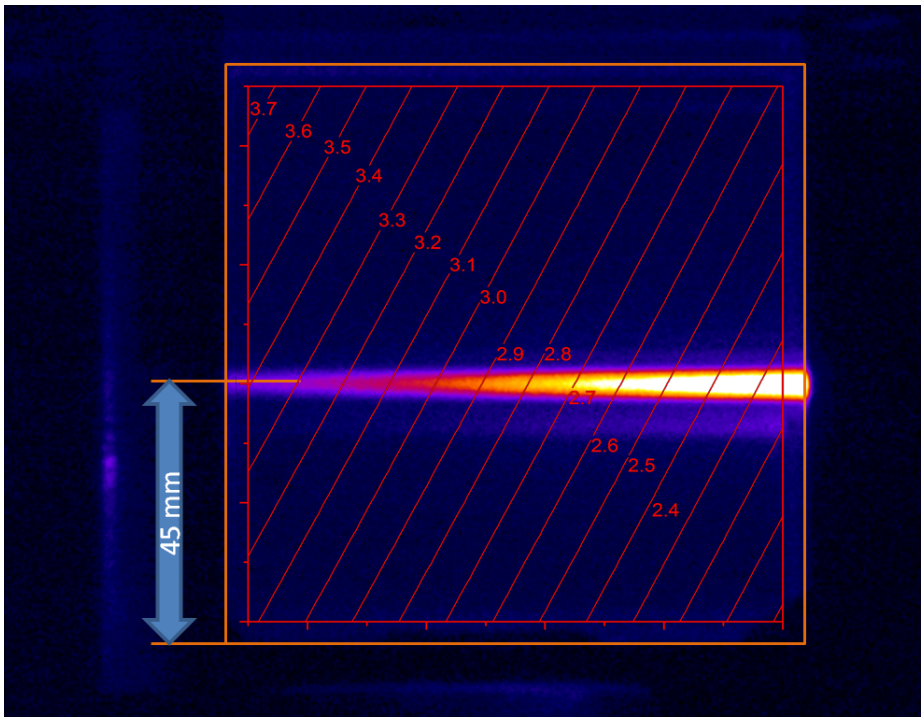

Fig.5.3. The location of the pump beam within the studied 10x10 mm crystal with respect to the 9x9 mm doping map obtained by EPMA analysis

Fig. 5.4 displays lineouts of both experimental data of figure 5.2. A clear fluorescence intensity distribution difference can be observed when the crystal is pumped along the same or the opposite direction of the doping gradient.

In Chapter 2, section 2.3, we have presented a model able to give the distribution of $N_{up}(x)$, the population density in the upper laser state as a function of the position within the crystal. It can be fed with any Yb^{3+} concentration distribution but considering a linear distribution appears sufficient to match experimental results. Let us then introduce the following expression for the doping distribution: $d(x) = d_0 + g.(x-L/2)$, where d_0 [at%] stands for the average doping, g [at%/cm] for the gradient and L is the crystal length. On Fig. 5.4, the recorded fluorescence profiles are compared to the model where $d_0 = 2.75$ at% and $L = 1$ cm have been considered. The sole adjusting parameter left was the gradient value g. The error signal between experimental data and the model was minimized when $g = 0.9$ at%/cm, i.e. for an Yb^{3+} distribution varying linearly between 2.3 and 3.2 at%/cm. Such gradient is in quite well accordance with the 2.2-2.3 to 3.4-3.5 at% value recorded with EPMA measurement.

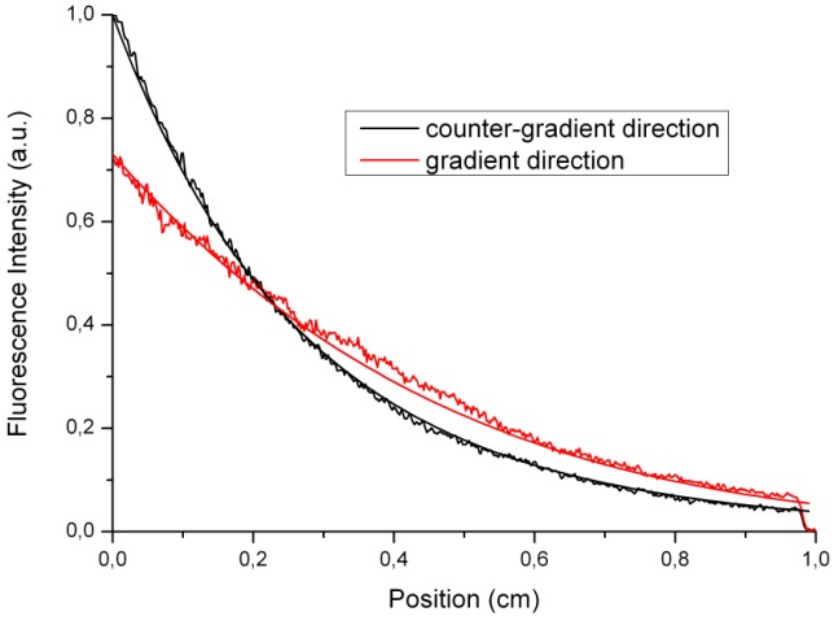

Fig.5.4. Experimental (noisy curves) and modeled (smooth curves) fluorescence distribution of a 1 cm long crystal. Experimental curves are obtained from lineout extracted from picture of fig. 5.2 whereas modeled curve are obtained with a linear doping distribution where $d_0 = 2.75$ at%, $g = 0.9$ at%/cm and $L = 1$ cm

We nevertheless conclude that, with this specific crystal and the laser power available for this experiment, even if the $g = 0.9$ at%/cm gradient allows a more homogeneous gain distribution, it is not yet sufficient to flatten the gain as illustrated on figure 2.3.

Using the same model as in Fig. 5.4, calculated $N_{up,g}(x)$ distribution expected for different g (0, 0.9, 1.9, 2.9, 3.9, 4.9 and 5.3 at%/cm) but the same $d_0 = 2.75$ at% are given on Fig. 5.5. The curve corresponding to our experimental fluorescence data is plotted in red.

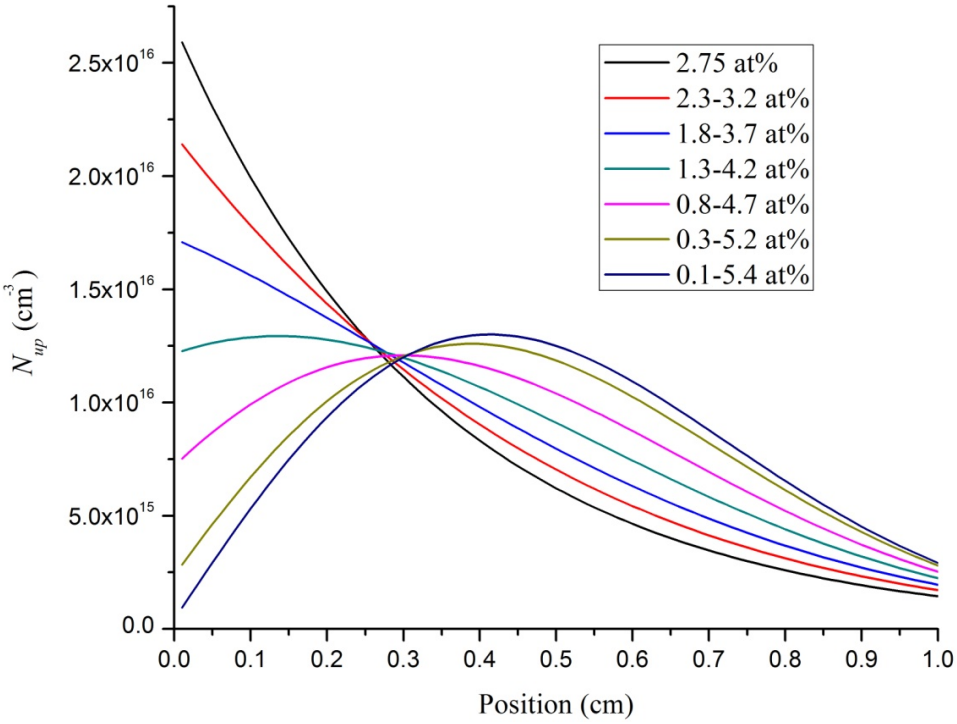

Fig.5.5. $N_{up,g}(x)$ distributions for 7 different gradients g (0, 0.9, 1.9, 2.9, 3.9, 4.9 and 5.3 at%/cm) in a 1.3 W/cm² pumped 1cm long YAG crystal which average Yb^{3+} concentration is 2.75 at%. Normalization is performed for the black curve (constant doping $g = 0$)

Although it still appears impossible to flatten $N_{up,g}(x)$ along this 1 cm long crystal, one can nevertheless identify a nominal gradient g_n for which the N_{up} contrast $C=(N^{max}-N^{min})/(N^{max}+N^{min})$ is minimized. $C(g)$ is displayed on figure 5.6 while keeping the same color reference as in figure 5.5.

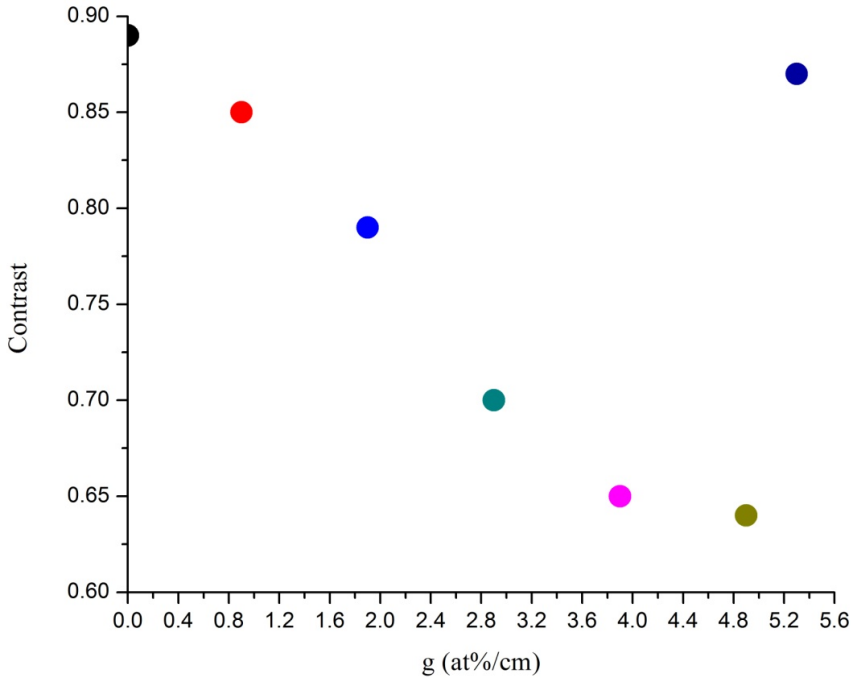

Fig.5.6.Contrast $C = (N^{max}-N^{min})/(N^{max}+N^{min})$ versus gradient g for a L = 1cm long, d_0 = 2.75 at% crystal

The worst case is constant doping for which $C = 0.89$. The best homogenization of N_{up} is achieved for $g = 3.9$ to 4.9 at%/cm doping gradient (pink and brown curves on figure 5.5), where C<65%. Fig.5.7 gives $C(g,I_p)$, a contrast map for different pumping intensities I_p and gradients g (we keep a 1 cm long crystal of 2.75 at% average doping value). The horizontal dash line corresponds to our maximum pump intensity (<2 W/cm²). The vertical dash line corresponds to our $g = 0.9$ at%/cm gradient. The intersection between these lines defines the vicinity of our point of operation.

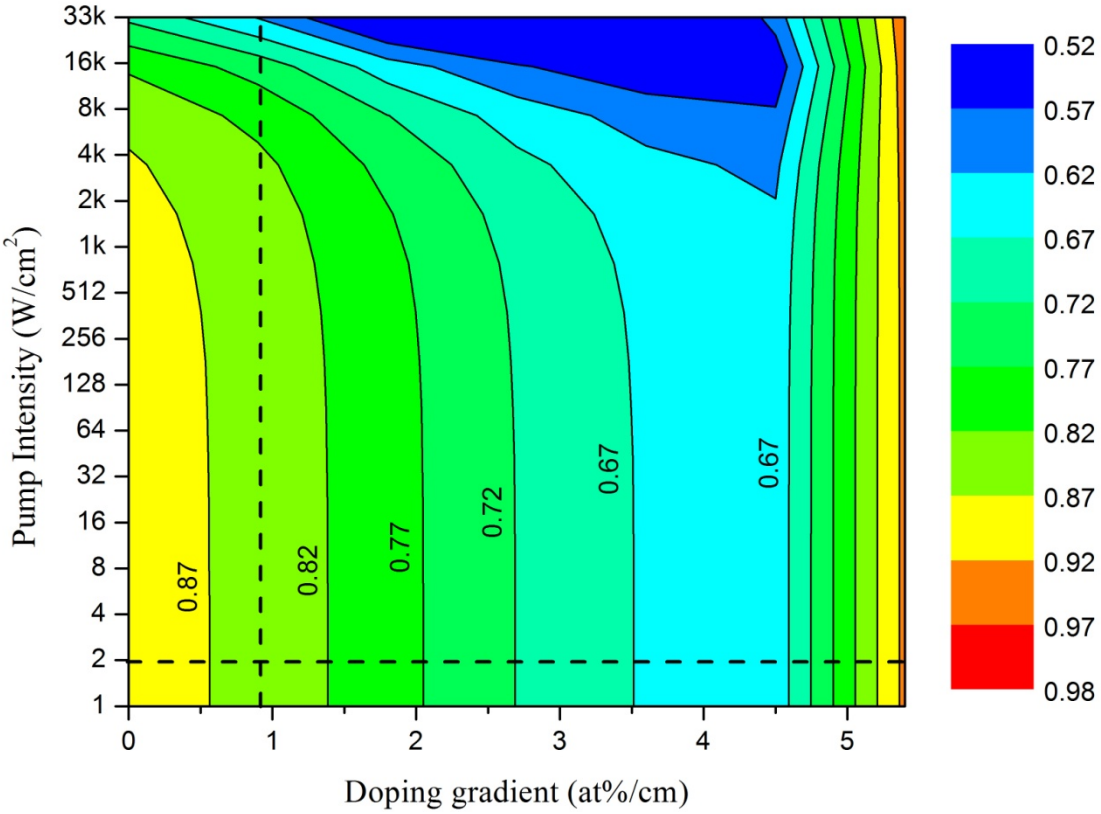

Fig.5.7. Upper state population density contrast map $C(g,I_p)$ for different pumping intensities I_p and gradient g (L = 1 cm long crystal of 2.75at% average doping value)

For the pump regime the crystal was operated in, the best achievable contrast would be around 65% providing a 4 at%/cm gradient (assuming a 2.75 at% average doping level in a 1cm long crystal) would have been available.

In this section, a very specific case corresponding to our experimental conditions was analyzed. Deriving any optimal gradient would be strongly related to the crystal length and pump power. We shall nevertheless state that this experimental case demonstrates our ability to achieve a more homogeneous population inversion with our gradient doped crystal: $C = 0.85$ instead of 0.89 for a 2.75 at% constant doped crystal.

The gradient distribution will provide a more homogeneous distribution of small signal gain offering advantages in ASE management. As it is shown in second chapter, the ASE issues are more stringent in the first layers near the pumped face of the gain media. With the gradient the small signal gain is reduced in this area, but it does not affect the overall amplification due to the gain increase along the rest of the amplification path.

5.1.2. Lucia configuration study

The Lucia laser chain is currently operating a room temperature (300 K) amplifier. A second amplifier head designed to work at a temperature within the 100-200 K range will be activated in the coming months. In both case, the gain medium is a circular disk which thickness and doping level were optimized for a constant Yb^{3+} distribution. I propose in this section to explore the optimum gradient doped crystal which could advantageously replace both disks. Considered cross sections are the followings:

Table 5.1: Cross sections @300K

σ_{abs_l}	Laser absorption cross section = $1.1\ 10^{-21} cm^2$
σ_{em_l}	Laser emission cross section = $2.4\ 10^{-20} cm^2$
σ_{abs_p}	Pump absorption cross section = $7.6\ 10^{-21} cm^2$
σ_{em_p}	Pump emission cross section = $2.2\ 10^{-21} cm^2$

Table 5.2: Cross sections @160K

σ_{abs_l}	Laser absorption cross section = $5.8\ 10^{-22} cm^2$
σ_{em_l}	Laser emission cross section = $5.7\ 10^{-20} cm^2$
σ_{abs_p}	Pump absorption cross section = $1.3\ 10^{-20} cm^2$
σ_{em_p}	Pump emission cross section = $9.75\ 10^{-22} cm^2$

5.1.2.1. *Room temperature case*

Lucia room temperature operated amplifier is 7 mm thick and 2 at% doped. Maximum pump intensity is 16 kW/cm². The disk is 60 mm wide but pumped over a surface (see figure 5.8) limited by:

- the 26 mm height pump delivery optical system output
- a 30 mm diameter ASE management mask

The maximum dimension L_{ASE} to be considered is then 30 mm. Considering the limit introduce for $g_0.L_{ASE} \leq 4$ in section 2.3.2, we obtain a maximum small signal gain value $g_{0,max} = 1.33\ cm^{-1}$. The exploration was performed within the following ranges:

- a doping mean value d_0 varying between 0 and 4 at%
- a doping ramp varying between 0 and 8 at% over the 7 mm thick disk (the maximum associated gradient being therefore equal to 11.4 at%/cm)

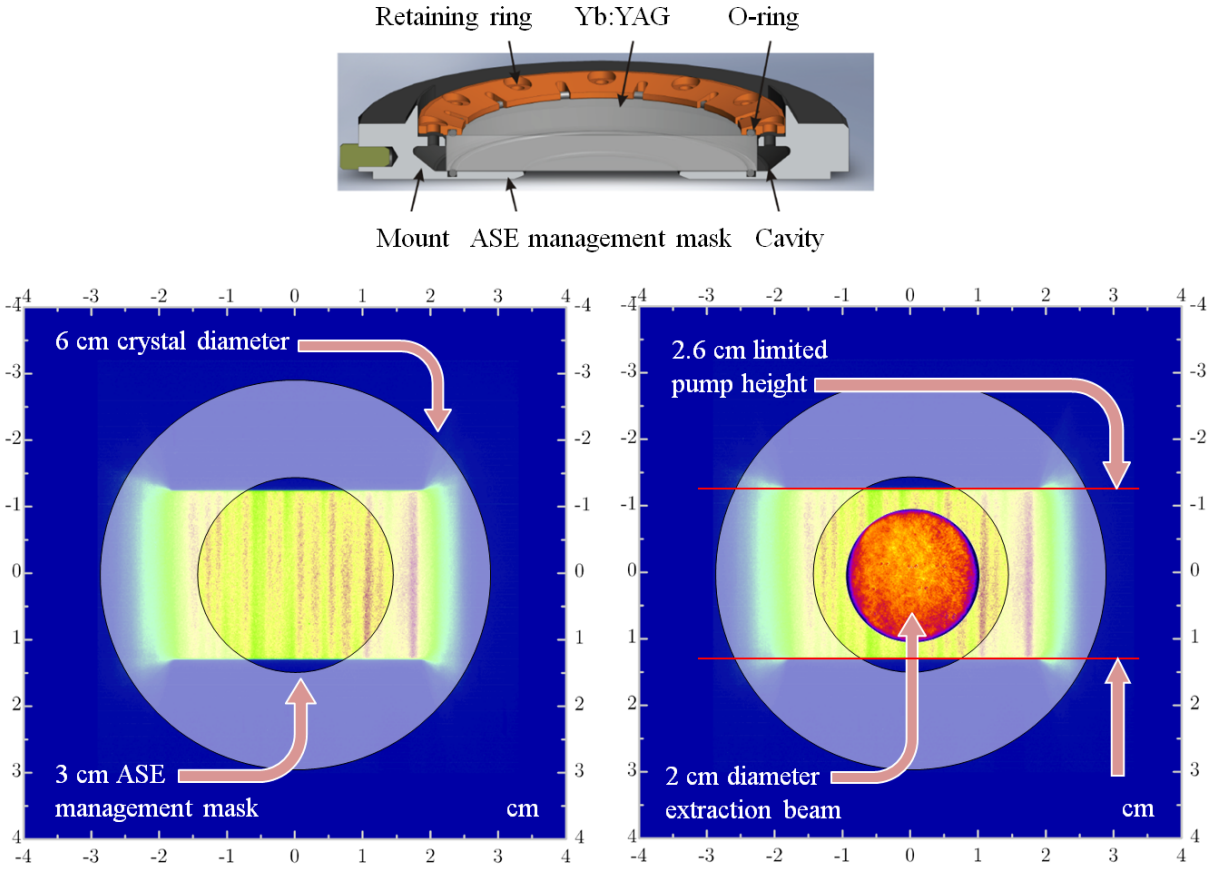

Fig.5.8. The background of both bottom pictures is the pump light distribution exiting the pump light delivery optical system (about 26x50 mm²). The amount of light reaching the 60 mm gain medium is limited by the 30 mm circular aperture crystal mount (top sketch). The 3 mm spaced 20 mm x 22 mm elliptical extraction beam footprints are also displayed on the right picture. The peripheral cavity around the YAG is designed to host an absorbing liquid if required for improved ASE management

At Lucia working point coordinates (0 at%/cm, 2 at%), the stored energy density is 9 J/cm². Figure 5.9 gives the stored energy density (J/cm²) map for the explored region. The iso-energy density 9 J/cm² line is materialized on the map: as expected, it is almost independent of the doping ramp. It defines a boundary below which Lucia room temperature energetic performances would not be satisfied.

This map was obtained without considering ASE losses. In practice, increasing the doping mean value far above 2 at% would actually not lead to a continuous increase of the stored energy density because at some point the gain medium will start seeing its gain being depleted by ASE related deleterious effects. We have defined such threshold while introducing $g_{0,max} = 1.33\ cm^{-1}$. A maximum gain value map was then derived to identify the safe operation area within the explored region. For each (doping ramp, mean doping) point, a maximum gain observed along the 7 mm thick crystal was recorded: the resulting map is given on figure 5.10.

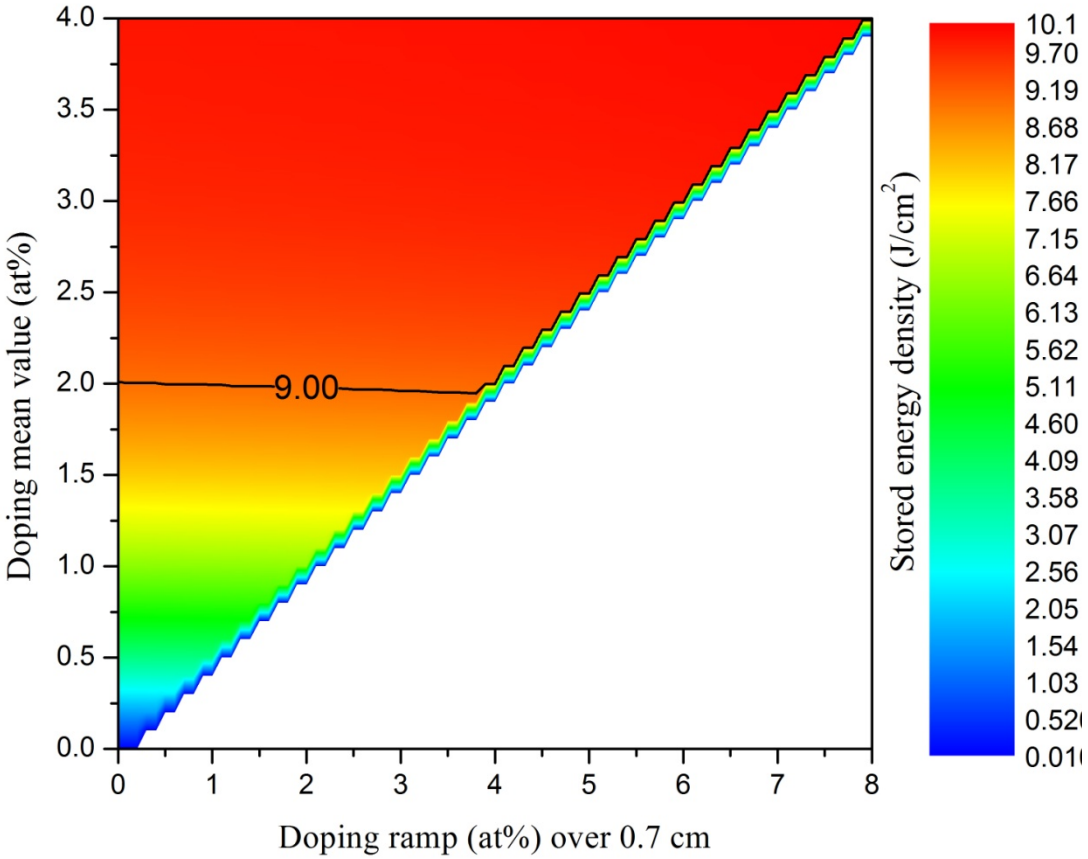

Fig.5.9. Stored energy density map versus doping ramp and mean value: for each specific doping ramp, a minimum average doping value exists below which this doping ramp is not defined: this explains the map white triangular area. The iso-energy density 9 J/cm² line above which the requested energetic performances will be reach is drawn

On this map, the 1.33 cm^{-1} threshold iso-gain curve (solid back) is reported together with the 9 J/cm² iso-energy density line, the first one defining an upper boundary and the second one the lower frontier of a small optimum region (dashes). The insert gives an enlarged vision of the Area of Interest (AoI) within which this optimum region falls. Lucia current operating point is marked with the blue circle (1.73 cm^{-1}) whereas the optimum one is marked in yellow (1.29 cm^{-1}).

In a similar approach to the one described on fig. 5.6, let us introduce a gain contrast $Cg_0 = (g_0^{max} - g_0^{min})/(g_0^{max} + g_0^{min})$. The map of figure 5.11 gives Cg_0 distribution. As a reference, the AoI rectangle is also displayed as well as the 9 J/cm² iso-energy density line and both current and optimum points. We observe a very low contrast for the optimum point, 2.4%, a situation noticeably better than the current contrast of 27%.

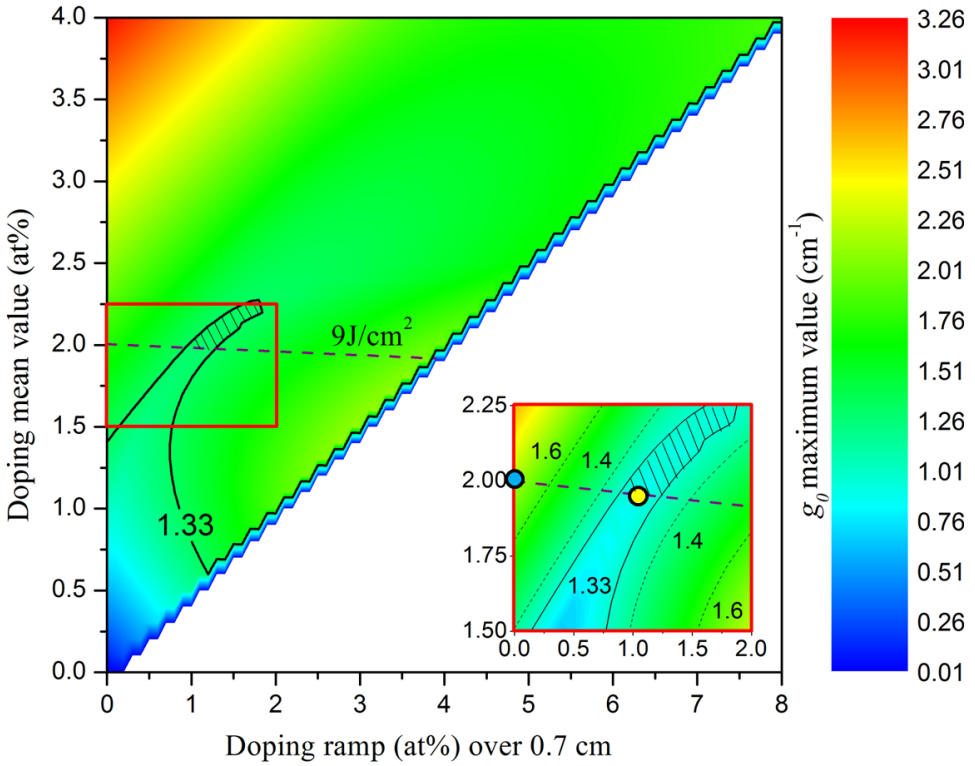

Fig.5.10. Max gain map vs. doping ramp and mean value. 1.33 cm^{-1} threshold iso-gain curve is drawn in solid back. Below this value, ASE triggered parasitic oscillation are expected to be severely limited, guaranteeing a satisfying efficiency for the amplifier. The iso-energy density 9 J/cm² line is also drawn (dashed purple line). The bottom right insert gives an enlarged vision of the area of interest

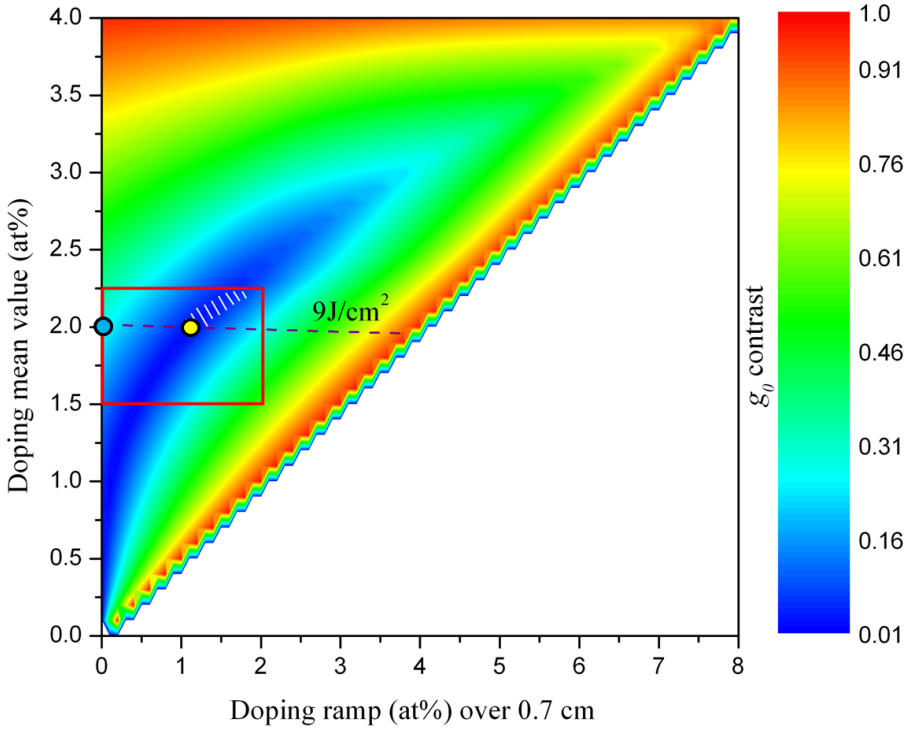

Fig.5.11. Gain contrast Cg_0 vs. doping ramp and mean value. Red rectangle gives the AoI. Iso-energy density 9 J/cm² line is the dashed purple line. The optimum region is white dashed. Lucia current operating point is marked with the blue circle (27%) and the optimum one is marked in yellow (2.4%)

For both current and optimum points, the gain spatial distribution is given in figure 5.12. It indeed reveals a strong improvement in terms of contrast from 27% down to less than 3%

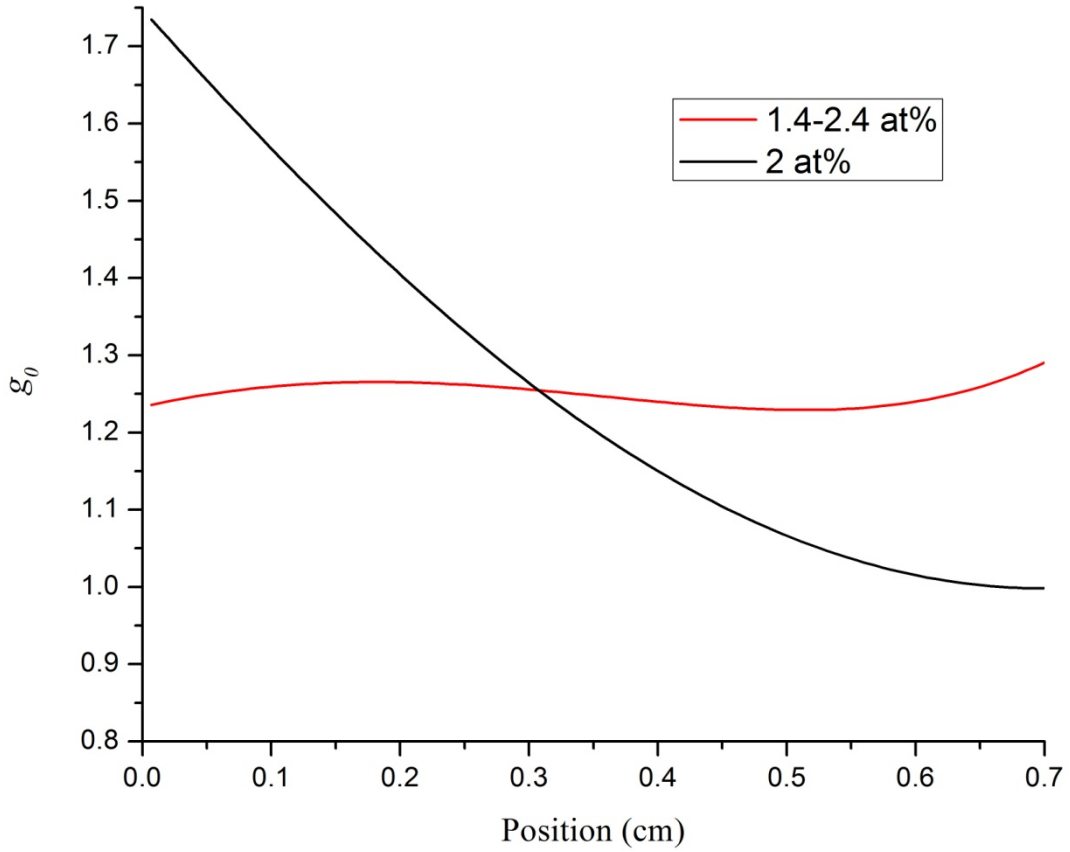

Fig.5.12. Small signal gain distribution over the 7 mm thick crystal for the current 2 at% constant doped crystal (black) and optimum 1.9 at% average / 0.9 at%/cm gradient crystal (red)

This study was performed for a 7 mm thick gain medium like the currently used Lucia gain medium. Another aspect the model allows studying concerns the optimum thickness. As mention in chapter 2, reducing the gain medium volume can be a critical engineering advantage when designing multi kJ laser facilities. This is clearly not a relevant consideration at the scale of a laboratory laser chain like Lucia. But the positive impact in terms of front surface temperature and internal temperature gradient is of interest. Figure 2.13 was already illustrating this effect by comparing two 7.5 mm thick crystal. Figure 5.13 compares the current Lucia 300 K amplifier crystal temperature profile with a thinner 6 mm gradient doped crystal.

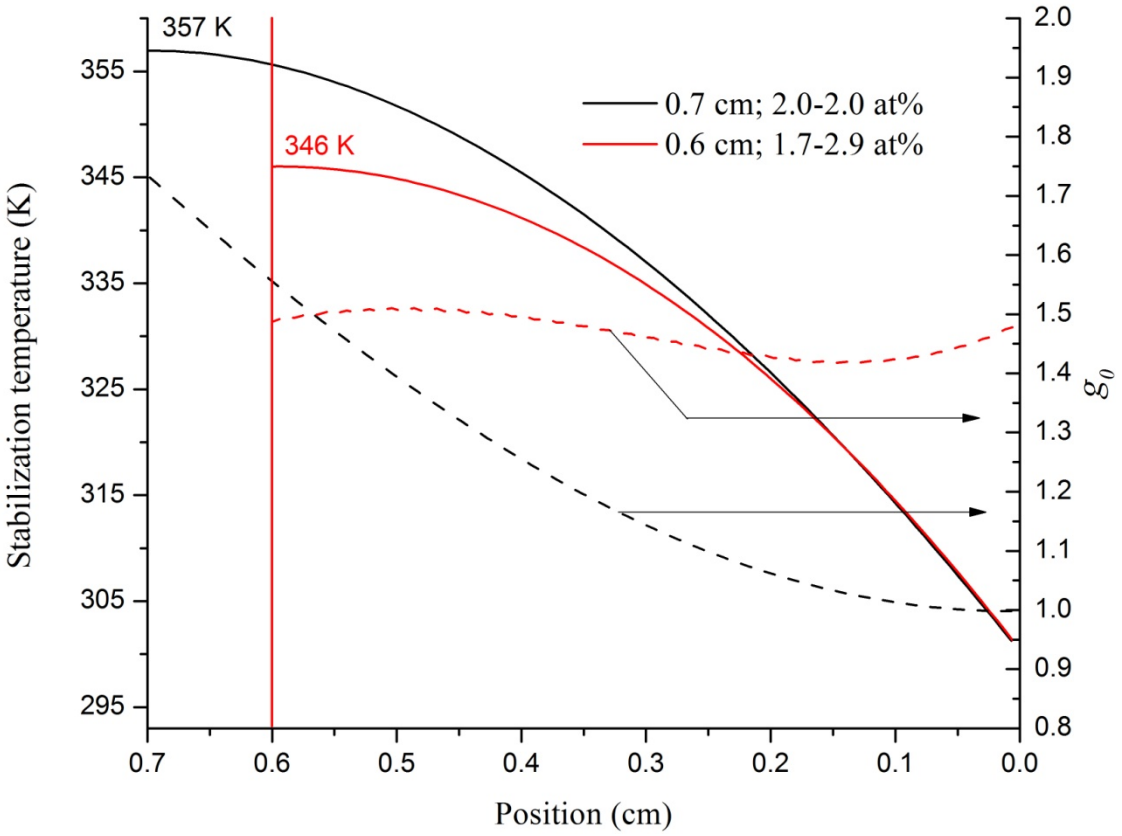

Fig.5.13. Temperatrue (bold curve, left scale) and gain (dashed curve, right scale) distributions for a 6 mm (red) and a 7 mm (black) crystal. The first one is uniformly doped at 2 at% while the thin one carries a 1.7 to 2.9 at% gradient

5.1.2.2. *Cryogenic temperature case*

Lucia cryogenic amplifier is 10 mm thick and 1 at% doped. Maximum pump brightness is 5.5 kW/cm². The disk is 77 mm wide but pumped over an 23.4 mm x 30.3 mm elliptical surface, leading to a $g_{0,max} = 1.32$ cm^{-1} similar to the previous 300 K case. At Lucia working point coordinates (0 at%/cm, 1 at%), the stored energy density is 3.3 J/cm². Figure 5.14 gives the stored energy density (J/cm²) map for the explored region. The iso-energy density 3.3 J/cm² line is materialized on the map: as expected, it is very slightly decreasing with the doping ramp. It defines a boundary below which Lucia cryogenic energetic performances would not be satisfied. We can observe that this boundary is set on the edge of an energy density plateau culminating at a 3.5 J/cm² energy density as materialized by the 3.4, 3.42 and 3.44 J/cm² iso-energy density curves.

Like for 300 K case, a maximum gain value map was derived to identify the ASE compatible area (Fig. 5.15).

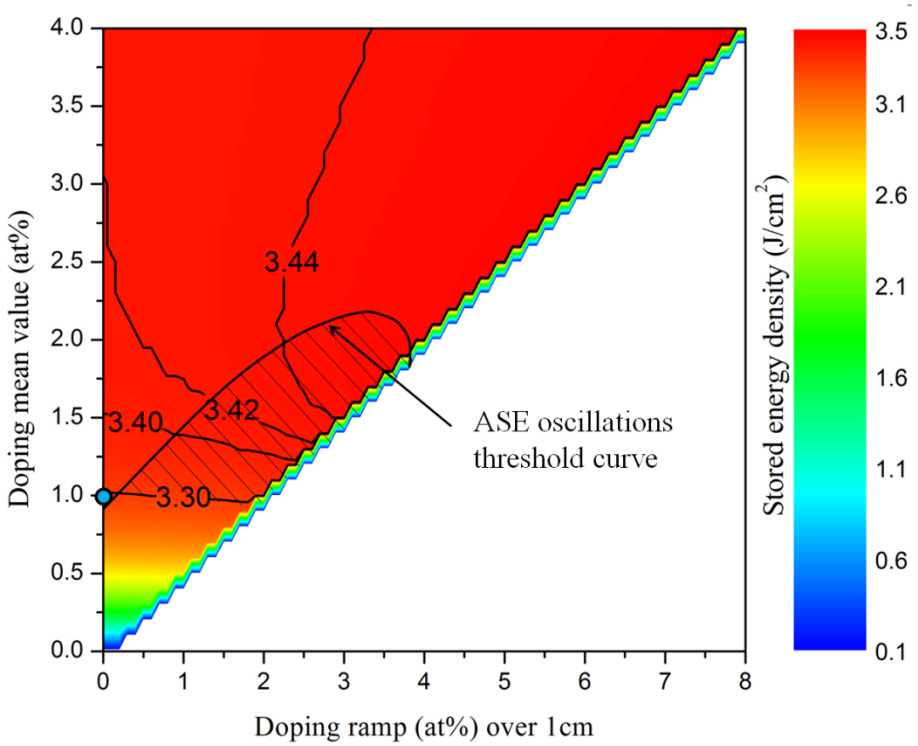

Fig .5.14. Stored energy density map versus doping ramp and mean value. The iso-energy density 3.3 J/cm² boundary above which the requested energetic performances will be reach is drawn. Lucia cryogenic amplifier operating point is marked with the blue circle (0,1). The optimum region (dashed) is defined by an upper boundary obtain from Fig. 5.15

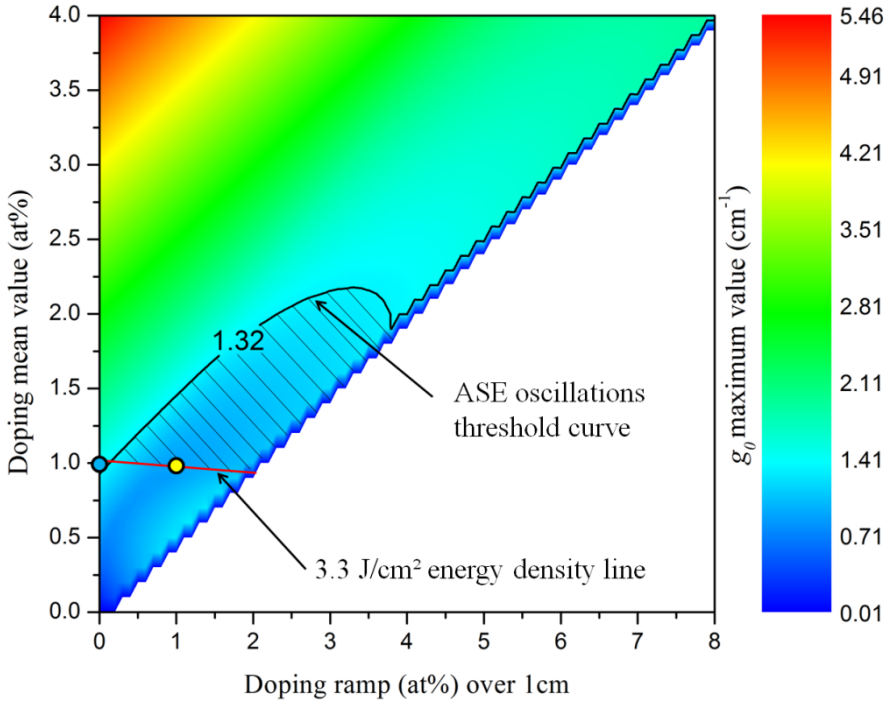

Fig.5.15. Maximum gain map vs. doping ramp & mean value. The 1.32 cm^{-1} threshold iso-gain curve is drawn in solid back. Below this value, ASE triggered parasitic oscillation are expected to be severely limited, guaranteeing a satisfying efficiency for the amplifier. The iso-energy density 3.3 J/cm² line is also drawn (purple line). The dashed area limited by these two curves defines the optimum region. The yellow circle is located at the lowest gain position along the 3.3 J/cm² energy density line

On this map, the 1.32 cm^{-1} threshold iso-gain curve (solid back) is reported together with the 3.3 J/cm² iso-energy density line, the first one defining an upper boundary and the second one the lower frontier of the optimum region (dashes). Since Lucia cryogenic amplifier was designed to satisfy the $g_0.L_{ASE} \leq 4$ criteria as close as possible, the associated blue circle obviously fall in the vicinity of the 1.32 cm^{-1} curve: its value is 1.41 cm^{-1}. With respect to ASE, a more optimum point marked in yellow can be identified where the maximum gain falls to 0.88 cm^{-1}. On the other hand, to maximize the stored energy, one would prefer to select a point located at the other extremity of the optimum region but, as can be seen on figure 5.14, the energy density is not evolving a lot over this area.

The map of figure 5.16 gives the Cg_0 distribution. As for the 300K, we observe a 10% contrast for the optimum point, a situation also noticeably better than the current contrast of 46%.

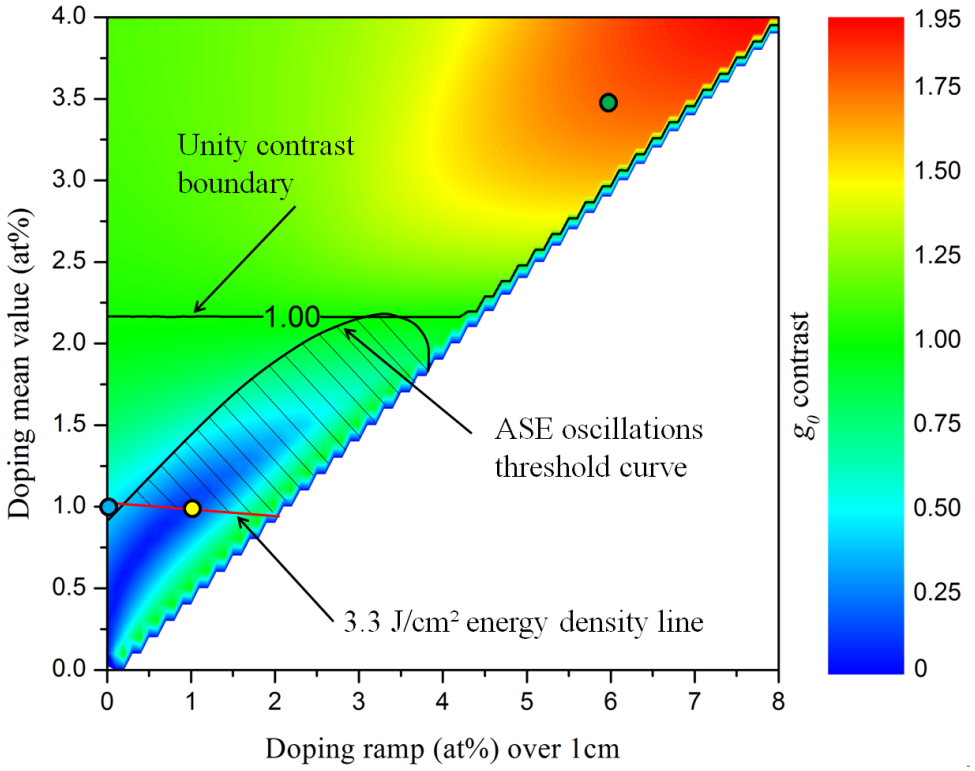

Fig.5.16. Gain contrast Cg_0 versus doping ramp and mean value. The dashed optimum region was defined on Fig. 5.15. The unity contrast line define the frontier of doping domains where the minimum gain become negative due to strong 1030 nm absorption (d_0>2.2at%)

At first sight, it can be surprising to observe that, above a 2.2 at% average Yb^{3+} concentration, we enter into a greater-than-100%-contrast regime for the gain. In order to explain this phenomenon, let us consider a specific point located where Cg_0 reaches a value above 150%: the green circle of (6 at%/cm, 3.5 at%) coordinates. Such 1 cm crystal would present a 0.5 at% doped entrance face to the pumping beam while the cooled side will carry a 6.5 at% concentration as illustrated on figure 5.17 (blue dashed line with the right scale). As references, the 1 at%/cm yellow optimum point crystal gradient is also displayed (0.5% to 1.5 at% red dashed line) as well as the 1 at% constant doping distribution (back dashed line).

The three bold curves give the associated gain distributions within the 1 cm crystals thicknesses. As expected the red gain curve is very flat with a 10% contrast and the black Lucia cryogenic amplifier curve illustrates the 46% contrast resulting from the stronger population inversion located at the pumped face of a constant doped crystal. The blue gain distribution shows that a strong population inversion takes place 2 to 3 mm after the pump entrance face of the (6 at%/cm, 3.5 at%) crystal. For such a high average doping level (3.5 at%), this crystal is too thick. Indeed, the last 3 mm of the crystal are actually absorbing (negative gain) the 1030 nm light. This negative gain area is grayed out on the graph. Having such a negative minimum value for the gain explains why the contrast (as defined) exceeds the 100% value.

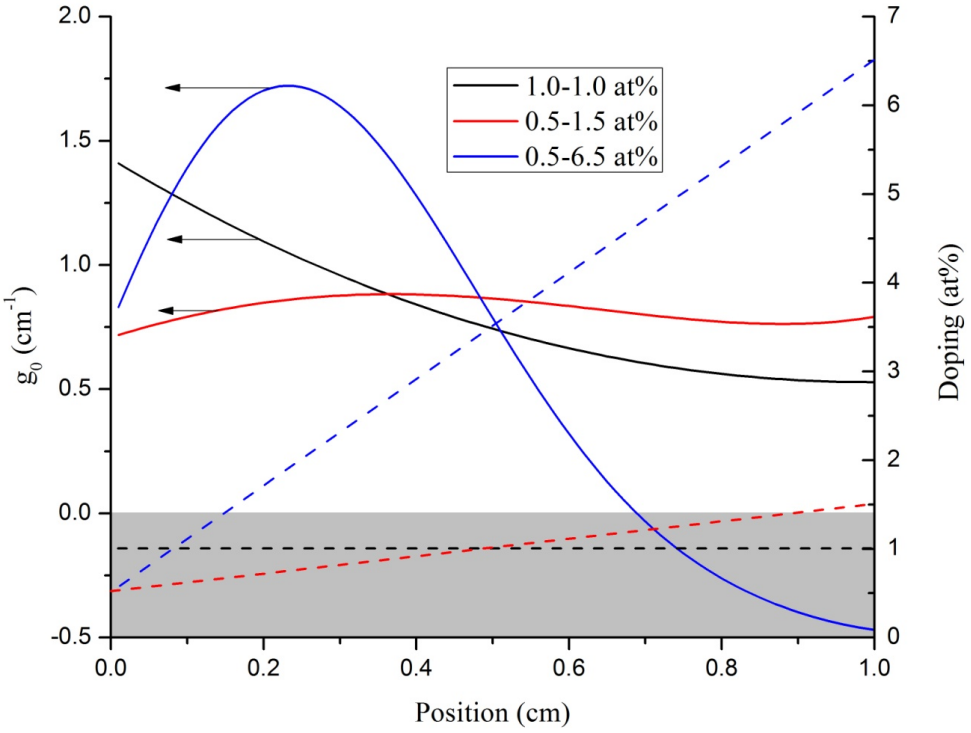

Fig.5.17. Gain (bold curves, left scale) and Yb^{3+} concentration (dash lines, right scale) distributions within three 1 cm thick crystals. Respective extreme doping values are given in the insert. The grayed out bottom area defines the negative gain location

Higher values of stored energy might be achieved by choosing the appropriate combination of pump power, doping mean value and doping ramp. This obviously influences also the storage efficiency (η_s). Table 5.3 compares the current configuration (1st column) based on a 1 at% constant doping gain medium with alternative solutions offered by gradient doped gain media. To obtain the values presented in the table, the $g_0 < 1.33$ cm^{-1} ASE limitation was imposed and the crystal thickness was kept at 1 cm (no thickness optimization is performed this time). By increasing the pump power, one can increase the stored energy density, while never exceeding a local gain above 1.33 cm^{-1}, by choosing the appropriate doping distribution. Increasing the pump intensity above 9 kW/cm^2 does not significantly improve the stored energy density due to the imposed limitation ($g_0 < 1.33$ cm^{-1}). The stored energy efficiency reaches a 62.7% optimum for 6 kW/cm^2 pump power and a crystal of 0.3 – 3.3 at% linear doping distribution. The stored energy amount can be significantly increased from 3.29

up to 4.78 J/cm^2 by increasing the pump power to 8 kW/cm^2 while keeping the 59.8% efficiency of the constant doped case value. The doping gradient necessary for this case is only $g = 1.1$ at%/cm, a value already achieved with HDC and easier to obtain than the 3 at%/cm of the previous case. It should be kept in mind that any pump power increase is related to major investments in laser diodes. Considering the cost of already commissioned Lucia pump sources, getting an extra 8 kW/cm^2 pump power would cost an additional 60 k€. The thickness of the crystal could also be reduced, but such optimization would make sense in order to achieve better cooling efficiency. And considering that the current cryo-cooling system is highly effective, this optimization does not really seem useful.

Table 5.3: Energetic improvement for cryogenic amplifier

Pump intensity (kW/cm2)	5.5	6	6.5	7	8	9
Stored energy density (J/cm2)	3.29	3.76	4.06	4.34	4.78	4.9
Storing efficiency (ηs)	59.8%	62.7%	62.5%	62.0%	59.8%	54.4%
Doping mean value (at%)	1	1.8	1.6	1.4	1	0.7
Doping gradient (at%)	0	3	2.4	2	1.1	0.3
Pumping system cost addition (k€)	0	16	32	48	60	92

5.2. Thermal load distribution

A somehow rather similar experiment was set up at the *Charles Fabry* Laboratory of the *Institut d'Optique Graduate School* in order to look at the same crystal thermal behavior under much stronger pump conditions. The crystal is indeed pumped this time with an 800 µm diameter 80 W CW laser beam delivered by a fiber coupled laser diode (400 µm diameter, 0.22 NA). Transverse thermal luminescence is observed through an IR camera (FLIR Systems Thermovision A40). The crystal is in contact with two water cooled copper heat sinks on both its horizontal faces (Fig. 5.18).

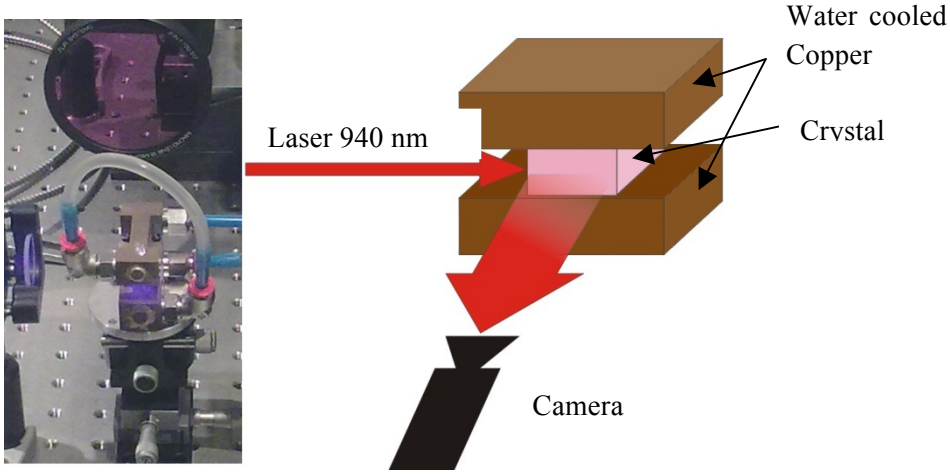

Fig.5.18. Experimental set-up for IR imaging. The HDC grown crystal under test is sandwiched between 2 copper heat sinks through which water is circulating. A 940 nm CW laser beam travels through the crystal while the front surface temperature distribution is monitored with an IR camera

Images of Fig. 5.19 give 4x11 mm² aperture views of the heat distribution on the observed lateral surface for two different relative orientations of the crystal and the laser beam. The entrance and exit faces of the crystal can be localized at the transition of the deep blue area of the pictures on (room temperature air around 300 K). The distance between these transitions (10 mm) gives the picture scale.

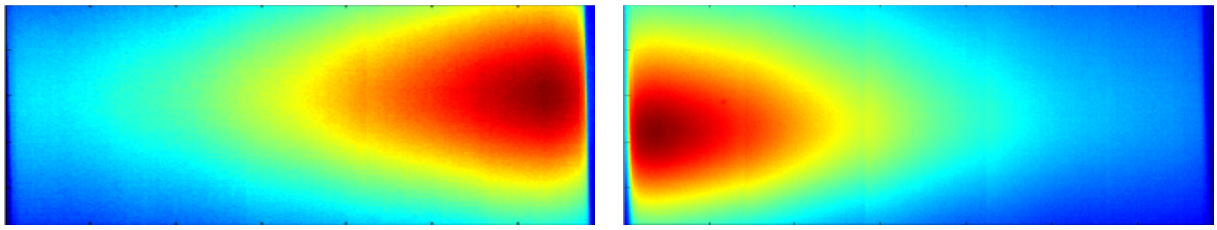

Fig.5.19. Temperature maps recorded with an IR camera for opposite relative positions of the gradient axis and the laser beam. Considering the 5x4 mm² camera aperture, these images have been obtained through a stitching process.

Lineouts extracted from these temperature maps (figure 5.20) reveal a 20 K difference for the peak temperature.

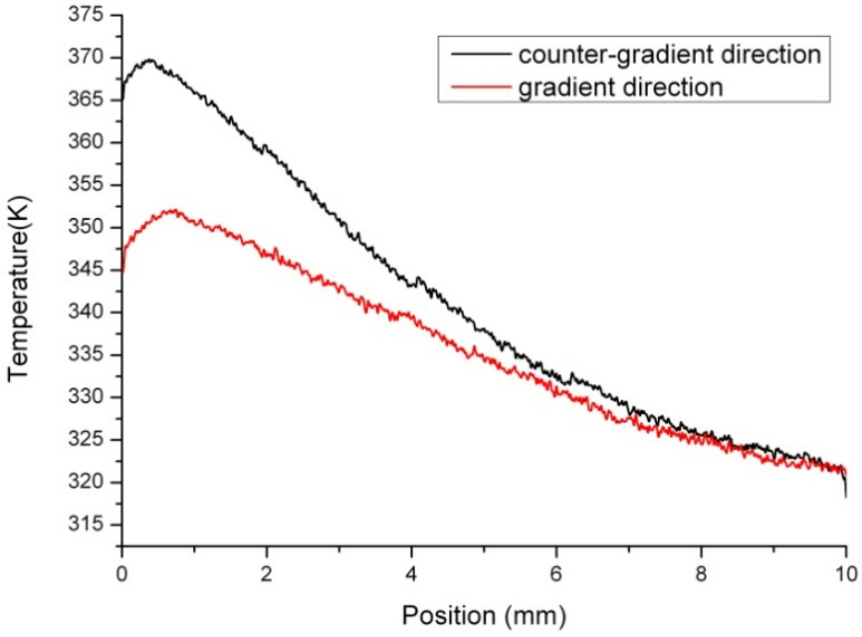

Fig.5.20. Heat load distribution observed on the surface of the tested sample

Like for the fluorescence measurement, we observe a clear impact of the gradient doping distribution. The temperature distribution is more homogeneous when pumping direction is towards of the increasing gradient direction (red curve). The observed thermal gradient is reduced by almost a factor 2: from ~50°C/cm for the counter gradient case down to 25°C/cm for the gradient case.

Unfortunately it is not possible to compare this 50% thermal homogeneity improvement with the 30% gain homogeneity improvement observed through fluorescence measurement. Although the crystal sample was the same, the pumping and cooling conditions were very different.

5.3. Laser oscillator configuration

The same crystal was used in order to investigate the impact in a lasing configuration for gradient and counter-gradient directions. These measurements were performed again at the *Charles Fabry* Laboratory of the *Institut d'Optique Graduate School*. The crystal is longitudinally pumped with fiber-coupled laser diode (80 W max power) in a range of ~12-22 A values for pump diode current. The crystal is tilted to Brewster angle because there is no AR coating applied on the faces of the crystal. A 20% output couplers were used. The crystal is cooled using the same scheme shown on the Fig.5.18. The water temperature for both cases was kept at 5°C. The laser output as a function of absorbed power is recorded for both directions (Fig. 5.21).

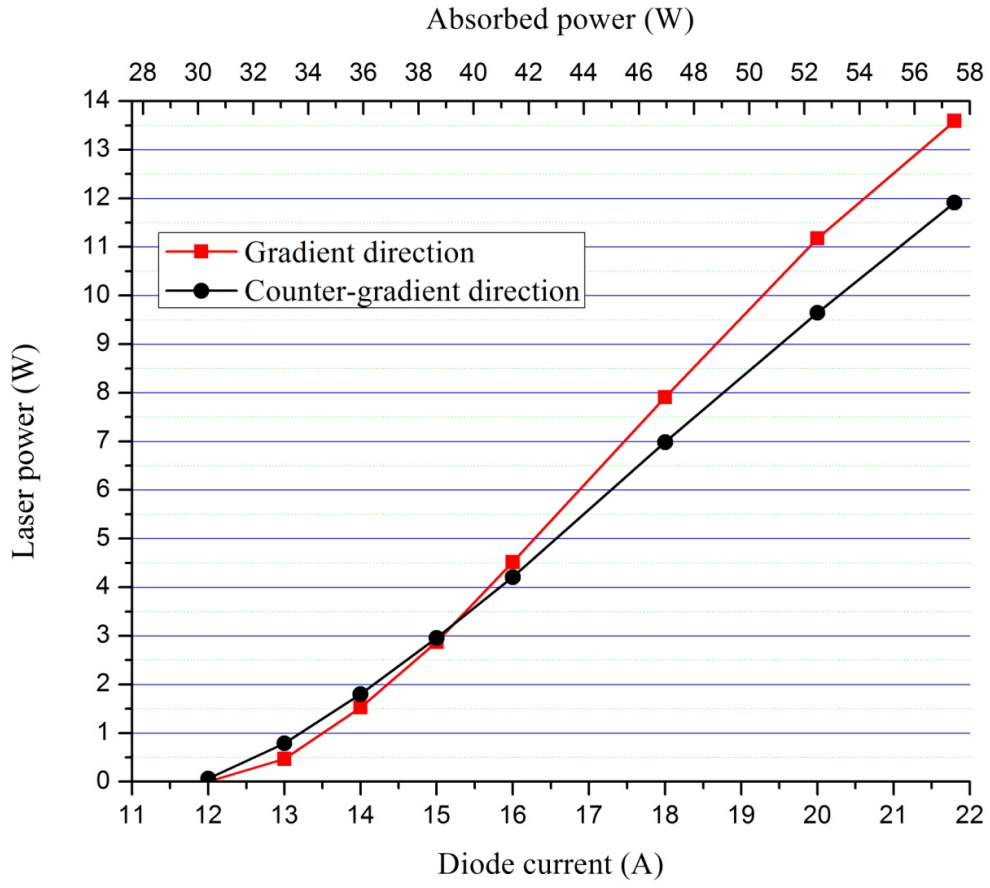

Fig. 5.21. Lasing power for gradient and counter-gradient directions vs. absorbed power

As can be seen, the lasing performances are not very different for both cases; although it is slightly better for gradient direction. The lasing threshold is almost the same for both cases: 11.8 A and 12.3 A for counter-gradient and gradient directions respectively. In terms of slope efficiency, respective values are 42% and 50%. The improvements related to the gradient case would be more obvious if the laser configuration and crystal doping distribution is optimized.

5.4. Conclusion

Effects of doping gradient crystals on both gain and thermal distribution were experimentally demonstrated. A clear 30% difference was observed for the maximum fluorescence intensity while flipping a $d_0 = 2.75$ at%, $g = 0.9$ at%/cm and $L = 1$ cm Yb^{3+}:YAG sample (Fig. 5.4). A similar experiment performed with an IR camera revealed a 20 K difference in the maximum temperature.

Our gain model proved to be able to match very well experimental fluorescence curves recorded in the W/cm² brightness regime. It was previously [5.1] experimentally benchmarked in the kW/cm² regime where Lucia amplifiers are operated. Of course a more complete code including the depletion of gain through ASE would need to be used in such regime. Nevertheless we applied our *ASE-free* model to explore the improvements gradient doped crystal could offer to both room temperature and cryogenic Lucia amplifiers. Being careful in considering results for which the gain is not exceeding the ASE depletion regime, it was possible to identify gradient doped crystal expected to improved performances of the currently uniformly doped gain medium.

Finally the same sample was used in a laser configuration, where a 20% slope efficiency increased was observed between counter-gradient and gradient directions.

5.5. References

[5.1] Albach D., “Amplified spontaneous emission and thermal management on a high average-power diode-pumped solid-state laser: the LUCIA laser system”. (doctoral thesis), Ecole Polytechnique, 2010

6. Large crystals growth with Bagdasarov method

6.1. Motivation and state of art

Within the frame of the current work, a quite significant amount of time was dedicated to explore the possibility to obtain large size high quality YAG crystals with HDC. Although these crystals are grown with a uniform distribution of doping ions, it high relevance to high average power DPSSL projects justify its presentation in the frame of this work. Large diameter crystals of laser quality are indeed extremely relevant for laser programs like the European High Power laser Energy Research facility (HiPER) [6.1]. HiPER's goal is to demonstrate Inertial Fusion Energy (IFE) production in a mode of operation similar to a reactor of a real IFE power plant. As of today the most promising scheme is to rely on a shock ignition approach where 48 beams ~12 kJ beams are distributed over a spherical D-T target (fig. 6.1).

Several studies have been performed over the past 3 years within the HiPER program preparatory phase. One of the essential goals of this phase was to define the requirements for the laser driver. Thermal management was of course a key factor in the laser design. Laser amplifiers used on current kJ to MJ-class large laser facilities (NIF [6.2], LMJ [6.3], Omega [6.4], LULI2000) rely on glass gain media which cannot be used for a 10 Hz operated facility like HiPER due to its poor thermal conductivity. Secondly, transverse lasing related to ASE gain is limiting the useful aperture to about 100 cm². And extracting 12 kJ over such a small surface is not compatible with state of the art laser damage thresholds available for coatings. The laser driver proposed architecture for HiPER therefore relies on a 12 beams bundle of 1kJ beamlets each of about 10x10 cm² aperture as illustrated on figure 6.1. Moreover, the doping level should be rather low (around 0.4 at%) in order to keep the gain below the parasitic oscillation threshold.

	Total energy (kJ)	Spots	energy per spot (kJ)	beam per bundle	energy per beam (kJ)
Compression	500	48	**10.4**	9	1.16
Shock Ignition	130	48	**2.7**	3	0.90
Total	630	48	13.125	12	-

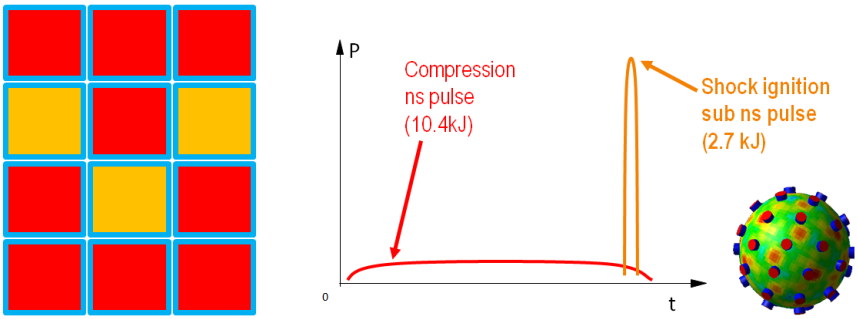

Fig.6.1. Proposed scheme to achieve ignition on a HiPER target: 48 beams distributed over a spherical Deuterium-Tritium target. Each beam is carrying a 10 Hz pulse train which individual pulses are shaped with an intense picosecond energetic pulse

We see that large size crystals or ceramics are therefore required. The growth of such crystals is not easy due to limitations imposed by the growth techniques. Cz method allows to obtain rather large crystals but defects such as cores and scattering particles are highly present in those crystals making them useless for DPSSL systems demanding a high quality of gain material. And cutting out these defective parts leads to a drastic reduction in the ultimately available size. For these reasons we were not able to find any information about YAG crystals of more than 30-40 mm diameter obtained with Cz method. Another method for growing Yb^{3+} doped YAG crystals is the so-called temperature gradient technique (TGT). This method is widely used for large YAG growth. The largest YAG crystals obtained by this method are reported by G. Zhao and Al. [6.5, 6.6] and exhibit sizes of 75 and 76mm. The critical negative factor to be mentioned is the presence of inhomogeneous doping distribution in Cz and TGT grown crystals which is discussed in [6.7] (not to confuse with doping gradient, because in the TGT case, the doping variation is non-desirable because it will lead to spatially non homogeneous amplification of the beam). Bagdasarov method helps to eliminate these problems and obtain high quality large crystals. The campaign on large crystal growth started in 2006 within the frame of a collaboration agreement between "Lazerayin Tekchnika" CSC, Yerevan, Armenia and Laboratoire LULI, CNRS, Ecole Polytechnique Palaiseau, France and continues up to present day. The primary aim was to obtain 60 mm, 2 at% doped 0.7 cm thick crystals for Lucia amplifier. Record breaking 14J/2Hz [6.8] was actually obtained with this crystal.

Currently it seems possible to obtain 10x10x4 cm high quality YAG crystals. In this chapter we will discuss results on 3 different sets of large crystal growth campaign: 60 mm for Lucia main amplifier, 77 mm for Lucia cryogenic amplifier and 92 mm Yb:Ce:YAG co-doped crystal for an undisclosed application.

6.2. Technological adjustments for large crystal growth with Bagdasarov method

Crystal growth with Bagdasarov in non-modified Laserayin Sapfir-2mg furnaces normally occurs in 70 mm large and 40 mm deep crucible therefore imposing limitations on both diameter and thickness of the crystal. The third dimension (length of the crucible) is long enough (more than 200 mm) and could even be increased further without major complicated technological changes.

Using a 70 mm wide crucible does not allow obtaining a crystal with 70 mm in diameter because the crystal near the lateral walls of the crucible cannot be really used due to the high concentration of stresses and also higher probability of metallic inclusions presence. The height of 40 mm neither allows growing 40 mm thick crystals due to the significant difference in the densities of the resulting crystal and the starting material (crackle): the obtained crystal is usually twice thinner than the original height of crackle. The width and the height of the crucible are limited by the aperture of the heater and also by the thermal shields spatial configuration. Since the regular width of boat shape crucibles does not exceed 70 mm, for this task, large crucibles with more than 100 mm in width are prepared. It requests also

the modification of the heaters and thermal shield configuration in order to fit the new width. For these first runs, the regular height is kept. Fig.6.2 shows the regular and "wide" crucibles. These crucibles are also quite shorter since we are interested in disc shape gain material production; building a shorter crucible therefore allows reducing unnecessary material waste.

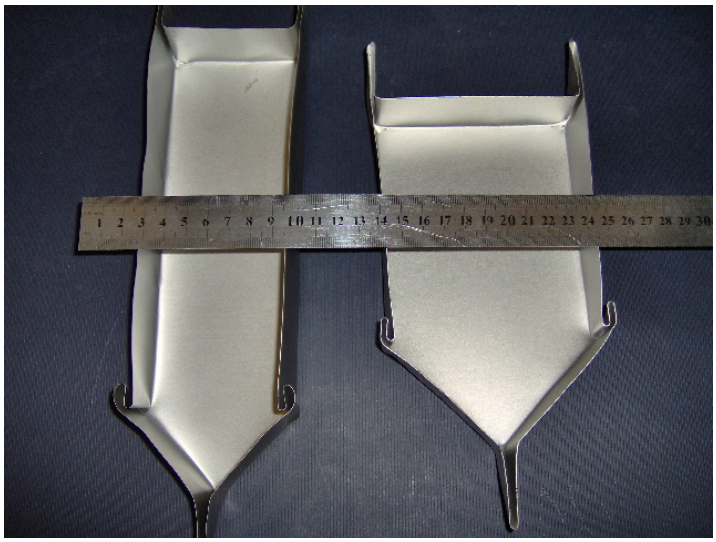

Fig.6.2. Regular (left) and "wide" (right) crucibles for HDC method

The depth of the crucibles used for these experiments are limited to 40 mm and will be increased for future experiments with further modification of furnace thermal elements configuration. The YAG seed, placed at the crucible bow (Fig. 3.2), is oriented along the requested preferential crystallographic axis, in our case the [111] direction perpendicular to the plane of Fig.6.2. High purity oxide powders for Y_2O_3 (X99.999%), Yb_2O_3 (X99.999%) and Al_2O_3 (X99.95%) are used for these crystals.

6.3. Growth Results

The first large crystals were obtained in 2008 with a diameter of 60 mm and a thickness of 7 mm. Doping level was set at 2 at% of trivalent Yb (Fig.6.3). These crystals are still successfully used for Lucia main amplifier.

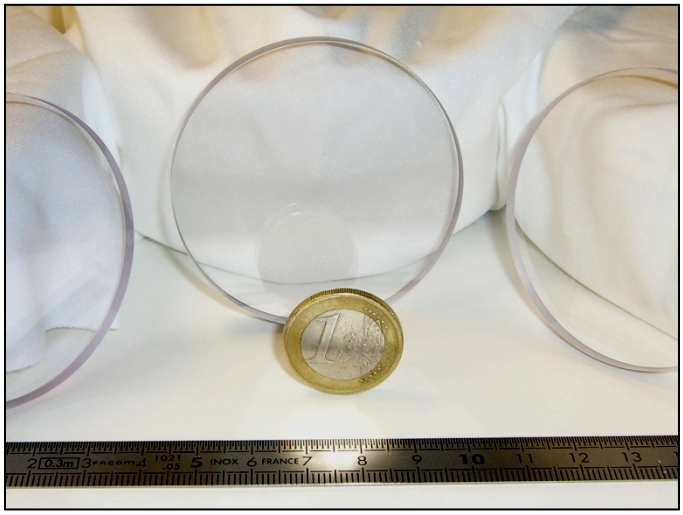

Fig.6.3. 60 mm diameter, 7 mm thick 2 at% doped crystals for Lucia main amplifier

Throughout the multiple meetings which took place during HiPER preparatory phase, it became obvious that the demand of larger sizes was crucial, therefore justifying a dedicated campaign aimed at producing crystals as large as possible. With the modifications detailed in the previous section, a crystal of 92 mm diameter was obtained. The thickness of the crystal is 8.1 mm with a 0.4 at% doping level of trivalent Yb, a value requested for HiPER. Also, a small amount (sub tenth of a percent) of the Ce ions is present in the crystal explaining its yellow color (Fig.6.4).

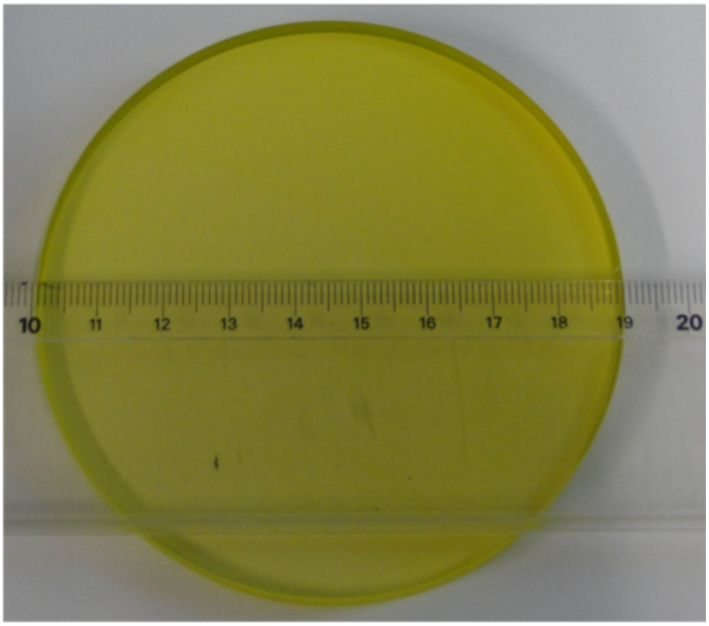

Fig.6.4. 92 mm diameter, 8.1 mm thick 0.4 at% doped crystal

The furnace used to obtain this crystal was indeed previously used for Ce/Nd co-doped YAG growth explaining the presence of Cerium ions. The Ce particles are very difficult to remove from the furnace internal elements and it eventually got immersed in the Yb doped melt.

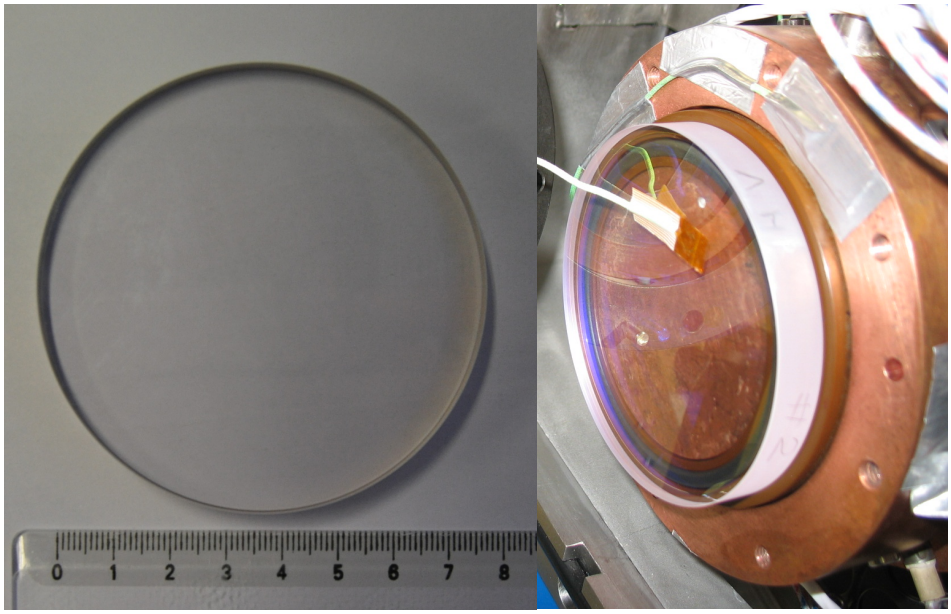

Fig.6.5. 77 mm diameter, 10 mm thick 1 at% doped crystals for Lucia cryogenic amplifier

Continuous know-how acquisition allowed us to improve the repeatability of the process and to reach a yield compatible with large crystal commercial manufacturing. The last campaign was dedicated to manufacturing of 77 mm large and 10 mm thick crystals with 1 at% of trivalent Yb doping to be used in Lucia cryogenic amplifier (Fig.6.5).

These crystals are currently used in Lucia cryogenic characterization experiments; results on which are expected in 2013.

6.4. Doping measurements

Doping measurements is needed in order to verify the homogeneity of Yb ions distribution in the 92 mm crystal. The absorption spectrum is recorded with a Cary 500 Spectrometer (Fig. 6.6) near the central part of the crystal. Using these spectral data and Lambert's law $T = \exp(-N\sigma z)$, where T is the transmission, N the number of absorbing atoms (x 1.38 10^{20} cm^{-3}, the density of doping ions at 1 at% of doping level), σ the absorption cross-section for 1 at.% and z the thickness, we obtain a Yb^{3+} doping concentration of 0.41±0.02 at %.

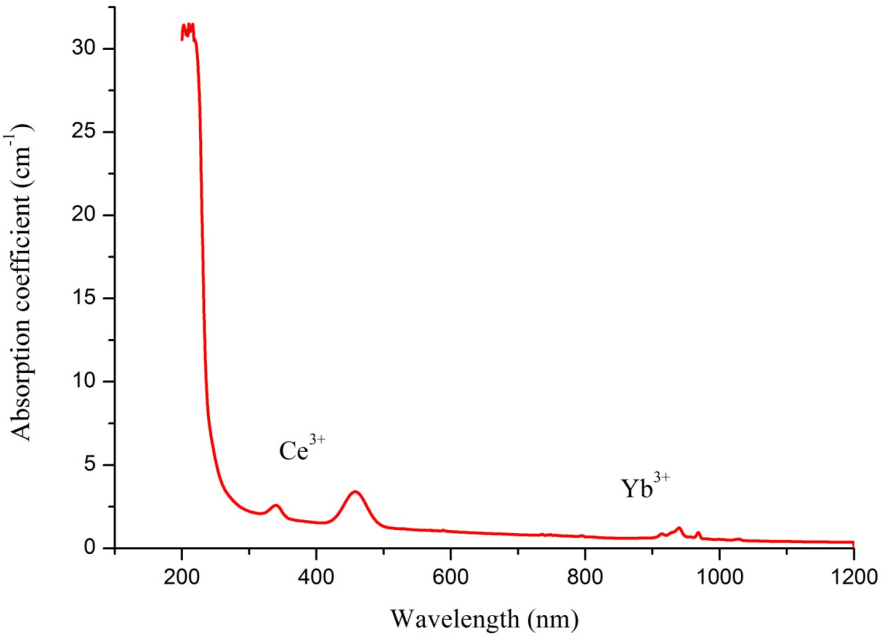

Fig.6.6. Absorption spectrum of 92 mm Ce:Yb:YAG crystal

On the absorption spectrum, we can easily observe Yb^{3+} as well as Ce^{3+} characteristic absorption peaks. To define the homogeneity of Yb^{3+} ions distribution, careful measurements are performed at several other locations. Transmission spectrum near Yb^{3+} absorption region is recorded for 6 different points (located at radial positions at 60° apart from each other's, Fig.6.7) 5 mm away from the periphery of the disk. Concentration is recorded for each point with the method described above. Fig. 6.7 shows the absorption spectrum near the 1030 nm wavelength and gives the resulting doping concentrations. The difference between extremes concentration values is about 0.04 at%, i.e. approximately a 10% variation around the nominal value of 0.4 at%. The current requirements on LUCIA laser system is 10% of doping

variation within the pumped region (which is only the central part of the crystal), we can therefore consider that the obtained crystal fully satisfies this homogeneity criteria.

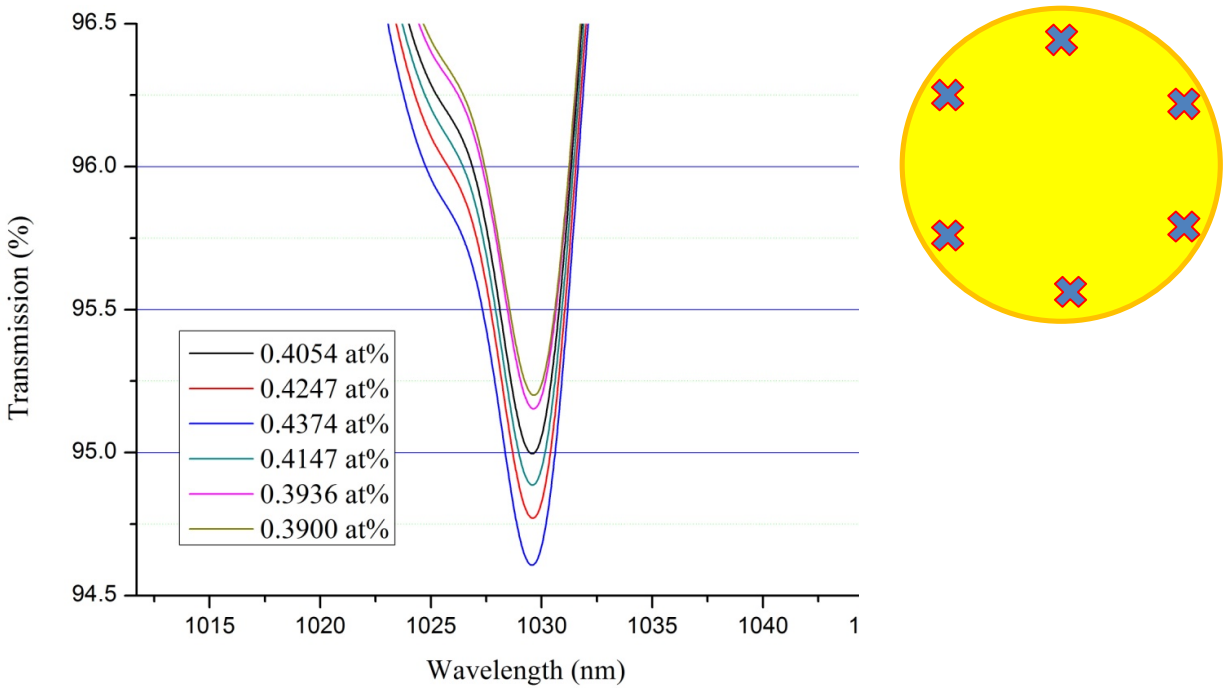

Fig.6.7. Transmission spectrum (left) around the 1030 nm absorption peak at 6 different locations (right) and extrapolated respective doping concentrations

Energy Dispersive X-ray spectroscopy (EDX) measurements were also performed in order to verify elements composition. No presence of impurities was observed; the Ce concentration is indeed too low for this technique. Yb^{3+} concentration value obtained was 0.39±0.07 at% which is in accordance with the previously obtained 0.41±0.02 at%.

6.5. Optical characterization

6.5.1. Large crystals

The 92 mm crystal was also evaluated in terms of optical characteristics. Microscopy observation does not reveal any bubbles or scattering particles, whereas no scattering of He-Ne laser beam travelling through the sample at different location can be detected. Birefringence behavior is first observed under crossed polarizers in the visible region as illustrated on Fig.6.8.

Internal stresses can be spotted near an edge of the crystal corresponding to a vicinity of the molybdenum crucible walls. Further verification is performed with infrared light in order to obtain a more quantitative measurement of the birefringence. A polarized laser beam is sent through the crystal and the intensity of transmitted light is recorded for different rotation angles of the analyzer with a photodiode. Three cases are illustrated on Fig.6.9: laser light free propagation (without crystal, black circle of Fig. 6.8), laser light travelling through the center of the crystal (free of stresses part, blue circle) and near the periphery (the most stressed point, red circle).

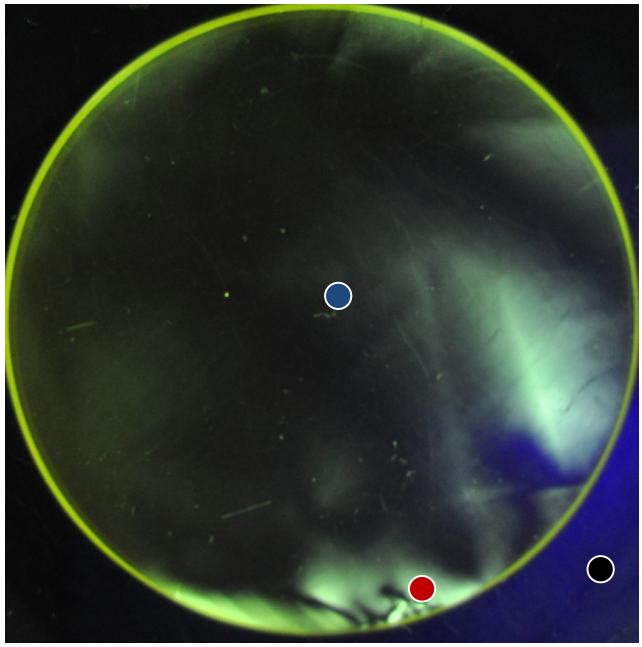

Fig.6.8. Large 92 mm diameter crystal observed under crossed polarizers with visible light. The three circles indicate the infrared measurement spots

This simple experiment does not allow us to measure any birefringence in infrared even though in the visible spectrum some strains are clearly observed.

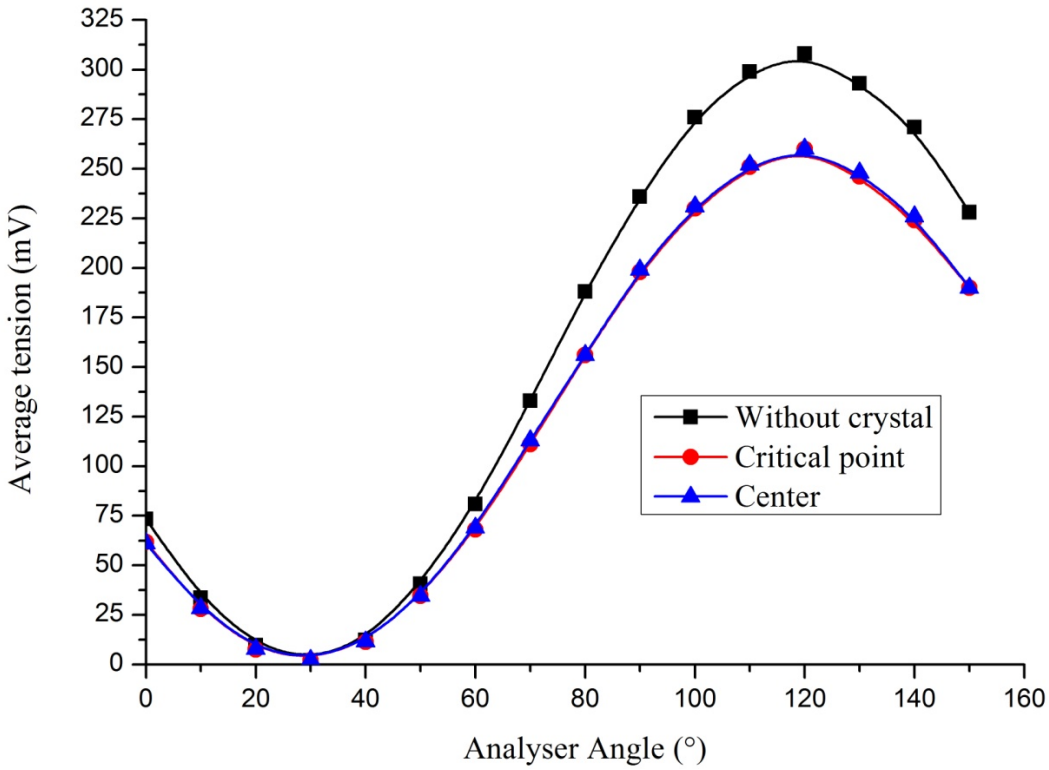

Fig.6.9. Transmitted light intensity (photodiode voltage) vs. analyzer angle for three different cases; measurement spots are indicated on Fig. 6.8 by circles (color code is kept here)

This is due to the fact that stress induced depolarization can be interpreted as a local wave plate with a phase difference $\Delta\varphi$. The transmission in Fig. 6.8 is registered with a commercial

camera in auto-exposure acquisition mode, so quantitative values cannot be deduced out of this picture. $\Delta\varphi$ is inversely proportional to the measurement wavelength. And, since the depolarization losses scales with $\sin^2(\Delta\varphi)$, the observed transmission drastically decreases when using longer wavelengths, like 1064 nm used for the second experiment [6.9]. This is very likely the reason why measurements in the infrared could not reveal any measurable difference.

6.5.2. Gradient crystals optical characterization

Birefringence and interferometric measurements have been performed on our gradient samples as illustrated in Fig. 6.10. These qualitative measurements reveal satisfying quality although the samples are not completely free of defects.

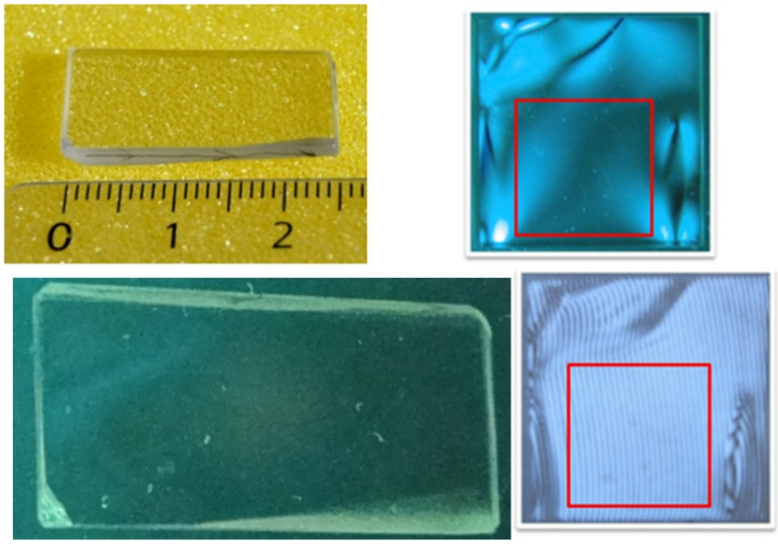

Fig.6.10. Birefringence and interferometric measurements of 1st (left) and 2nd (right) boule samples

Birefringence analysis of the first sample (performed perpendicularly to the gradient axis) reveals the absence of constraints, whereas, for the second boule sample, we observe strains especially near the edges (observations are made along the gradient axis). The presence of these stresses might be related to the very special geometry of second boule (longer and narrower crucible). Nevertheless, within this 20x20x10 mm3 sample, a clear 12x12 mm2 (red square) useful area appears free of defects.

We observed that increased doping level or gradient amplitude does not impact the optical quality of the crystals. Therefore global optical quality improvement shall be addressed solely through careful growth conditions (growth rate, crucible size, temperature sequence…) adjustment.

Transmission measurements of uniformly and gradient doped crystals are performed with a 800 nm Ti:Sapphire laser at IOGS facility. At this wavelength, the absorption for trivalent Yb in YAG matrix is absent, so the only limiting factor for transmission of optically almost perfect crystals should be Fresnel losses. Four our crystals, we indeed obtained transmission values limited only by reflection losses from both faces. The measurement is

performed at several points of the crystals without revealing any detectable difference. Microscopy (LEICA *MZ* 12.5) observations reveal no bubbles or scattering particles, whereas no scattering of He-Ne laser beam travelling through the sample could be detected.

6.6. Structural characterization

Besides the optical characterization, structural characterizations are also performed via X-ray radiation of the samples. X-rays are widely used in material characterization. In chapter 4, we describe how x-rays can be used for material composition verification (x-ray fluorescence techniques). In this section, we present x-rays based techniques used as a crystalline quality characterization tool. Materials have been experimentally studied by x-ray diffraction methods first in 1911 by von Laue, Friedrich and Knipping. They obtained the first X-ray diffraction patterns on rock salt. From this day to 1917 Bragg, von Laue, Darwin and Ewald developed the theoretical foundation for this phenomenon. Then the subject was advanced by many others, particularly Lang, Authier, Takagi, Taupin and Kato who greatly contributed to the development of experimental and theoretical tools for crystals distortions and defects studies by X-ray methods [6.10]. Nowadays, X-ray diffraction methods together with electron and neutron scattering techniques offer a large range of material characterization methods. Their respective advantages and disadvantages are presented in Table 6.1.

Table 6.1: Characteristics of electron, neutron and X-radiations [6.10]

Characteristic	Electrons	Neutrons	X-rays
Absorption	High	Very low	Low
Penetration	< 1 μm	~cm	~mm
Rocking curve width	Degree	< Arc second	Arc seconds
Strain sensitivity	10-3	10-7	10-7
Spatial resolution	1 mm	30 μm	1 μm
Destructive	Yes	No	No
Cost	High	Very high	Medium
Convenience	Good	Poor	Good

Every radiation hitting the crystals is absorbed or scattered. The absorption of x-rays is comparably low (Table 6.1) which, together with other advantages, makes x-ray scattering a widely used technique for laser crystals characterization.

Bragg provided a simple but very useful description of crystal diffraction: $n\lambda = 2d\sin\theta$, where n is the diffraction order, λ the wavelength, d the distance between diffracting planes and θ the so called Bragg (Fig. 6.11)

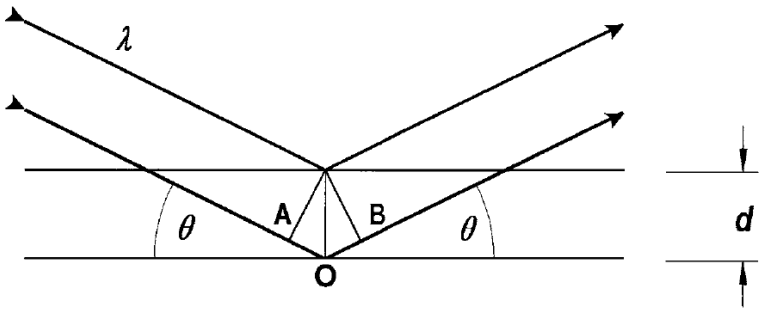

Fig.6.11. Diffraction of plane waves from successive crystal planes. θ is the angle between the incident ray and the scattering planes

For a cubic system (as YAG is), the Bragg's law can be used to obtain lattice spacing following the relation $d = a/\sqrt{h^2 + k^2 + l^2}$ where a is the lattice constant of the cubic crystal while h,k,l are the Miller indices of the Bragg plane.

As we have seen from the first chapter (Fig.1.9), YAG structural characteristics change a little within low doping ranges [6.11], so the impact of the doping value as well as the presence/absence of a gradient should be negligible on the crystalline quality of the samples. That is why we present here only some of our measurements although it fully reflects the characteristics of other crystals as well. In order to characterize our crystals, two x-ray scattering techniques are used: high resolution x-ray diffractometry and topography.

6.6.1. X-ray topography

X-ray topograms give spatial maps of the intensity of the diffracted beam over the whole surface of the crystal. The diffracted intensity is affected by the local defects (phase and grain boundaries, inclusions, dislocations, strain fields,…) giving then contrast variations in the resulting image. The method is sensitive enough to reveal not only large domain dislocation but also individual dislocations [6.10].

The x-ray topogram of 2 at% doped 60 mm diameter and 7 mm thick crystal used on Lucia amplifier is presented on Fig.6.12 (left). The topogram shows no significant contrast difference illustrating the high quality of the crystal. This image can be compared with the similar topogram of Yb doped CaF_2 crystal [6.12]. High contrast differences can clearly be observed in this crystal (Fig.6.12 right) revealing the presence of multiple defects and inhomogeneities.

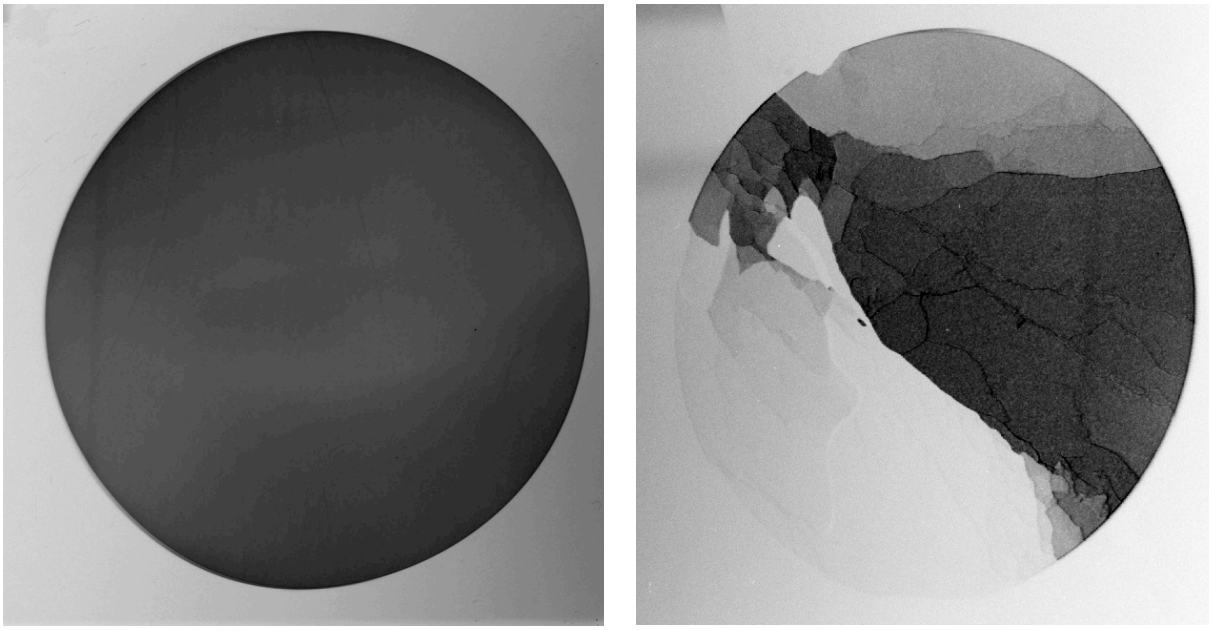

Fig.6.12. X-Ray topogram of the 60 mm crystal used for Lucia main amplifier (left) and Yb:CaF_2 crystal (although high quality undoped CaF_2 are rather easy to produce in large size, doping such matrix has been proved uneasy up to the present day)

6.6.2. Triple axis diffractometry

X-ray topography gives a full-aperture single-angle-of-observation diffraction map offering a qualitative description of the sample. In order to have access to more quantitative information, techniques giving access to rocking curves can be used. We were offered the opportunity to have access to x-ray diffractometry equipment of the Centre de Recherche sur les Ions, les Matériaux et la Photonique (CIMAP) in Caen.

Figure 6.11 illustrates an ideal case when diffraction occurs along a single direction, being generated by a perfect crystalline structure. If the source is monochromatic, the diffraction will occur at this single angular direction defined by Bragg's law.

In practice, a crystal can be subject to lattice constant variations Δa leading to an angular dispersion $\Delta\theta$ of the diffracted beams. The smallest $\Delta\theta$ is, the closest to a perfect crystal we are. At CIMAP, a triple axis diffractometer allowed us to record so-called rocking curves of our sample. Such curves give the diffraction signal intensity as a function of θ and are widely used to characterize YAG single crystals [6.13-17]. This method allows recovering the lattice parameter (from θ) as well as characterizing the crystal quality (from $\Delta\theta$).

Experiments were performed on a Philips X'Pert MRD triple axis diffractometer operating at CuKα1 radiation (1.54056 Å) illustrated on Fig. 6.13.

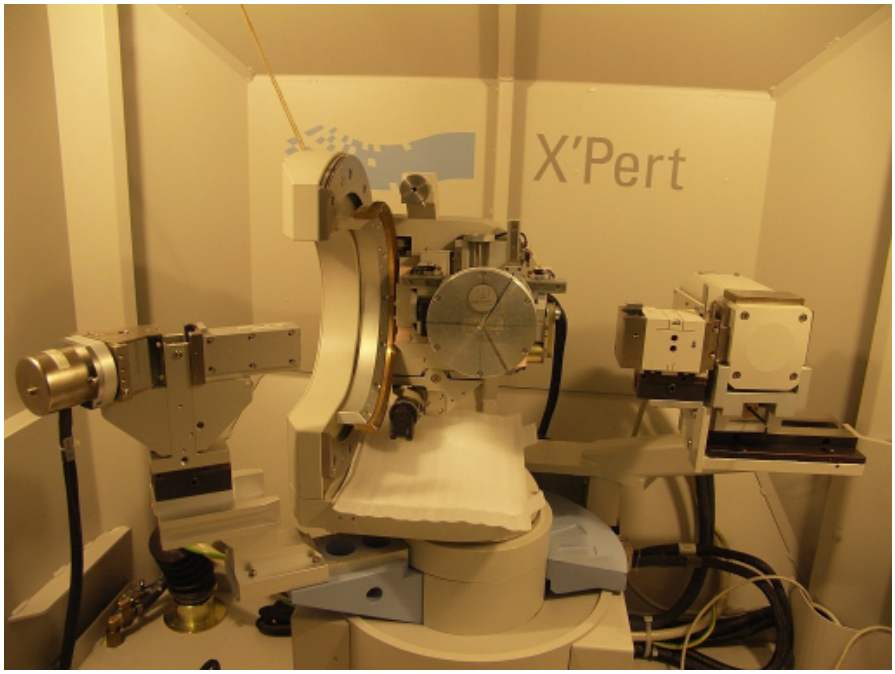

Fig.6.13. CIMAP triple axis diffractometer

The results of these measurements on three crystals cut from the 3rd gradient boule (chapter 4) are presented below. These crystals are 10 at% doped, 10 mm in diameter and 3 mm thick. They are cut with its normal oriented along the [111] crystallographic axis. The 2θ scan was performed for [444] and [420] crystallographic planes (Fig. 6.14a and b).

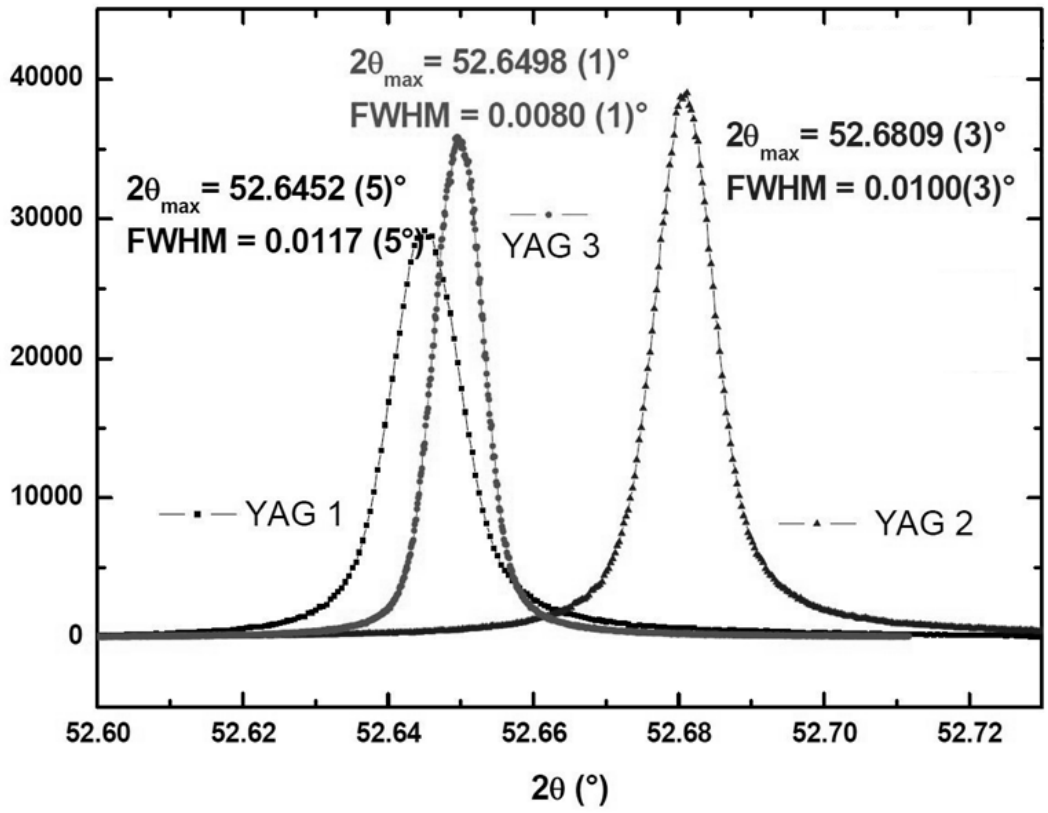

Fig.6.14a. [444] axis rocking curves. Vertical axis gives the intensity in cps/s

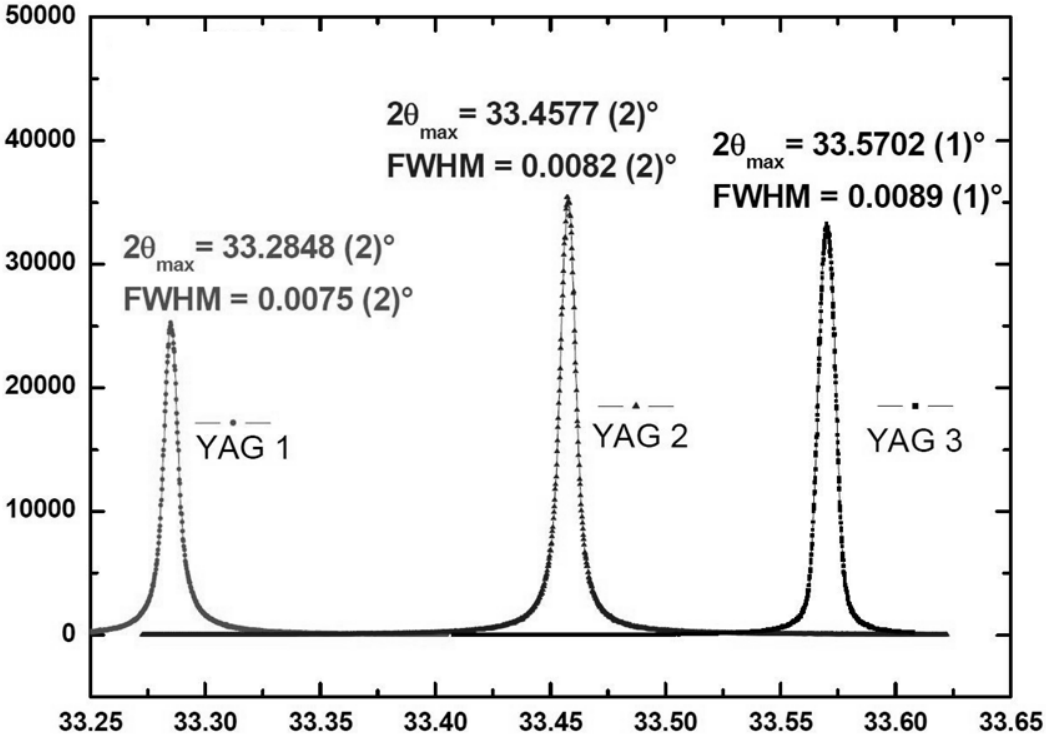

Fig.6.14b. [420] axis rocking curves. Vertical axis gives the intensity in cps/s

Rocking curves width never exceed 0.0117°, a value to be compared with the ones presented in [6.13], where authors obtain 0.0099 and claim a good crystalline structure of their samples.

However the peak angular positions differ from sample to sample. The above given lattice spacing formula leads to lattices values displayed in table 6.2. We observe that the lattice constant for our samples agrees within less than 1% with data collected from the literature. Within the same boule we also notice a similar dispersion.

Table 6.2: Experimental lattice constant compared to literature sources

source	YAG 1	YAG 2	YAG 3	[6.11]	[6.15]	[6.16]	[6.18]
a (Å)	12.035	12.028	12.034	11.99	12.003	11.9	12.006

6.7. Outlook

Foreseen changes of the growth furnace heating elements will increase the growth possibilities in terms of diametrical dimension. This probably will require several temperature field calibration measurements and hardware adjustment cycles. In parallel to this, it is very important to be able to increase the height of the crystal. This demands more complicated technological changes but still stays feasible in near future if the appropriate investments are done in order to rebuild all heating/shielding/transporting units. This will also allow obtaining gradient crystals with larger diameters.

6.8. References

[6.1] Dunne M., "A high-power laser fusion facility for Europe", Nature physics, 2 (2006)

[6.2] https://lasers.llnl.gov/

[6.3] http://www-lmj.cea.fr/

[6.4] http://www.lle.rochester.edu/omega_facility/omega/

[6.5] Zhao G., Si J., Xu X., Xu J., Song H., Zhou Y., "Growth of large-sized Yb:YAG single crystals by temperature gradient technique", Journal of Crystal Growth 252 (2003) 355–359.

[6.6] Zhao G. , X. Zeng, J. Xu, Y. Xu, Y. Zhou, Characteristics of large-sized Ce:YAG scintillation crystal grown by temperature gradient technique Journal of Crystal Growth 253 (2003) 290–296

[6.7] Xu X., Zhao Z.,Zhao G., Song P. X., Xu J., Deng P., "Comparison of Yb:YAG crystals grown by CZ and TGT method, Journal of Crystal Growth 257 (2003) 297-300"

[6.8] Thierry Gonçalvès-Novo T., Albach D., Vincent B., Arzakantsyan M., and Chanteloup J.-C. , "14 J / 2 Hz Yb^{3+}:YAG diode pumped", accepted for publication Optics Express

[6.9] Koechner W., "Solid-State Laser Engineering", Springer, 1999

[6.10] Bowen D. K., Tanner B. K. "High Resolution X-ray Diffractometry and Topography" (1998)

[6.11] Dobrzycki Ł., Bulska E., Pawlak D. A., Frukacz Z., Wozniak K. "Structure of YAG Crystals Doped/Substituted with Erbium and Ytterbium" Inorg. Chem. 2004, 43, 7656-7664

[6.12] personal communication J. Hein, IOQ, F.Schiller Universität, Jena, Germany

[6.13] Zenga X., Zhao G., Xu X., Li H., Xu J., Zhao Z., He X., Panga H., Jie M., Yan C., "Comparison of spectroscopic parameters of 15 at% Yb:$YAlO_3$ and 15 at% Yb:$Y_3Al_5O_{12}$", Journal of Crystal Growth 274 (2005) 106–112

[6.14] Cornacchia F., Alshourbagy F., Toncelli A., Tonelli M., Ogino H., Yoshikawa A., Fukuda T. "Growth and spectroscopic properties of Er:YAG crystalline fibers" Journal of Crystal Growth, Volume 275, Issues 3–4, 1 March 2005, Pages 534–540

[6.15] Wirkowicz M., Skórczakowski M., Jabczyñski J., Bajor A., Tymicki E., Kaczmarek B., £Ukasiewicz T. "Investigation of structural, optical and lasing properties of YAG:Yb single crystals" OPTO-ELECTRONICS REVIEW **13**(3), 213.220

[6.16] Xu X., Zhao Z., Xu J., Deng P. "Distribution of ytterbium in Yb:YAG crystals and lattice parameters of the crystals" Journal of Crystal Growth 255 (2003) 338–341

[6.17] Chani V., Yoshikawa A., Kuwano Y., Inaba K., Omote K., Fukuda T. "Preparation and characterization of Yb:$Y_3Al_5O_{12}$ fiber crystals"

[6.18] Lee H.M., Cheng C.C., Huang C.Y., “The synthesis and optical property of solid-state-prepared YAG:Ce phosphorby a spray-drying method” Materials Research Bulletin, Volume 44, Issue 5, 6 May 2009, Pages 1081–1085

Conclusion

This thesis is the synthesis of a research dedicated to the development of Yb:YAG crystals with controlled doping distribution. This work is performed within the frame of the Lucia project at LULI and in collaboration with *Laserayin Tekhnika CSC*. Besides these main actors, more than ten other laboratories were involved in experiments described in this manuscript.

The Lucia project is heading towards its 100 J / 10 Hz operation goal, although it is now operating at 2 Hz with a maximum extracted energy of 14 J. This achievement is performed with two pre-amplifiers and one room temperature operated amplifier. Since 2012, a second cryogenic amplifier is in its commissioning phase. With the help of this amplifier, it is predicted to reach the 30 J level by the end of 2014.

The advantages of gradient doped crystals are illustrated with simulations developed in the context of the active mirror concept. The targeted issues are thermal management and ASE induced gain depletion. Thermal management is an especially important issue for high repetition rate (10 Hz and more) operation, while ASE parasitic oscillations play a significant negative role in large size gain media. Both are inherent to kW average power laser chains. For classical crystal (i.e., with homogeneous distribution of dopant), improved thermal management favors thinner gain material. But then, higher doping values should be applied to maintain the stored energy capability and therefore, the associated higher cross section lead to higher losses related to ASE parasitic oscillations (especially for large size gain media). On another hand, a thicker gain medium with lower doping would allow staying below ASE parasitic oscillation threshold, but will greatly increase the difficulty for heat extraction, creating thermal lens and deformation potentially inducing fractures risk. In the frames of this thesis, it is shown that a carefully chosen doping distribution might bring up to 35% of gain media volume reduction by keeping material thin enough in pump/extraction direction while providing necessary conditions for ASE parasitic oscillation suppression. This combines the advantages of both constant doping extreme cases while avoiding the associated drawbacks.

These significant advantages triggered a real motivation to explore the possibility to grow such optimized gain medium.

The advantage of doping gradients to improve thermal management of lasers was already demonstrated for Nd:YAG crystal rods. But Nd is characterized by a segregation coefficient much lower than unity for most of YAG melt growth techniques; there is then no particular difficulty to obtain non-homogeneously distribution in this matrix. This distribution is naturally caused by segregation processes of Nd ions in YAG matrix. In case of Yb, segregation coefficient is very close to unity in YAG for melt growth techniques (normal growth). Usually, final Yb:YAG crystals demonstrate quite satisfying homogeneity of dopant distribution (which is a challenge for Nd:YAG growth). The overview of melt growth techniques illustrates the incompatibility of most of them for gradient crystal growth. Only special type

of Czochralski growth and Bagdasarov method can potentially serve for those purposes. Although the suggested disc Cz growth approach seems to offer an interesting opportunity for cladding growth at the periphery of a disc shaped gain media, real experiments have yet to be performed.

Beyond important developments and characterizations provided by Kh. S Bagdasarov and his group at his time, the high flexibility offered by this method still explains why it continuously develops and adapts to the newer challenges imposed by the ever more demanding crystal market.

The characterization experimental campaign performed in the frame of this thesis will found the basis for further more detailed experiments in a specifically designed experimental furnace. The summary of all these foreseen experiments will then provide a solid base to build a mathematical model for studying and predicting temperature and mass transport processes for Yb:YAG crystallization via Bagdasarov method.

In order to investigate the influence of starting and in-situ growth conditions on final distribution of trivalent Yb ions in YAG, 4 growth sequences are performed. The quest for an accurate measurement of the final doping distribution motivated the exploration of several composition verification techniques. Ultimately, the most satisfying techniques are selected as EPMA analysis together with spectrometry. Doping distributions in different crystals extracted from the four grown gradient boules are measured and doping gradients are found exhibiting the maximum value of 2 at%/cm. A quite simple, but reliable, model for final doping distribution prediction depending on starting and growth conditions is proposed. The gradient along non-growth axis directions is also studied allowing obtaining a growth front map for every moment of the growth process. For our experiments, it revealed the presence of flat and slightly inclined growth front.

The obtained doping gradient distribution crystals are tested for gain and thermal distribution. A clear 30% difference is observed for the maximum fluorescence intensity while flipping a 0.9 at%/cm doping gradient and 1 cm thick Yb^{3+}:YAG sample. A similar experiment performed with an IR camera reveals a 20 K difference in the maximum temperature for gradient and counter-gradient directions. The ASE-free mathematical model shows that, with a 4 at%/cm gradient, the performance of room temperature and cryogenic amplifiers of the Lucia system could significantly be improved. The same sample used for thermal and gain distribution experiments is used in a laser configuration where a 20% slope efficiency increase is observed between counter-gradient and gradient directions.

Finally the results on large crystal growth campaign is presented, including the 60 mm crystals in used for more than two years in Lucia room temperature amplifier, the 77 mm crystals produced for cryogenic amplifier and a 92 mm sample produced for demonstrative purposes. The technological changes required for large size crystals are presented briefly. Also birefringence, optical homogeneity tests on gradient and uniform doped samples give very satisfactory results. The structural (rocking curve and topogram) measurements show respectively very narrow peak and almost no contrast, indicating single-crystalline structure. The lattice constant calculation indicates a small dilatation, which is characteristic for middle

parts of Bagdasarov grown boules. These results confirm the high quality of the laser crystals obtained by Bagdasarov technique.

The current work is an encouraging start in gradient doped Yb:YAG materials exploration and offer interesting perspectives for combining the large crystal growth technique with gradient growth, leading to the laser material of the future where dedicated crystal genesis engineering will allow the processing of accurately tailored laser gain medium for very specific needs.

A. Rate equations: Numeric model

A.1. Introduction

The aim of this annex is to present the numerical model used to calculate the pump/laser light intensity evolution within the gain medium and its impact on population inversion variation. Trivalent Ytterbium ions in YAG satisfy a quasi-three level energetic system. The pump light excites the doping ions and populates the third level creating N_3 number of ions at this energetic level. From there, a non-radiative transition occurs and the ions migrate towards the second level increasing the number N_2. The depopulation of this level and return to the ground state occurs with fluorescence of photons at the emission wavelength λ_l. The lifetime of the second level determines the fluorescence time τ_{21}.

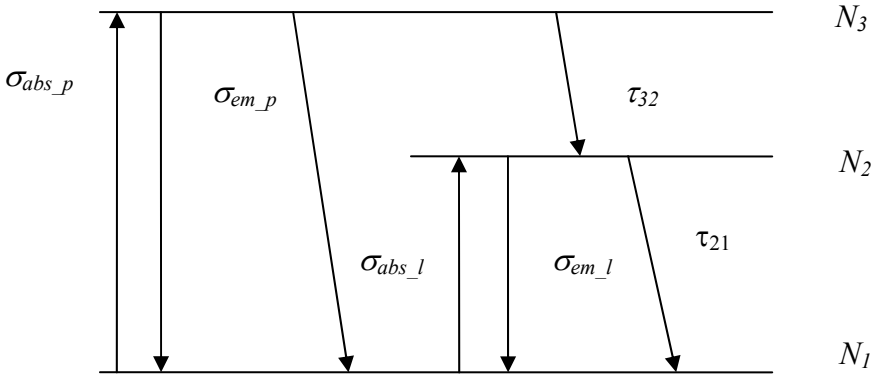

Fig. A1. Energetic diagram of Yb^{3+}:YAG with relevant constants. For cross-sections σ, the pumping is symbolized by the index "*p*", whereas laser action is indicated by the index "*l*"

The non-radiative transition from level 3 to level 2 is very fast ($\tau_{21} >> \tau_{32}$), of the order of picoseconds, thus allowing to neglect the population of the third level: $n_3 \approx 0$. This approximation transforms the system into a two levels one, where the population temporal evolution for both states is described by the following equations:

$$\frac{\partial n_2}{\partial t} = \left(\sigma_{abs\_p} n_1 - \sigma_{em\_p} n_2\right)\frac{I_p \lambda_p}{hc} + \left(\sigma_{abs\_l} n_1 - \sigma_{em\_l} n_2\right)\frac{I_l \lambda_l}{hc} - \frac{n_2}{\tau_{21}} \quad (1)$$

$$\frac{\partial n_1}{\partial t} = -\frac{\partial n_2}{\partial t}$$

Let us introduce the total number of doping ions $N_{tot} = n_1 + n_2$ and the fraction of ions in the upper state $\beta = n_2/N_{tot} < 1$. We obtain then the following differential equation describing the population inversion evolution during the pump.

$$\frac{\partial \beta(z,t)}{\partial t} = \left[\sigma_{abs\_p} - \beta\left(\sigma_{em\_p} + \sigma_{abs\_p}\right)\right]\frac{I_p \lambda_p}{hc} - \left[\sigma_{abs\_l} - \beta\left(\sigma_{em\_l} + \sigma_{abs\_l}\right)\right]\frac{I_l \lambda_l}{hc} - \frac{\beta}{\tau_{21}} \quad (2)$$

The differential equation for intensities of pump and laser lights is:

$$\frac{\partial I(z,t)}{\partial z} = g_0 I(z,t) \quad (3)$$

where $g_0 = N_{tot}[\beta(\sigma_{em} + \sigma_{abs}) - \sigma_{abs}]$ is the small signal gain (in absence of saturation). Combining the last two equations, we obtain the sets of rate equations to be solved by the numerical model.

For pumping:
$$\begin{cases} \frac{\partial I_p}{\partial z} = N_{tot}\left[\beta\left(\sigma_{em\_p} + \sigma_{abs\_p}\right) - \sigma_{abs\_p}\right] I_p \\ \frac{\partial \beta}{\partial t} = \left[\sigma_{abs\_p} - \beta\left(\sigma_{em\_p} + \sigma_{abs\_p}\right)\right] \frac{I_p \lambda_p}{hc} - \frac{\beta}{\tau_{21}} \end{cases} \quad (4)$$

For lasing:
$$\begin{cases} \frac{\partial I_l}{\partial z} = N_{tot}\left[\beta\left(\sigma_{em\_l} + \sigma_{abs\_l}\right) - \sigma_{abs\_l}\right] I_l \\ \frac{\partial \beta}{\partial t} = \left[\sigma_{abs\_p} - \beta\left(\sigma_{em\_p} + \sigma_{abs\_p}\right)\right] \frac{I_l \lambda_l}{hc} - \frac{\beta}{\tau_{21}} \end{cases} \quad (5)$$

A.2. Splitting Method and pump phase

To solve the above set of partial differential equations, the most widely used numerical integration scheme is the so called *splitting method*. This approach illustrates a general strategy in sciences where, to solve a complex problem, one addresses a sequence of sub-problems of simpler structure. In is *Discourse on Method*, René Descartes did not write anything different when he stated his second principle: "*The second was to divide each of the difficulties which I encountered into as many parts as possible, and as might be required for an easier solution*"

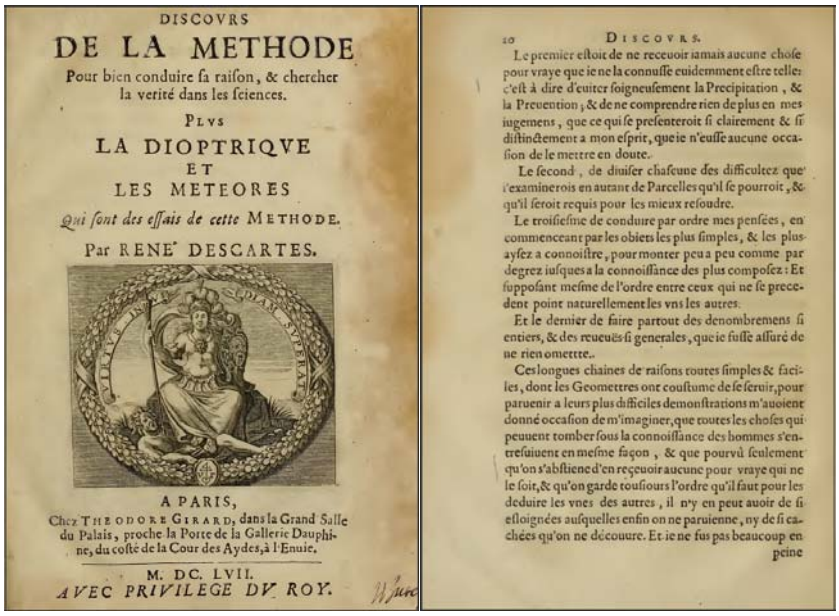
DISCOVRS
DE LA METHODE
Pour bien conduire sa raison, & chercher la verité dans les sciences.
PLVS
LA DIOPTRIQVE
ET
LES METEORES
Qui sont des essais de cette METHODE.
Par RENE' DESCARTES.
A PARIS,
Chez THEODORE GIRARD, dans la Grand Salle du Palais, proche la Porte de la Gallerie Dauphine, du costé de la Cour des Aydes, à l'Enuie.
M. DC. LVII.
AVEC PRIVILEGE DV ROY.

10 DISCOVRS.
Le premier estoit de ne receuoir iamais aucune chose pour vraye que ie ne la connusse euidemment estre telle: c'est à dire d'euiter soigneusement la Precipitation, & la Preuention; & de ne comprendre rien de plus en mes iugemens, que ce qui se presenteroit si clairement & si distinctement a mon esprit, que ie n'euusse aucune occasion de le mettre en doute.
Le second, de diuiser chacune des difficultez que i'examinerois en autant de Parcelles qu'il se pourroit, & qu'il seroit requis pour les mieux resoudre.
Le troisiesme de conduire par ordre mes pensées, en commenceant par les obiets les plus simples, & les plus-ayfez a connoistre, pour monter peu a peu comme par degrez iusques a la connoissance des plus composez: Et supposant mesme de l'ordre entre ceux qui ne se precedent point naturellement les vns les autres.
Et le dernier de faire partout des denombremens si entiers, & des reueuës si generales, que ie fusse assuré de ne rien omettre.
Ces longues chaines de raisons toutes simples & faciles, dont les Geometres ont coustume de se seruir, pour paruenir a leurs plus difficiles demonstrations m'auoient donné occasion de m'imaginer, que toutes les choses qui peuuent tomber sous la connoissance des hommes s'entresuiuent en mesme façon, & que pourvû seulement qu'on s'abstiene d'en receuoir aucune pour vraye qui ne le soit, & qu'on garde tousiours l'ordre qu'il faut pour les deduire les vnes des autres, il n'y en peut auoir de si esloignées ausquelles enfin on ne paruienne, ny de si cachées qu'on ne découure. Et ie ne fus pas beaucoup en peine

Fig. A2. Discours de la méthode of René Descartes ; The second paragraph reads : "Le second, de diviser chacune des difficultés que j'examinerais, en autant de parcelles qu'il se pourroit, et qu'il seroit requis pour les mieux résoudre."

For the first phase, let us consider that the gain medium is pumped at 940 nm by a 1 ms rectangular pulse. The initial population inversion density $\beta(\mathrm{t} = 0)$ equals 0. The principle of the method is the following: the crystal and pump are split into thin spatial and temporal slices. The finer is the splitting the more precise is the result given by the model, but it significantly increases the time of the calculation. Satisfying splitting numbers were found to be $N = M = 100$ for both cases. As illustrated on Fig. A3, the first temporal slice of the pump

pulse ($\delta t = \tau/N$ with τ, the pump duration and N, the number of slices) successively travels through all the gain medium spatial slices ($\delta z = L_C/M$, with L_c the gain medium length, and M, the number of spatial slices) and by this modifies population inversion β. Then the second pump slice performs an identical travel within the crystal carrying the new population density resulting from the first pump slice travel.

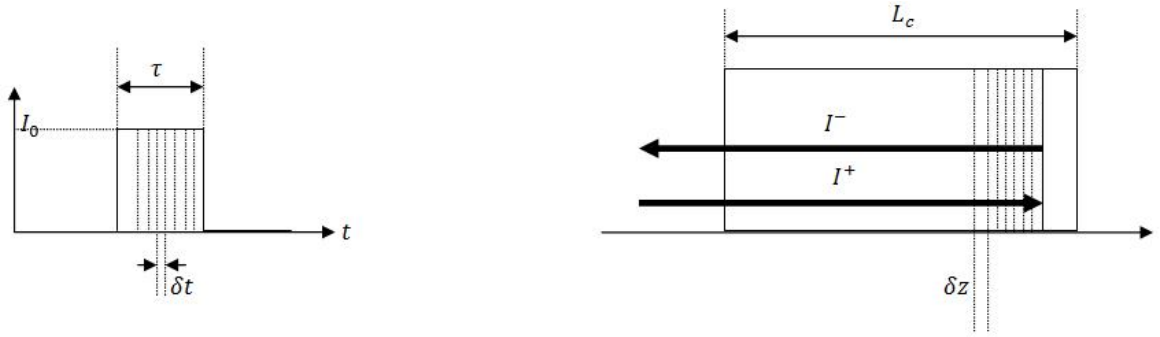

Fig. A3. Temporal and spatial slicing of the pump pulse (left) and gain medium (right)

Now let us have a more detailed look at the first slice propagation. Due to our initial conditions, β equals zero and we consider it constant during the whole travel of each single temporal slice, so the set of rate equations (4) is simplified into:

$$\begin{cases} \frac{\partial I_p}{\partial z} = -N_{tot}\sigma_{abs\_p} I_p \\ \frac{\partial \beta}{\partial t} = 0 \end{cases} \quad (6)$$

The only equation needed to be solved for the pump first slice is the simple absorption equation. In order to take into account the active mirror architecture, the pump light is described as a sum of two counter-propagating pump pulses: $I(z) = I^+(z) + I^-(z)$ where the first term represents propagation in the z axis positive direction and the second term represents the backward reflected beam propagating in the negative direction of z axis.

After traveling through m crystal slices, the onward pump intensity $I^+(z)$ located at the interface $m/m+1$ (cf. figure A4) is:

$$I_p^+(m\delta z, \delta t) = I_p^+((m-1)\delta z, \delta t)e^{-N_{tot}\sigma_{abs\_p}\delta z}, \text{ with } 1 \le m \le M \quad (7)$$

We have therefore a simple absorption multiplier $e^{-N_{tot}\sigma_{abs\_p}\delta z}$ for each slice. Let us call $I_p^+(0) = I_{p0}$, the pump intensity entering the first slice. The pump intensity exiting slice m has travelled through m slides and can be expressed as:

$$I_p^+(m\delta z, \delta t) = I_{p0}e^{-N_{tot}\sigma_{abs\_p}m\delta z} \quad (8)$$

At the end of the crystal, the pump intensity exiting the last slice $m=M$ has travelled through M slices and we have:

$$I_p^+(M\delta z, \delta t) = I_{p0}e^{-N_{tot}\sigma_{abs\_p}M\delta z} = I_{p0}e^{-N_{tot}\sigma_{abs\_p}L_C} \quad (9)$$

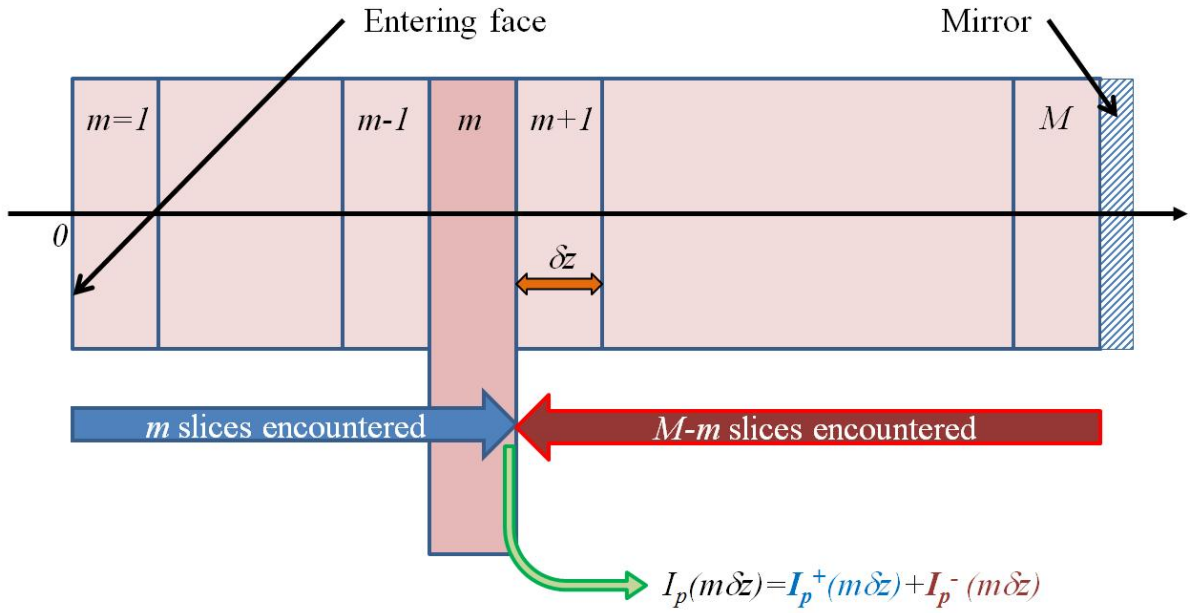

Fig. A4. Pump light travel through the gain medium. At any coordinate z, the total pump is $I^+ + I^-$

After reflection on the back surface of reflectivity R, we have, for the forward intensity I_p^-, (i.e. the pump intensity entering back into the last slide) the following expression:

$$I_p^-(M\delta z, \delta t) = RI_p^+(M\delta z, \delta t) = RI_{p0}e^{-N_{tot}\sigma_{abs\_p}L_C} \quad (10)$$

The expression of I_p^- at the interface *m/m+1* (see figure A4) is similar to (7) with the same multiplier $e^{-N_{tot}\sigma_{abs\_p}\delta z}$:

$$I_p^-(m\delta z, \delta t) = I_p^-((m+1)\delta z, \delta t)e^{-N_{tot}\sigma_{abs\_p}\delta z} \quad (11)$$

At this specific location, the forward intensity I_p^- enters into slice m a second time. It has then travelled through *(M-m)* slices leading to:

$$I_p^-(m\delta z, \delta t) = I_p^-(M\delta z, \delta t)e^{-N_{tot}\sigma_{abs\_p}(M-m)\delta z} \quad (12)$$

Considering the expression (10) on the mirror surface, we obtain:

$$I_p^-(m\delta z, \delta t) = RI_{p0}e^{-N_{tot}\sigma_{abs\_p}2L_c}e^{N_{tot}\sigma_{abs\_p}m\delta z}, \quad (13)$$

We have then the following expression for the pump intensity at the *m/m+1* cell interface:

$$I_p(m\delta z, \delta t) = I_p^+(m\delta z, \delta t) + I_p^-(m\delta z, \delta t)$$
$$= e^{-N_{tot}\sigma_{abs\_p}m\delta z} + RI_{p0}e^{-N_{tot}\sigma_{abs\_p}2L_c}e^{N_{tot}\sigma_{abs\_p}m\delta z} \quad (14)$$

As already mention, the population inversion β is considered as constant through this entire sequence, which is of course an approximation. Indeed, after exiting slice m, the onward intensity will modify β for all incoming slices *m+1* through M. Therefore, the backward intensity heading towards the *m/(m+1)* interface will in fact travel through a gain medium already modify in terms of population inversion. The impact on β is calculated only after the full propagation of the pump within the crystal.

Having obtained the full pump intensity distribution for all spatial slices, we can now evaluate β by integrating for each spatial slice m (with $1 < m < M$) the second differential equation of (4) for this first temporal slice ($0 < t < \delta t$):

$$\frac{\partial\beta(m\delta z,t)}{\partial t} = \left[\sigma_{abs\_p} - \beta(m\delta z,t)\left(\sigma_{\sigma_{em\_p}} + \sigma_{abs\_p}\right)\right]\frac{I_p(m\delta z,\delta t)\lambda_p}{hc} - \frac{\beta(m\delta z,t)}{\tau_{21}} \tag{15}$$

In order to solve this differential equation, let us rearrange it as follows:

$$\frac{\partial\beta(m\delta z,t)}{\partial t} + \left[\left(\sigma_{em\_p} + \sigma_{abs\_p}\right)\frac{I_p(m\delta z,\delta t)\lambda_p}{hc} + \frac{1}{\tau_{21}}\right]\beta(m\delta z,t) = \sigma_{abs\_p}\frac{I_p(m\delta z,\delta t)\lambda_p}{hc} \tag{16}$$

We introduce the following variables:

$$\left.\begin{aligned} C &= \left(\sigma_{em\_p} + \sigma_{abs\_p}\right)\frac{I_p(m\delta z,\delta t)\lambda_p}{hc} + \frac{1}{\tau_{21}} \\ A &= \sigma_{abs\_p}\frac{I_p(m\delta z,\delta t)\lambda_p}{hc} \end{aligned}\right\}, \tag{17}$$

These variables are constant within this integration step and vary for different spatial and temporal slices. Although C and A are therefore depending of both m and n, for the sake of clarity, they are not indexed.

Equation (16) can be rewritten:

$$\frac{\partial\beta(m\delta z,t)}{\partial t} + C\beta(m\delta z,t) = A \tag{18}$$

It can be solved by the method of constant variation and we first consider $A=0$ to resolve the homogeneous equation:

$$\frac{\partial\beta(m\delta z,t)}{\partial t} + C\beta(m\delta z,t) = 0 \Rightarrow \beta(m\delta z,t) = He^{-Ct} \tag{19}$$

Considering now H as time dependent $H = H(t)$, the population inversion temporal evolution can now be expressed as:

$$\frac{\partial\beta(m\delta z,t)}{\partial t} = \frac{\partial H}{\partial t}e^{-Ct} - HCe^{-Ct} \tag{20}$$

While comparing with (18), we found:

$$A = \frac{\partial H}{\partial t}e^{-Ct} \tag{21}$$

With the following solution:

$$H(t) = \frac{A}{C}e^{Ct} + H_C, \tag{22}$$

with H_c an integration constant.

And then, using this expression of $H(t)$ in (19), we get for β:

$$\beta((m\delta z,t)) = \frac{A}{C} + H_c\, e^{-Ct} \tag{23}$$

H_c can be found from the initial population inversion distribution $\beta(m\delta z, t = 0) = 0$:

$$H_c = -\frac{A}{C} \tag{24}$$

And now, the exact solution for β after the first temporal slice δt is:

$$\beta(m\delta z, \delta t) = \frac{A}{C}(1 - e^{-C\delta t}) \tag{25}$$

This distribution can now be used as the new initial distribution for the second pump slice and so on… Let us then jump in time and consider the n^{th} temporal slice: the rate equations will be solved considering $\beta((n-1)\delta t)$ as the initial condition.

For this new temporal slice, the population inversion is still considered as temporarily constant (but now equal to $\beta((n-1)\delta t)$) but it now carries a non-constant spatial distribution *β(z)*. The expression for intensity at the interface *m/m+1* is:

$$I_p(m\delta z, n\delta t) = I_p^+(m\delta z, n\delta t) + I_p^-(m\delta z, n\delta t) \tag{26}$$

By analogy with expression (7), the onward component is:

$$I_p^+(m\delta z, n\delta t) = I_p^+((m-1)\delta z, n\delta t)e^{N_{tot}\{-\sigma_{abs\_p}+(\sigma_{abs\_p}+\sigma_{ems\_p})\beta(m\delta z,(n-1)\delta t)\}\delta z} \tag{27}$$

For the first slice (equation (7) and (8)), the initial β distribution did not present any spatial variation. But for temporal slice *n*, the new initial β distribution to be consider express as $\beta(z,(n-1)\delta t)$. Therefore the expression of the Intensity multiplier is:

$$e^{N_{tot}\{-\sigma_{abs\_p}+(\sigma_{abs\_p}+\sigma_{ems\_p})\beta(m\delta z,(n-1)\delta t)\}\delta z} \tag{28}$$

Consequently, the onward component of the Intensity after the m^{th} spatial slice becomes:

$$I_p^+(m\delta z, n\delta t) = I_{p0}e^{N_{tot}\{-m\sigma_{abs\_p}+(\sigma_{abs\_p}+\sigma_{ems\_p})\sum_{r=1}^{m}\beta(r\delta z,(n-1)\delta t)\}\delta z} \tag{29}$$

with the summation taking place over all slices *r* = 1 to *m*. By introducing (8) in (29), one gets:

$$I_p^+(m\delta z, n\delta t) = I_p^+(m\delta z, \delta t)e^{N_{tot}\{(\sigma_{abs\_p}+\sigma_{ems\_p})\sum_{r=1}^{m}\beta(r\delta z,(n-1)\delta t)\}\delta z} \tag{30}$$

At the end of the crystal, the pump intensity exiting the last slice *m* = *M*, has travelled through *M* slices and we have:

$$I_p^+(M\delta z, n\delta t) = I_{p0}e^{N_{tot}\{-M\sigma_{abs\_p}+(\sigma_{abs\_p}+\sigma_{ems\_p})\sum_{r=1}^{M}\beta(r\delta z,(n-1)\delta t)\}\delta z} \tag{31}$$

After reflection on the back surface of reflectivity *R*, we have, for the forward intensity I_p^- (i.e. the pump intensity entering back into the last slide) the following expression:

$$\begin{aligned} I_p^-(M\delta z, n\delta t) &= RI_p^+(M\delta z, n\delta t) \\ &= RI_{p0}e^{N_{tot}\{-M\sigma_{abs\_p}+(\sigma_{abs\_p}+\sigma_{ems\_p})\sum_{r=1}^{M}\beta(r\delta z,(n-1)\delta t)\}\delta z} \end{aligned} \tag{32}$$

The expression of I_p^- at the interface *m/m+1* is similar to (27):

$$I_p^-(m\delta z, n\delta t) = I_p^-((m+1)\delta z, n\delta t)e^{-N_{tot}\{\sigma_{abs\_p}-(\sigma_{abs\_p}+\sigma_{ems\_p})\beta((m+1)\delta z,(n-1)\delta t)\}\delta z} \quad (33)$$

At this specific location, the forward intensity I_p^- enters into slice *m* a second time. It has then travelled through (*M-m)* slices leading to:

$$I_p^-(m\delta z, n\delta t) = I_p^-(M\delta z, n\delta t)e^{-N_{tot}\{(M-m)\sigma_{abs\_p}-(\sigma_{abs\_p}+\sigma_{ems\_p})\sum_{r=m}^{M}\beta(r\delta z,(n-1)\delta t)\}\delta z}, \quad (34)$$

with the summation taking place over all slices *r* = M to *m*. Considering the expression on the mirror surface (32), we obtain:

$$I_p^-(m\delta z, n\delta t) = RI_{p0}e^{N_{tot}\left\{-M\sigma_{abs_p}+\left(\sigma_{abs_p}+\sigma_{ems_p}\right)\sum_{r=1}^{M}\beta(r\delta z,(n-1)\delta t)\right\}\delta z}$$

$$e^{-N_{tot}\{(M-m)\sigma_{abs\_p}-(\sigma_{abs\_p}+\sigma_{ems\_p})\sum_{r=m}^{M}\beta(r\delta z,(n-1)\delta t)\}\delta z} \quad (35)$$

which can be rewritten as:

$$I_p^-(m\delta z, n\delta t) = RI_{p0}e^{-N_{tot}\sigma_{abs\_p}2L_c}e^{N_{tot}\sigma_{abs\_p}m\delta z}$$

$$e^{N_{tot}\{(\sigma_{abs\_p}+\sigma_{ems\_p})\sum_{r=1}^{M}\beta(r\delta z,(n-1)\delta t)\}\delta z}$$

$$e^{N_{tot}\{(\sigma_{abs\_p}+\sigma_{ems\_p})\sum_{r=m}^{M}\beta(r\delta z,(n-1)\delta t)\}\delta z} \quad (36)$$

By introducing (13) into the last expression, one gets:

$$I_p^-(m\delta z, n\delta t) = I_p^-(m\delta z, \delta t)$$

$$e^{N_{tot}\{(\sigma_{abs\_p}+\sigma_{ems\_p})\sum_{r=1}^{M}\beta(r\delta z,(n-1)\delta t)\}\delta z}$$

$$e^{N_{tot}\{(\sigma_{abs\_p}+\sigma_{ems\_p})\sum_{r=m}^{M}\beta(r\delta z,(n-1)\delta t)\}\delta z} \quad (37)$$

Let us now calculate the spatial distribution of population inversion after n^{th} temporal slice. The integration process ($(n-1)\delta t < t < n\delta t$) is identical to the one described through equations (15) to (23). New initial condition and values of *A* and C will be used in (23):

$$\left.\begin{aligned} C &= \left(\sigma_{em\_p}+\sigma_{abs\_p}\right)\frac{I_p(m\delta z,n\delta t)\lambda_p}{hc}+\frac{1}{\tau_{21}} \\ A &= \sigma_{abs\_p}\frac{I_p(m\delta z,n\delta t)\lambda_p}{hc} \end{aligned}\right\} \quad (38)$$

$$\beta(m\delta z,t) = \frac{A}{C}+H_c\,e^{-Ct}, \qquad \beta(m\delta z,t=0) = \beta(m\delta z,(n-1)\delta t) \quad (39)$$

H_c carries a new, more general, expression:

$$H_c = \beta(m\delta z,(n-1)\delta t) - \frac{A}{C} \quad (40)$$

And the exact solution after another time slice δ*t* is:

$$\beta(m\delta z, n\delta t) = \frac{A}{C}(1 - e^{-C\delta t}) + \beta(m\delta z, (n-1)\delta t)\, e^{-C\delta t} \tag{41}$$

Finally, combining both the solution for pump intensity evolution and for population inversion, the rate equations set can be represented using (26), (27), (33) and (41):

$$\begin{cases} I_p(m\delta z, n\delta t) = I_p^+\big((m-1)\delta z, n\delta t\big)e^{N_{tot}\left\{-\sigma_{abs\_p}+\left(\sigma_{abs\_p}+\sigma_{ems_p}\right)\beta(m\delta z,(n-1)\delta t)\right\}\delta z} + \\ \qquad\qquad I_p^-((m+1), n\delta t)e^{-N_{tot}\{\sigma_{abs\_p}-(\sigma_{abs\_p}+\sigma_{ems\_p})\beta((m+1)\delta z,(n-1)\delta t)\}\delta z} \\ \beta(m\delta z, n\delta t) = \frac{A}{C}(1 - e^{-C\delta t}) + \beta(m\delta z, (n-1)\delta t)\, e^{-C\delta t} \\ \qquad\qquad m = 1 \ldots M \\ \qquad\qquad n = 1..N \end{cases} \tag{42}$$

With following initial and boundary conditions and notations:

$$\left.\begin{aligned} C &= \left(\sigma_{em\_p} + \sigma_{abs\_p}\right)\frac{I_p(m\delta z, n\delta t)\lambda_p}{hc} + \frac{1}{\tau_{21}} \\ A &= \sigma_{abs\_p}\frac{I_p(m\delta z, n\delta t)\lambda_p}{hc} \end{aligned}\right\} \tag{43}$$

$\beta_p(t=0) = \beta(m\delta z, 0\delta t) = 0$ *and* $I_p(z=0) = I_p(0\delta z, n\delta t) = I_p$

A.3. Amplification for single pass

The principle is completely the same for the laser pulse amplification case. We just have to use the set of indices associated with the lasing wavelength (1030nm) and the appropriate initial conditions. The model uses the following set of rate equations:

$$\begin{cases} I_l(m\delta z, n\delta t) = I_l^+\big((m-1)\delta z, n\delta t\big)e^{N_{tot}\{-\sigma_{abs\_l}+(\sigma_{abs\_l}+\sigma_{ems\_l})\beta(m\delta z,(n-1)\delta t)\}\delta z} + \\ \qquad\qquad I_p^-((m+1), n\delta t)e^{-N_{tot}\{\sigma_{abs\_l}-(\sigma_{abs\_l}+\sigma_{ems\_l})\beta((m+1)\delta z,(n-1)\delta t)\}\delta z} \\ \beta(m\delta z, n\delta t) = \dfrac{A}{C}(1 - e^{-C\delta t}) + \beta(m\delta z, (n-1)\delta t)\, e^{-C\delta t} \\ \qquad\qquad m = 1 \ldots M \\ \qquad\qquad n = 1..N \end{cases}$$

Special attention has to be paid to initial conditions. Since extraction occurs after pumping, the population inversion when the first laser temporal slice starts its travel is equal to the final distribution obtained after the last pump slices traveled through the gain media. We have then the following notations and initial/boundary conditions:

$\beta_l(z, t=0) = \beta_p(z, t = \tau = N\delta t)$

$I_l(z=0) = I_l(0\delta z, n\delta t) = I_l$

B. Heat transport

This annex aims at describing the code developed to model temperature distribution within a pumped gain medium of arbitrary dopant distribution for active mirror architecture. The heat transport is described by the following partial differential equation:

$$\rho C_P \frac{\partial T}{\partial t} = \nabla(k \cdot \nabla T) + Q \tag{1}$$

Where ρ is the density, C_p is the heat capacity, k is the heat conductivity, T the temperature and Q is a thermal load. Let us consider a one dimensional approach for temperature distribution estimation. The heat source term is considered uniform in the plane perpendicular to the pump source axis. We have therefore the following equation and boundary conditions:

$$\rho C_P \frac{\partial}{\partial t} T(z,t) = \frac{\partial}{\partial z} k(z,t) \frac{\partial}{\partial z} T(z,t) + k(z,t) \frac{\partial^2}{\partial z^2} T(z,t) + Q(z,t) \tag{2a}$$

$$k \left(\frac{\partial T}{\partial z} \right)_{z=0} = h_{air} \left(T(0,t) - T_{air} \right) \tag{2b}$$

$$k \left(\frac{\partial T}{\partial z} \right)_{z=L} = -h_{water} \left(T(L,t) - T_{water} \right) \tag{2c}$$

where h_{air}, T_{air} and h_{water}, T_{water}, are heat exchange coefficients and temperatures for air and water (water is used as a coolant in Lucia system) and L is the gain medium length. As an initial condition ($t = 0$), we assume that, the gain medium has the same temperature as the air.

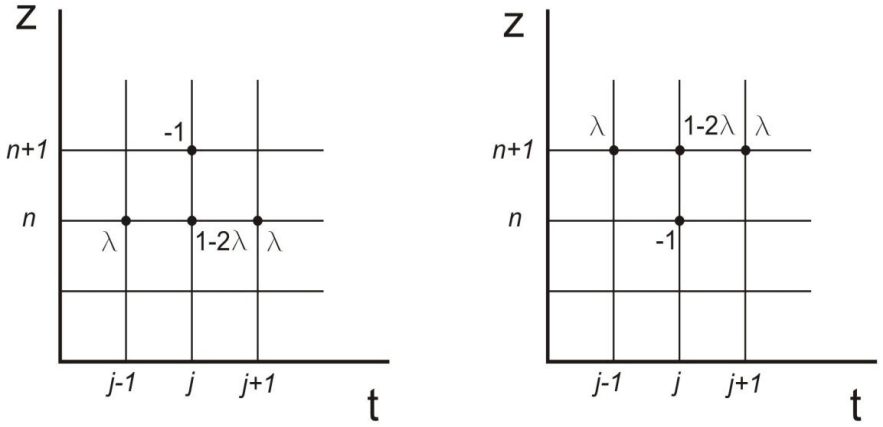

Fig. B1. Two simple schemes for finite differences method: explicit or forward (left) and implicit or backward (right). Horizontal axis is related to time whereas the vertical one is related to space coordinate. j is the time index, n the space index.

Through space and time coordinates z and t, the heat conductivity $k(z,t)$ is a function of both doping concentration and temperature. Indeed the doping distribution varies within the gain medium thickness along the z axis while the temperature evolves during time.

To start with, let us consider $k = const$ and .

A Finite Elements Method based 1D mathematical model is developed to solve equation (2a). For simplification purposes, let us introduce $\lambda = k\Delta t/\left(\rho C_P \cdot \Delta z\mathrm{I}\right)$, where *Δt* and *Δz* are respectively time and space steps. Two approaches are schematically shown on the Fig. B1.

But convergence can only be achieved if $\Delta t \le \Delta z^2/k$. Therefore, to avoid this limitation, we have chosen to develop our model with the *implicit method* (Fig. 1, right), also called *backward method*. Then, due to this discretization and upper considerations, the heat equation (still without heat source) turns into:

$$\rho C_P \frac{T_j^{n+1} - T_j^n}{\Delta t} = k \frac{T_{j+1}^{n+1} - 2T_j^{n+1} + T_{j-1}^{n+1}}{\Delta z^2} \tag{4}$$

For the current term we have:

$$T_j^n = T_j^{n+1}\left(1+2\lambda\right) - \lambda T_{j+1}^{n+1} - \lambda T_{j-1}^{n+1}, \tag{5}$$

The implementation of the boundary conditions is illustrated on the sketch of Fig. B2:

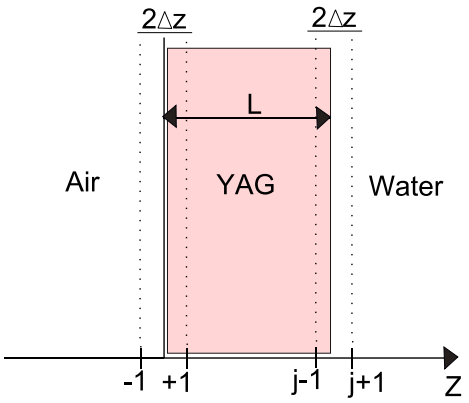

Fig. B2. Boundary Conditions

For $z = 0$ (left boundary condition), we have for (2b):

$$\frac{T_1^{n+1} - T_{-1}^{n+1}}{2\Delta z} = \frac{h_{air}}{k}\left(T_0^{n+1} - T_{air}\right) \tag{6}$$

Introducing $\varkappa = -2h_{air}\Delta z/k$, we can rewrite it as:

$$T_{-1}^{n+1} = T_1^{n+1} + \varkappa.\left(T_{air} - T_0^{n+1}\right) \tag{7}$$

Combining (5) and (7) for $T_{j=0}^n$, we get:

$$\begin{aligned} T_0^n &= T_0^{n+1}\left(1+2\lambda\right) - \lambda T_1^{n+1} - \lambda\left(T_1^{n+1} + \varkappa\left(T_{air} - T_0^{n+1}\right)\right) \\ T_0^{n+1}&\left(1+2\lambda+\lambda\varkappa\right) - 2\lambda T_1^{n+1} = T_0^n + \lambda\varkappa T_{air} \end{aligned} \tag{8}$$

Similarly, for the right boundary condition, introducing $\delta = 2h_{water}\Delta z/k$ with (2c) leads to:

$$\begin{aligned} T_j^n &= T_j^{n+1}\left(1+2\lambda+\lambda\delta\right)-2\lambda T_{j-1}^{n+1}-\lambda\delta T_{water} \\ T_j^{n+1}\left(1+2\lambda+\lambda\delta\right)-2\lambda T_{j-1}^{n+1} &= T_j^n+\lambda\delta T_{water} \end{aligned}, \tag{9}$$

A matrix representation for (8) and (9) is:

$$\begin{pmatrix} \left(1+2\lambda+\lambda\varkappa\right) & -2\lambda & 0 & 0 & \cdots & 0 \\ -\lambda & 1+2\lambda & -\lambda & 0 & \cdots & 0 \\ 0 & -\lambda & 1+2\lambda & -\lambda & \vdots & \vdots \\ \vdots & \vdots & \vdots & \vdots & \vdots & \vdots \\ 0 & \cdots & \cdots & \cdots & -2\lambda & \left(1+2\lambda+\lambda\delta\right) \end{pmatrix} \begin{pmatrix} T_0^{n+1} \\ T_1^{n+1} \\ \vdots \\ T_j^{n+1} \end{pmatrix} = \begin{pmatrix} T_0^n+\lambda\varkappa T_{air} \\ T_1^n \\ T_2^n \\ \vdots \\ T_j^n+\lambda\delta T_{water} \end{pmatrix} \tag{10}$$

Now let us now give space dependence to heat conductivity: $k=\varepsilon(z)$. Then, heat transfer equation (1) turns into:

$$\frac{\partial}{\partial t}T\left(z,t\right)=\frac{1}{\rho C_P}\left(\frac{\partial}{\partial z}\varepsilon\left(z\right)\right)\left(\frac{\partial}{\partial z}T\left(z,t\right)\right)+\frac{\varepsilon(z)}{\rho C_P}\frac{\partial^2}{\partial z^2}T\left(z,t\right) \tag{11}$$

Using the same discretization as before, we obtain:

$$\frac{T_j^{n+1}-T_j^n}{\Delta t}=\frac{1}{\rho C_P}\frac{\varepsilon_{j+1}-\varepsilon_{j-1}}{2\Delta z}.\frac{T_{j+1}^{n+1}-T_{j-1}^{n+1}}{2\Delta z}+\frac{\varepsilon_j}{\rho C_P}.\frac{T_{j+1}^{n+1}-2T_j^{n+1}+T_{j-1}^{n+1}}{\Delta z^2} \tag{12}$$

$$T_j^n=\left(\frac{\gamma}{4}\left(\varepsilon_{j+1}-\varepsilon_{j-1}\right)-\varepsilon_j\gamma\right)T_{j-1}^{n+1}+\left(2\varepsilon_j\gamma+1\right)T_j^{n+1}-\left(\frac{\gamma}{4}\left(\varepsilon_{j+1}-\varepsilon_{j-1}\right)+\varepsilon_j\gamma\right)T_{j+1}^{n+1} \tag{13}$$

where $\gamma=\Delta t\Big/\left(\rho C_P\left(\Delta z\right)^2\right)$.

Considering that we have $\left(\varepsilon_{j+1}-\varepsilon_{j-1}\right)\Big/2\Delta z=\left(\varepsilon_{j+1}-\varepsilon_j\right)\Big/\Delta z$, (13) can then be rewritten as:

$$T_j^n=\left(\frac{\gamma}{2}\left(\varepsilon_{j+1}-\varepsilon_j\right)-\varepsilon_j\gamma\right)T_{j-1}^{n+1}+\left(2\varepsilon_j\gamma+1\right)T_j^{n+1}-\left(\frac{\gamma}{2}\left(\varepsilon_{j+1}-\varepsilon_j\right)+\varepsilon_j\gamma\right)T_{j+1}^{n+1} \tag{14}$$

Introducing $\mu_{j+1}=\left(\frac{\gamma}{2}\left(\varepsilon_{j+1}-\varepsilon_j\right)-\varepsilon_j\gamma\right)$ and $\nu_{j+1}=\left(\frac{\gamma}{2}\left(\varepsilon_{j+1}-\varepsilon_j\right)+\varepsilon_j\gamma\right)$, (14) becomes :

$$T_j^n=\mu_{j+1}T_{j-1}^{n+1}+\left(2\varepsilon_j\gamma+1\right)T_j^{n+1}-\nu_{j+1}T_{j+1}^{n+1} \tag{15}$$

Let us now take into account k dependence with z while expressing the boundary conditions. For left boundary, equation (7) transforms into:

$$T_{-1}^{n+1} = -2\Delta z A T_{air} + 2\Delta z A T_0^{n+1} + T_1^{n+1}, \tag{16}$$

with $A = -h_{air}/\varepsilon(z)$. For $j = 0$, (15) becomes:

$$T_0^n = \mu_1 T_{-1}^{n+1} + (2\varepsilon_0\gamma + 1)T_0^{n+1} - \nu_1 T_1^{n+1} \tag{17}$$

and introducing (16) into (17) leads to :

$$T_0^n = \left(2\mu_1\Delta z A + (2\varepsilon_0\gamma + 1)\right)T_0^{n+1} - 2\mu_1\Delta z A T_{air} + (\mu_1 - \mu_2)T_1^{n+1}, \tag{18}$$

Similarly, for the heat equation at the right boundary, we have:

$$T_j^n = \left(2\varphi_j\Delta z B + (2\varepsilon_j\gamma + 1)\right)T_j^{n+1} - 2\psi_j\Delta z B T_{water} + (\varphi_j - \psi_j)T_{j-1}^{n+1}, \tag{19}$$

where $B = -h_{water}/k$, $\varphi_j = \left(\frac{\gamma}{2}(\varepsilon_j - \varepsilon_{j-1}) - \varepsilon_j\gamma\right)$ and $\psi_j = \left(\frac{\gamma}{2}(\varepsilon_j - \varepsilon_{j-1}) + \varepsilon_j\gamma\right)$

With this scheme, the one-dimensional model of a thermal system consisting of a thick plane with asymmetric boundary conditions can be fully described. The presence of a thermal load $Q(z)$ can now be introduce and (11) rewritten as:

$$\frac{\partial}{\partial t}T(z,t) = \frac{1}{\rho C_P}\left(\frac{\partial}{\partial z}\varepsilon(z)\right)\left(\frac{\partial}{\partial z}T(z,t)\right) + \frac{\varepsilon(z)}{\rho C_P}\frac{\partial^2}{\partial z^2}T(z,t) + Q(z) \tag{20}$$

A discretized expression is equation (12) to which the term $Q_j/\rho C_P$ is simply added in the right hand, leading to:

$$T_j^n = \left(\frac{\gamma}{4}(\varepsilon_{j+1} - \varepsilon_{j-1}) - \varepsilon_j\gamma\right)T_{j-1}^{n+1} + (2\varepsilon_j\gamma + 1)T_j^{n+1} - \left(\frac{\gamma}{4}(\varepsilon_{j+1} - \varepsilon_{j-1}) + \varepsilon_j\gamma\right)T_{j+1}^{n+1} + \frac{\Delta t}{\rho C_P}Q_j \tag{21}$$

A matrix representation is as following:

$$\begin{pmatrix} T_0^n \\ \vdots \\ T_j^n \end{pmatrix} = \begin{pmatrix} \cdots & \cdots & \cdots \\ \vdots & \ddots & \vdots \\ \cdots & \cdots & \cdots \end{pmatrix}\begin{pmatrix} T_0^{n+1} \\ \vdots \\ T_j^{n+1} \end{pmatrix} + \begin{pmatrix} Q_0 \\ \vdots \\ Q_j \end{pmatrix}$$

where $Q_0 \ldots Q_j$ represents the set of discrete values for thermal load. As it can be seen, its introduction does not imply major changes in the logic of calculations. The steady-state case can be modeled by considering a time long enough from the pumping beginning.